2013

Creep-fatigue Crack Initiation And Propagation Of A Notched Stainless Steel

Scott Keller
University of Central Florida

CREEP-FATIGUE CRACK INITIATION AND PROPAGATION OF A NOTCHED STAINLESS STEEL

by

SCOTT G. KELLER
B.S. University of Central Florida, 2008
M.S. University of Central Florida, 2009

A dissertation submitted in partial fulfillment of the requirements
for the degree of Doctor of Philosophy
in the Department of Mechanical and Aerospace Engineering
in the College of Engineering and Computer Science
at the University of Central Florida
Orlando, Florida

Spring Term
2013

Major Professor: Ali P. Gordon

ABSTRACT

Premature failures of vital gas turbine components, such as blades and vanes, have been the result of increasing demands of power generation facilities. As power needs fluctuate throughout the day, operators are quickly firing up gas turbines as a means of providing instant power. Traditionally, these engines run at constant operating conditions; however, contemporary operating conditions call for these engines to be applied on an "as necessary" basis. The result of the cyclic startup and shutdown of gas turbines has led to a phenomenon known as creep-fatigue (CF). A coupling of two primary failure mechanisms in gas turbines, CF conditions exacerbate the mechanisms of creep and fatigue, ultimately leading to a premature failure of components. Traditionally, independent creep and fatigue analyses are conducted to determine the limiting life factor of gas turbines. Recently, fracture mechanics approaches have been successfully used in extending the traditional analyses to include fatigue- and creep-crack growth analyses. Founded on existing approaches to creep-fatigue crack growth analyses, including experimental elastic and plastic fracture mechanics approaches, a coupled creep-fatigue crack initiation and propagation model is developed.

To bring these models to fruition, the current study utilizes the development of an experimental setup capable of subjecting a modified fracture specimen to creep-fatigue conditions. With two test temperatures key to turbine components, a blunt notch compact tension specimen was subjected to trapezoidal load waveforms with various lengths of holds at maximum load. A developed direct current potential drop (DCPD) system was used to monitor crack initiation and crack lengths throughout the duration of tests. Numerical simulations on a representative specimen were conducted, to correlate and predict key fracture mechanics parameters used in the development of creep-fatigue crack initiation and propagation models.

Metallurgical analysis of specimens was conducted, implementing both optical and scanning electron microscopy. From the experimental and numerical studies, a model for both the initiation and propagation of cracks on a single specimen is furnished. Through the use of elastic-plastic fracture mechanics parameters, the proposed models are observed to predict crack initiation and replicate crack propagation rates based on the experimental conditions. Assisting in the implementation of the proposed models, intended uses and applications for the models are provided, simplifying the life prediction analyses for components expected to fail due to creep-fatigue service conditions.

To my parents
With the deepest love and gratitude

ACKNOWLEDGMENTS

This dissertation would not have been possible without the help and support of several individuals through professional and personal affiliations. Their contributions have helped to develop this body of work and I am indebted for all of their contributions.

The support provided by my advisor, Dr. Ali Gordon, served as the backbone throughout my academic career and I cannot begin to thank him enough. Through his guidance, teaching, advising and patience, Dr. Gordon was always a motivating factor. There was never a time that I could not rely on his expertise and guidance to overcome any obstacle throughout this, and other, investigations and am truly grateful for his full support.

I would like to thank my dissertation committee members, Dr. Faissal Moslehy, Dr. Seetha Raghavan, Dr. Challapalli Suryanarayana, and Dr. Kevin Mackie, for their insightful and helpful contributions. Their support has helped to focus my research and improved the contents of this work.

A special thanks goes to a fellow researcher and personal friend, Justin Karl. His expertise in mechanical testing proved essential in completing some of the tasks within this dissertation. Whether it was helping with a late night experimental setup/teardown or the occasional tennis match, his assistance was invaluable. Another research assistant, Allen Owji, is credited with portions of the macroscopic imaging contained within this dissertation and his assistance is appreciated. Additionally, members of the Mechanics of Materials Research Group, including Thomas Bouchenot, Steven Kraft, Calvin Stewart, Bryan Zuanetti, Charles Mansfield, Nathan Mutter, Jay Zhang, amongst others, are thanked for their efforts.

Several individuals outside of the university were extremely helpful, including Dave Day and Rick Nelson from Power Systems Manufacturing, Kenneth Blount from Epsilon

Technology, Tory Jensen from MTS Systems, Michael Gilhooly from GE, and Joe Cardinal from Southwest Research Institute. Their contributions greatly enhanced the work contained herein and are thanked for their assistance and expertise.

I am grateful for the friendship and support from several of my close friends, including Brandon and Nikki, the Stovall family, Jacob, and the Sidebottom family. Much of my time spent outside of the lab was with these individuals and I appreciate their generosity and cherish their friendship. In many ways, they have all become my extended family and provided memories to last a lifetime. To the Dinner Club Crew, thank you for the welcome distraction from research and class, and for forcing me to leave the lab late at night. The support provided outside of the academic realm made it possible to continue on in my academic endeavors and provided a solid foundation for life in general.

Lastly, none of this would have been possible without the unwavering love and support from my family: Mom and Dad, Joanne, Elizabeth, Justin, and Mike. I have learned so much from each of them regarding life, love, happiness, and family, shaping the individual that I have become. These lessons allowed me to understand love, recognizing it fully when I met Allison. Her love, support and patience was crucial to the completion of this work. To her and her family, I look forward to growing our families into one. In no way would I have been able to complete this work without the full support of any of them and I am extremely blessed for the family and friends I am surrounded by.

TABLE OF CONTENTS

LIST OF FIGURES xi
LIST OF TABLES xix
LIST OF NOMENCLATURE xx
CHAPTER 1 INTRODUCTION 1
1.1 Background and Motivation 1
1.2 Research Objectives 5
CHAPTER 2 LITERATURE REVIEW AND BACKGROUND 8
2.1 Fatigue Crack Initiation 8
2.1.1 Material Response at Notch Tip 9
2.1.2 Local Strain Approaches to Fatigue Crack Initiation 17
2.1.3 Linear Elastic Fracture Mechanics Approaches to Crack Initiation 20
2.2 Fatigue and Creep Crack Propagation 26
2.2.1 Linear Elastic Fracture Mechanics 28
2.2.2 Elastic-Plastic Fracture Mechanics 33
2.2.3 Time-Dependent Fracture Mechanics 37
2.3 Creep-Fatigue Life Estimation 39
2.3.1 Creep-Fatigue Experimental Approaches 40
2.3.2 Creep-Fatigue Numerical Approaches 49
2.4 Mechanical Behavior of SS 304 55
2.4.1 Tensile Properties 58
2.4.2 Creep Properties 60
2.4.3 Fatigue and Fracture Properties 62
2.5 Application of Analytical Life Models 67
2.5.1 Relevant Life Prediction Methodologies Overview 67
2.5.2 Future Work in Creep-Fatigue Analytical Modeling 70
CHAPTER 3 EXPERIMENTAL APPROACH 73
3.1 Overview of Experimental Approach 73
3.2 Tensile Testing 76
3.3 Creep-Fatigue Specimen Design 78
3.4 Creep-Fatigue Testing 83

3.4.1 MTS Test Frame and Fixtures 85
3.4.2 Crack Mouth Opening Displacement Gage 89
3.4.3 Direct Current Potential Drop Method 91
3.5 High Temperature Testing 93
3.5.1 Stress-Free Oxidation Testing 93
3.5.2 Creep-Fatigue Environmental Chamber and Frame 95
3.6 Metallurgical Analysis 98
3.6.1 Optical Microscopy 99
3.6.2 Scanning Electron Microscopy 101
3.7 Experimental Data Post Processing 102
3.8 Data Management and Organization 104
CHAPTER 4 EXPERIMENTAL RESULTS AND MICROSCOPY 106
4.1 Tensile Test Results 106
4.2 Stress-Free Oxidation Test Results 113
4.3 Creep-Fatigue Simulation and Test Results 115
4.3.1 Monotonic Numerical Simulations 118
4.3.2 Comments on Experimental Data 127
4.3.3 Crack Initiation Results 134
4.3.4 Crack Propagation Results 143
4.3.5 Microscopy 148
CHAPTER 5 CREEP-FATIGUE MODEL CORRELATIONS 168
5.1 Motivation 168
5.2 Crack Initiation and Crack Propagation Model Development 170
5.2.1 Creep-Fatigue Crack Initiation Model 170
5.2.2 Creep-Fatigue Crack Propagation Model 173
5.3 Parameter and Constant Estimation 176
5.4 Crack Initiation and Crack Propagation Model Correlations 179
CHAPTER 6 CREEP-FATIGUE MODEL IMPLEMENTATION 185
6.1 Implementation of Creep-Fatigue Model 185
6.2 Creep-Fatigue Model Extrapolations 190
6.3 Extension of Models to Linear Elastic Scenarios 200

6.4 Summary of Capabilities and Limitations 202
6.4.1 Creep-Fatigue Crack Initiation Model 202
6.4.2 Creep-Fatigue Crack Propagation Model 204
CHAPTER 7 CONCLUSIONS 208
CHAPTER 8 RECOMMENDATIONS 211
APPENDIX A SPECIMEN AND FIXTURE DRAWINGS 214
APPENDIX B CURVE FITTING SOURCE CODE 225
APPENDIX C EXPERIMENTAL SPECIMEN DATA 236
REFERENCES 259

LIST OF FIGURES

Figure 1.1: General Electric 7FA Heavy Duty Industrial Gas Turbine [General Electric 7FA, 2012]. 1

Figure 2.1: Amplification of stress due to a geometric discontinuity [Riley et al., 2007]. 10

Figure 2.2: Relative stress gradient at an arbitrary notch tip [Filippini, 2000]. 14

Figure 2.3: Number of cycles to crack initiation implementing Neuber's rule and the Smith-Watson-Topper approach for mean stress life prediction [Lazzarin et al., 1997]. 18

Figure 2.4: Prediction of failure lives for SS304 at high temperature utilizing Neuber's rule with R = -1 loading [Sakane and Ohnami, 1986]. 19

Figure 2.5: Relationship of the average local-strain accumulation value to fatigue crack initiation at room temperature [Furuya and Shimada, 1986]. 20

Figure 2.6: Blunted notch tip of Al2024-T351 subjected to 3.5% NaCl stress corrosion cracking [Creager and Paris, 1967]. 21

Figure 2.7: Relationship between Eq. (2.19) and crack initiation for various fatigue tests [Tanaka et al., 1983]. 23

Figure 2.8: Fatigue crack initiation predicting using the normalize form of Eq. (2.20) [Boukharouba et al., 1995]. 24

Figure 2.9: Traditional approaches for local strain and fracture mechanics approaches to analytical and numerical life prediction. 26

Figure 2.10: Fatigue crack growth curve identifying the three stages of fatigue crack growth, with LEFM asymptotic values. 27

Figure 2.11: Broad tend of crack growth data on Al 7075-T6 amongst various test programs [Paris and Erdogan, 1963]. 28

Figure 2.12: Fatigue crack growth with the incorporation of the load effect [Forman et al., 1967]. 29

Figure 2.13: Plastic wake as a result of crack extension under constant amplitude load control testing [Elber, 1971]. 30

Figure 2.14: Figure 2.14: Correlation of fatigue crack growth rates with ΔK and ΔKeff for Al 2024-T3 [Newman, 1984]. 31

Figure 2.15: Crack growth rates where short and long crack rates are shown, with initial rates for short cracks higher than that for long cracks [El Haddad et al., 1980]. 32

Figure 2.16: Calculation of ΔJ during cyclic loading, taking into account crack closure [Dowling and Begley, 1976]. 34

Figure 2.17: Crack growth rates obtained under linear elastic and gross plasticity conditions [Dowling and Begley, 1976]. 35

Figure 2.18: Creep-Fatigue crack growth rates as a function of the total *J*-integral range with and without hold times [Merah et al., 1999]. 36

Figure 2.19: Fatigue crack growth rates with and without holds, related to LEFM methods through approximation the C^* parameter [Saxena et al., 1981]. 38

Figure 2.20: Location of specimen obtained from turbine blade used in creep life prediction experiments [Marahleh et al., 2006]. 41

Figure 2.21: Full scale superalloy aircraft turbine blade used in experimental investigations [Yan and Nie, 2008]. 42

Figure 2.22: Hold time effect on fatigue crack growth in IN 718 [Saxena et al., 1981]. 44

Figure 2.23: Correlation between Stage II crack growth and ΔJ [Baik and Kim, 2000]. 45

Figure 2.24: Effect of overload on CFCG rates using $(da/dt)_{avg}$ approach [Yoon (II) et al., 1993]. 46

Figure 2.25: Comparison of experimental and analytical values of $(C_t)_{avg}$ incorporating the creep reversal parameter [Grover and Saxena, 1999]. 48

Figure 2.26: Crack growth prediction of SS304 at 650°C under various waveforms using the MATMOD and CRACKMOD constitutive models [Lee and Kim, 1996]. 51

Figure 2.27: Comparison of experimental and simulated long crack growth data using the Chaboche model with Cohesive Zone crack model [Bouvard et al., 2009]. 53

Figure 2.28: Comparison of experimental and predicted cycles to crack initiation based on Chaboche material model with damage accumulation law [Rauch and Roos, 2008]. 54

Figure 2.29: Traditional approachs for crack growth analyses, including elastic, plastic and time-dependent formulations 55

Figure 2.30: Typical microstructure of SS304 with MC inclusion clusters, [ASM, 2007]. 56

Figure 2.31: Mass gain of virgin and nitrided samples exposed to 1472°F (800°C) [Issartel et al., 2004] 58

Figure 2.32: Full-range (left) and amplified small-strain (right) stress-strain curves for SS304 from room temperature to 800°F (427°C) [Mills, 1988]. 59

Figure 2.33: Fracture surface appearances of a fracture SS304 specimen under (left) light microscope and (right) scanning electron microscope [Mills, 1988]. 60

Figure 2.34: Dependence of (left) minimum creep rate and (right) activation area on mean effective stress in creep studies on SS304 [Chopra and Nateson, 1977]. 61

Figure 2.35: Maximum principal (let) and maximum effective (right) stress versus rupture time for uniaxial and triaxial stress states [Kim et al., 1991]..... 62

Figure 2.36: Crack extension rates for constant (left) and alternating (right) load patterns on SS304 at 1000°F (538°C) [Han and Kim, 2001]. 63

Figure 2.37: Fatigue crack propagation rates for SS304 at room and elevated temperatures [James and Schwenk, 1971]..... 64

Figure 2.38: Acceleration of crack growth rates for increasing *R*-ratio under constant amplitude loading [Fan et al., 2008]. 65

Figure 3.1: Tensile and Creep-Fatigue specimen orientation in the sheet of raw material..... 77

Figure 3.2: Picture of high temperature tensile test with associated measurement devices. 79

Figure 3.3: Example of a creep-fatigue test specimen, with dimensions specified by ASTM Standards [ASTM E2670-10]. 80

Figure 3.4: Blunt notched creep-fatigue specimen utilized in this investigation. 80

Figure 3.5: Specimen orientation for C(T) specimens machined from plate. 81

Figure 3.6: Blunt notch C(T) specimen post-polishing process..... 83

Figure 3.7: Schematic of experimental setup used in this investigation. 84

Figure 3.8: MTS Insight 5kN implemented in this investigation. 85

Figure 3.9: Example of plastic strain response on blunt notch C(T) specimen subjected to plasticity-inducing load. 86

Figure 3.10: Tension testing clevises used with extension arms to allow for testing in furnace. 87

Figure 3.11: One cycle of load control waveforms used in creep-fatigue load-control routines. 88

Figure 3.12: Epsilon 3548 CMOD gage with high temperature extension arms. 90

Figure 3.13: Blunt notch C(T) specimen with CMOD gage inserted and DCPD lead wires and thermocouple welded to specimen. 92

Figure 3.14: Raw material remaining from specimen machining used to obtain SFO specimens. 94

Figure 3.15: Barnstead Thermolyne 48000 furnace used in SFO tests. 95

Figure 3.16: Custom 80/20 frame used to position CMOD gage and ceramic band heater. 96

Figure 3.17: Complete experimental setup, including CMOD, DCPD system and furnace controller. 98

Figure 3.18: Optical microscopy center at MPCL. 99

Figure 3.19: Sectioning procedures used to mount, polish and inspect SFO (top) and creep-fatigue (bottom) specimens under a metallographic microscope. 100

Figure 4.1: Full range stress-strain curves for room and elevated temperatures. 107

Figure 4.2: Expanded view of the stress-strain curves in the low strain regime with fitted Ramberg-Osgood approximation. 108

Figure 4.3: Tensile specimens tests at test temperatures of (left) 68°F (20°C) (center) 600°F (315°C) and (right) 800°F (427°C). 110

Figure 4.4: Fracture surface of tensile specimen, Ten1, tested at 68°F (20°C). 111

Figure 4.5: Fracture surface of tensile specimen, Ten2, tested at 600°F (315°C). 111

Figure 4.6: Fracture surface of tensile specimen, Ten3, tested at 800°F (427°C). 112

Figure 4.7: Overview of SS304 Stress-Free Oxidation specimens. 114

Figure 4.8: Stress-free oxidation specimens tested at 600°F (315°C). 114

Figure 4.9: Stress-free oxidation specimens tested at 800°F (427°C). 115

Figure 4.10: Load waveform used during crack initiation and propagation experiments. 117

Figure 4.11: Correlation of material model used in FEA simulations with experimental tensile data at elevated temperatures. 119

Figure 4.12: One half of a creep-fatigue specimen used in numerically simulating the response of the material under a monotonic load. 120

Figure 4.13: Simulated stress distribution along the notch tip for 600°F (315°C) and 800°F (427°C) simulations subjected to a 800lbf (3.56kN) and 825lbf (3.67kN) load, respectively. 121

Figure 4.14: Simulated plastic strain distribution along the notch tip for 600°F (315°C) and 800°F (427°C) simulations subjected to a 800lbf (3.56kN) and 825lbf (3.67kN) load, respectively. 122

Figure 4.15: Stress values, in y-direction extracted along the length of the notch tip for 600°F (315°C) and 800°F (427°C) simulations subjected to a 800lbf (3.56kN) and 825lbf (3.67kN) load, respectively. 124

Figure 4.16: Strain values, in y-direction, extracted along the length of the notch tip for 600°F (315°C) and 800°F (427°C) simulations subjected to a 800lbf (3.56kN) and 825lbf (3.67kN) load, respectively. 124

Figure 4.17: Simulated stress distribution through the width and mid-plane of the creep-fatigue specimen used in calculating χ for 600°F (315°C) and 800°F (427°C) simulations subjected to a 800lbf (3.56kN) and 825lbf (3.67kN) load, respectively. 125

Figure 4.18: Method of J-integral calculation for increasing number of contours for a 3D simulation in ANSYS. 126

Figure 4.19: Calculation of *J*-integral at the notch tip through the thickness of the simulated specimen in ANSYS. 127

Figure 4.20: Nonlinear behavior in the load versus load-line displacement curve for the first cycle of a CF specimen, BN11. 129

Figure 4.21: Example of the load versus load-line displacement for the first one hundred cycles of a specimen, BN11, in Fig. 4.20. 129

Figure 4.22: Method of calculating J_1 and ΔJ for C(T) specimens, based on method of [Dowling and Begley, 1976]. 130

Figure 4.23: Example of the load versus load-line displacement for the entirety of a test during CFCIG experiments, with data from BN10 with 50s tensile hold. 131

Figure 4.24: Example of the maximum load-line deflection versus cycle for an entire test, e.g. BN7. 132

Figure 4.25: Example of the crack length as a function of cycle count, calculated from the DCPD monitoring system. 133

Figure 4.26: Example of crack initiation determination based on a 10% increase or decrease of the CMOD or DCPD measurement, respectively. 136

Figure 4.27: Example of crack initiation determination based on the bisection method utilizing the slopes of the steady-state and unstable portions of the (left) CMOD gage displacement or (right) the derivative of the CMOD gage displacement with respect to the change in cycles. 137

Figure 4.28: Comparison of the crack initiation cycle to failure cycle for all specimens using the three different crack initiation criterions. 138

Figure 4.29: Saturation of the calculated *J* for the first cycle based on the tensile hold period during experiments..... 139

Figure 4.30: Load ratio effect on the crack initiation, in which the lower load ratio produced a shorter life to crack initiation. 141

Figure 4.31: Crack initiation based on the calculated *J* for the first cycle at the two load ratios implemented in experimental routines. 141

Figure 4.32: Crack growth rate curves at 600°F (315°C) and 800°F (427°C)..... 145

Figure 4.33: Crack growth rate curves for load ratios of $R = 0.05$ and $R = 0.1$ at both test temperatures. 146

Figure 4.34: Crack growth rate curves based on the duration of a positive tensile hold period for both test temperatures. 147

Figure 4.35: Crack growth rate curves based on the ratio of the load rise time to hold time. ... 148

Figure 4.36: Overview of blunt notch C(T) specimen notch roots prior to separation of specimens. 150

Figure 4.37: Overview of crack profiles for all blunt notch C(T) specimens prior to separation of specimens. 151

Figure 4.38: Overview of fracture surfaces of C(T) specimens upon separation of specimens 152

Figure 4.39: Example of the large scale plasticity observed during the duration of a single creep-fatigue experiment. 153

Figure 4.40: Extent of secondary cracking for a specimen with a (left) high initial *J*, as in BN5 and a (right) low initial *J*, as in BN15. 153

Figure 4.41: Heat tint observed on specimens exposed to (top) 600°F (315°C) and (bottom) 800°F (427°C). 154

Figure 4.42: Transition from plane-strain crack growth to extensive plasticity and ductile tearing. 155

Figure 4.43: Grain structure of the subject SS304 used in this investigation. 156

Figure 4.44: Large secondary crack observed in the notch root of specimen BN9, subjected to a temperature of 800°F (427°C) with a tensile hold period of 10s. 157

Figure 4.45: Competing dominant cracks observed near the center of the notch root in specimen BN3, subjected to a temperature of 800°F (427°C) with a tensile hold period of 20s. .. 158

Figure 4.46: Secondary crack observed in the root of a notch for specimen BN8, subjected to a temperature of 800°F (427°C) with a tensile hold period of 20s. 158

Figure 4.47: Crack surfaces of specimens tested at 800°F (427°C) with hold periods of 2, 10, 20, 50 and 100s. 159

Figure 4.48: Sample fracture surfaces of specimens tested at 600°F (315°C) as viewed under the SEM. 161

Figure 4.49: Sample fracture surfaces of specimens tested at 800°F (427°C) as viewed under the SEM. 162

Figure 4.50: Fatigue striations on the surface of large flake observed on fracture surface of BN6. 163

Figure 4.51: Transition region (left) from crack growth to ductile tearing on BN11 tested at 600°F (315°C) with a tensile hold of 20s, with a magnified view provided (right). 164

Figure 4.52 Stage I crack growth striations in vicinity close to the notch, shown on BN13 tested at 600°F (315°C) with a tensile hold of 20s, with a magnified view provided (right).: . 165

Figure 4.53: Stage II-III crack growth striations near the end of the crack, shown on BN14 tested at 600F (315C) with a tensile hold of 50s, with a magnified view provided (right). 165

Figure 4.54: Extensive secondary crack observed on fracture surfaces of specimens subjected to (left) 600°F (315°C) and (right) 800°F (427°C). 166

Figure 5.1: Effects of load ratio, *R*, on the observed and simulated crack initiation of SS304. 172

Figure 5.2: Observed and simulated crack propagation of SS304 under creep-fatigue conditions. 174

Figure 5.3: Schematic of constant determination using the Microsoft Excel approach. 178

Figure 5.4: Schematic of constant determination using the Eureqa approach. 179

Figure 5.5: Experimental and predicted crack initiation results using the proposed creep-fatigue crack initiation model. 180

Figure 5.6: Experimental and predicted crack propagation results using the proposed creep-fatigue crack propagation model. 181

Figure 5.7: Correlation of crack initiation life using the proposed creep-fatigue crack initiation model on SS304 at 600°F (315°C) and 800°F (427°C). 182

Figure 5.8: Correlation of crack propagation rates using the proposed creep-fatigue crack propagation model on SS304 at 600°F (315°C) and 800°F (427°C). 183

Figure 5.9: The affect of constants on predicted behavior used in the (left) crack initiation and (right) crack propagation models. 184

Figure 6.1: Schematic of suggested implementation routine for the proposed crack initiation model..... 187

Figure 6.2: Schematic of suggested implementation routine for the proposed crack propagation model..... 189

Figure 6.3: Predictions of crack initiation cycle based on various J_1 and R values..... 191

Figure 6.4: Effect of modifying the J_1 exponent, p, to unity on the predicted number of cycles. 193

Figure 6.5: Effect of modifying the load ratio exponent, q, to unity on the predicted number of cycles..... 194

Figure 6.6: Predictions of crack propagation rates over various load ratio values. 195

Figure 6.7: The effect of increasing either exponent a, b, or c results in a lower predicted crack propagation rate. 197

Figure 6.8: Effect of decreasing the J_{stab} parameter for identical test conditions, resulting in a lower acceleration of crack growth rates. 198

Figure 6.9: A decrease in the J_c constant results in a increase in both the predicted crack growth rate and the acceleration of predicted rates..... 199

Figure 6.10: Effect of compensating the proportional constant, C, to account for uncertainty in the instability-related constant, J_c. 200

Figure 6.11: The effect of dropping ΔJ below the ΔJ_{stab} value on crack propagation rate predictions..... 206

LIST OF TABLES

Table 2.1: MATMOD and CRACKMOD Model constants for SS304 [Lee and Kim, 1996]..... 51

Table 2.2: Chemical composition of SS304 and SS304L, typical [ASM, 2007]..... 56

Table 2.3: Tensile properties from SS304 at select temperatures [ASM, 2007]..... 59

Table 3.1: Experimental test matrix of tensile specimens..... 73

Table 3.2: Experimental test matrix of blunt notch fracture specimens..... 74

Table 3.3: Test matrix for Stress-Free Oxidation experiments. 74

Table 3.4: Specifications of MTS servohydraulic test frame..... 78

Table 3.5: Specifications of MTS High-Temperature Extensometer. 78

Table 3.6: Blunt notch creep-fatigue fracture specimen dimensions..... 81

Table 3.7: Specifications of MTS Insight 5 test frame. 86

Table 3.8: Epsilon Tech CMOD Gage - 3548COD..... 90

Table 3.9: Industrial Heater Corp. B74772 Heater. 97

Table 3.10: Kalling's Etchant Composition 101

Table 4.1: Material properties obtained from tensile tests..... 107

Table 4.2: Completed experimental test matrix, including failure cycle and final crack length. 116

Table 4.3: Stress-strain values used in MKIN material model for 600°F (315°C) and 800°F (427°C)..... 118

Table 4.4: Numerical results for 600°F (315°C) and 800°F (427°C) simulations subjected to a 800lbf (3.56kN) and 825lbf (3.67kN) load, respectively..... 121

Table 4.5: Crack initiation life based on the three individual initiation criteria. 135

Table 5.1: Optimized Creep-Fatigue Crack Initiation Model Constants 179

Table 5.2: Optimized Creep-Fatigue Crack Propagation Model Constants..... 179

Table 6.1: Benchmark parameters used in the crack initiation and propagation models used to correlate with predictions..... 190

LIST OF NOMENCLATURE

Variable

δ	Load-Line Displacement [*in/in* (*mm/mm*)]
ε	Strain: [*in/in* (*m/m*)]
ε_f	Fracture Strain: [*in/in* (*m/m*)]
v	Poisson's Ratio: [in^2/in^2 (mm^2/mm^2)]
σ	Stress: [*ksi* (*MPa*)]
σ_f	Fracture Stress: [*ksi* (*MPa*)]
σ_o	Flow Stress: [*ksi* (*MPa*)]
σ_y	Yield Stress: [*ksi* (*MPa*)]
σ_{uts}	Ultimate Tensile Stress: [*ksi* (*MPa*)]
a	Crack Length: [*in* (*mm*)]
a	Constant in creep-fatigue crack propagation model
a_c	Critical Crack Length: [*in* (*mm*)]
a_t	Transitional Crack Length: [*in* (*mm*)]
A_n	Nominal Area: [in^2 (m^2)]
b	Constant in creep-fatigue crack propagation model
B	Specimen Thickness: [*in* (*mm*)]
c	Constant in creep-fatigue crack propagation model
da/dt	Crack Tip Velocity: [*in/s* (*mm/s*)]
da/dN	Crack Extension Per Cycle: [*in/cycle* (*mm/cycle*)]
E	Elastic Modulus: [*Msi* (*GPa*)]
H	Strength Coefficient [*ksi* (*MPa*)]

J	Energy Release Rate/Elastic-Plastic Crack Parameter: [*lbf/in* (*N/mm*)]
J_1	J-Integral approximation for the first load cycle: [*lbf/in* (*N/mm*)]
J_c	Asymptotic ΔJ for Stage III crack growth: [*lbf/in* (*N/mm*)]
ΔJ	Cyclic *J*-Integral: [*lbf/in* (*N/mm*)]
ΔJ_{stab}	Stable ΔJ-value used in crack propagation model: [*lbf/in* (*N/mm*)]
K	Stress Intensity Factor: [$ksi\sqrt{in}$ ($MPa\sqrt{m}$)]
ΔK	Stress Intensity Factor Range: [$ksi\sqrt{in}$ ($MPa\sqrt{m}$)]
K_c	Critical Stress Intensity Factor: [$ksi\sqrt{in}$ ($MPa\sqrt{m}$)]
K_I	Mode I Stress Intensity Factor: [$ksi\sqrt{in}$ ($MPa\sqrt{m}$)]
K_{Ic}	Mode I Plane Strain Fracture Toughness: [$ksi\sqrt{in}$ ($MPa\sqrt{m}$)]
K_t	Stress Concentration: [*ksi/ksi* (*MPa/MPa*)]
n	Number of measurements (Roughness Parameter)
n	Strain Hardening Exponent [Ramberg-Osgood Relationship]
p	Constant in creep-fatigue crack initiation model
P	Load: [*lbf* (*N*)]
r	Distance from Crack Tip: [*in* (*mm*)]
q	Constant in creep-fatigue crack initiation model
Ra	Surface Roughness Parameter
R	Load Ratio, Min/Max: [*lbf/lbf* (*N/N*)]
R_s	Stress Ratio, Min/Max: [*ksi/ksi* (*MPa/MPa*)]
$\dot{V}$	Load-Line Displacement Rate: [*in/s* (*mm/s*)]
V_m	Crack Mouth Opening Displacement: [*in/in* (*mm/mm*)]
W	Specimen Width: [*in* (*mm*)]

z	Height of measurements relative to a zero plane (Roughness Parameter)

Abbreviations

Avg	Average
Cor	Correlated
Env	Environment
Eq./Eqs.	Equation/Equations
Fig./Figs.	Figure/Figures
Ox	Oxidation

Acronyms

ASTM	American Society for Testing and Materials
CCG	Creep Crack Growth
CF	Creep-Fatigue
CFCG	Cree-Fatigue Crack Growth
CFCIG	Creep-Fatigue Crack Initiation and Growth
CMOD	Crack Mouth Opening Displacement
C(T)	Compact Tension (type of fracture specimen)
CTOD	Crack Tip Opening Displacement (aka *CMOD*)
DAQ	Data Acquisition
DCPD	Direct Current Potential Drop
EDM	Electron Discharge Machining
EPFM	Elastic Plastic Fracture Mechanics
FCG	Fatigue Crack Growth
GB	Gigabyte

LEFM	Linear-Elastic Fracture Mechanics
SCC	Stress Corrosion Cracking
T/C	Thermocouple
TB	Terabyte
TDFM	Time-Dependent Fracture Mechanics
VAL	Variable Amplitude Loading
VB	Visual Basic Programming Language

CHAPTER 1
INTRODUCTION

Material response due to creep-fatigue (CF) loading conditions has become a primary concern amongst engineers, notably within the industrial gas turbine (IGT) field. In regards to life assessment, analytical models are necessary to accurately predict the life of components subjected to a myriad of conditions, including high loads, harsh temperatures and corrosive environments. Advances in materials, processing and coatings have allowed the engineering envelope to be pushed, in terms of design and structural lifing. As a result, advances in analyses that more accurately replicate the material behavior in simulated service conditions must be a priority.

1.1 Background and Motivation

Industrial gas turbines, such as the General Electric 7FA shown in Fig. 1.1, are routinely cycled through startup and shutdown sequences with varying time intervals of continuous operation. Traditionally, gas turbines used in power generation are expected to remain under steady operating conditions, i.e., constant mechanical and thermal loading, with minimal cycling.

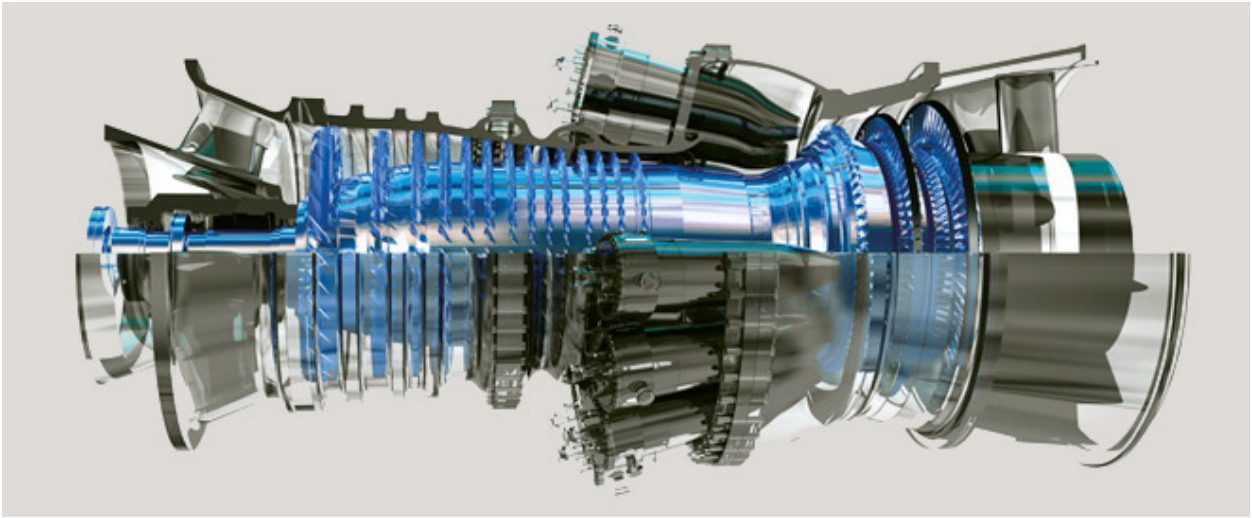

Figure 1.1: General Electric 7FA Heavy Duty Industrial Gas Turbine [General Electric 7FA, 2012].

As daily power demand fluctuates, power plants have utilized peaking units, i.e., peakers, with increasing frequency [Jaber, et al., 2003]. Peakers have the ability to provide power to the grid almost immediately after startup, providing a satisfactory method of supplying more power on demand as demand fluctuates throughout the day. The effect of cycling IGTs through the startup and shutdown routines results in increased damage attributed to fatigue, resulting in mixed-mode failures of critical components, combining creep and fatigue failure modes.

Creep-Fatigue (CF) is essentially a coupling of the two failure modes: a result of unique load histories and high temperatures imparted on components. Routinely, these components include complex geometries that contain favorable locations for the initiation of cracks, e.g. a cooling hole in an actively cooled turbine blade. With the combination of cyclic degradation and time-dependent inelastic deformation due to creep, shorter life predictions are expected, even in advanced Nickel-based superalloy components. Traditional analyses customarily decouple the creep and fatigue mechanisms, requiring independent simulations and life calculations. Test standards have been developed to investigate each individual phenomenon, e.g., fatigue crack growth (ASTM E647), creep crack growth (ASTM E1457), and creep-fatigue testing (ASTM E2714-09) and crack growth (ASTM E2760-10) test standards. A compromise is then made based on experimental results and numerical simulations of the independent analyses. As the demand for more reliable and efficient components increases, simulating and predicting the true mixed-mode failure behavior is necessary.

Fracture mechanics approaches are routinely employed in crack growth analyses. A number of crack propagation models are readily available for standalone fatigue and/or creep crack growth analyses, e.g. [Forman et al., 1967; Bassani and McClintock, 1981]; however, when simulated together, the tools required for analyses are far less developed. Research over

the past few decades has yielded substantial information regarding material response, most notably that crack growth rates are highly dependent on the load history, particularly in regards to the shape of the load waveform [Saxena, 1993]. The area of interest is, therefore, the trapezoidal-shaped load histories that have proportional rise and hold times and the fracture mechanics parameters used to characterize the growth rates.

Traditionally, the linear elastic fracture mechanics (LEFM) crack tip stress field parameter K, or stress intensity factor, is utilized in crack analyses. Using such modifying parameters in the analysis of fatigue crack propagation studies has been popular, after correlations between the cyclic stress intensity range, ΔK, and crack growth rates were first made in the late 1950s [Paris et al., 1961]. The groundbreaking research provided the framework for the future of fatigue crack growth analyses [Paris, 1998]. Implementation of LEFM parameters necessitates limited, localized plasticity within the component. In the event of non-negligible plastic deformation, e.g. extensive blunting of the crack tip or notch, elastic-plastic fracture mechanics (EPFM) parameters must be employed. Computing the path-independent J-integral provides a stress field modifying parameter under general plasticity [Rice, 1968]. Shortly after fatigue crack growth analyses implemented fracture mechanics, additional time-dependent analyses were scrutinized.

When cracks initiate and propagate under a constant load, time-dependent fracture mechanics (TDFM) parameters are necessary, e.g. [Landes and Begley, 1976]. By converting the J-integral into a rate integral, fracture mechanics approaches can be used to study the rate of cracking in material subjected to constant loads at various temperatures for extended time periods. Utilizing the C^* approach, the crack growth as a result of creep can be readily analyzed [Saxena et al., 1981]. Advancements during the 1980s extended the C^* approach to include

small scale creep, as well as non-steady-state creep crack growth (CCG), with the C_t parameter [Saxena, 1986]. With the more generalized parameters, a variety of CCG conditions have been investigated and characterized independently.

Ideally, simulations and crack life estimation could be made with a single model, incorporating all stages of crack growth. Extending beyond exclusively time-independent or time-dependent crack growth processes and analyses, novel creep-fatigue crack models are necessary. Recently, approaches to analyze the effects of creep and fatigue crack growth simultaneously are gaining exposure and popularity, with many incorporating fracture mechanics-based parameters, e.g. [Baik and Kim, 2007; Zhang et al., 2012]. In general, these unified creep-fatigue crack growth (CFCG) models use superposition principles to add the effects that both fatigue and creep have on crack growth. While being useful in life estimation, the models typically apply to long crack growth, disregarding the initiation and short crack growth. Naturally, the progression of CFCG models should be such that all stages are unified through increasingly more physically-based models.

To date, coupled creep-fatigue crack initiation and propagation (CFCIG) models emanating from blunt notches have yet to be developed. Coupled initiation and propagation models capable of replicating experimental data and extrapolating to components subjected to CF conditions are imperative to the structural life analysis; therefore, it is the goal of this research to develop an advanced deterministic tool to be applied in the design and life analysis phase of components operating under creep-fatigue conditions. While the investigation will focus on a specific alloy, 304 Stainless Steel, the proposed coupled analytical models are intended for a variety of metals utilized in components subjected to creep-fatigue conditions.

1.2 Research Objectives

Building upon the work of previous researchers, a novel approach to studying the crack initiation and growth behavior will be presented. Previous work has been shown to incorporate crack advancement due to coupled creep and fatigue processes by utilizing a superposition principle. In addition to using simple Paris-law behavior in the fatigue component, many of the models tend to only include terms relating to creep and fatigue crack growth. Other factors, such as oxidation and nonlinear behavior during loading, can contribute to advanced cracking rates. With the understanding of where research must be directed, this dissertation will detail the framework for a novel creep-fatigue crack initiation and propagation model and accomplish the following goals:

- **Implement a component-like test specimen in experimental and numerical approaches.** During the late 1970s, an SAE Round Robin was conducted to develop a test specimen that could mimic stress concentrations found in components currently in service. The blunt notch, or "keyhole", specimen was rather large (h = 6 in and w = 5 in) and thin (b = 0.375 in), which goes against the conventional dimensions found in pertinent ASTM standards; therefore, a modified compact tension (C(T)) specimen utilizing a keyhole notch, as opposed to a V-notch, more closely adhering to ASTM-recommended dimensions will be employed. The main task will be to implement a modified form of the C(T) fracture specimen and prove that it can be suitably used to determine the crack initiation and early propagation behavior of a component-like specimen.
- **Design and implement a universal creep-fatigue test system to be used on a standard load frame.** Traditionally, creep-fatigue experiments are conducted on large

servohydraulic load frames with extensive fixturing and monitoring equipment. Two main components are required: a furnace to heat the specimen and a crack monitoring system, such as a direct current potential drop (DCPD) system. Used in conjunction with a load frame, standard creep-fatigue experiments can be carried out with these systems. During the course of the dissertation, a closed-loop PID-controlled furnace and DCPD crack monitoring system are to be developed for CFCG experiments. Implementing the systems on an electromechanical (EM) load frame will be required, as experiments will be conducted on an MTS EM load frame.

- **Develop experimental routines to investigate the effect of rise and hold times during loading on crack initiation and propagation.** Research has shown that the life of a component is typically dominated by fatigue processes, creep processes or some combination thereof. Primarily, the material behavior is affected by both the loading regime and the hold regime of a mechanical test. The goal then is to study the effects of the relationship between the rise time and hold time during trapezoidal-waveform tests and accurately model the observed behavior. Routines will include various hold times to identify any significant effects of creep during load application and oxidation of specimens due to high temperature environments.
- **Propose a novel analytical crack initiation and growth model, or coupled models, that incorporates crack initiation and growth, incorporating all stages of crack growth.** The primary focus of this dissertation is to propose a novel crack initiation and propagation model or coupled models. Emphasis will be placed on developing a comprehensive model, one that incorporates temperature dependency, capable of relating crack initiation and growth via fracture mechanics parameter estimations. Effort will be

made to utilize as many existing creep, fatigue and fracture parameters as possible, allowing for immediate implementation in commercially available finite element packages. Ultimately, the task will be to prove the capability of a novel, unified analytical crack growth model that is capable of replicating and simulating crack initiation and propagation in components subjected to creep-fatigue conditions.

Following the brief summary of the background, motivation and research goals provided within this chapter, Chapter 2 provides a detailed literature review, encompassing mechanics and creep-fatigue topics directed at life prediction methodologies. Experimental routines, including mechanical and metallurgical analysis procedures, follow in Chapter 3. The remaining sections, Chapters 4-7, overview the experimental results, as well as the development of the novel coupled crack initiation and propagation models. Chapter 8 concludes the dissertation with recommendations on avenues for further research regarding crack initiation and growth modeling of components subjected to creep-fatigue conditions. Additional material, e.g., individual test results and relevant computer codes, are provided in the appendices.

CHAPTER 2
LITERATURE REVIEW AND BACKGROUND

Fundamental mechanics of materials topics are readily found in undergraduate educational engineering texts, e.g. [Hertzberg, 1989; Dowling, 2013]. Encompassing related topics from stress and strain to deformation and fracture, such texts serve as exemplary sources of general mechanical behavior of materials and related analytical life prediction formulations. Not only applicable to undergraduate engineering education, practicing engineers routinely reference such texts to assist in the implementation of advanced life prediction methodologies found in scientific journals. It is, therefore, not within the scope of this review to detail the fundamentals of related mechanics; rather, readers are directed to such texts for general topics in the areas of mechanics, deformation and fracture.

The following literature review will provide the necessary foundation for relevant topics to creep-fatigue crack growth. Key areas of interest are material behavior at notches including crack initiation and propagation, short and long crack growth behavior, fatigue and creep crack growth and specimen geometry effects. Additionally, information from literature regarding the mechanical behavior of the primary subject material, SS304, is provided. Cumulatively, the chapter will reveal the need for continued research in the area of creep-fatigue crack initiation and growth, providing the framework for the current research investigation.

2.1 Fatigue Crack Initiation

From a fatigue life standpoint, the initiation of a crack in a component accounts for a majority of the total life of the component [Dowling, 1979; Benachour et al., 2011]. Traditionally, analyses divide the initiation and propagation processes into separate phases and implement different approaches to quantify the total life spent in each, e.g. [Lazzarin et al.,

1997]. While fracture mechanics approaches have dominated the fatigue crack propagation stages, a variety of approaches have been proposed to study the initiation of fatigue cracks from notches, including plastic strain and critical plane approaches, e.g. [Furuya and Shimada, 1986; Leidermark et al., 2011]. More commonly, the stress and strain response is approximated by local strain or fracture mechanics approaches [Dowling, 1979]. Additionally, the use of finite element methods (FEM) to assess the notch stress and severity of stress concentration will be briefly mentioned.

Prior to application of such techniques to fatigue crack initiation in components, a review of common notch stress-modifying approaches is provided. Emphasis is directed towards fatigue crack initiation mechanisms, as this is the expected crack initiation mechanism in the current experimental investigation. Creep crack initiation studies, e.g. [Piques et al., 1986; Davies, 2009; Sugiura et al., 2010], are also available, based on similar methods for fatigue crack initiation studies, and are discussed in detail in this section. Readers are directed to such sources for relevant and necessary information on creep crack initiation methodologies.

2.1.1 Material Response at Notch Tip

The presence of a notch within a component requires the approximation of the local response and the material sensitivity to the existence of notches, as a reduction in fatigue life can be expected [Dowling, 2013]. Accurate life predictions, therefore, require the accurate definition of the stress field local to the notch root. To account for the increase in stress at the notch, three main approaches have been routinely implemented to predict the elastic or elastic-plastic response due to a mechanical load: stress concentration approach, the stress gradient approach, or the notch stress intensity approach.

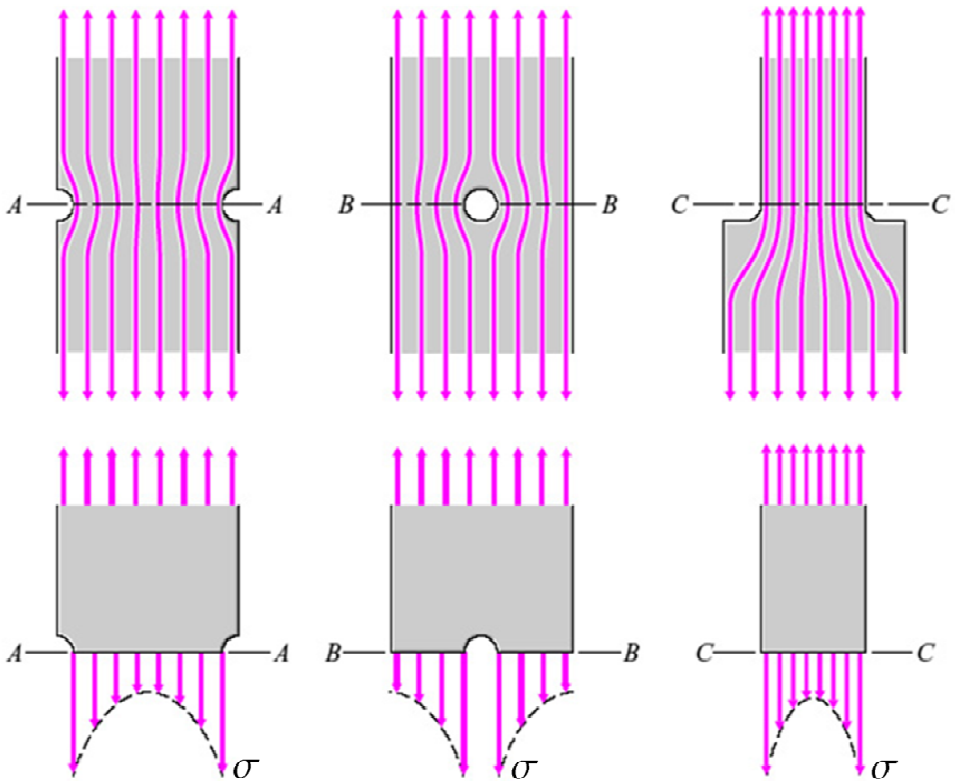

Figure 2.1: Amplification of stress due to a geometric discontinuity [Riley et al., 2007].

2.1.1.1 Stress Concentration Approach

The stress concentration approach to notch stress approximation became widely popular after the work of Inglis [Norton, 2006]. Subsequently, Peterson's *Stress Concentration Factors* has done much to standardize the analysis of notches with thousands of solutions for common geometries found in service [Peterson, 1974; Pilkey, 1997]. Literary works are available with the explicit goal of defining the stress concentration for specific geometries subjected to distinct loading, e.g. [Leven and Frocht, 1952; Neal et al., 1979]. The basis of a stress concentration factor is the amplification of stress near a geometric discontinuity, Fig. 2.1. For linear, elastic and isotropic materials, the stress at a notch tip, σ, is related to the nominal stress, S, i.e.,

$$\sigma = K_t S . \tag{2.1}$$

Equation (2.1) is appropriate for simple, monotonic cases; however, when plasticity and cyclic loads are expected, more suitable methods of notch root stress and strain approximation are needed.

In the event that Eq. (2.1) predicts a stress that is above the yield strength of the given material, notch tip plasticity is routinely approximated with Neuber's rule or Glinka's approach. Neuber's rule postulates that the geometric mean of the stress and strain concentration factors, K_σ and K_ε, remains "equal to the Hookian stress concentration factor [Neuber, 1961]," i.e.,

$$\sqrt{K_\sigma K_\varepsilon} = \sqrt{\frac{\sigma}{S}\frac{\varepsilon}{e}} = K_t . \tag{2.2}$$

Glinka's approach, also known as the strain energy density approach, asserts that during plasticity, the energy density in the plastic zone, W_σ, is equivalent to the energy calculated on an elastic basis [Glinka, 1985], i.e.,

$$\int_0^{e_{ij}} S_{ij}\, de_{ij} = \int_0^{e_{ij}} \sigma_{ij}\, d\varepsilon_{ij} . \tag{2.3}$$

Implementing either Eq. (2.2) or (2.3) into the Ramberg-Osgood type relationship, and after some omitted substitutions, the response at the notch tip due to a monotonic load can be iteratively determined, e.g.,

$$\frac{\left(K_t S\right)^2}{E} = \frac{\sigma^2}{E} + \sigma\left(\frac{\sigma}{K}\right)^{1/n} \tag{2.4}$$

or

$$\frac{\left(K_t S\right)^2}{E} = \frac{\sigma^2}{E} + \frac{2\sigma}{n+1}\left(\frac{\sigma}{K}\right)^{1/n} . \tag{2.5}$$

Here, K and n are the strength coefficient and exponent, respectively, and the material exhibits small scale yield, i.e. nominally elastic behavior. By eliminating the notch strain, the resulting stress at the tip is readily obtained for simple, monotonic loading.

The extension of Eqs. (2.2) and (2.3) to cyclically loaded components requires the development of the fatigue notch factor. It was observed through experimental procedures that the stress concentration in fatigue was typically less than K_t for monotonic loading, leading to the definition of the fatigue notch factor, K_f [Schijve, 1980], i.e.,

$$K_f = \frac{S_{f1}}{S_{fk}}, \tag{2.6}$$

where S_{f1} is the fatigue limit of an unnotched material and S_{fk} is the fatigue limit of the notched component. Depending on the material, the notch sensitivity was formulated, relating the fatigue notch factor with the stress concentration factor, e.g. [Peterson, 1974],

$$q = \frac{K_f - 1}{K_t - 1}, \tag{2.7}$$

where q ranges from 0 to 1, with 1 being a material highly sensitive to notches. Substitution of Eq. (2.6) into (2.4) and (2.5) allows for determination of the fatigue notch factor and subsequently, the cyclic counterparts are furnished, as overviewed in [Stephens et al., 2001], i.e.,

$$\frac{\left(K_f \Delta S\right)^2}{E} = \frac{\left(\Delta\sigma\right)^2}{E} + 2\Delta\sigma\left(\frac{\Delta\sigma}{2K'}\right)^{1/n'} \tag{2.8}$$

and

$$\frac{\left(K_f \Delta S\right)^2}{E} = \frac{\left(\Delta\sigma\right)^2}{E} + \frac{4\Delta\sigma}{n'+1}\left(\frac{\Delta\sigma}{2K'}\right)^{1/n'}. \tag{2.9}$$

Equations (2.4), (2.5), (2.8) and (2.9) can subsequently be used in life approximation analyses. By rearranging Eq. (2.8) or (2.9) and solving for the notch tip stress range, $\Delta\sigma$, traditional stress-life predictions are furnished via Basquin's equation or stress-life graphs for the desired material.

The choice of one notch tip approximation technique over the other, e.g. Glinka over Neuber or vice versa, depends on the experimental data available. Investigations have been conducted into the appropriateness of each model with respect to cyclic loading and revealed that Neuber's rule typically overestimates, whereas Glinka's approach underestimates the notch tip strain [Knop et al., 2000]. Additionally, plane-stress notch strains were more accurately predicted via Neuber's rule and plane-strain notch tip strains via Glinka's approach. Ultimately, the experimental data will reveal the correct notch approach to be used during life prediction calculations.

2.1.1.2 Stress Gradient Approach

Another approach to characterizing the notch tip stresses is through the use of the stress gradient approach [Schijve, 1980]. The stress gradient approach views the relationship between the stress concentration factor and the fatigue notch factor as a function of the relative stress gradient, χ [Filippini, 2000], i.e.,

$$\chi = \frac{1}{\sigma_{max}} \left. \frac{\partial \sigma_y}{\partial x} \right|_{x=x_0}, \tag{2.10}$$

where σ_{max} corresponds to the maximum stress that occurs at a distance of x_0 from the notch. Through definition of the stress field gradient, shown in Fig. 2.2, the stress field around the notch is possible of being approximated.

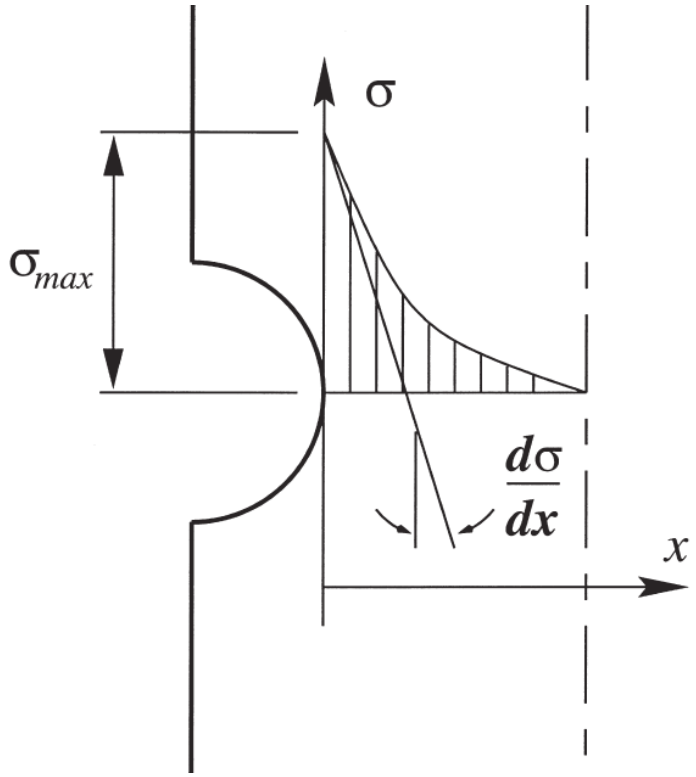

Figure 2.2: Relative stress gradient at an arbitrary notch tip [Filippini, 2000].

A main benefit of the stress gradient approach is that it readily accounts for the size effect on fatigue life limits and the applicability to structures is straightforward in that nominal stresses need not be calculated. Through the introduction of additional parameters and substitutions, the ratio of the fatigue notch factor and the stress concentration factor can be established [Schijve, 2009], i.e.,

$$\frac{K_f}{K_t} = \frac{1}{1+\sqrt{A^*/\rho}}. \tag{2.11}$$

Equation (2.11) makes use of a material constant, A^*, and the notch root radius, ρ. Neuber and Peterson have proposed similar laws, with similar functions to describe the notch factor relationship [Schijve, 2009]. Life predictions based on standard stress- or strain-based approaches in Eqs. (2.8) or (2.9), or through more exotic approaches, e.g., the volumetric method of Adib-Ramezani and Jeong [2007], can subsequently be implemented.

2.1.1.3 Notch Stress Intensity Approach

A third approach taken to analyze the stress at the notch of a component is known as the notch stress intensity approach. This approach uses the stress intensity factor, K, to relate the notch tip stress, σ, to the radius of the notch, r, i.e.,

$$\sigma = \frac{2K}{\sqrt{\pi r}}. \tag{2.12}$$

Recalling the expression for the notch tip stress in Eq. (2.1), the stress concentration factor can be approximated for blunt notches [Creager and Paris, 1961; Dowling, 1979], i.e.,

$$K_t = \frac{2K}{S\sqrt{\pi r}}. \tag{2.13}$$

Concerns over the applicability and extension of fracture mechanics to the approximation of the stress concentration factor were raised; however, later works provided more appropriate formulations [Dowling and Wilson, 1984].

Implementing the expression for the stress intensity factor provided in ASTM E399, Heckel and Wagner derived a maximum notch stress based on the maximum Hookean stress and notch tip radius, ρ, for bluntly notched compact tension (C(T)) specimens in the absence of a crack [Heckel and Wagner, 1975], i.e.,

$$\sigma = \frac{2}{\sqrt{\pi\rho}} K = \frac{2\sigma_N \sqrt{a}}{\sqrt{\pi\rho}} f\left(\frac{a}{W}\right). \tag{2.14}$$

Equation (2.14) makes used of the nominal stress, σ_N, calculated based on direct and bending loads on the specimen and the geometry shape function, $f(a/W)$, that is dependent on the ratio of the crack length, a, to specimen width, W. The effect of the notch stress on crack growth rates was captured upon initiation and growth, and it was shown the nonlinear stresses at a sharp notch

is dominated by the maximum Hookean stress in Eq. (2.14). Estimation of the notch tip response then allows for calculation of life, whether to initiation or total failure of the specimen.

2.1.1.4 Finite Element Analysis of Notches

In conjunction to the analytical approaches in Sections 2.1.1.1 – 2.1.1.3, the finite element method/analysis (FEM/FEA) is routinely employed to analyze the stress field at notches, e.g. [Glinka and Newport, 1987; Palazotto and Mercer, 90; Kacianauskas et al., 2005]. Analytical solutions for Neuber's rule and Glinka's approach to notched tensile specimens with various notch geometries are readily available in literature, e.g. [Noda and Takase, 1999]. Development of new fracture specimen geometries, notably the development of compliance equations, is aided by FEA, e.g. [Piascik and Newman, 1996]. Elastic-Plastic analyses are capable of predicting notch tip strains for both monotonic and cyclic loading conditions, e.g. [Wilson, 1974], with some incorporating viscoplastic analyses capable of replicating a myriad of material behaviors, e.g. [Knop et al., 2000]. Extensive work has been conducted in the area of finite elements and the use of FEM techniques to analyze the notch stress is widely accepted.

Limitations to the finite element method do exist, typically relating back to the mesh quality around the notch [Kacianauskas et al., 2005]. The notch angle has shown to have restrictions on the accuracy of predictions, limiting the severity of the notch in simulations [Hedia and Shabara, 2022]. Accuracy is also related the fidelity of the material model with actual material behavior. Degradation of material due to load and thermal conditions are not always captured, and require the use of additional approaches, e.g. damage mechanics, to be explained in Section 2.3.1.

2.1.2 Local Strain Approaches to Fatigue Crack Initiation

The local strain method, as briefly outlined in Section 2.1.1.1, provides the basis of calculating the life, commonly the life to crack initiation. Standard analyses include strain-life approximations for both constant amplitude loading, e.g. [Vardar and Kalenderoglu, 1989] and variable amplitude loading, e.g. [Wetzel, 1977]. Additionally, theses approaches have been extended to analyses involving high temperature experimental testing, e.g. [Sakane and Ohnami, 1987].

Constant amplitude fatigue loading routines readily allow for determination of crack initiation based on the Coffin-Manson equation. Based on the applied total strain range, $\Delta\varepsilon$, the number of reversals to failure, N_f, can be analytical solved, i.e.,

$$\frac{\Delta\varepsilon}{2} = \frac{\sigma'_f}{E}\left(2N_f\right)^b + \varepsilon'_f\left(2N_f\right)^c, \tag{2.15}$$

where σ'_f is the fatigue strength coefficient, ε'_f is the fatigue ductility coefficient, and b and c are the fatigue strength and ductility exponents respectively [Stephens et al., 2001]. Mean stresses have been shown to reduce the fatigue life of components, leading to modifications to Eq. (2.15), such as the Smith-Watson-Topper (SWT) mean stress correction, i.e.,

$$\sigma_{max}\frac{\Delta\varepsilon}{2} = \frac{\left(\sigma'_f\right)^2}{E}\left(2N_f\right)^{2b} + \sigma'_f\varepsilon'_f\left(2N_f\right)^{b+c}. \tag{2.16}$$

Other mean stress approaches have been developed, e.g. the Morrow mean stress approach, and used in conjunction with notch tip approximation techniques [Newport and Glinka, 1990]. Variable amplitude loading (VAL) requires the use of a damage summation process, such as the Palmgren-Miner rule, to determine the equivalent number of cycles to failure for constant amplitude loading, e.g. [Dowling et al., 1977; Wu, 1988; Knop et al., 2000]; however, emphasis will be placed on constant amplitude loading.

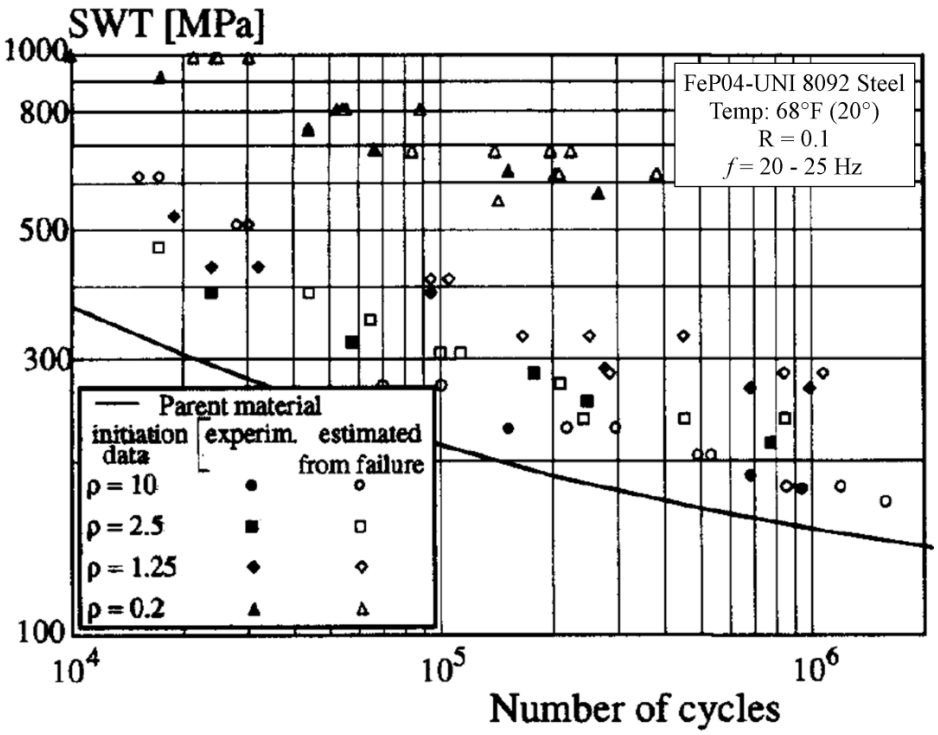

Figure 2.3: Number of cycles to crack initiation implementing Neuber's rule and the Smith-Watson-Topper approach for mean stress life prediction [Lazzarin et al., 1997].

Implementation of Neuber's rule in Eq. (2.16), fatigue lives to crack initiation for standard steels specimens have been calculated, Fig. 2.3 [Lazzarin et al., 1997]. It was observed that the more severe the stress concentration, the more conservative Neuber's rule became in fatigue crack initiation life predictions. Comparison of Neuber's rule and Glinka's approach for predictions was also investigated, with Neuber's rule being more accurate for plane stress conditions and Glinka's approach more suitable for plane strain conditions [Lazzarin et al., 1997]. Improvements to Neuber's rule have been proposed; however, only moderate (~1%) increases in accuracy were reported [Wu, 1988].

High temperature application of Neuber's rule on notched tensile specimens of SS304 has been conducted [Sakane and Ohnami, 1986]. Experimental data was obtained from strain-controlled tests on smooth and notched tensile specimens at 1112°F (600°C). Resulting strain-life curves were split into separate regimes of crack initiation, crack propagation and total life.

Predictions of crack initiation and total life were then made, based on increasing values of the stress concentration factor, Fig. 2.4. It was observed that Neuber's rule is highly conservative for failure cycle predictions and reasonably accurate for crack initiation estimations.

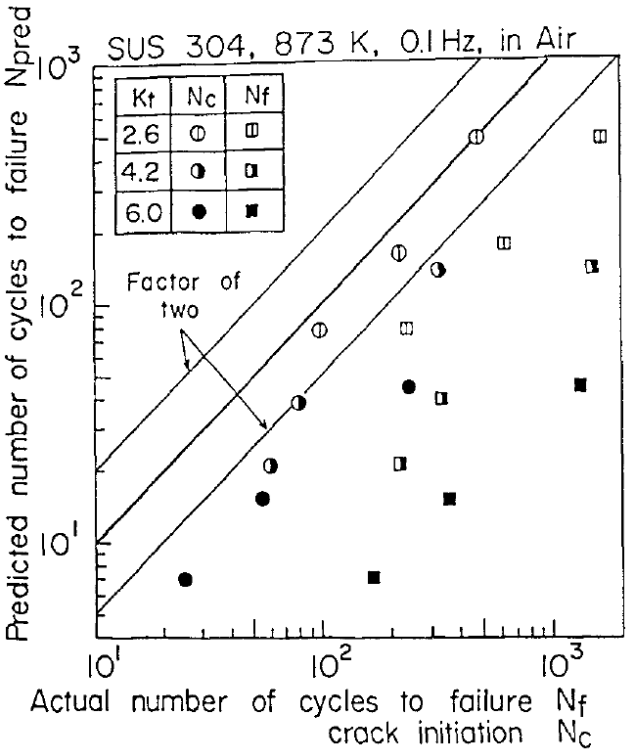

Figure 2.4: Prediction of failure lives for SS304 at high temperature utilizing Neuber's rule with R = -1 loading [Sakane and Ohnami, 1986].

Notch tip plasticity has been proposed as another local strain approach to fatigue crack initiation calculations [Furuya and Shimada, 1986]. The average local strain accumulation can be used to determine the number of cycles to crack initiation by integrating the local deformation history up to crack initiation, i.e.,

$$\Delta\bar{\varepsilon}_l = \frac{1}{N_c}\int_0^{N_c} \Delta\varepsilon_l dN\,, \tag{2.17}$$

where $\Delta\bar{\varepsilon}_l$ is the total average local strain measured directly on experimental specimens and N_c is the number of cycles to crack initiation. Results indicate a strong relationship between crack

initiation and the average local strain parameter, Fig. 2.5. Extending this approach, it was shown that an effective crack-tip strain element could be used to bridge the gap between crack initiation and propagation [Shimada and Furuya, 1987]; however, the propagation was limited to within the effective crack-tip strain element.

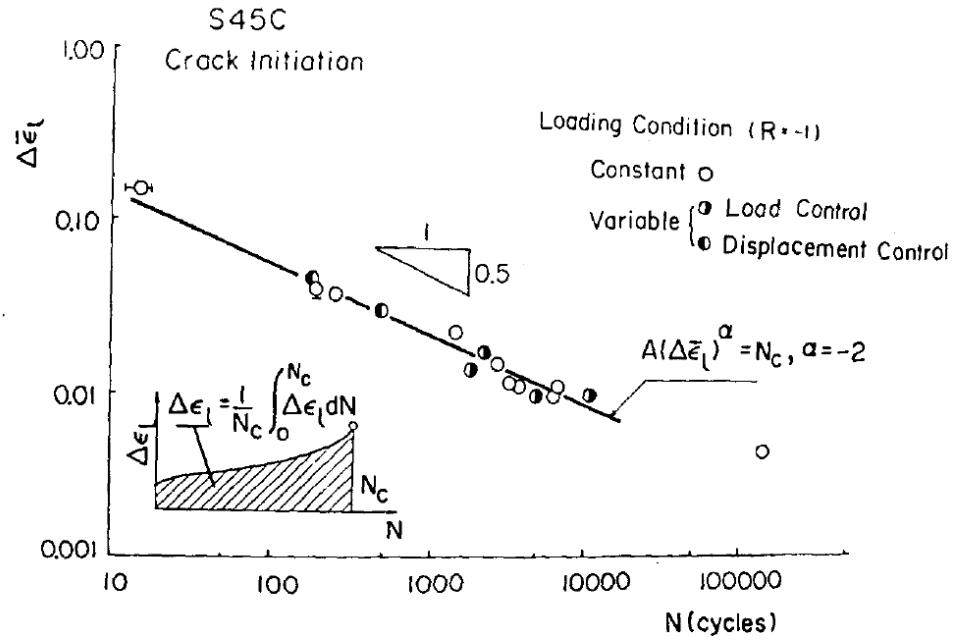

Figure 2.5: Relationship of the average local-strain accumulation value to fatigue crack initiation at room temperature [Furuya and Shimada, 1986].

2.1.3 Linear Elastic Fracture Mechanics Approaches to Crack Initiation

With the success of fracture mechanics parameters successfully modeling fatigue crack growth rates, the extension to crack initiation has been investigated, e.g. [Heckel and Wagner, 1975; Dowling, 1984]. Implementing Eq. (2.13) to estimate the true stress concentration, research attempts have been aimed at identifying the fatigue crack initiation lives, with limited amounts of success and drawbacks [Tanaka et al., 1983]. Improvements to analytical formulations for the stress concentration estimation from fracture mechanics approaches for C(T) specimens following ASTM guidelines have been developed, with maximum errors of

approximately 15% for the most blunted notches [Dowling and Wilson, 1984]. As the notch tip sharpens, the approximation becomes accurate to within 1%. On this basis, crack initiation processes follow for bluntly notched specimens.

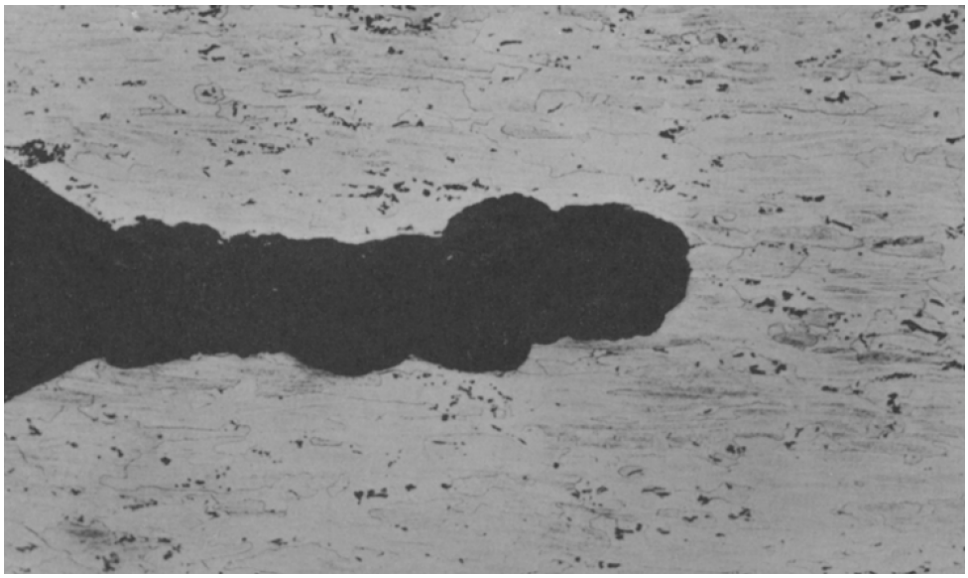

Figure 2.6: Blunted notch tip of Al2024-T351 subjected to 3.5% NaCl stress corrosion cracking [Creager and Paris, 1967].

One of the earliest extensions of the fracture mechanics approach to blunted notches arose from observation of stress corrosion cracking (SCC) in aluminum [Creager and Paris, 1967]. Studying dissolution mechanisms related to SCC, it was observed that the crack was more accurately described as a blunted notch; not the typical crack ending with a zero radius of curvature, Fig. 2.6. By carefully selecting the origin to be a distance of $\rho/2$ away from the notch tip, where ρ is the radius of curvature of notch, the elastic stress field components can be presented in typical fracture mechanics approaches, i.e.,

$$\sigma_x = \frac{K_I}{\sqrt{2\pi r}} cos\frac{\theta}{2}\left[1 - sin\frac{\theta}{2} sin\frac{3\theta}{2}\right] - \frac{K_I}{\sqrt{2\pi r}}\frac{\rho}{2r} cos\frac{3\theta}{2}, \tag{2.18a}$$

$$\sigma_y = \frac{K_I}{\sqrt{2\pi r}} cos\frac{\theta}{2}\left[1 + sin\frac{\theta}{2} sin\frac{3\theta}{2}\right] + \frac{K_I}{\sqrt{2\pi r}}\frac{\rho}{2r} cos\frac{3\theta}{2}, \tag{2.18b}$$

$$\tau_{xy} = \frac{K_I}{\sqrt{2\pi r}} sin\frac{\theta}{2} cos\frac{\theta}{2} cos\frac{3\theta}{2} - \frac{K_I}{\sqrt{2\pi r}} \frac{\rho}{2r} sin\frac{3\theta}{2}. \quad (2.18c)$$

Taking Eq. (2.18b), Heckel and Wagner extended the blunt notch approximation to a C(T) specimen with a keyhole notch by implementing ASTM E399 stress intensity factor calculations to describe crack initiation [Heckel and Wagner, 1975]. Results, in the form of maximum elastic, Hookean stress versus crack initiation and fracture life, agreed with Neuber's postulation that the elastic stress at the notch tip controls the fatigue life.

Extending a blocked slip-band model to deep notches in components, like that of the C(T) specimen used by Heckel and Wagner, researchers developed a notch stress intensity relation to predict initiation [Tanaka et al., 1983]. Incorporating the strength of smooth specimens, the notch factor for fatigue specimens with deep notches could be approximated, i.e.,

$$\frac{\Delta K_\rho}{\Delta K_0} = \sqrt{\left(1 + \frac{\rho}{\rho_0}\right)}, \quad (2.19)$$

where ΔK_0 and ρ_0 are material constants which, under uniaxial loading, are related back to the fatigue strength of uniaxial specimens subjected to a cyclic stress range. The relationship between the relative apparent stress intensity range (left hand side of Eq. (2.19)) and the square root of the relative notch-tip radius (right hand side of Eq. (2.19)) is observed to correlate well with applied stress intensity ranges and various notch tip radii, Fig. 2.7. The implication of this relation is that fatigue lives can be readily predicted using fracture mechanics approximations for notched components, resulting in stress-life predictions similar to that of smooth specimens. The resulting curve generated by the relationship in Eq. (2.19) readily captures crack initiation in low cycle and high cycle fatigue.

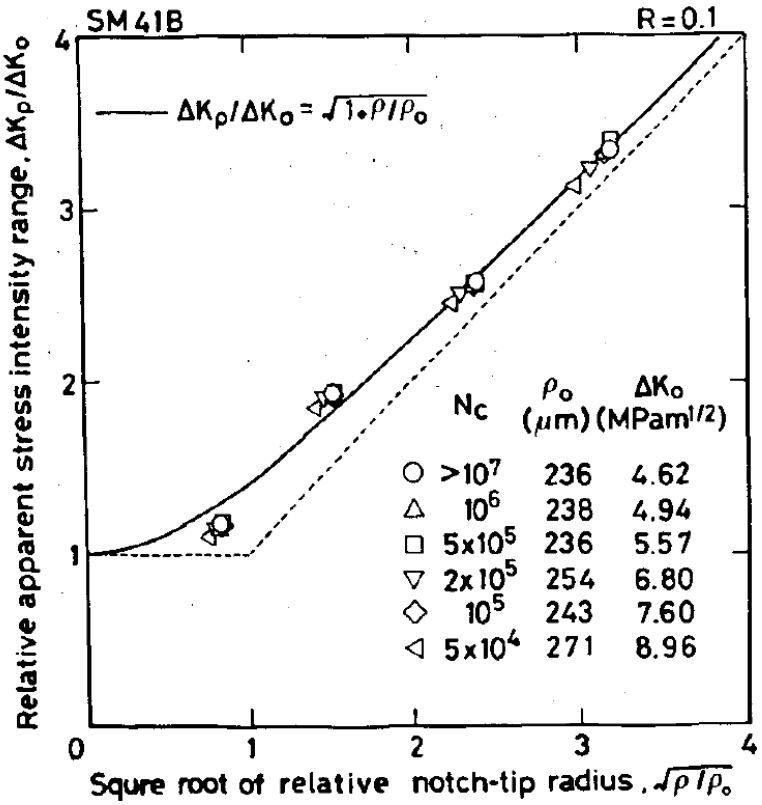

Figure 2.7: Relationship between Eq. (2.19) and crack initiation for various fatigue tests [Tanaka et al., 1983].

Process zone and critical distance approaches commonly employ the fracture mechanics approach to notch stress approximations [Pulvinage, 1998]. Boukharouba et al. [1995], suggested a notch stress field intensity parameter involving a characteristic distance, X_c, from the tip in which maximum stress was a constant, i.e.,

$$K = \sigma_y\left(X_c\right)\sqrt{2\pi}\left(\frac{\rho}{2}+X_c\right)^{\alpha}, \tag{2.20}$$

where ρ is the notch acuity and α is a the function dependent on the notch acuity angle [Boukharouba et al., 1995]. Normalizing the cyclic form of Eq. (2.20) by the notch acuity, crack initiation was readily predicted, Fig. 2.8. Due to difficulty in identifying the stress value at a point in the initiation process zone, notch sensitivity was calculated on the stress gradient approach, e.g.,

$$q = \frac{\left(1 - \frac{X_c C}{\rho + X_0}\right)}{H}, \tag{2.21}$$

where C and H are material constants and X_0 is a function of X_c and H. Use of Eqs. (2.20) and (2.21) allowed for a reduction of fatigue experiments required and provided a condition to predict crack initiation based on physical geometry measurements. Additionally, the process zone approach has been successfully applied to brittle materials, regarding crack initiation and instability [Tsuji and Ando, 1998].

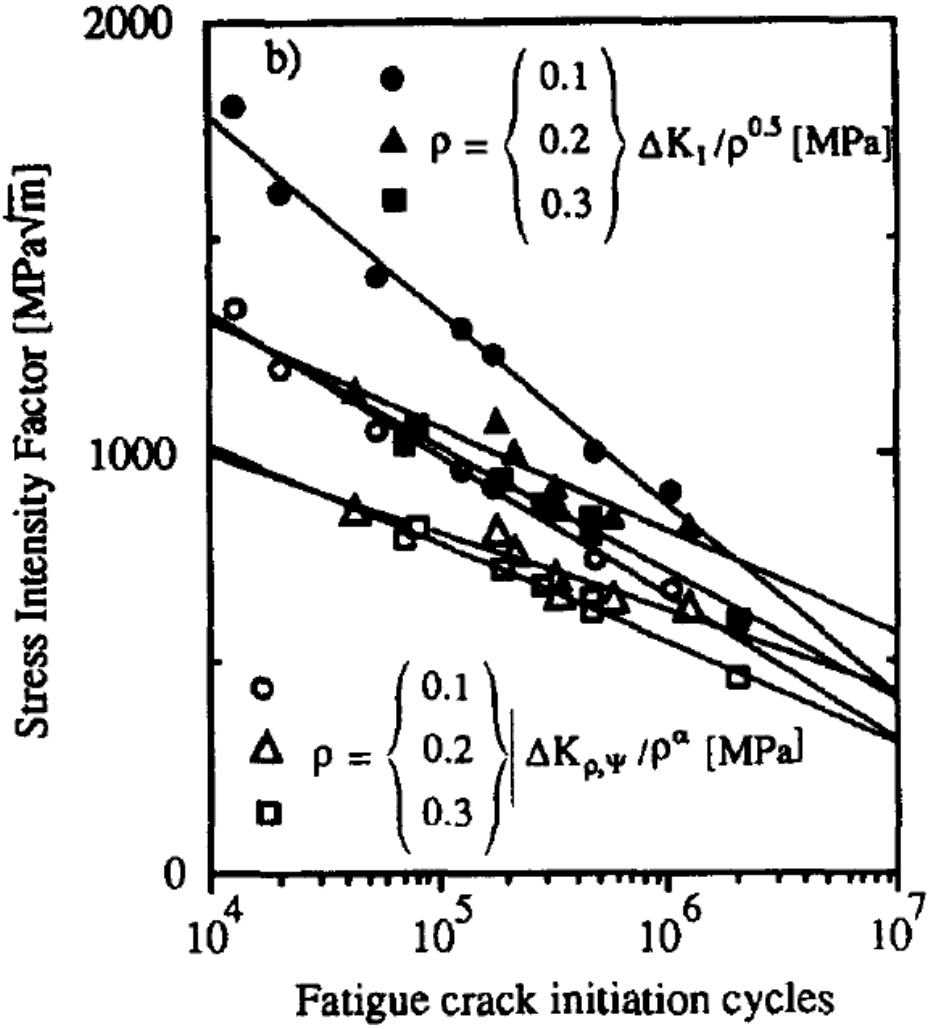

Figure 2.8: Fatigue crack initiation predicting using the normalize form of Eq. (2.20) [Boukharouba et al., 1995].

The shape of the notch, whether the notch is elliptical, circular, U-shaped, etc., has an effect on the initiation due to the process zone involved [Smith (I), 2010; Smith (II), 2010]. A fracture criterion taking into account the shape of the flaw is proposed, making use of a shape parameter, μ, i.e.,

$$\frac{K_{cr}}{K_{IC}} = 1 + \frac{\rho_c \sqrt{\pi\rho}}{\mu K_{IC}}. \tag{2.21}$$

The shape of the notch determines the value of μ, e.g. $\mu = 2.0$ for a parabolic flaw and $\mu = 2.12$ for a U-shaped flaw, which correlated to predictions within 6% of actual crack initiation. More simplistic analyses are available to correlate size with crack initiation, e.g. [Benachour et al., 2011]; however, suffer from over simplification and lack of physical significance.

The two main approaches overviewed used in resolving the crack initiation life employed the local strain and the fracture mechanics approaches. The main difference between the two methodologies was the determination of stress at the notch tip, using either the stress concentration factor, stress gradient approach or the blunt notch stress intensity approach. A summary assessment of the constituent components necessary for life prediction using these approaches is provided, either to crack initiation or complete failure of specimen, Fig. 2.9. Here, failure of the specimen is complete rupture of the specimen and does account for crack growth. Routinely, this approach is taken to provide a baseline for more advanced analyses. The process for simple finite element analyses is included, to be discussed in future sections, effectively eliminating the need for the analytical notch tip formulation selection.

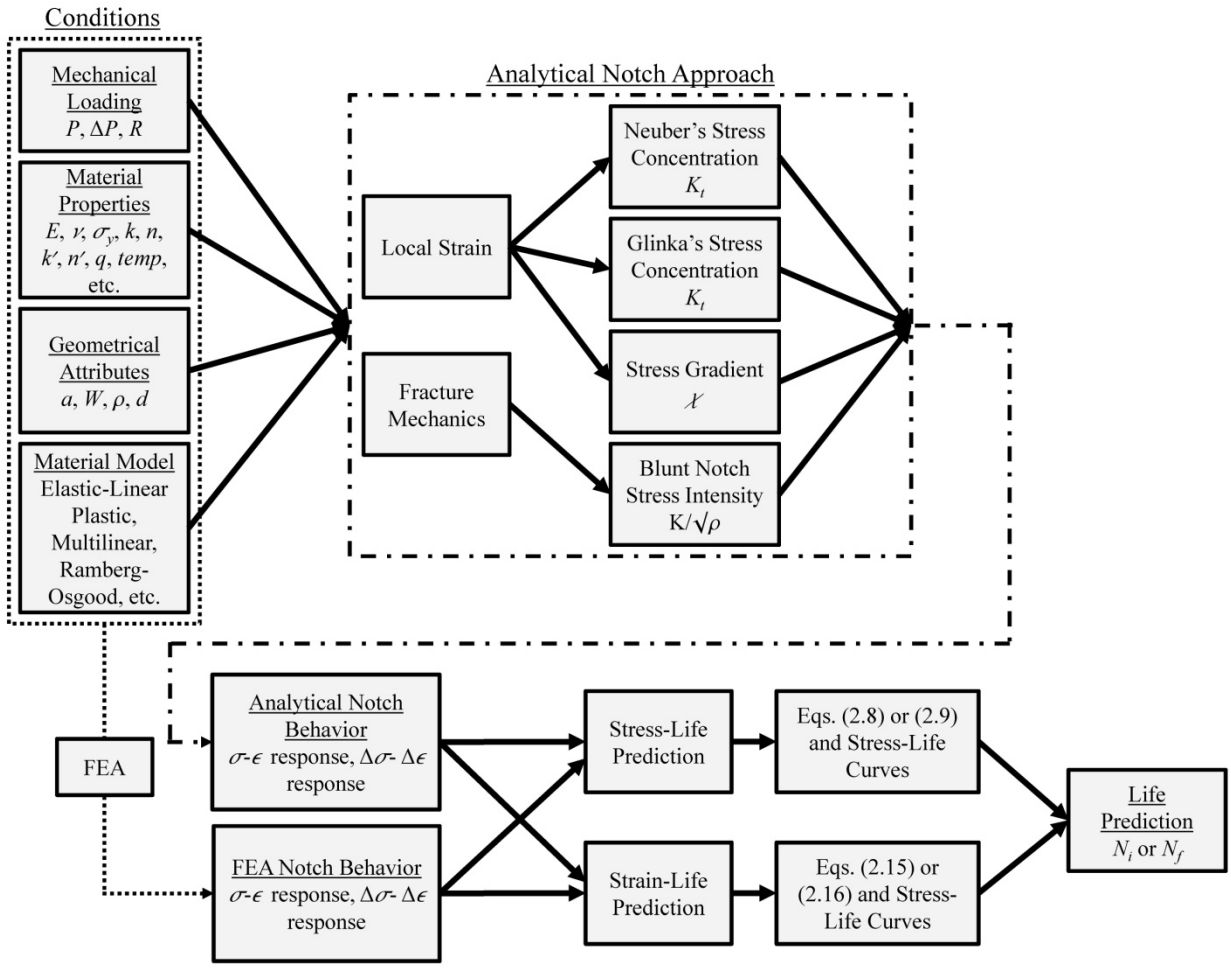

Figure 2.9: Traditional approaches for local strain and fracture mechanics approaches to analytical and numerical life prediction.

2.2 Fatigue and Creep Crack Propagation

Fracture mechanics approaches to crack propagation have become the established standard for evaluating fatigue crack growth lives. Since the introduction of Irwin's stress intensity factor, a consistent supply of analytical formulations for fatigue crack propagation have been proposed [Newman, 2000]. Initially, models for crack propagation involved LEFM methods; however, subsequent models were extended to account for plasticity and time-dependent effects through the development of appropriate stress field modifying parameters. Continued research has revealed additional factors influencing crack propagation rates, e.g. small

crack versus long crack growth and stress ratio effects, allowing increased accuracy in fatigue crack life predictions.

Crack propagation, based on extension per cycle, is routinely split into three ideal regimes for LEFM and EPFM growth, Fig. 2.10. Crack initiation and short crack growth is commonly referred to as the Stage I growth, where long-crack behavior is observed in Stage II and propagation-to-failure is observed in Stage III [Sanford, 2003]. Asymptotic behavior is observed in Stages I and III of LEFM growth, with the threshold and critical stress intensity factors defined based on the regime, respectively. Emphasis will be placed on Stage II and III growth, with some discussion of short crack and long crack behavior.

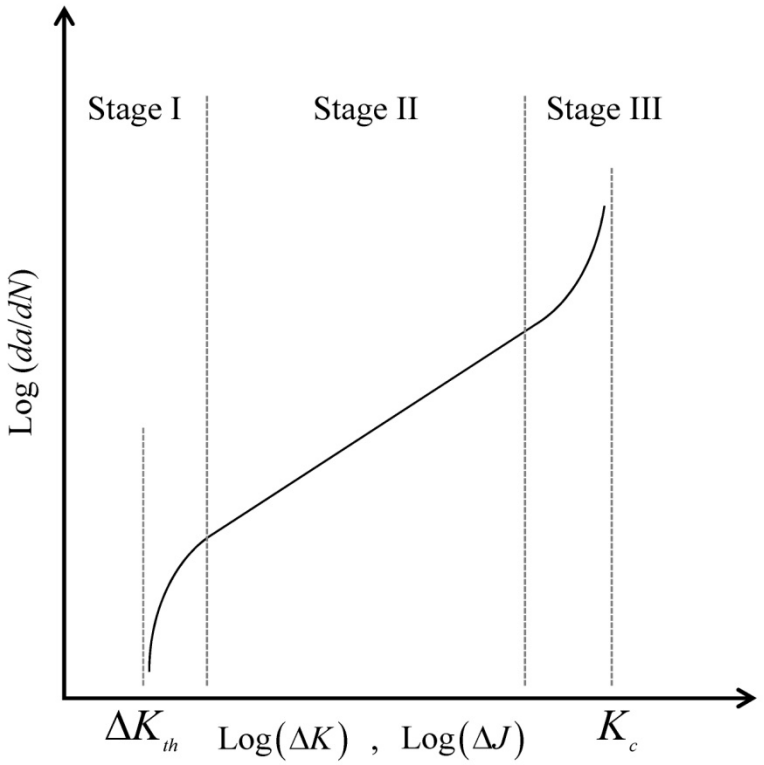

Figure 2.10: Fatigue crack growth curve identifying the three stages of fatigue crack growth, with LEFM asymptotic values.

2.2.1 Linear Elastic Fracture Mechanics

Understanding the importance of the stress intensity factor in crack tip stress fields, Paris, et al. identified the stress intensity factor as the vital parameter to the fatigue crack propagation process [Paris et al., 1961]. By plotting the crack growth rate, in terms of extension per cycle, versus the stress intensity on a log-log scale, the linear portion during Stage II crack growth can be modeled as a power-law relationship, i.e.,

$$\frac{da}{dN} = C\left(\Delta K\right)^{m}, \tag{2.22}$$

where C and m are fitting constants. Implementing the model for fatigue crack growth data obtained from experimental data and literature revealed a general trend for the Stage II crack growth, Fig. 2.11 [Paris and Erdogan, 1963]. After obtaining the constants in Eq. (2.22), simple integration would furnish the number of cycles required to grow a crack from an initial length to a predetermined final length, based on Stage II crack growth rates.

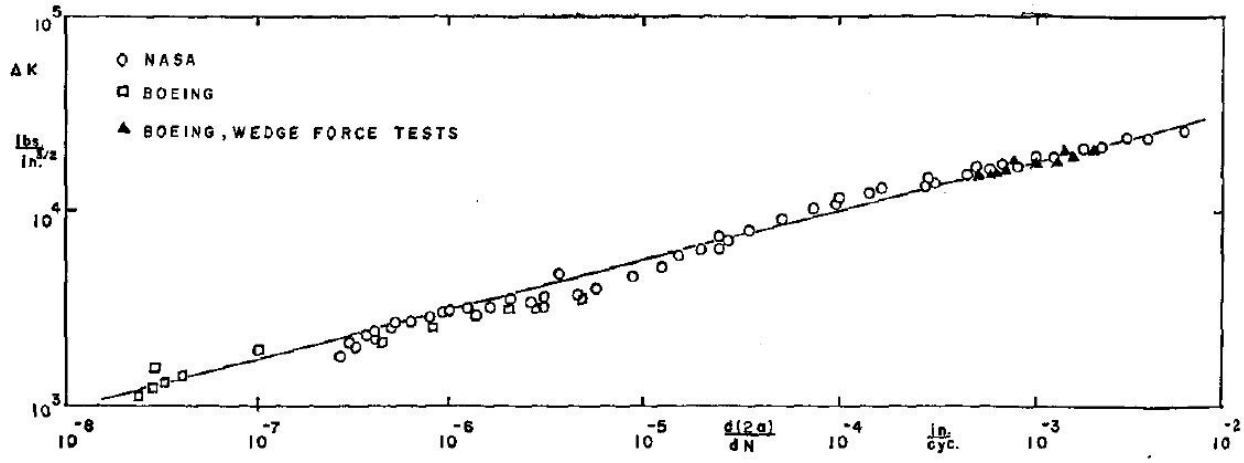

Figure 2.11: Broad tend of crack growth data on Al 7075-T6 amongst various test programs [Paris and Erdogan, 1963].

Load interaction and mean stress effects were observed to affect the crack growth rate [Forman et al., 1967]. Incorporating the stress ratio, R, and the critical stress intensity for fracture, K_c, the Paris model could be further extended, e.g.,

$$\frac{da}{dN} = \frac{C(\Delta K)^m}{(1-R)K_c - \Delta K}. \tag{2.23}$$

Unique to this formulation is that the asymptotic behavior of crack growth in stage III is accurately accounted for through the incorporation of the material fracture toughness term in the denominator. Results clearly indicated that the load ratio effect on crack growth was readily captured, as well as the upturn near the asymptote signifying instability, Fig. 2.12.

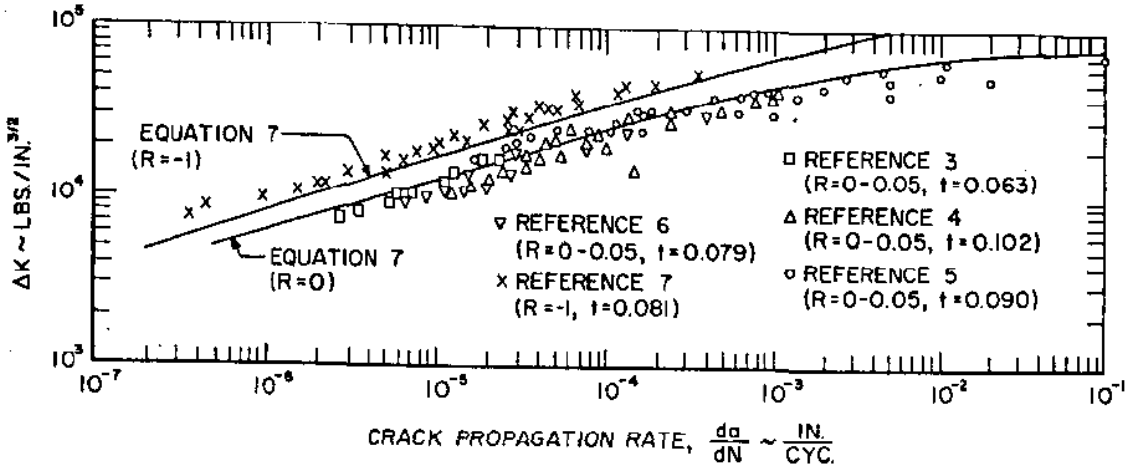

Figure 2.12: Fatigue crack growth with the incorporation of the load effect [Forman et al., 1967].

Crack closure was experimentally proven to alter the rates of fatigue crack growth rates [Elber, 1971]. As a crack grows, the plastic zone size increases due to the increase in stress intensity, leaving behind a plastic wake related to the experimental control routine, Fig. 2.13. During unloading, the plastic deformation results in crack closure prior to complete removal of load. To account for the acceleration or retardation of crack growth, methods such as the opening load approximation have been proposed, e.g. [Newman, 1974]. By calculating the crack opening stress, σ_o, an effective stress intensity range, ΔK_{eff}, have been proposed, i.e.,

$$K_{eff} = \left(1 - \frac{\sigma_o}{\sigma_{\max}} \Big/ \left(1 - R\right)\right) \Delta K \,. \tag{2.24}$$

This relation is used in place of the standard ΔK in Eq. (2.22), allowing for more accurate representation of the data, Fig. 2.14. Subsequent approaches have been proposed, with sufficient accuracy for most models and few limitations [Donald and Paris, 1999]. To avoid closure, high load ratios, $R \geq 0.7$, are considered closure free; however, plasticity-induced closure has still been observed [Yamada and Newman, 2009]. Crack growth models, therefore, should incorporate load-ratio effects to adequately predict crack growth rates in all regimes.

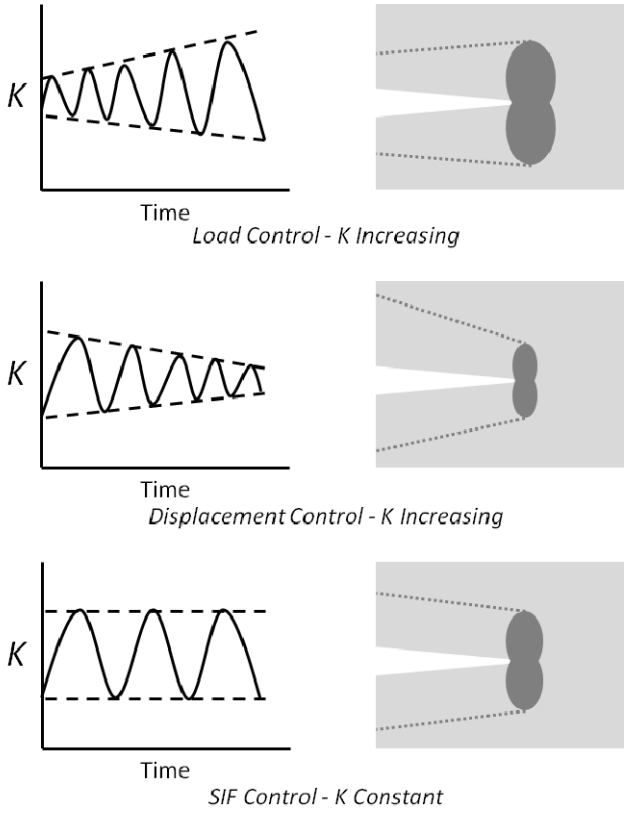

Figure 2.13: Plastic wake as a result of crack extension under constant amplitude load control testing [Elber, 1971].

Other aspects affecting crack closure, e.g. oxide-induced or roughness-induced crack closure, have been shown to affect closure in a nonlinear manner and require the use of more complex, multiple-mechanism models [Newman et al., 2003]. It was determined that if plasticity-induced crack closure was the only mechanism, crack growth rates were only dependent on the load ratio, *R*. Linear summation of crack closure mechanisms failed to adequately capture total closure process, due to the nonlinear interaction of mechanisms [Newman et al., 2003]. Nonlinear models, such as the proposed CROP model, are more suitable when several closure mechanisms are expected or observed.

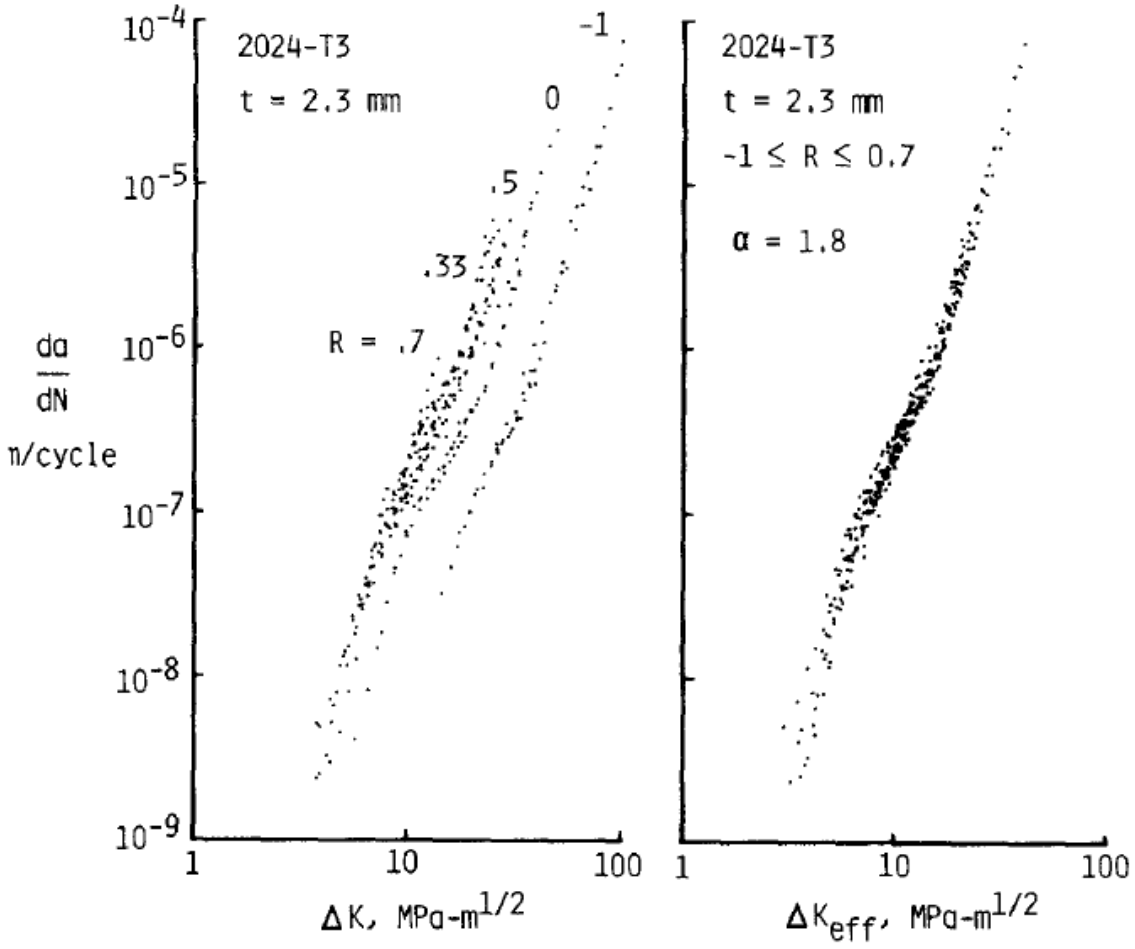

Figure 2.14: Figure 2.14: Correlation of fatigue crack growth rates with ΔK and ΔKeff for Al 2024-T3 [Newman, 1984].

The speed at which cracks propagate also depend greatly on the perceived size of the crack [Kitagawa and Takahashi, 1976]. For the short crack case, crack growth rates are elevated until a transition from short crack-to-long crack occurs, in which the crack growth rate reaches a minimum then increases until unstable propagation, Fig. 2.15 [El Haddad et al., 1980]. The transition from short crack to long crack has been reported, e.g. 0.02in (0.5mm) by [Furuya and Shimada, 1984] or between 0.04 – 0.16in (1-3mm) by [Sansoz et al., 2001]. Experimental plasticity analyses were shown to accurately account for the initiation and speed of short cracks and the ability to couple it with long crack propagation [Shimada and Furuya, 1987].

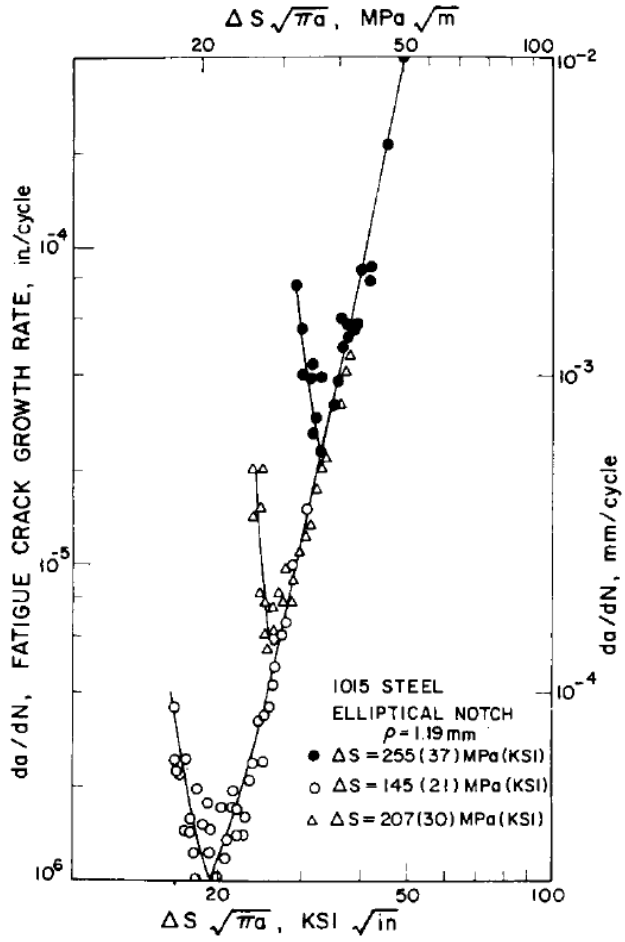

Figure 2.15: Crack growth rates where short and long crack rates are shown, with initial rates for short cracks higher than that for long cracks [El Haddad et al., 1980].

2.2.2 Elastic-Plastic Fracture Mechanics

Excessive plastic deformation at the crack tip violates the requisite conditions for LEFM approaches in fatigue crack propagation. For static cases, the *J*-integral proposed by Rice used a path independent integral to characterize the strain concentration near notches [Rice, 1968]. In doing so, plasticity in components with notches and cracks could be analyzed via fracture mechanics approaches. Stress and strain fields could then be represented by the Hutchinson-Rice-Rosengren (HRR) equations, i.e.,

$$\sigma_{ij} = \sigma_0 \left(\frac{J}{\alpha \sigma_0 \varepsilon_0 I_n r} \right)^{\frac{1}{1+n}} f_{ij}(n,\theta), \tag{2.25a}$$

$$\varepsilon_{ij} = \alpha \varepsilon_0 \left(\frac{J}{\alpha \sigma_0 \varepsilon_0 I_n r} \right)^{\frac{n}{1+n}} g_{ij}(n,\theta), \tag{2.25b}$$

where σ_0, ε_0, α and n are the Ramberg-Osgood constants, I_n is an integration constant dependent on n and f_{ij}, g_{ij} are functions to describe the angular variation of stress and strain, respectively [Sanford, 2003]. Much like K in LEFM for Eq. (18), J modifies the stress field around the crack and has been proven to be independent of specimen thickness, with limit load failures of small specimens to 8in (203mm) thick specimens [Begley and Landes, 1972].

In the event of gross plasticity during cyclic loading, the *J*-integral has been successfully extended to a cyclic parameter, ΔJ, by [Dowling and Begley, 1976; Branco and Radon, 1976]. By extending the definition of the *J*-integral to multiple loading events, the area under the load-load-line deflection curve for subsequent cycles is used in calculating the value of ΔJ from experimental data, as shown in Fig. 2.16 [Dowling and Begley, 1976]. Similar to Eq. (2.22), Stage II crack growth can be modeled as a function of the cyclic parameter, e.g.,

$$\frac{da}{dN} = C\left(\Delta J\right)^m, \tag{2.26}$$

where C and m are fitting constants. Comparisons between FCG data during gross plasticity and FCG data obtained with linear elastic data show good correlations in all stages of crack growth, Fig. 2.17. Rate effects and crack closure are still notable in experimental data, necessitating corrections to be made, similar to those of Eq. (2.23) [Dowling and Iyyer, 1987].

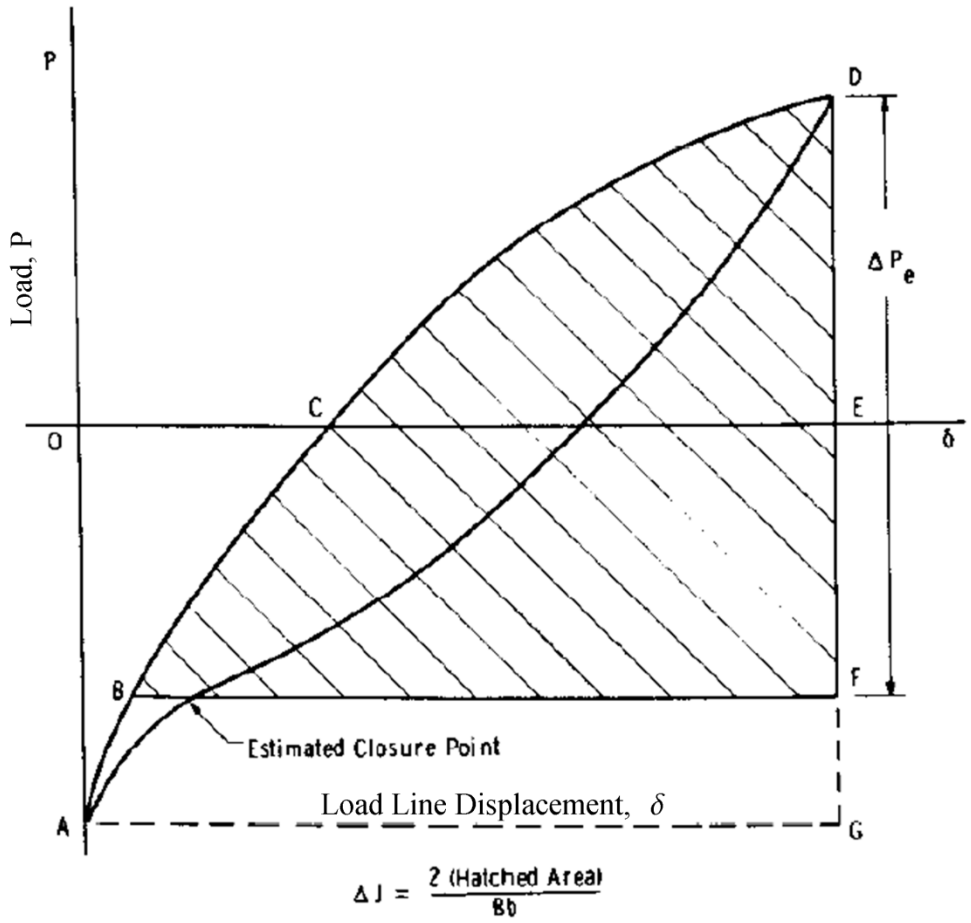

Figure 2.16: Calculation of ΔJ during cyclic loading, taking into account crack closure [Dowling and Begley, 1976].

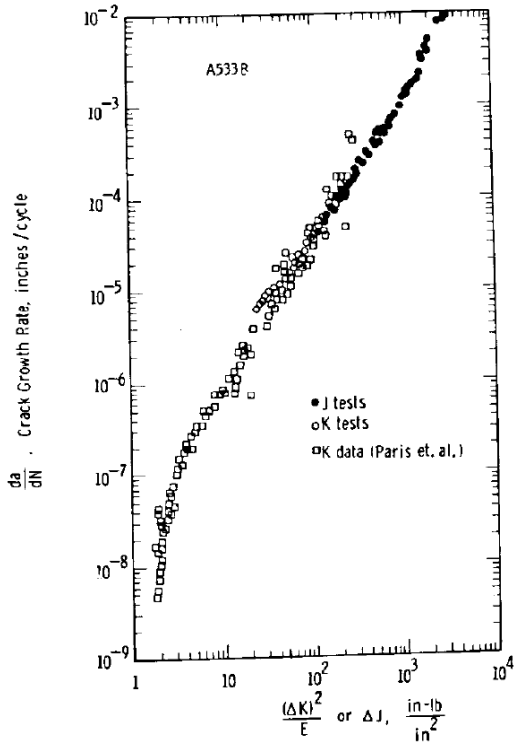

Figure 2.17: Crack growth rates obtained under linear elastic and gross plasticity conditions [Dowling and Begley, 1976].

Of particular interest are short cracks that originate from notches, as localized plasticity predates the crack initiation and propagation in cyclically loaded specimens [El Haddad et al., 1980]. By implementing Neuber's rule, one of the early estimations of ΔJ was proposed as a function of the stress and strain ranges, geometric properties and material parameters, i.e.,

$$\Delta J = 2\pi F^2 \left(l + l_0\right)\left[\frac{f(n)}{n+1}\left(\frac{\Delta\sigma\Delta\varepsilon}{E}\right) - \left(\frac{2f(n)}{n+1}\right)\frac{\Delta\sigma^2}{2E}\right], \tag{2.27}$$

where F is a geometry dependent constant, l is the crack length, l_0 is a material constant, and $f(n)$ is a function of the strain hardening exponent, n. The material parameter, l_0, constitutes the essential modifying parameter to correctly model short crack behavior, in which ΔK

approximations typically overestimate. Experimental and numerical routines have included the use of the crack tip opening displacement (CTOD) and its relation to J, allowing for accurate test control and data acquisition during testing [Tracey, 1976; Shih, 1981].

More recently, creep-fatigue crack growth has been investigated with the cyclic J parameter [Merah et al., 1999]. Implementing SS304 at high temperatures, both ΔK and ΔJ were observed to correlate well with crack growth data. A combination of fatigue and creep ΔJ components, ΔJ_f and ΔJ_c, respectively, was implemented to accurately capture the crack growth rates, Fig. 2.18. Rate effects were observed, requiring a correction, as noted by [Dowling and Iyyer, 1987]. During hold time tests, ΔJ was found to be inadequate, due to the lack of a time-dependency in Eq. (2.26), resulting in hold-time cracking being taken into account using ΔJ and t_h through multiplicative terms, avoiding the use of traditional time-dependent fracture mechanics approaches.

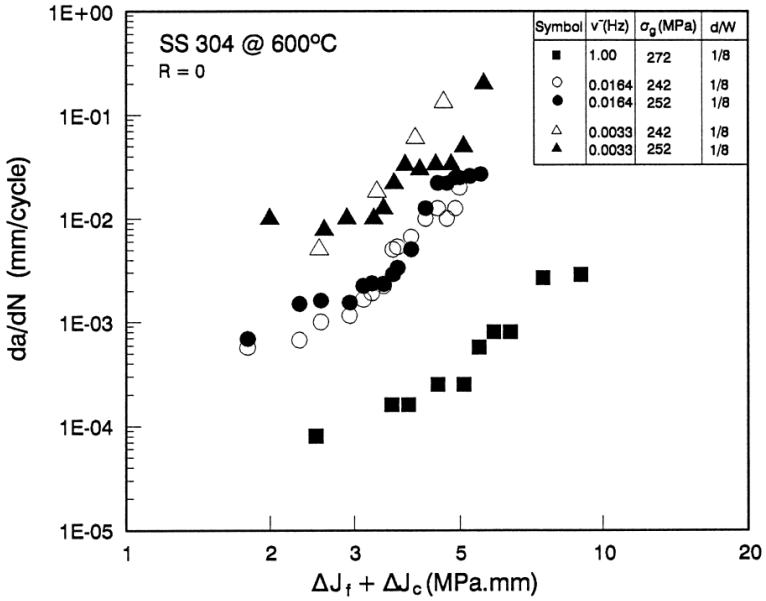

Figure 2.18: Creep-Fatigue crack growth rates as a function of the total J-integral range with and without hold times [Merah et al., 1999].

2.2.3 Time-Dependent Fracture Mechanics

Extension of cracks under the application of fixed load conditions gives rise to time-dependent fracture mechanics. More commonly referred to as creep crack growth, TDFM utilizes analytical solutions to depict the transient behavior of cracks. Developed in the work of Landes and Begley, the C^* parameter is the characterizing crack tip parameter under extensive small scale creep conditions [Landes and Begley, 1976], i.e.,

$$C^* = \int_{\Gamma} \dot{W} dy - \mathbf{T} \frac{\partial \dot{\mathbf{u}}}{\partial \mathbf{x}} ds, \tag{2.28}$$

where $\boldsymbol{T}$ is the surface traction vector and $\dot{\boldsymbol{u}}$ is the displacement rate vector. With the strain energy density in a rate form, $\dot{W}$, conventional steady-state creep rates are applicable [Riedel and Rice, 1980; Bassani and McClintock, 1981], e.g.,

$$\dot{\varepsilon} = \frac{\dot{\sigma}}{E} + \dot{\varepsilon}_0 \left(\frac{\sigma}{\sigma_0} \right)^n. \tag{2.29}$$

Implementing Eqs. (2.28-29) into stress field equations, the crack tip stress and strain rates can then be characterized, based on having achieved steady-state creep conditions [Saxena, et al., 1981], i.e.,

$$\sigma \propto \left(\frac{C^*}{r} \right)^{\frac{1}{k+1}}, \tag{2.30a}$$

$$\dot{\varepsilon} \propto \left(\frac{C^*}{r} \right)^{\frac{k}{k+1}}. \tag{2.30b}$$

The advantage of C^* is observed, as the time-dependent crack growth due to small-scale creep can be accounted for through the use of EPFM crack tip parameters and related back to LEFM parameters, Fig. 2.19.

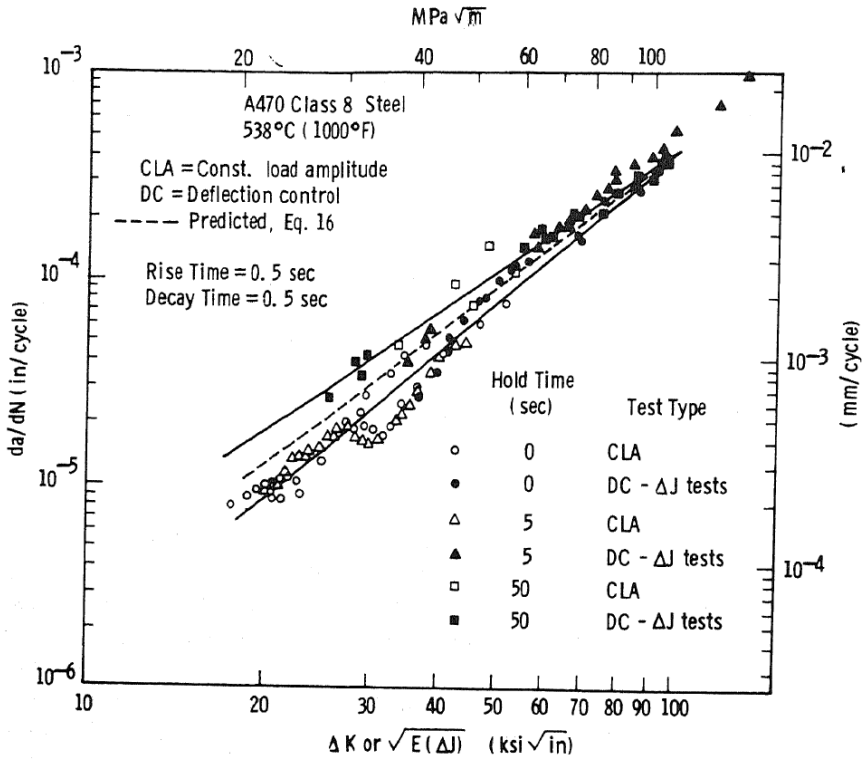

Figure 2.19: Fatigue crack growth rates with and without holds, related to LEFM methods through approximation the C^* parameter [Saxena et al., 1981].

Incorporation of primary creep into Eq. (2.29) necessitates that another parameter be defined, ensuring the creep strain rate dominates the elastic strain rate [Saxena, 1993]. As such, $C(t)$ is introduced as a stress amplitude parameter, capable of describing elastic, power-law and elastic, primary and power-law materials. For the latter, two time constants, t_{TP} and t_2, are introduced to define $C(t)$, i.e.,

$$C(t) = \left[1 + \left(\frac{t_{TP}}{t}\right) + \left(\frac{t_2}{t}\right)^{p/(p+1)}\right] C_s^* . \tag{2.31}$$

Due to the restriction that $C(t)$ must be calculated and the fact that under extensive creep conditions, $C(t)$ and C^* are equivalent, Saxena proposed the C_t parameter [Saxena, 1986].

The C_t parameter allows for the unification of small scale creep, transient creep and steady-state creep into one single parameter [Saxena, 1986]. The instantaneous value is furnished by analysis of the load, P, versus creep deflection rate, $\dot{V}$, i.e.

$$C_t = -\frac{1}{B}\frac{\partial U^*}{\partial a}, \tag{2.32}$$

where U^* is the area between two curves for specimens with crack lengths a and $a + \Delta a$. At steady state conditions, Eq. (2.32) can be simplified and represented by C^*, i.e.,

$$C^* = \frac{P\dot{V}_c}{BW} f\left(a/W\right), \tag{2.33}$$

and calculated based on experimental data and specimen geometry. Utilizing all TDFM developments, notably formulations based on the J-integral and the C_t parameter, creep-fatigue crack growth models can be furnished based on experimental data, as discussed in Section 2.3.1.2.

2.3 Creep-Fatigue Life Estimation

The development of fracture mechanics approaches to assess crack growth in components, whether independent of time or not, readily translate to creep-fatigue life estimation techniques. In addition to traditional fracture mechanics approaches, other experimental and numerical routines have been developed to assess and predict the life of components subjected to CF conditions. Experimental routines include the use of smooth, notched, and cracked specimens, and in some rare cases, actual components. Numerical approaches involve traditional viscoplastic material modeling, as well as damage-based approaches. Although the main focus of this research is experimentally-based analytical model development, numerical models commonly used in life prediction will be discussed for the sake of comprehensiveness.

2.3.1 Creep-Fatigue Experimental Approaches

Experimental investigations into CF behavior are divided into two distinct groups, i.e. non-fracture mechanics-based and fracture mechanics-based approaches. The difference, typically, depends on the specimen implemented and whether or not stable crack growth can be observed for some distance. The results from different investigations vary significantly, with different methods of quantifying life.

2.3.1.1 Non-Fracture Mechanics-Based Approaches

Experimental investigations involving standard tensile specimens have recently been used in creep-fatigue investigations, e.g. [Gao et al., 2005]. In low cycle fatigue (LCF) testing, fully-reversed bending, CF conditions were observed to initiate minor cracks and coalesce into major cracks. The number of minor cracks was observed to increase with both the hold time duration and increased strain ranges. No life prediction methodology was provided, merely the assertion that the failure of specimens was dominated by Stage II crack growth.

Creep, fatigue and creep-fatigue behavior of a gas turbine disc has been studied using smooth cylindrical specimens, e.g. [Hyde et al., 1997]. Two separate types of tensile specimens were used in tensile, creep and fully-reversed fatigue testing, with the difference being a shorter gage length in fatigue tests to prevent buckling. Fatigue tests utilized a simplistic Basquin's law for life prediction, whereas creep and creep-fatigue life prediction involved the use of damage mechanics. A healing effect was observed to be due to the periodic unloading and a continuum damage rate equation, $\dot{\omega}$, was proposed to incorporate a healing parameter, h, i.e.,

$$\dot{\omega} = B\frac{\sigma^{\chi}}{\left(1-\omega+hft\right)^{\phi}}, \tag{2.34}$$

where B, χ and ϕ are fitting constants, f is the loading cycle frequency and t is time. Equation (2.34) is implemented in numerical simulations, modifying the response of the material to account for the healing observed due to fatigue reversals. Relationships based on the hold time on the life of specimens were made, notably experiments with dwell times of 1, 4, and 18s were up to three times longer than experiments with dwells of 28 and 98s, establishing the healing effect due to cyclic loading.

Experiments on specimens cut from turbine blades are commonly conducted. In testing the creep life of IN-738, five blades were obtained in the virgin, 30,000, 45,000, 60,000 and 80,000 hour service-exposure condition [Marahleh et al., 2006]. Specimens were cut from blades, as shown in Fig. 2.20, and subjected to creep-like conditions to failure. Results helped to establish the remaining creep life, in terms of the Larson-Miller parameter, of components after periods of service exposure, in an effort to limit the cost of early replacement.

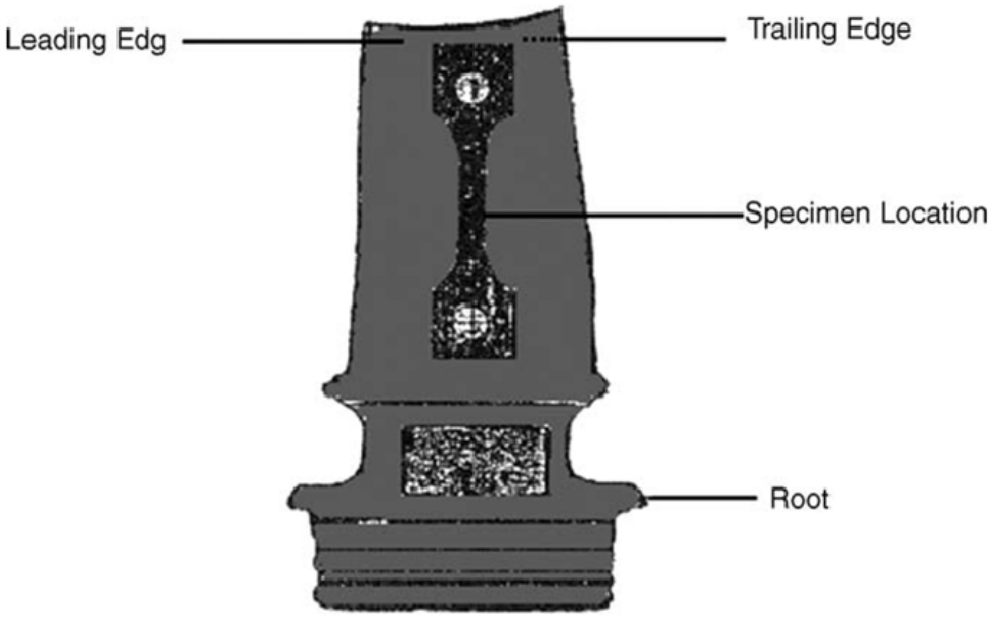

Figure 2.20: Location of specimen obtained from turbine blade used in creep life prediction experiments [Marahleh et al., 2006].

Creep-Fatigue experiments on full-scale turbine blades are less common than made-from-blade specimens, due to the complexity of experimental fixtures required. Stemming from the discrepancies between specimens and actual parts, statistical life prediction techniques have been employed [Yan and Nie, 2008]. Using directionally-solidified superalloy aircraft blades, creep-fatigue experiments were conducted to identify regions of critical stress in new and used blades, Fig. 2.21. The development of the experimental fixturing allowed for several variations of experiments to be conducted and standard CF test results correlated well with data obtained from in-service components. Ultimately, the proof-of-concept experiments successfully revealed the benefit and ability to testing full scale components, as opposed to representative specimens.

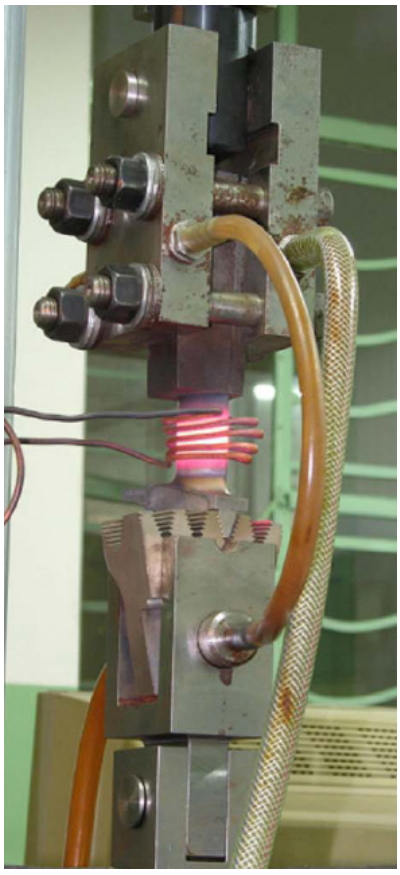

Figure 2.21: Full scale superalloy aircraft turbine blade used in experimental investigations [Yan and Nie, 2008].

2.3.1.2 Fracture Mechanics-Based Approaches

Major strides in creep-fatigue testing have revolved around the development of advanced computer-controlled routines and increasingly complex representative analytical models. Using LEFM, EPFM, and TDFM methods, researchers have proposed models to observe the effects of hold times on fatigue crack growth rates, e.g. [Saxena et al., 1981]. The goal has been to calculate the remaining life based on the observed and calculated parameters, as would be done using Eqs. (2.22) and (2.23), in tests that involve both creep and fatigue mechanisms. All of the investigations within this section used traditional fracture mechanics specimens with pre-cracks and requisite experimental equipment. Investigations were purely on propagation of cracks, ignoring the initiation processes.

Approximation techniques using simplifying assumptions have been employed based on LEFM methods. Estimating the total cycle crack growth can be separated into the cycle- and time-dependent components, respectively, i.e.

$$\frac{da}{dN} = \left.\frac{da}{dN}\right|_f + \left.\frac{da}{dN}\right|_h = C\left(\Delta K\right)^m + A'\left(\Delta K\right)^{2p} t_h^{(1-p)}, \tag{2.35}$$

where C and m are the Paris law constants and A' is function of material constants b and p [Saxena et al., 1981]. Short hold times in FCG tests were readily accounted for with Eq. (2.35), as shown in Fig. 2.22. Time-dependent fracture mechanics parameters, notably C^*, were not employed and it was noted that the Paris formulation for the cyclic contribution to crack growth may not be adequate to capture crack growth in Stage I or III.

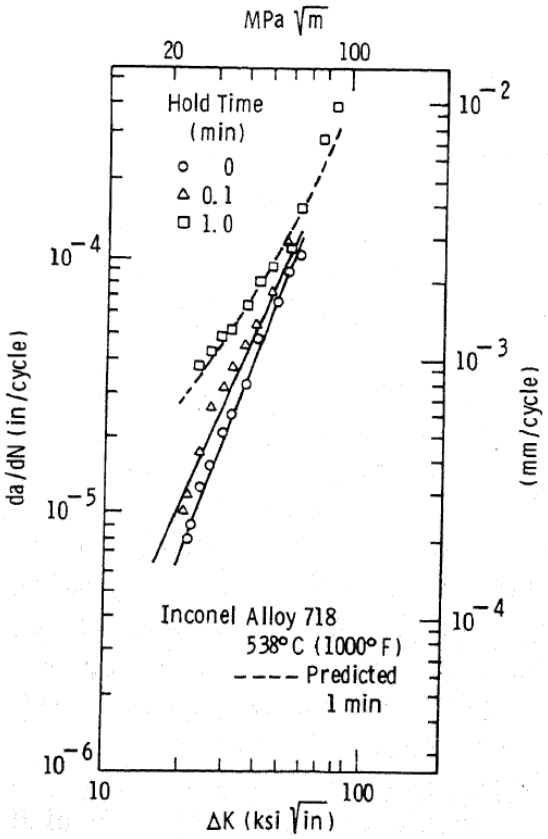

Figure 2.22: Hold time effect on fatigue crack growth in IN 718 [Saxena et al., 1981].

Incorporating EPFM methods in CFCG testing, without the development of an analytical model to predict behavior, ΔJ has been used to correlate crack growth rates [Baik and Kim, 2000]. Specifically, investigation of the combined effects of applied load, frequency and hold time and the applicability of ΔK and ΔJ to account for crack growth was conducted. Due to anticipated plasticity ahead of the crack tip at higher loadings, an expression for ΔJ under load-control was utilized, i.e.

$$\Delta J = \frac{2}{Bb}\left[\xi A_c + \zeta \Delta P\left(V_{\max} - V_{\min}\right)\right], \tag{2.36}$$

where B is the specimen thickness, b is the ligament (W-a), ξ and ζ are material functions, ΔP is the load range between P_{max} and P_{min} and V_{max} and V_{min} are the load-line displacements at P_{max}

and P_{min}, respectively. Replacing Eq. (2.36) in the Paris law, Stage II crack growth was readily correlated to the EPFM parameter, Fig. 2.23. Experiments with hold times revealed a similar trend; however, no correlation was presented within the research, even where one could be observed.

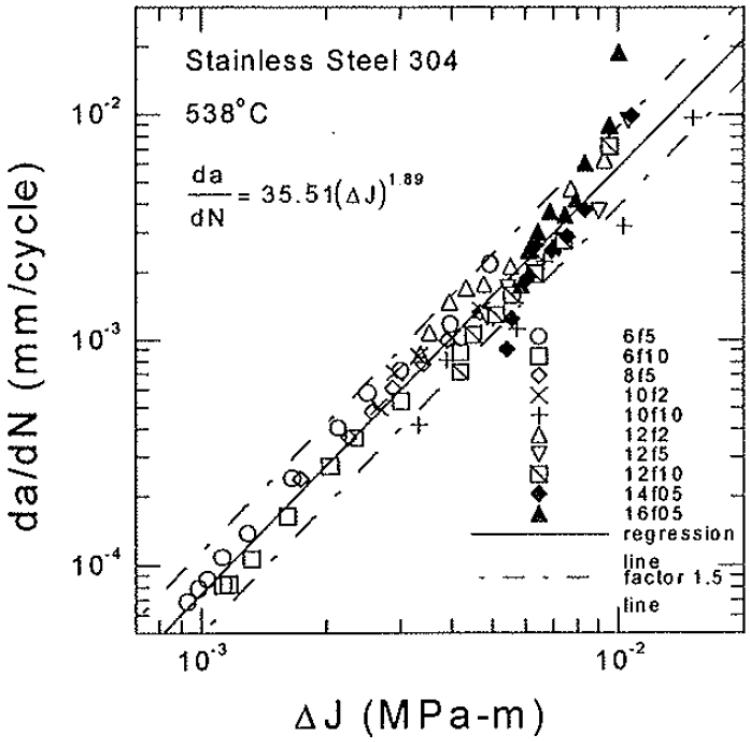

Figure 2.23: Correlation between Stage II crack growth and ΔJ [Baik and Kim, 2000].

The development of C^*, $C(t)$ and C_t make TDFM methods attractive to researchers investigating CFCG. In a general overview paper, several forms of TDFM models are explained and methodologies were provided for calculation of the parameters based on observable measurements [Saxena, 1993]. Estimating $(C_t)_{avg}$ based on a time average of C_t over the length of hold period, a cumulative crack growth model was proposed, i.e.

$$\frac{da}{dN} = C\left(\Delta K\right)^m + D\left[\left(C_t\right)_{avg}\right]^p t_h, \tag{2.37}$$

where C, m, D and p are material constants and t_h is the length of the hold time [Yoon (I) et al., 1993]. Hold times of 10 seconds and 10 minutes or greater revealed different failure mechanisms, with the greater than or equal to 10 minute hold times having extensive creep cavities near the crack tip. Extending this approach, the effect of overloads was observed to increase the time-dependent crack growth rates due to enhanced void nucleation, Fig. 2.24 [Yoon (II) et al., 1993].

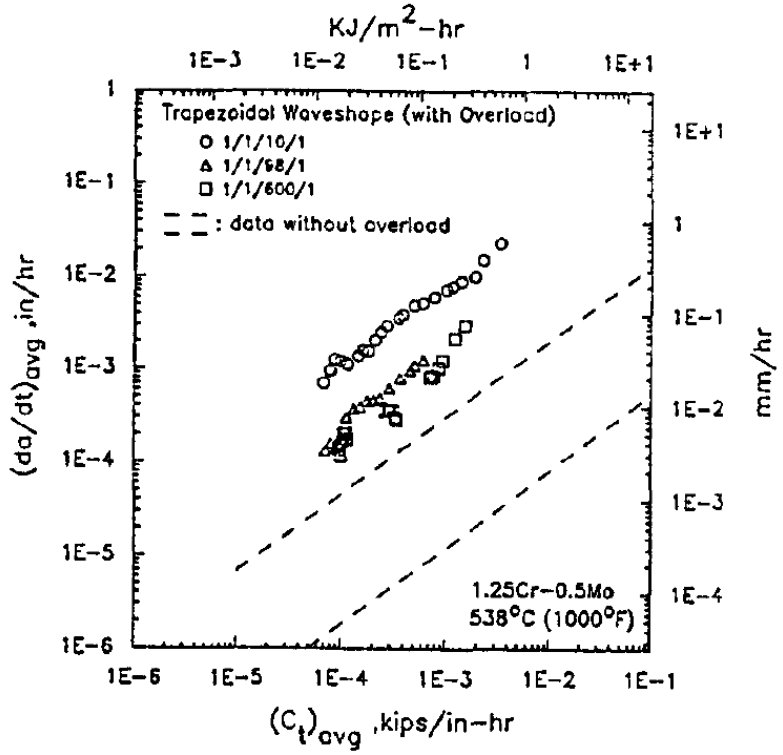

Figure 2.24: Effect of overload on CFCG rates using $(da/dt)_{avg}$ approach [Yoon (II) et al., 1993].

Additional models predicting creep-fatigue life estimation including multiplicative laws, interaction models and more comprehensive FCG components. Crack growth rates with and without hold times were found to be more accurately modeled using a multiplicative law with rates in terms of crack velocity, da/dt, i.e.,

$$\left(\frac{da}{dt}\right)_h = \left(\frac{da}{dt}\right)_c^{\Psi} \left(\frac{da}{dt}\right)_f^{(1-\Psi)}, \tag{2.38}$$

where Ψ is a damage function based on damage due to creep, D_c, and fatigue, D_f [Baik and Kim, 2007]. Results revealed good correlation at low loads and stress intensity factors; however, correlations failed at higher loads when crack speeds were greater.

The creep-fatigue interaction during experiments has been shown to be directly related to the size of the creep and cyclic plastic zone [Grover and Saxena, 1999]. Through the introduction of a creep reversal parameter, C_R, new estimates are more accurate in estimating the crack tip parameter C_t. The advantage is that by quantifying the effect the cyclic plasticity has on reversing the creep deformation, several assumptions involved with using C_t can be eliminated. Comparisons of experimentally obtained and predicted $(C_t)_{avg}$ values incorporating the creep reversal parameter were in agreement, Fig. 2.25. Limitations are imposed, such that the relationship between the creep zone and cyclic plastic zone size stays nearly constant, making the parameter limited to materials with a Norton creep law exponent, n, of less than 3.

Recently, a cumulative crack growth model aimed at incorporating an interaction term using a more simplistic approach was proposed [Yang et al., 2011]. Similar to previous cumulative crack growth models, the superposition principle is employed in which an interaction term is added, i.e.

$$\frac{da}{dN} = \left(\frac{da}{dN}\right)_f + \left(\frac{da}{dN}\right)_c + \left(\frac{da}{dN}\right)_{interaction}. \tag{2.39}$$

Initiation behavior was not included, and outdated, simplified crack growth models were utilized for the fatigue and creep contributions. While the current research of Yang et al., is based on the proposal of Saxena [Saxena, 1993], future investigations are necessary to account for both crack

initiation and crack propagation from notched components, while incorporating more complex analytical formulations.

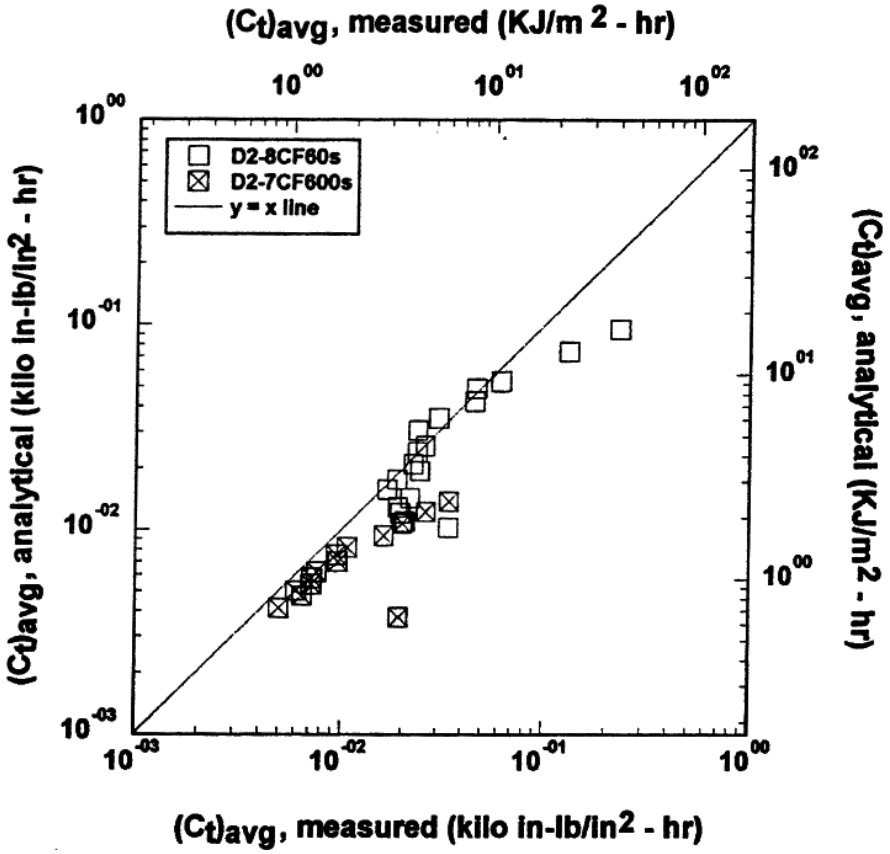

Figure 2.25: Comparison of experimental and analytical values of $(C_t)_{avg}$ incorporating the creep reversal parameter [Grover and Saxena, 1999].

Working with a more complex fatigue model and TDFM methods, several superposition models similar to Eq. (2.35) were proposed [Zhang et al., 2012]. In predicting more complete life estimations, Walker and Forman fatigue models were used as opposed to the traditional Paris law, i.e.

$$\frac{da}{dN} = C\left[\frac{\Delta K}{(1-R)^{1-\varsigma}}\right]^m + \frac{1}{f} DC^{*\phi}, \tag{2.40a}$$

$$\frac{da}{dN} = \frac{C(\Delta K)^m}{(1-R)K_c - \Delta K} + \frac{1}{f} DC^{*\phi}. \tag{2.40b}$$

where the second term in Eqs. (2.40a) and (2.40b) account for the creep-fatigue loading, based on the loading frequency, f, and two material constants, D and ϕ. Increasing complexity of the second term to include frequency and critical stress intensities lead to even more complex crack growth models. Consistency between all of the proposed models and existing models was established, with the benefit of being able to account for frequency effects in the both terms of the crack growth model [Zhang et al., 2012].

Through the incorporation of increasingly complex analytical models based on fracture parameters, crack growth due to creep-fatigue conditions are capable of more accurately simulating the behavior of experimental data. While the majority of these approaches are based on the long crack growth, numerical analyses are bridging the gap between experimental data in terms of crack initiation and propagation.

2.3.2 Creep-Fatigue Numerical Approaches

Numerical approaches to creep-fatigue life prediction commonly involve the use of viscoplastic material models and damage mechanics. Viscoplastic material models have the capability of predicting various material behaviors, including hardening and softening processes, at room and elevated temperatures by simulating the inelastic strain rate. Full stress and strain response is readily predicted through the use of finite element analyses. The incorporation of damage mechanics models into constitutive relations allows crack initiation, void nucleation and void coalescence to be simulated in response to creep, fatigue or creep-fatigue loading conditions.

Damage mechanics have been long apart of life prediction techniques, with the Palmgren-Miner rule commonly used for fatigue life calculations [Fatemi and Yang, 1998]. Understanding the importance of such a model, researchers continued to investigate and propose variables to account for various types of damage. Essentially, variables are introduced into analytical formulations, e.g. Eq. (2.34) proposed by [Hyde et al., 1997], allowing for the tracking and evolution of a material based on the accrued damage. Constitutive models are therefore attractive to predict the damage, allowing full-life predictions to be made. For an overview of selected leading damage models, including crack growth models, readers are directed to the work of [Fatemi and Yang, 1998].

The Miller MATMOD model is a viscoplastic material model that was originally developed in 1976 [Miller (I), 1976; Miller (II), 1976]. Through the back stress and drag stress, a generic function can be manipulated to account for a variety of phenomenon, including creep, fatigue and creep-fatigue. Combining strain hardening and temperature affects, as well as steady-state creep rates and previous strain history, the inelastic strain rate at any time may be calculated, i.e.

$$\dot{\varepsilon}_p = B\theta' \left\{ sinh\left(\frac{\left|\sigma - X\right|}{D} \right)^{1.5} \right\}^n sgn\left(\sigma - X\right). \tag{2.41}$$

where B is a constant and θ' is a temperature-dependent factor. In the late 1980's, the model was updated with FATIGMOD-ET and CRACKMOD to account for analysis of non-propagating cracks, short crack growth and crack closure effects [Miller et al., 1988]. MATMOD, FATIGUEMOD-ET, and CRACKMOD are constitutive material behavior models aimed at predicting the stress-strain behavior of the material, capturing hardening/softening, crack initiation, and crack propagation.

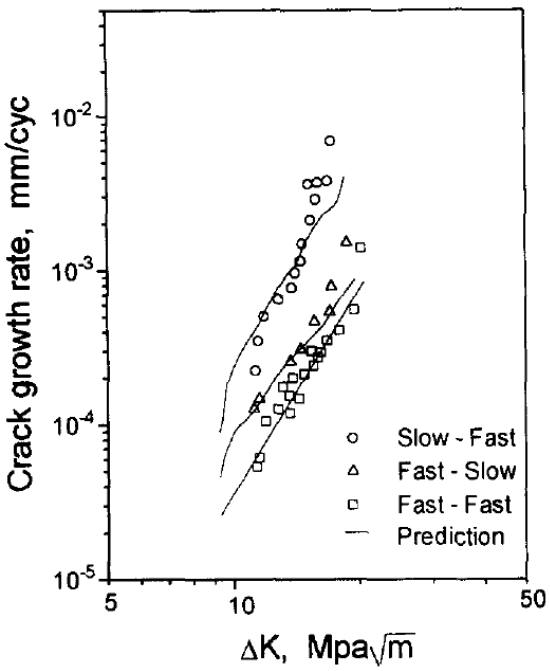

Figure 2.26: Crack growth prediction of SS304 at 650°C under various waveforms using the MATMOD and CRACKMOD constitutive models [Lee and Kim, 1996].

***Table 2.1**: MATMOD and CRACKMOD Model constants for SS304 [Lee and Kim, 1996].*

Constant	Value	Constant	Value
A	1.00×10^{14}	δ	0.6
B	10	C_1	0.382×10^{-10}
α	808	C_2	0.28×10^{-3}
H_1	0.48	m_1	2.215
H_2	10	m_2	1.382
Q	91000 cal/mol	n	6
k	1.9859 cal/mol	λ	9.296

To predict the effect waveforms have on material behavior, experimental data was obtained from fatigue testing with modified load-unload speeds, i.e. fast loading – fast unloading, fast loading – slow unloading, and slow loading – fast unloading [Lee and Kim, 1996]. Utilizing MATMOD and CRACKMOD, creep-fatigue crack growth was accurately simulated based on varying load waveforms on SS304 at 650°C, Fig. 2.26, with constants provided in Table 2.1. Additionally, through the development of damage variables during the

simulation, the failure mode could be determined for each stage of crack growth, enabling the ability to differentiate between either fatigue- or creep-dominant mechanisms.

Another leading viscoplastic material model, the Chaboche model, was proposed around the same time as the MATMOD model [Chaboche, 1977]. While allowing for the incorporation of multiple hardening laws, the inelastic strain rate is function of the yield surface (von Mises) developed in time-independent plasticity, i.e.,

$$\dot{\boldsymbol{\varepsilon}}_{\mathrm{p}} = \frac{3}{2}\left\langle \left(\frac{J\left(\boldsymbol{\sigma}-\mathbf{X}\right)-k-R}{D} \right)^{n} \right\rangle \frac{\boldsymbol{\sigma}'-\mathbf{X}'}{J\left(\boldsymbol{\sigma}-\mathbf{X}\right)}, \tag{2.42}$$

Here, the 3D plastic strain tensor increment can be related to the viscous flow function, $\dot{p}$, current stress, $\boldsymbol{\sigma}$, kinematic hardening stress tensor, $\boldsymbol{X}$, the von Mises distance in the deviatoric stress space $J(\boldsymbol{\sigma}-\mathbf{X})$, isotropic hardening value, R, yield stress, y, drag stress, D and the deviatoric components of stress and kinematic hardening, $\boldsymbol{\sigma}'$ and $\boldsymbol{X}'$, respectively. Isotropic and kinematic hardening follow nonlinear relationships, i.e.,

$$\dot{R} = b(Q-R)\dot{p}, \tag{2.43}$$

$$\dot{\mathbf{X}} = \sum \frac{2}{3} C_i \dot{\boldsymbol{\varepsilon}}_{\mathrm{p}} - \gamma_i \mathbf{X} \dot{p}, \tag{2.44}$$

where the nonlinear terms depend on the previous history response and material constants, b, Q, C, and γ. During the simulation, elastic and plastic response is determined, allowing for the future response to be accurately predicted.

In addition to the hardening and softening behavior of materials, several, more complex material behavior models can be readily implemented, e.g. [Chaboche, 2008], making it a popular model amongst researchers [Zhan and Tong, 2004]. Extensions of the Chaboche model to account for crack growth have utilized the cohesive zone approach [Bouvard et al., 2009]. By

incorporating the cohesive zone element to accumulate damage during loading periods, short crack propagation and load regimes with overloads are able to accurately be simulated. Long crack growth behavior was subsequently modeled during the fatigue regime, with results following experimental data, Fig. 2.27.

Coupling constitutive modeling with full scale testing, the lives of turbine components have been assessed and simulated simultaneously [Rauch and Roos, 2008]. In effort to model the behavior at the turbine blade-disc connection, experimental apparatuses were developed from physical components, similar to those of Fig. 2.21, and low cycle fatigue experiments were conducted under simulated service conditions. Damage accumulation was introduced for creep and fatigue damage, based on accumulated plastic strain using the Chaboche viscoplastic material model. With the developed method of damage accumulation, life to crack initiation was readily achieved, with more accurate predictions at higher blade loads, Fig. 2.28.

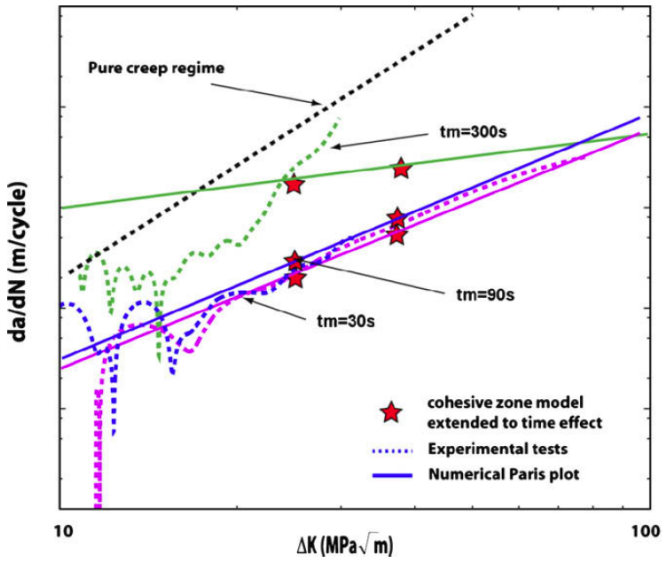

Figure 2.27: Comparison of experimental and simulated long crack growth data using the Chaboche model with Cohesive Zone crack model [Bouvard et al., 2009].

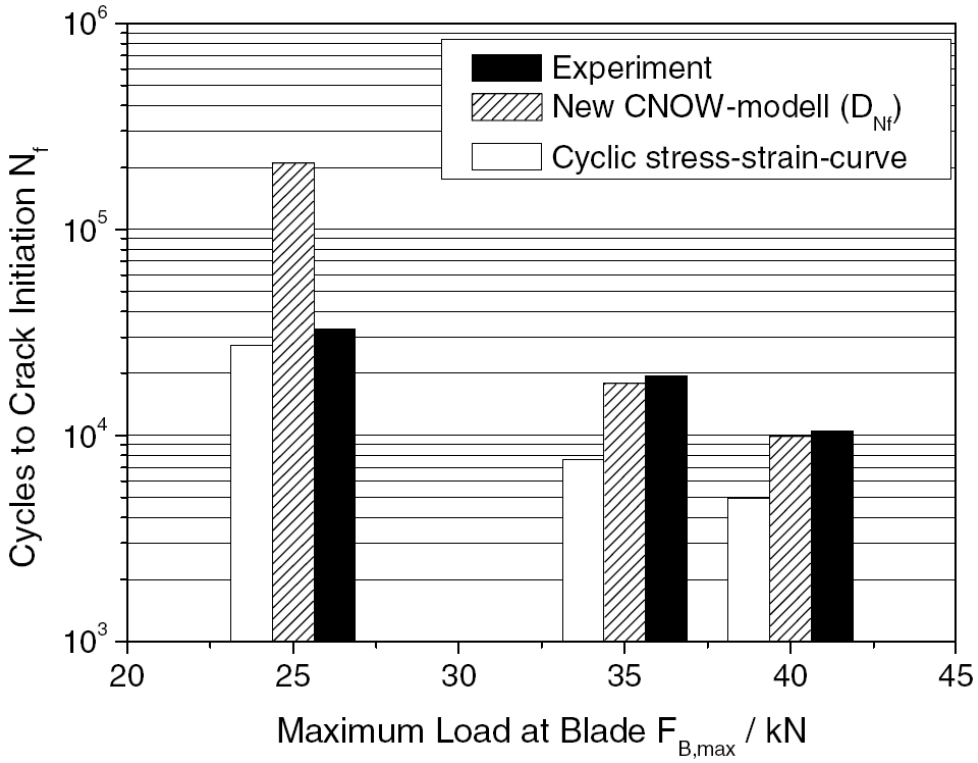

Figure 2.28: Comparison of experimental and predicted cycles to crack initiation based on Chaboche material model with damage accumulation law [Rauch and Roos, 2008].

Blending viscoplastic material modeling with long crack propagation theories, and through the use of high-performance computers, it is feasible to predict behavior of complex components under extreme conditions. While there are substantial requisites to conducting such analyses, there are clear advantages to doing so, as in [Rauch and Roos, 2008]. Ultimately, full life predictions could be made using this approach, or a more simplistic, yet useful, approach.

Incorporating the analytical formulations developed in Section 2.2 and the application to life estimation in this section, a summary of the requisite information needed to make a prediction for crack growth is provided, Fig. 2.29. Depending on the load conditions and type of specimens available, several different options are available for predicting fatigue, creep, and creep-fatigue crack growth. The selection of the model to be implemented will depend on the

definition of a crack, i.e. small or long crack, and the definition of instability, whether to stage III crack growth or rupture upon reaching instability.

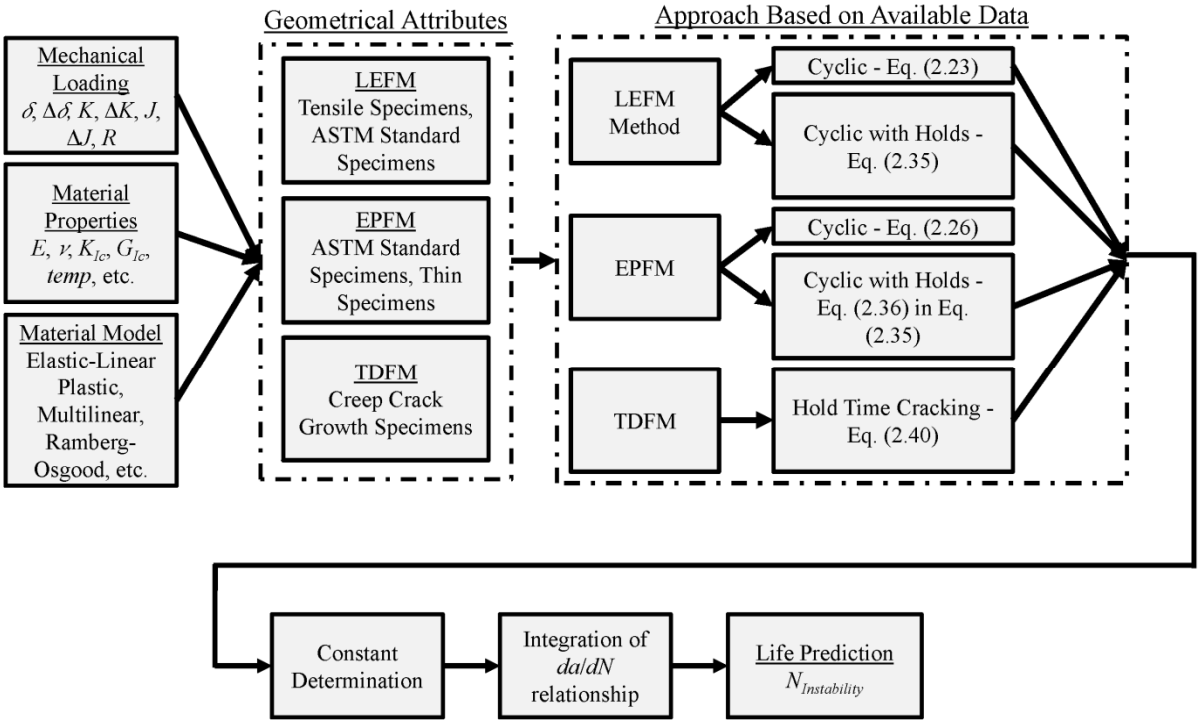

Figure 2.29: Traditional approachs for crack growth analyses, including elastic, plastic and time-dependent formulations

2.4 Mechanical Behavior of SS 304

The preceding sections have provided an overview on the techniques related to creep-fatigue crack growth analyses. While the techniques were developed using specific materials, they are applicable to a broad range of materials, including the subject SS304 used in this investigation.

Stainless steels have become commonplace in a handful of trades, ranging from food to medical to transportation industries [ASM, 2007]. Having excellent properties at both cryogenic and elevated temperatures, austenitic stainless steels are suitable for decorative and structural components, with hardening achieved by cold working. Having a face centered cubic (FCC)

structure, austenitic SS304 is an all-around structural alloy with good corrosion and oxidation resistance [ASM, 2007]. Chemical composition can vary substantially, with Chromium content between 16-25% and Nickel content up to 20%, with example compositions provided, Table 2.1. A representative microstructure is provided, showing typical MC inclusion clusters, Fig. 2.30 [Mills, 1988].

***Table 2.2**: Chemical composition of SS304 and SS304L, typical [ASM, 2007].*

Alloy	C	Mn	Si	Cr	Ni	P	S	Fe
SS304	0.08	2.0	1.0	18.0-20.0	8.0-10.5	0.045	0.03	bal.
SS304L	0.03	2.0	1.0	18.0-20.0	8.0-12.0	0.045	0.03	bal.

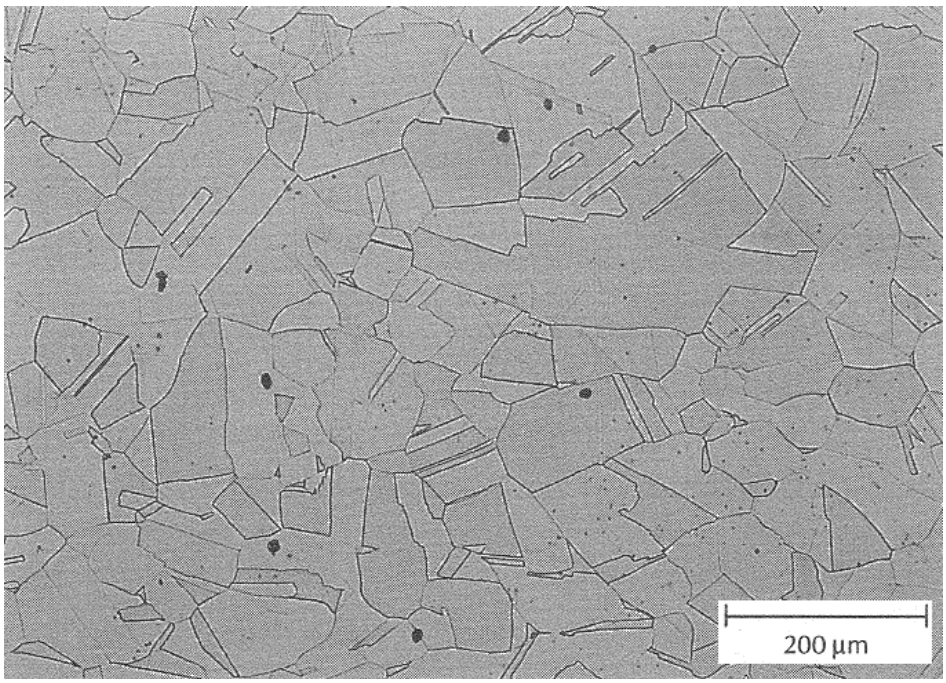

Figure 2.30: Typical microstructure of SS304 with MC inclusion clusters, [ASM, 2007].

Embrittlement of SS304 is a concern during the experimental portion of the investigation, namely sensitization, 475°C and sigma-phase embrittlement [ASM, 2007]. Due to the presence of carbides, the cooling process and existence of detrimental phases, strict control over the forming and processing of the material is essential. As such, all specimens used in testing should be obtained from a single batch of material, to limit the amount of disparity between material conditions. Additionally, test temperatures will be chosen that limit the negative effects and combined failure mechanisms that are presented by high temperature embrittlement processes.

Another area of interest in testing SS304 at elevated temperatures is the extent of oxidation that may occur on the surface, resulting in favorable crack initiation locations. In stress free oxidation studies, standard and nitrided SS304 samples were exposed to a temperature of 1472°F (800°C) and the mass change tracked throughout the duration of tests, as shown in Fig. 2.31 [Issartel et al., 2004]. Upon inspection of the surfaces, after 100 hours of stress-free exposure time, the oxide thickness was observed to be less than 30μm. Nitriding of specimens successfully reduced the oxide layer, approximately 2.7μm thick, after 100 hours. The extent of surface oxidation for the given time and temperature will be used during the development of the experimental test matrix in this investigation.

Relevant tensile, creep, fatigue and creep-fatigue properties will be provided within the following sections. Data is obtained from a variety of sources, including ASM handbooks and research publications. All data is provided as a reference for typical behavior under identified conditions and loadings, with an emphasis on properties relevant to the conditions imposed during the investigation.

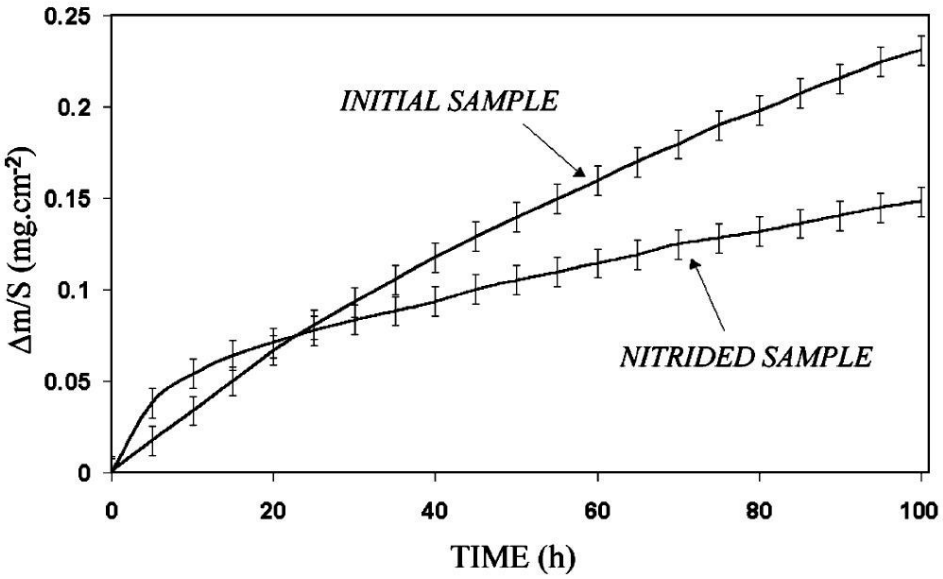

Figure 2.31: Mass gain of virgin and nitrided samples exposed to 1472°F (800°C) [Issartel et al., 2004]

2.4.1 Tensile Properties

The tensile properties for general SS304 used in preliminary specimen design were obtained from ASM stress-strain curves [ASM, 2007]. Full range stress-strain curves are provided for specimens at room temperature, up to 800°F (427°C), Fig. 2.32. A magnified view in the small strain region is provided, allowing for the determination of the elastic moduli and yield strengths, Fig. 2.32. Material properties for the provided temperatures were extrapolated from the stress-strain curves and reported in Table 2.2.

Temperature is observed to have a significant effect on SS304, with properties decreasing significantly between room temperature and 800°F (427°C). While no significant softening is seen in the elastic modulus, the yield strength is nearly half that of the room temperature strength at the highest test temperature. Extensive strain-hardening of the material is observed at all temperatures. Increasing the temperature also decreases the rupture strain of the material; nearly

half at 800°F (427°C) when compared to room temperature. Even so, SS304 remains a ductile material even at elevated temperatures, with a failure strain of roughly 50%.

***Table 2.3**: Tensile properties from SS304 at select temperatures [ASM, 2007].*

Temperature, *T* °F (°C)	**Elastic Modulus, *E*** Msi (GPa)	**Yield Strength, σ_y** ksi (MPa)	**Ultimate Strength, σ_{uts}** ksi (MPa)	**Rupture Strain, ϵ_f** (%)
68 (20)	25.448 (175.46)	36.3 (250)	83.8 (578)	86.2
400 (204)	25.448 (175.46)	57.2 (394)	63.8 (440)	53.1
600 (315)	25.448 (175.46)	22.7 (157)	60.0 (414)	48.5
800 (427)	25.448 (175.46)	20.5 (141)	58.5 (403)	46.9

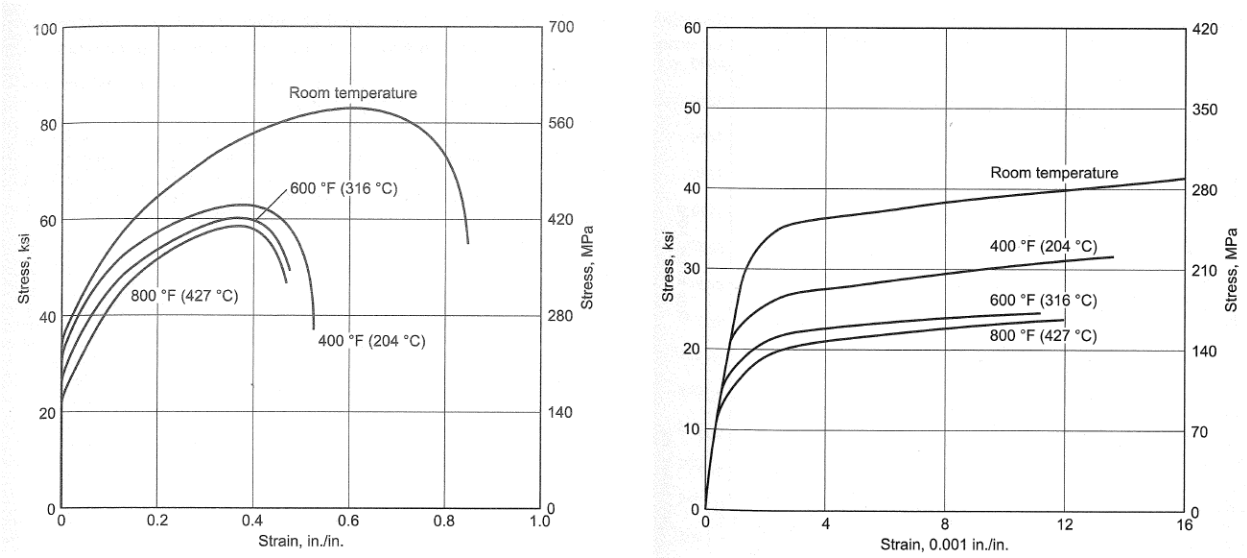

Figure 2.32: Full-range (left) and amplified small-strain (right) stress-strain curves for SS304 from room temperature to 800°F (427°C) [Mills, 1988].

Fracture of SS304 is primarily a result of microvoid coalescence at all temperatures [ASM, 2007]. Typically, the inclusions within the material will promote nucleation of the voids, leading to growth and subsequent coalescence. In terms of the types of inclusions, most commonly MC-type inclusions will be dispersed throughout the matrix, with the size leading to the amount of plasticity observed during fracture. The fracture appearance of a typical SS304 component is provided, at two levels of magnification, providing insight into the failure

mechanism, Fig. 2.33 [Mills, 1988]. In general, gross plasticity will be necessary for voids to coalesce and result in fracture.

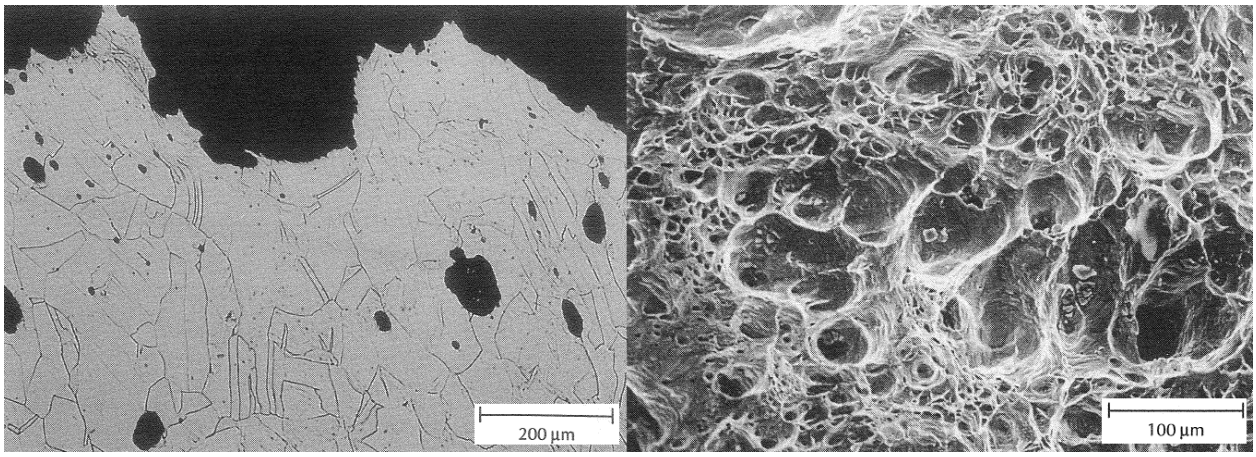

Figure 2.33: Fracture surface appearances of a fracture SS304 specimen under (left) light microscope and (right) scanning electron microscope [Mills, 1988].

2.4.2 Creep Properties

Creep data was commonly found in literature; however, results were routinely reported in manners other than traditional creep strain versus time graphs. A majority of the reported results came in stress-rupture presentation, with some of the data reported for the minimum creep rate at given stress levels, e.g. [Chopra and Natesan, 1977]. Other, less obscure methods of reporting creep results included the elongation at failure and the extent of grain boundary sliding during the creep test.

Attempting to understand the high temperature behavior of SS304, the effective stress dependencies on activation energy and general creep behavior have been investigated [Chopra and Natesan, 1977]. Two main observations included the effective stress dependence on minimum creep and the activation energy, as shown in Fig. 2.34. It was determined that the recovery process played an important role in creep at 1112°F (600°C) and 1292°F (700°C), as

dislocation density is reduced by recovery. Ultimately, it was determined that the activation energy required for creep deformation was close to the activation energy required for lattice self-diffusion.

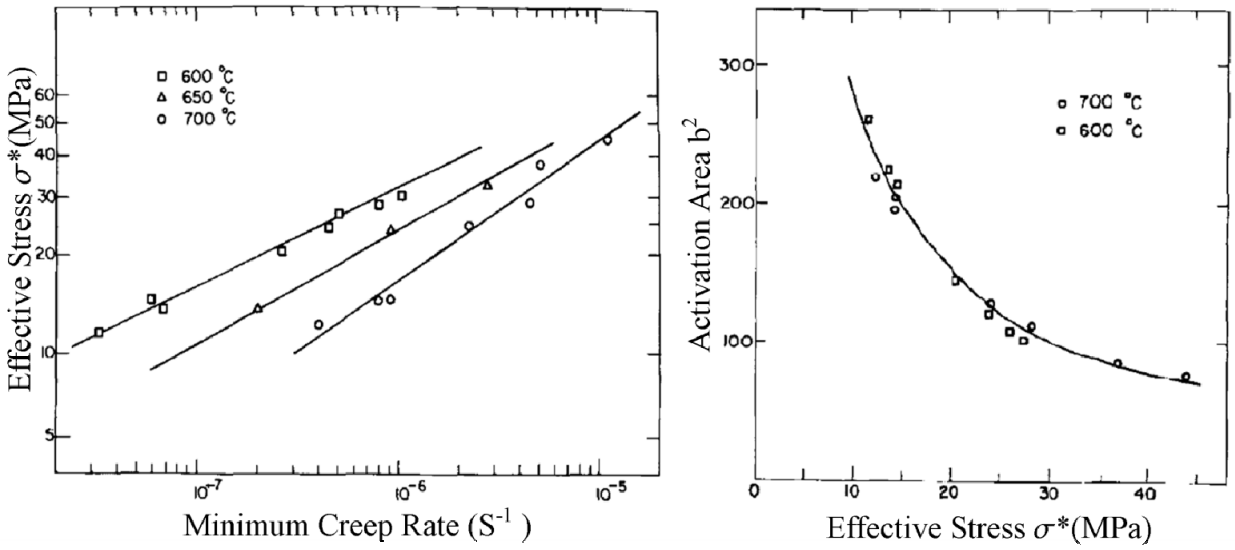

Figure 2.34: Dependence of (left) minimum creep rate and (right) activation area on mean effective stress in creep studies on SS304 [Chopra and Nateson, 1977].

The effect of axial and multiaxial stress states on the prediction of creep rupture was investigated in effort to extend multiaxial creep rupture formulations [Kim et al., 1991]. The principal and effective stress for both uniaxial and triaxial stress states were scrutinized in predicting life of specimens subjected to creep conditions, Fig. 2.35. The discrepancies between the two data representations indicate that the effective stress is not an appropriate term to collapse the data to a single relationship. A principal facet stress, as proposed by [Nix et al., 1989], is able to collapse the data to a single curve and accurately predict rupture time. Void formation and coalescence was noted to grow perpendicular to the applied load, with gross coalescence significantly affecting the rupture life of specimens [Kim et al., 1991].

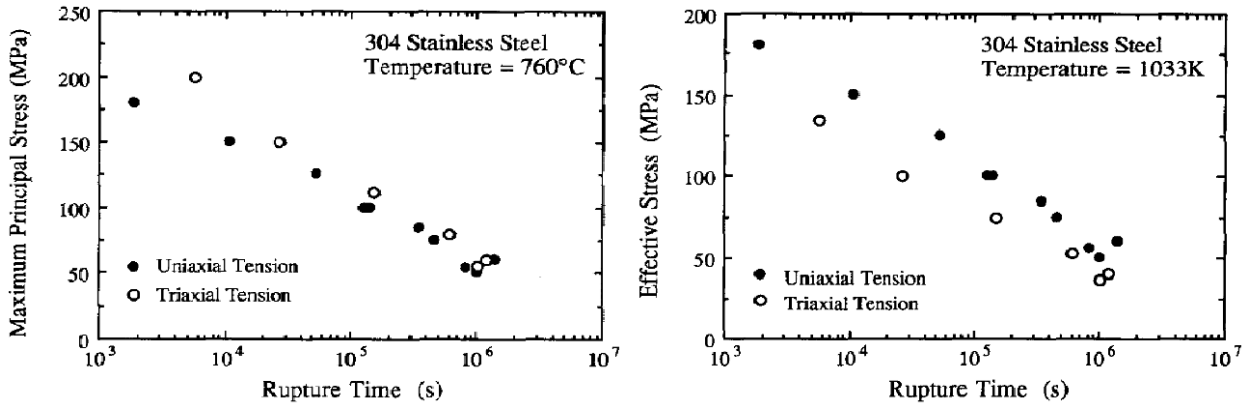

Figure 2.35: Maximum principal (let) and maximum effective (right) stress versus rupture time for uniaxial and triaxial stress states [Kim et al., 1991].

Creep crack growth testing of SS304 under plasticity-dominated fields ahead of crack tips have revealed mixed results in terms of correlating parameters [Han and Kim, 2001]. In correlating the *J*-integral to creep crack growth, wide separation among data sets was observed under constant load tests, prompting the authors to develop an additional parameter, C_{pc}. Encompassing both creep and plasticity, C_{pc} is an extension of the $C^*(t)$ parameter and closely related to the formulation of $\dot{J}$. Establishing the relationship between the developed C_{pc} and $\dot{J}$ parameters, crack extension rates were successfully predicted under constant and alternating loading, Fig. 2.36. Ultimately it was determined that *J* is not suitable to correlate time-dependent crack growth rates, even when plasticity dominates the crack tip field.

2.4.3 Fatigue and Fracture Properties

The fatigue behavior, including smooth and notched behavior, for SS304 has been thoroughly investigated. Experimental data is readily available for fatigue lives, including fatigue crack growth data under load control with- and without-hold times, e.g. [James and Schwenk, 1971; ASM, 1986]. Low cycle fatigue data, at room and elevated temperatures, represented in standard strain versus cycles to failure graphs is available, e.g. [Bayoumi and Abd

El Latif, 1995]. Various fracture mechanics studies on SS304, including creep-fatigue load conditions, have been conducted, e.g. [Lee and Kim, 1996; Merah et al., 1999]. With a substantial amount of data available in literature, the primary focus will be on fatigue and creep-fatigue crack growth at elevated temperatures.

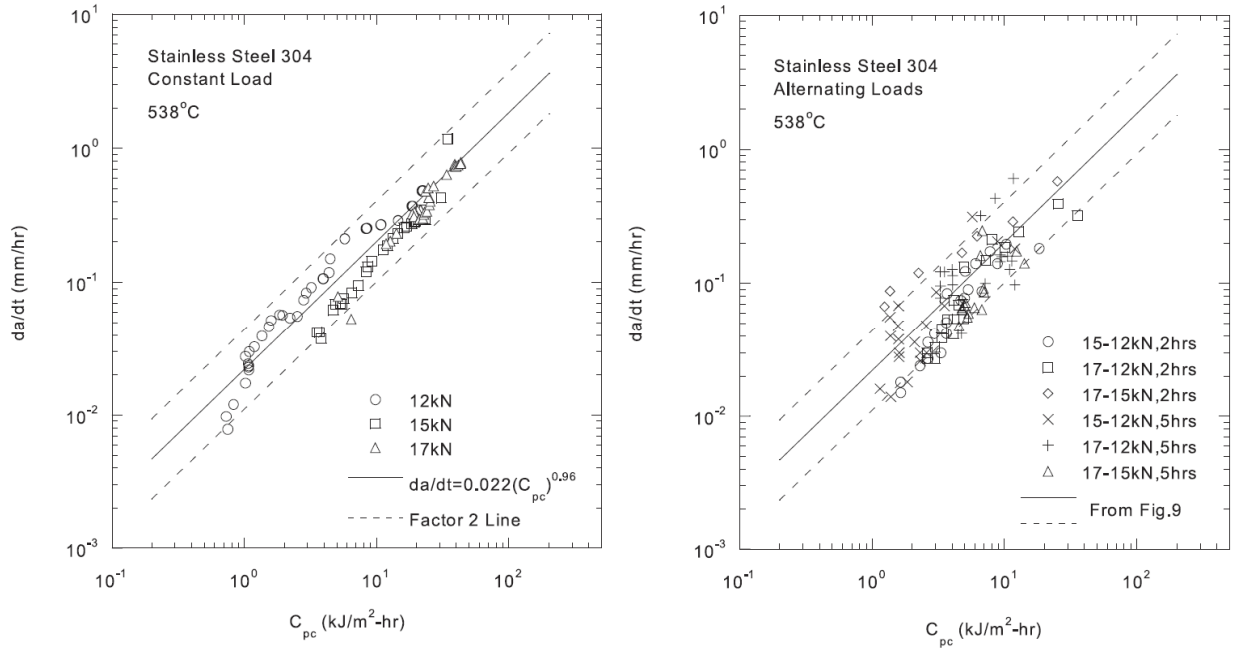

Figure 2.36: Crack extension rates for constant (left) and alternating (right) load patterns on SS304 at 1000°F (538°C) [Han and Kim, 2001].

Fatigue crack studies on SS304 at elevated temperatures for single edge notch (SEN) and C(T) type specimens revealed a two slope Paris-law behavior [James and Schwenk, 1971]. For all specimens tested, including at room temperature, a slope transition is noted in the lower ΔK range, as shown in Fig. 2.37. Notch and crack initiation effects were eliminated as contributing to the bi-slope behavior, as pre-cracks were generated and propagated to 0.05in (1.27mm) prior to starting FCG testing. The increasing rate was proposed to fit to an Arrhenius-type of

behavior, including a temperature term; however, the linear relationship of the Paris-law was inadequate at representing the data within the large temperature range.

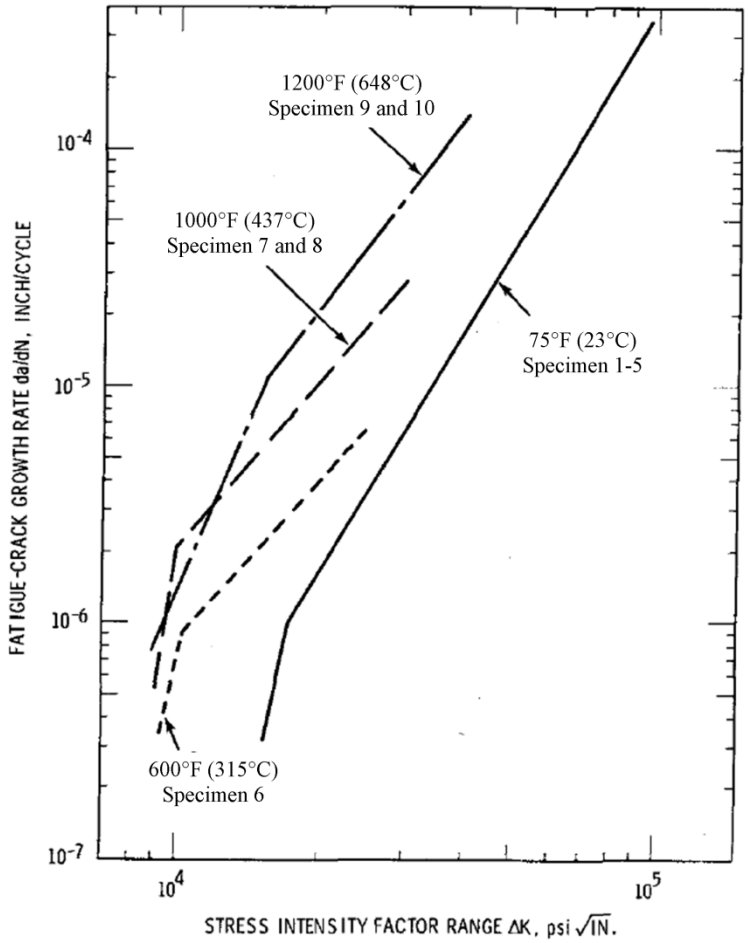

Figure 2.37: Fatigue crack propagation rates for SS304 at room and elevated temperatures [James and Schwenk, 1971].

Common parameters effecting long crack growth rates, such as the load ratio and frequency and hold time are observed to effect SS304 crack growth rates [Fan et al., 2008; Merah et al., 1999; Lee and Kim, 1996]. The load ratio is readily observed to effect the crack growth rates of SS304L, as an increase in the ratio results in increased rates for comparable stress intensity ranges, as shown in Fig. 2.38 [Fan et al., 2008]. Frequency of loading and length

of hold time on crack growth rates have been readily observed at elevated temperatures, with rates increasing for slower load cycles and longer holds, as previously shown in Figs. 2.18 and 2.26, respectively [Merah et al., 1999; Lee and Kim, 1996]. As common with other materials, larger load ratios, longer holds and longer load cycle times results in the reduction of lives of specimens.

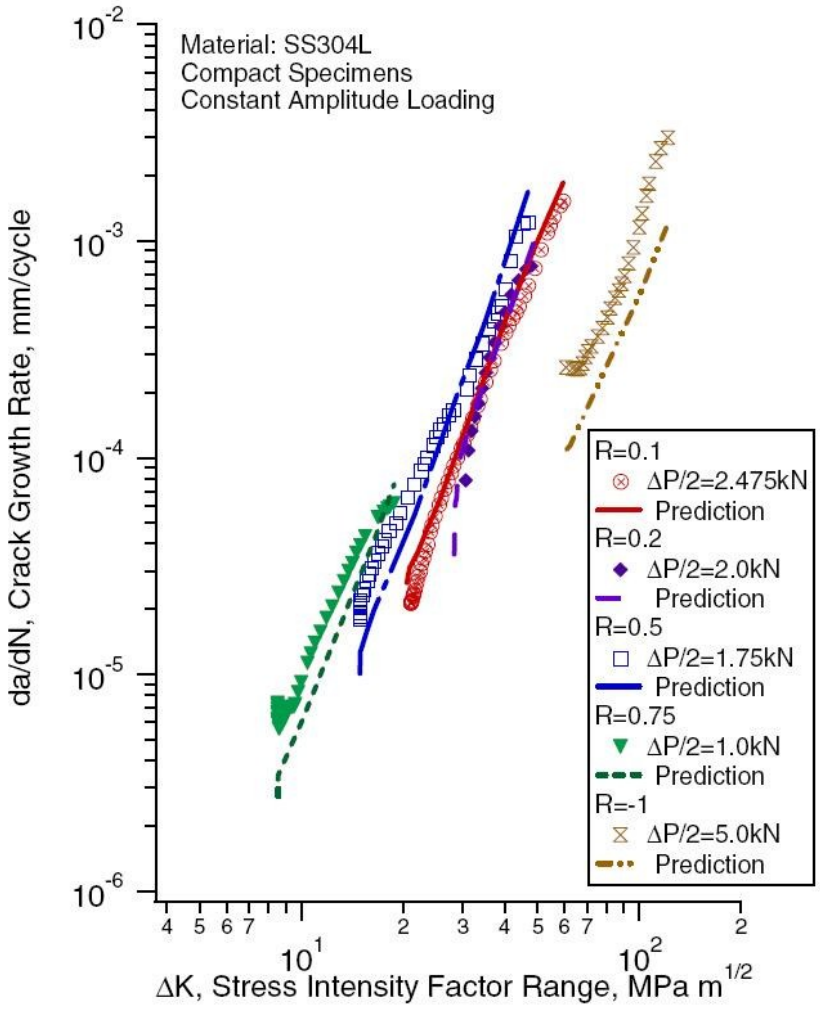

Figure 2.38: Acceleration of crack growth rates for increasing *R*-ratio under constant amplitude loading [Fan et al., 2008].

Creep-fatigue behavior of SS304 has been approached in several investigations. Thermal-mechanical fatigue (TMF) of SS304, in which both temperature and load were cycled, was employed in the investigation of LCF behavior under creep-fatigue conditions [Kuwabara and Nitta, 1979]. A strain partitioning approach was used to predict the thermal fatigue life of components within a factor of 1.5. The load waveform effect under LCF conditions revealed a dependency on the creep cavity formation rate [Lee et al., 1990]. Incorporating a damage evolution parameter to account for the transformation of failures due to transgranular or intergranular mechanisms, predictions of life based on a plastic strain range model were in agreement with experimental data only for slow-fast loading-unloading behavior. Additionally, statistical approaches have been used to predict probability of crack lengths [Kitamura et al., 1995]. In all of these cases, the number of cycles to failure was predicted, without explicitly calculating the crack length or growth per cycle

In CFCG studies, LEFM and EPFM methods have been implemented to study the high temperature cracking behavior of SS304 [Lee and Kim, 1996]. Correlations with ΔK and ΔJ were simulated using the MATMOD and CRACKMOD constitutive equations at 1200°F (650°C) under fast-fast, fast-slow and slow-fast loading waveforms, as previously shown in Fig. 2.26. The cavity formation was reliant upon the loading frequency, with slower load waveforms resulting in larger numbers of cavities normal to the principal stress axis. Incorporating a hold time into plasticity-based crack growth rates in SS304, it was shown that combining fatigue- and creep-based ΔJ parameters resulted in a better agreement between experimental and predicted crack growth rates, as shown in Fig. 2.18 [Merah et al., 1999]. As with previous studies, the main focus of these works was on crack growth and not on coupled initiation and propagation of cracks in SS304.

2.5 Application of Analytical Life Models

The preceding sections within this chapter have outlined several leading analytical life prediction models commonly used in research and industry settings. Application of these models is not always straightforward, nor are the components required for a complete analysis always clear. The objective of this section is to provide a brief summary and overview of the strengths and limitations to particular analyses. Building on the models in literature, the need for future research will be reiterated, as well as the goals and objectives of this investigation.

2.5.1 Relevant Life Prediction Methodologies Overview

The approaches to life prediction presented in Chapter 2 represent increasingly complex analyses used in structural life assessment. While some methods are simplistic in nature, e.g. stress-life approaches, the predictions furnished can be highly accurate compared to experimental data. Crack growth life predictions have been continuously updated to account for additional phenomena affecting the actual observed behavior of cracks. The tradeoff between simplistic and more advanced approaches thus becomes a balance between the ability to collect experimental data and to properly implement such routines into practice. As such, main advantages and limitations to the various approaches will be provided and discussed.

2.5.1.1 Fatigue Crack Initiation Approaches

A main benefit to using the approach outlined in Fig. 2.9 is in the simplicity of the components used to make the life prediction. Knowing the applied loading, material properties, geometry of the specimen, and fitting constants for an appropriate material model, analytical models can be solved through simple calculations. When cyclic material parameters are not explicitly known, approximations are readily furnished from monotonic material parameters [Dowling, 2013]. Furthermore, the formulas outlined in Section 2.1 are readily implementable

into standard calculation software, e.g. Mathcad or MATLAB, allowing for quick calculations. Multiaxial stress states can influence the life of a component, in which case, analytical multiaxial life formulations are readily implementable in a similar fashion. With the ability to automate these equations into calculation software, estimated stress and strain ranges, either via analytical or numerical means, life predictions can be made with minimal efforts.

The simplicity of the equations used in the methods in Fig. 2.9 is observed in both analytical and numerical approaches. Regarding analytical models, the ability to capture comprehensive behavior of the material is limited to the complexity of the formulation. While simple models may provide fundamental baseline values, shortcomings may arise in the ability to capture all of the phenomena occurring within the specimen. Mean stress corrections are necessary and variable amplitude loading must be accounted for in cumulative damage formulations, e.g. Palmgren-Miner rule. As more complex load histories, or multiaxial fatigue effects, are intended to be included in life predictions, more complex experimental data will be required, increasing the cost of such life predictions. Furthermore, the ability to predict long term behavior in accelerated experimental test programs must be evaluated and the applicability to the design of components assessed.

2.5.1.2 Fatigue and Creep Crack Approaches

Many of advantages and limitations of the previous section are applicable to the analytical formulations for life prediction based on integration of cyclic crack growth formulations. Basic LEFM crack growth experiments can provide enough data to formulate constants to be used in the Paris law or more complex formulations, i.e. Eqs. (2.22) and (2.23), as shown in Fig. 2.29. Through the use of standard calculation software, the number of cycles until instability is reached is readily calculated. Advanced software dedicated to the integration of

fatigue crack growth formulations, with even more advanced LEFM crack growth laws and stress intensity factor calculators, is commercially available, e.g. NASGRO [NASGRO, 2012]. Currently, such software is only available for fatigue crack growth; however, as more research is conducted into creep and creep-fatigue crack growth, extensions could be made to existing fatigue crack growth platforms.

As the complexity of the formulation increases, i.e. using EPFM and TDFM methods, two major drawbacks are encountered. The first requires the use of more sophisticated test programs, utilizing more expensive test specimens, expensive extensometry and crack growth monitoring techniques. Depending on specimen material and thickness requirements for the type of test conducted, costs for such testing can become prohibitive. Secondly, some of the formulations, as overviewed in [Saxena, 1993], are extremely complex and require the fitting of several constants, as well as establishing transition times between different stages fatigue and creep. Calculation software can assist in making the fit process more straightforward; however, implementing this into component design may not be straightforward in structural analysis.

A common theme among more complex analyses is that more extensive testing and evaluation is necessary to implement in structural analysis. Life prediction then becomes a tradeoff between the ability to obtain experimental data and the ability to interpret the results and implement into design, enabling the life assessment of components in service. Coupling experimental and analytical results with numerical modeling and simulation is ideal, enabling more accurate life predictions to be made. Therefore, it is necessary that continued work in the area of crack initiation and growth analysis be conducted, with the goal of establishing a bridge between simplicity, the ability to capture key phenomena, implement in design practice and couple with common numerical simulations.

2.5.2 Future Work in Creep-Fatigue Analytical Modeling

The development of analytical models, whether incorporating the use of existing parameters or through the development of new fatigue and fracture parameters, should be directed toward the end user. Models should be readily implementable into analyses that are currently in use in industry and academia. Developing routines and models that, although simplistic or employ simplifying assumptions and approximations, are readily integratable into structural lifing is essential to the advancement of fracture mechanics in life prediction of components. Tradeoffs between complexity and ease-of-use must be made, which is dictated by the behavior of components and the ability to replicate the response in experimental investigations.

Several key parameters are necessary in effectively studying creep-fatigue crack initiation and growth. The ability to do testing should be able to be carried out on a variety of load frames, including tabletop electromechanical load frames not traditionally used in creep or fatigue testing. Specimen design should allow for the inclusion of standard crack monitoring devices, such as a crack mouth opening displacement gages and the attachment of potential drop wire leads. Experimental investigations should be able to incorporate the crack initiation and growth of cracks, as opposed to treating these events separately. By simplifying the experimental routines, while limiting the cost of testing, the number of experiments should increase, enabling more data to be obtained across additional test conditions.

Correlating the experimental data with an analytical model should be straightforward, with minimal effort in ascertaining any material specific constants. Furthermore, parameters that affect creep-fatigue crack initiation and growth rates should be able to be accounted for, such as the stress ratio, and capture any observable interactions between fatigue, creep and

environmental aspects. Ultimately, the results from experimental routines should be captured within a comprehensive crack initiation and growth formulation that is capable of seamlessly integrating into traditional structural analyses.

As outlined in the previous chapter, the objective of this experimental investigation includes several aspects related to creep-fatigue crack initiation and growth. Experimental data is to be obtained on a specimen design that is able to capture initiation and growth, while keeping manufacturing costs at a minimum. Specimens are to be tested in a custom experimental setup, incorporating standard crack growth monitoring techniques, with an emphasis on convenience and portability. Subsequently, the final form of the analytical model to replicate the observed data should allow constants to be determined with simplicity, avoiding over complication and furnishing accurate results.

As the objectives imply, the majority of the effort in this investigation will rely heavily on the development and implementation of experimental procedures. Limiting the amount of error and variability between material data published in literature and material data obtained from test material, a number of experiments shall be performed. Tensile specimens shall be obtained from the stock of material that all specimens are machined from, allowing for the determination of monotonic material properties for the material used. Creep-Fatigue specimens shall be obtained from the material using standard machining practices, e.g. wire electrical discharge machining (EDM). By obtaining all specimens from a single material source, errors associated with using historical material data will be minimized, providing accuracy in predictions.

Experimental control routines shall be created that enable the investigation of crack initiation and propagation due to creep-fatigue loading conditions. These routines must be

capable of assessing: cyclic crack growth rates, static crack growth rates, the contribution of the interaction between creep and fatigue on crack growth rates, and, if warranted, any environmental contribution to crack growth rates. Ultimately, the proposed analytical model or models shall be capable of replicating and predicting crack initiation and propagation based on key features related to the mechanical loading. The remaining chapters will outline the experimental work, analytical model development, and related correlations and predictions of the crack initiation and propagation for a particular material.

CHAPTER 3
EXPERIMENTAL APPROACH

The nature of the research contained within this dissertation required extensive mechanical experimentation. Experiments included tensile and fracture mechanics testing in laboratory and elevated temperature environments. Stress-based tests required the development of experimental routines, load frame fixturing equipment, crack monitoring systems and an environmental furnace required to complete the test matrix. In addition to the stress-based tests, stress-free oxidation experiments were conducted on raw material obtained from the pre-machined slab of raw material. Upon completion of the mechanical experiments, metallurgical analysis of specimens was conducted, namely assorted forms of microscopy. Experiments were carried out in the Mechanical Properties Characterization Laboratory (MPCL) at the University of Central Florida (UCF). Metallurgical analysis was performed within the MPCL, as well as at the Materials Characterization Facility (MCF) located in Research Park at UCF.

3.1 Overview of Experimental Approach

The experimental approach taken within the scope of this research was developed to identify key parameters vital to the development of a novel fracture mechanics-based CFCIG life prediction model. To do so, three sets of experiments were developed based on stress- and stress-free experiments, Tables 3.1 through 3.3. Results based on this test program are combined with simulations to develop a robust lifing model.

***Table 3.1**: Experimental test matrix of tensile specimens.*

Specimen	**Temperature, *T*** °F (°C)	**Strain Rate** s^{-1}	**Specimen Orientation**
Ten1	68°F (20°C)	0.001	T
Ten2	600°F (315°C)	0.001	T
Ten3	800°F (427°C)	0.001	T

***Table 3.2**: Experimental test matrix of blunt notch fracture specimens.*

Specimen	**Temperature, *T*** °F (°C)	**Load, *P*** lbf (kN)	**Load Ratio, *R***	**Rise Time, t_r** (s)	**Hold Time, t_h** (s)	**Specimen Orientation**
BN1	600 (315)	825 (3.67)	0.1	$t_r = 2$	0	T-L
BN2	800 (427)	800 (3.56)	0.1	$t_r = 2$	0	T-L
BN3	800 (427)	800 (3.56)	0.1	$t_r = t_h/10$	20s	T-L
BN4	800 (427)	800 (3.56)	0.1	$t_r = t_h/10$	100s	T-L
BN5	800 (427)	800 (3.56)	0.1	$t_r = t_h/5$	10s	T-L
BN6	800 (427)	800 (3.56)	0.1	$t_r = t_h/5$	50s	T-L
BN7	800 (427)	800 (3.56)	0.05	$t_r = t_h/10$	20s	T-L
BN8	800 (427)	800 (3.56)	0.05	$t_r = t_h/10$	100s	T-L
BN9	800 (427)	800 (3.56)	0.05	$t_r = t_h/5$	10s	T-L
BN10	800 (427)	800 (3.56)	0.05	$t_r = t_h/5$	50s	T-L
BN11	600 (315)	825 (3.67)	0.1	$t_r = t_h/10$	20s	T-L
BN12	600 (315)	825 (3.67)	0.1	$t_r = t_h/10$	100s	T-L
BN13	600 (315)	825 (3.67)	0.1	$t_r = t_h/5$	10s	T-L
BN14	600 (315)	825 (3.67)	0.1	$t_r = t_h/5$	50s	T-L
BN15	600 (315)	825 (3.67)	0.05	$t_r = t_h/10$	20s	T-L
BN16	600 (315)	825 (3.67)	0.05	$t_r = t_h/10$	100s	T-L
BN17	600 (315)	825 (3.67)	0.05	$t_r = t_h/5$	10s	T-L
BN18	600 (315)	825 (3.67)	0.05	$t_r = t_h/5$	50s	T-L

***Table 3.3**: Test matrix for Stress-Free Oxidation experiments.*

Specimen	**Temperature, *T*** °F (°C)	**Exposure Time** (hrs)
SFO1	800 (427)	1
SFO2	800 (427)	3
SFO3	800 (427)	10
SFO4	800 (427)	30
SFO5	800 (427)	100
SFO6	800 (427)	200
SFO7	600 (315)	1
SFO8	600 (315)	3
SFO9	600 (315)	10
SFO10	600 (315)	30
SFO11	600 (315)	100
SFO12	600 (315)	200

The mechanical matrix provides two types of mechanical experiments, i.e., tensile (Table 3.1) and fracture mechanics tests (Table 3.2). Tensile testing was required to determine properties of the raw material, to be discussed in the following section, Section 3.2. The properties obtained by the tensile tests were then utilized during the fracture mechanics testing. Parameters used in the fracture test matrix were developed to simulate service conditions within peaker gas turbines, with quick startup and short hold times. During fracture testing, several monitoring techniques were implemented, discussed in Section 3.6, capable of calculating several fracture mechanics parameters, including K, J, C^*, etc. Based on the results from the tensile and fracture mechanics testing, the dependencies on load and material properties essential to the CFCIG model were observed and, when warranted, utilized.

Major contributing factors affecting crack initiation and growth, based on literature and firsthand experience, are contained in Table 3.2. To single out the contribution that the temperature, load, stress ratio and rise time-hold time relation have on both initiation and growth, the matrix includes various values selected to analyze the effect each has on the material response. Loads were chosen that would result in similar stress-strain responses at the notch tip, based on the tensile tests conducted at temperature and subsequent numerical modeling. The hold times include short and long periods, allowing for the evolution of crack growth during hold times to be observed. Crack closure effects, most commonly accounted for by various R values, are to be observed through two different stress ratios. Interaction of creep and fatigue effects during load times will be accounted for through the load rise conditions. Ultimately, several key parameters in creep-fatigue crack initiation and growth were capable of being experimentally observed by the implementation of Table 3.2.

Stress-Free Oxidation (SFO) tests, outlined in Table 3.3, were necessary to develop the environmental effect that elevated temperatures have on crack initiation and growth. By placing specimens in elevated temperatures without load, the extent of stress-free oxidation was analyzed. Through sectioning individual specimens, the depth of oxidation in the stress-free state was readily compared with the depth of oxidation in tensile and fracture mechanics specimens. Metallurgical procedures followed are outlined in Section 3.7. Side by side comparisons of the two types of specimens, i.e. stress and stress-free samples, provided valuable qualitative data used in the development of the analytical model.

Together, all mechanical and metallurgical experiments were imperative in the development of an advanced coupled crack initiation and growth model. Subsequent sections provide all relevant information regarding test equipment, test methods and specimen preparation. Additionally, specimen drawings and necessary fixturing devices are included in Appendix A.

3.2 Tensile Testing

Tensile testing is required to obtain elastic and plastic material properties at specified temperatures. Key properties that are obtained are the elastic modulus, E, 0.2% yield strength, σ_y, ultimate strength, σ_{uts}, fracture strength, σ_f, and fracture strain, ε_f. In order to obtain values representative of the material being tested, tensile specimens were machined from the slab of raw material, as shown in Fig. 3.1. Specimens were designed in compliance with ASTM E8 and E21, standard test methods for tensile test of metallic materials at room and elevated temperatures, respectively [ASTM E8/E8M-09; ASTM E21-09].

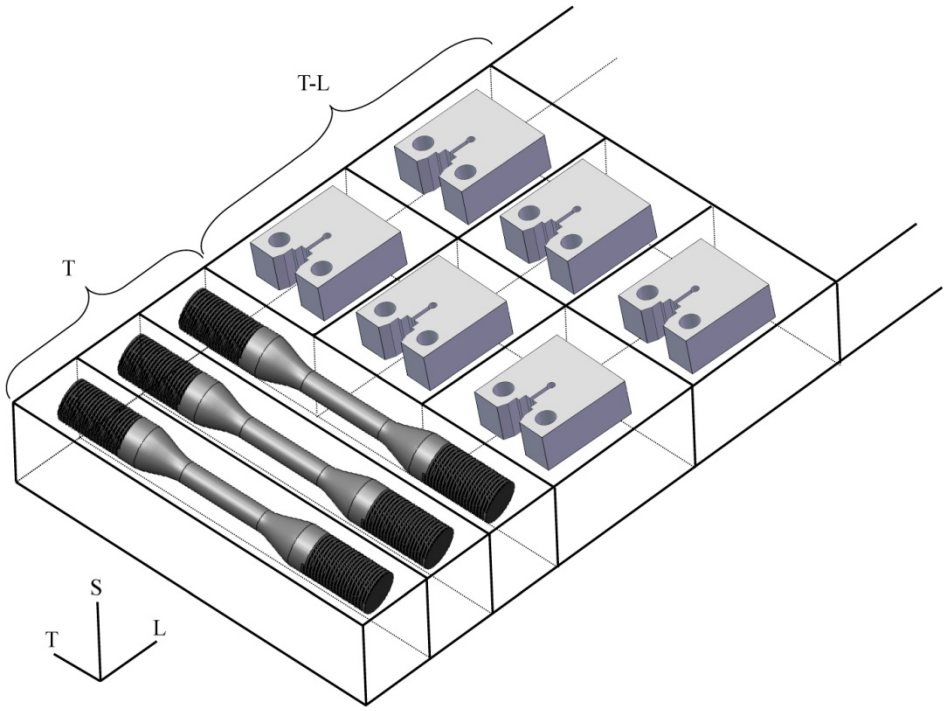

Figure 3.1: Tensile and Creep-Fatigue specimen orientation in the sheet of raw material.

A single tensile specimen is to be tested at each of the test temperatures. The rationale behind testing the actual material being used was in effort to reduce the inherent error associated with the use of averaged data from literature. The orientation of the tensile specimens, shown in Fig. 3.1, was such that the fracture surface will be of the same orientation as that of the blunt notch fracture specimens, discussed in the following section. By orienting the specimens in this direction, with a fracture surface perpendicular to the T-direction, the directionality of grains introduced by the rolling process were aligned in a similar fashion for both the tensile and fracture mechanics specimens.

For the tensile testing portion of this research, an MTS servohydraulic test frame running TestStar IIs software was utilized. Relevant capabilities and limits are provided, Table 3.4. Strain measurements were recorded via an MTS High-Temperature Axial Extensometer, model 632.53. Model-specific details for the extensometer are provided, Table 3.5. For experiments

running at elevated temperatures, an Ameritherm HotShot 3.5kW induction heater was used, with a maximum operating temperature of 2200°F (1200°C). Temperature was controlled and maintained by the use of a WATLOW temperature controller, utilizing a K-type thermocouple. An example of the experimental setup, including an example test specimen at temperature, is provided, Fig. 3.2. Ultimately, select elastic and plastic properties were determined for the batch of material used during the experimental portion of this research.

***Table 3.4**: Specifications of MTS servohydraulic test frame.*	
Column Configuration	Double
Force Capacity	25 kip (111 kN)
Maximum Test Speed	2.0 in/sec (50.8 mm/sec)
Maximum Test Frequency	~5 Hz
Maximum Data Acquisition	70 kHz
Control Software	TestStar IIs

***Table 3.5:** Specifications of MTS High-Temperature Extensometer.*	
Model	632.53E-14
Gage Length	0.500 in (12.0 mm)
Maximum Travel	+0.100, -0.050 in (+2.54, -1.27 mm)
Maximum Strain	+20%, -10%
Maximum Operating Frequency	2 Hz
Maximum Temperature	2200°F (1200°C)

3.3 Creep-Fatigue Specimen Design

Specific requirements regarding the size, dimension, and surface conditions for the blunt-notch creep-fatigue fracture specimens were adhered to during the specimen design when possible. The ASTM standards regarding plane strain fracture toughness testing and, more generally, fracture toughness testing, E399 and E1820, respectively, provide samples of standard specimen geometries, e.g. Fig. 3.3 [ASTM E399-09$^{\varepsilon 2}$; ASTM E1820-09$^{\varepsilon 1}$, ASTM E2760-10].

The driving parameter is the specimen width, W, with all subsequent dimensions being a function of W.

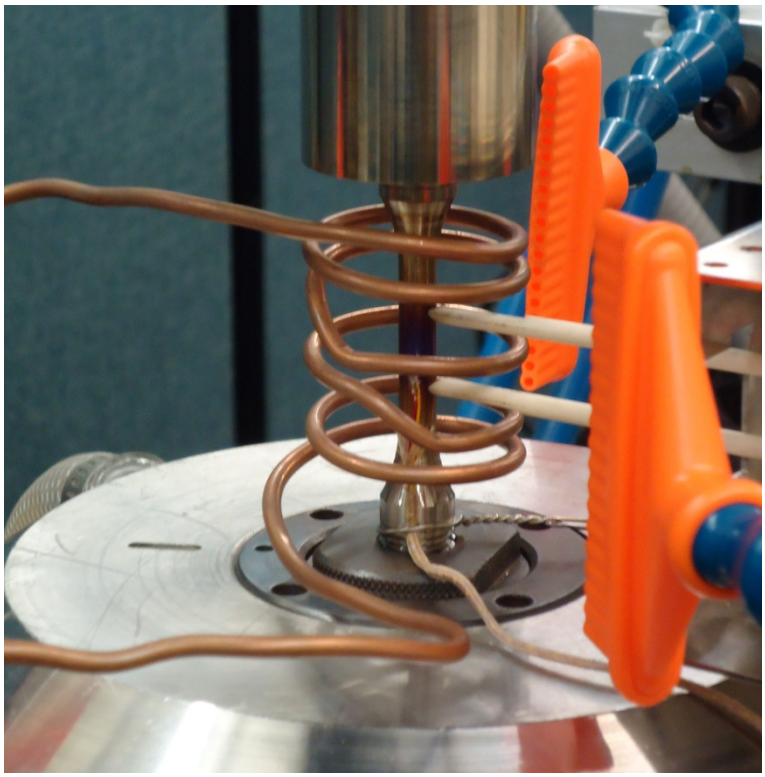

Figure 3.2: Picture of high temperature tensile test with associated measurement devices.

Following ASTM standards as a guideline, a blunt notch creep-fatigue specimen was designed and implemented, as shown in Fig. 3.4. Relevant specimen dimensions are provided, Table 3.6. A modification to the notch tip was implemented to simulate a component with a stress concentration similar to that found in service components. Typically, a sharp starter V-notch is machined at the tip to force crack initiation to occur at one location during pre-cracking routines [ASTM E1820-09$^{\varepsilon 1}$]. As this investigation was focused on crack initiation, in addition to crack propagation, a blunt-notch was used in favor of the V-notch. This allowed for the observation and understanding of the manner in which notch and crack tip parameters, e.g. K_t, χ, K and J, could be applied to the initiation processes of CFCIG. Although the modification in

thickness of the specimen will be discussed in detail in Chapter 4, the reduced thickness allowed for both LEFM and EPFM parameters to be used in analysis of experimental data.

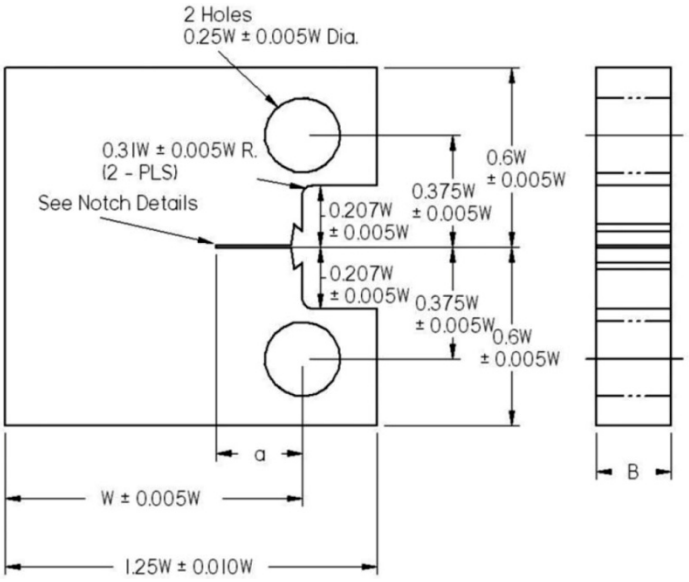

Figure 3.3: Example of a creep-fatigue test specimen, with dimensions specified by ASTM Standards [ASTM E2670-10].

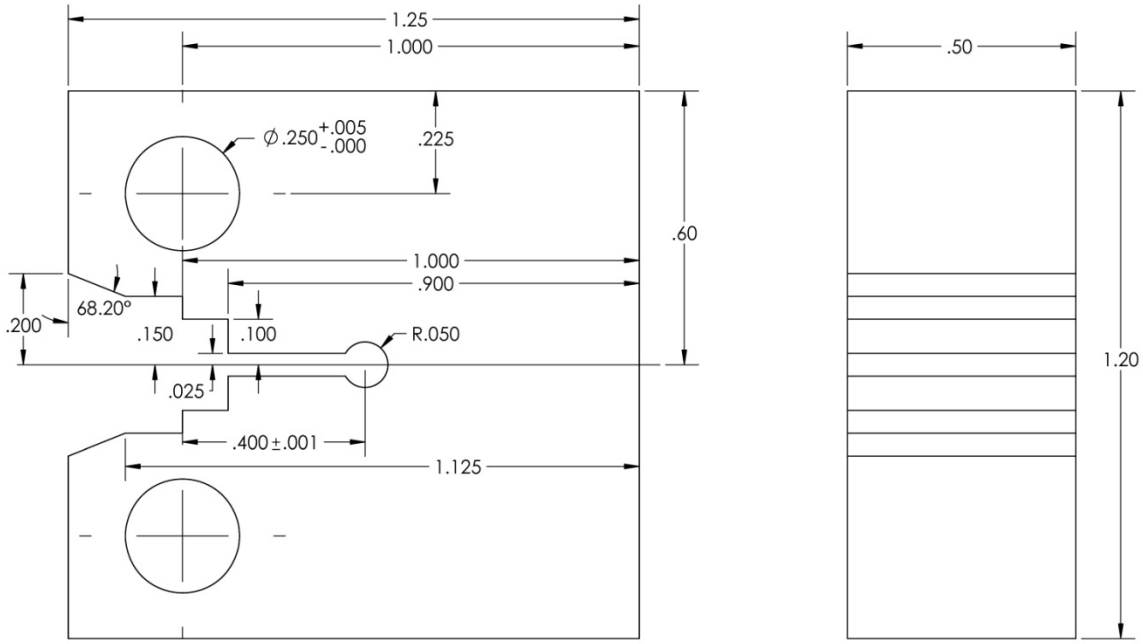

Figure 3.4: Blunt notched creep-fatigue specimen utilized in this investigation.

Table 3.6: *Blunt notch creep-fatigue fracture specimen dimensions.*	
Width, *W*	1.00 in (25.4 mm)
Thickness, *B*	0.500 in (12.7 mm)
Initial Notch Depth, *a*	0.450 in (11.4 mm)
Notch Depth to Width Ratio, *a/W*	0.45
Notch Radius to Width Ratio, *ρ/W*	0.05

Specimens were machined from the raw material, as shown in Fig. 3.1, by wire electrical discharge machining (EDM). Wire EDM processes allowed for the intricate mouth opening geometries to be cut accurately, while maintaining the tolerances required around the notch. The orientation of the blunt notch specimens was T-L, Fig. 3.5. This particular orientation was chosen, as a majority of experimental data contained within literature was obtained for T-L or L-T oriented fracture specimens, e.g. [ASM, 2007]. While the microstructure may be more uniform in other orientations, this orientation lends itself to traditional machining practices and reduces the number of operations required to manufacture components from raw plate [Keller, 2009].

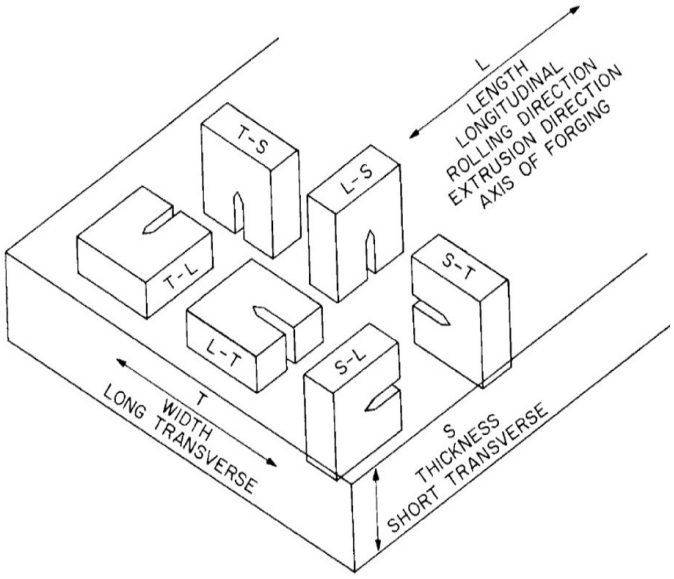

Figure 3.5: Specimen orientation for C(T) specimens machined from plate.

Crack initiation and propagation is dependent not only upon the geometry of the specimen, but also the surface condition of the specimen. Deep pits and tooling marks can significantly affect the crack propagation path, diverting the crack tip from the natural path in an unflawed specimen. To ensure specimen sides were free of gouges, deep pits and excessive tooling marks, specimens were obtained from a local machine shop with a surface roughness rating of 64 Ra or less. Surface roughness is a measurement of the average of absolute peaks and valleys on the surface of a specimen, i.e.,

$$R_a = \frac{1}{n}\sum_{i=1}^{n}|z_i| \tag{3.1}$$

where n is the number of measurements and z is the height of a measurement relative to a selected zero plane on the surface of the specimen. By dictating the maximum surface roughness of the specimens, subsequent processing of the specimens prior to testing was made easier.

Upon receipt of the specimens, a polishing routine was implemented to further reduce the surface roughness on specimen sides. The surface preparation procedure was to wet sand specimens for one minute with 240, 320, 400 and 600 grit sandpaper. In between each subsequent increase in grit, the specimens were rotated 90° to ensure complete removal of material was achieved from the previous step. Final preparation included wet sanding the surfaces with 1200 grit sandpaper for one minute. The resulting faces on the fracture specimens were mirror-like, with no visible imperfections, as shown in Fig. 3.6.

As a result of the polishing process, the crack was assumed to freely propagate without influence from surface defects. Tight control of tolerances regarding notch depth and crack mouth dimensions ensured that dependent calculations, e.g. K and J, were accordingly accurate to ASTM standards. Careful control over specimen preparation provided the necessary conditions for accurate and reliable crack initiation and crack propagation experiments.

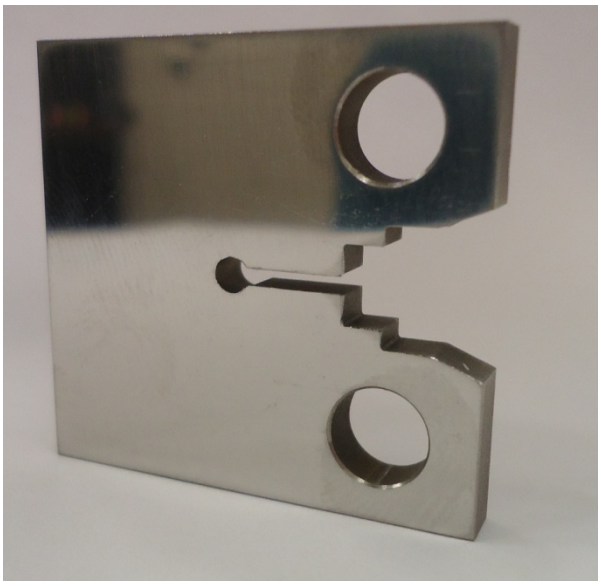

Figure 3.6: Blunt notch C(T) specimen post-polishing process.

3.4 Creep-Fatigue Testing

Creep-Fatigue experiments conducted during the experimental portion of this research incorporated the use of an MTS Insight 5kN load frame and TestWorks v4.12 Creator. Utilizing this universal load frame required the development of both load frame fixtures and test control routines. The necessary load frame fixtures included attachment clevises and extension arms, with drawings provided in Appendix A. Control routines were developed within TestWorks that monitored load, displacement and crack mouth opening displacement (CMOD), as well as controlled the internal DAQ system. In situ specimen monitoring of both CMOD and DCPD crack length measurements required the incorporation of a high temperature CMOD gage and a DCPD measurement system. A schematic of the creep-fatigue experimental setup is provided, as shown in Fig. 3.7. With all of the components assembled, and the incorporation of a high-temperature furnace discussed in Section 3.5, high-fidelity creep-fatigue crack growth studies were capable.

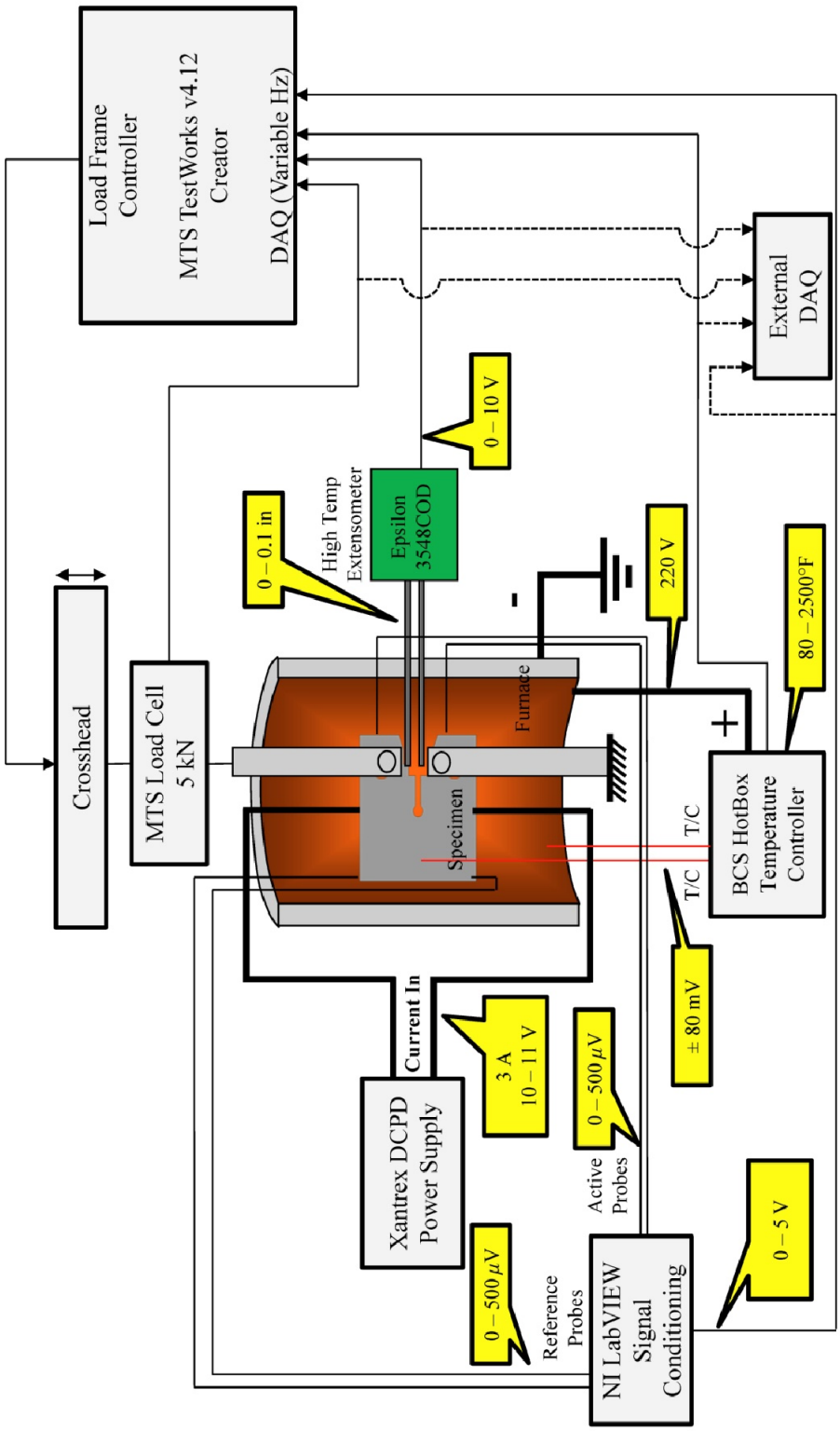

Figure 3.7: Schematic of experimental setup used in this investigation.

3.4.1 MTS Test Frame and Fixtures

An electromechanical load frame, an MTS Insight 5kN, was used for the creep-fatigue experiments at room and elevated temperatures, as shown in Fig. 3.8. The capabilities of the load frame were limited by the load cell and crosshead velocity, with relevant specifications provided, Table 3.7. Despite the lower load and load-rate capacity, elastic and plastic notch tip strains could be imparted on the test specimen, as predicted by finite element simulations, Fig. 3.9. Standard universal couplers with through pins were attached to the load cell and frame base, allowing for the use of custom adapters to be affixed in the frame.

Figure 3.8: MTS Insight 5kN implemented in this investigation.

Table 3.7: Specifications of MTS Insight 5 test frame.	
Column Configuration	Double
Force Capacity	1.1 kip (5.0 kN)
Maximum Test Speed	0.33 in/sec(8.38 mm/sec)
Maximum Test Frequency	~1 Hz
Maximum Data Acquisition	500 Hz
Control Software	TestWorks 4

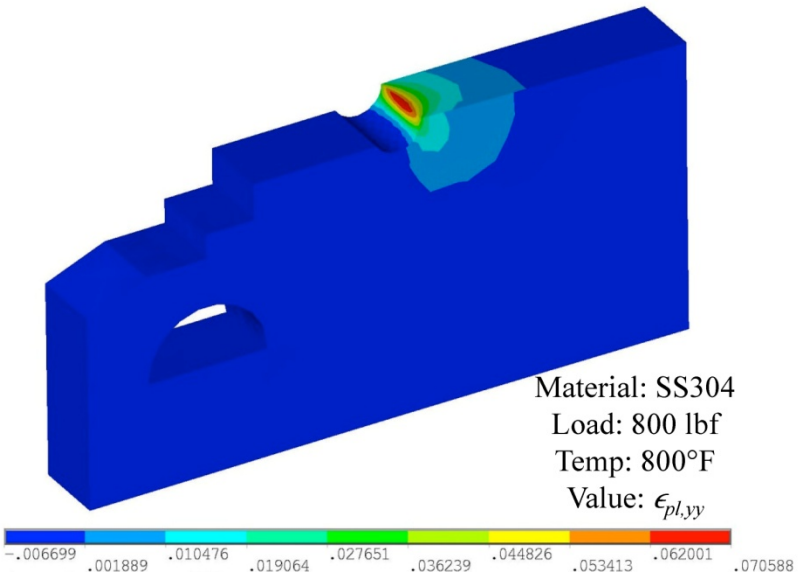

Figure 3.9: Example of plastic strain response on blunt notch C(T) specimen subjected to plasticity-inducing load.

The specimen width, *W*, not only dictated the dimensions of the overall specimen, but also the size of the required fracture testing adapters, as shown in Fig. 3.10 [ASTM E1820-09$^{\varepsilon 1}$]. The clevis design required a threaded connection used in fastening it to the extended loading arms, provided in the Appendix. The extended loading arms provided sufficient space for the furnace and extensometry to encompass and clip into the specimen, respectively, while utilizing existing load frame attachments. The clevis and extended loading arms were machined out of AISI 4140 and 4340, respectively, providing sufficiently high strength and stiffness throughout the range of temperatures that were implemented.

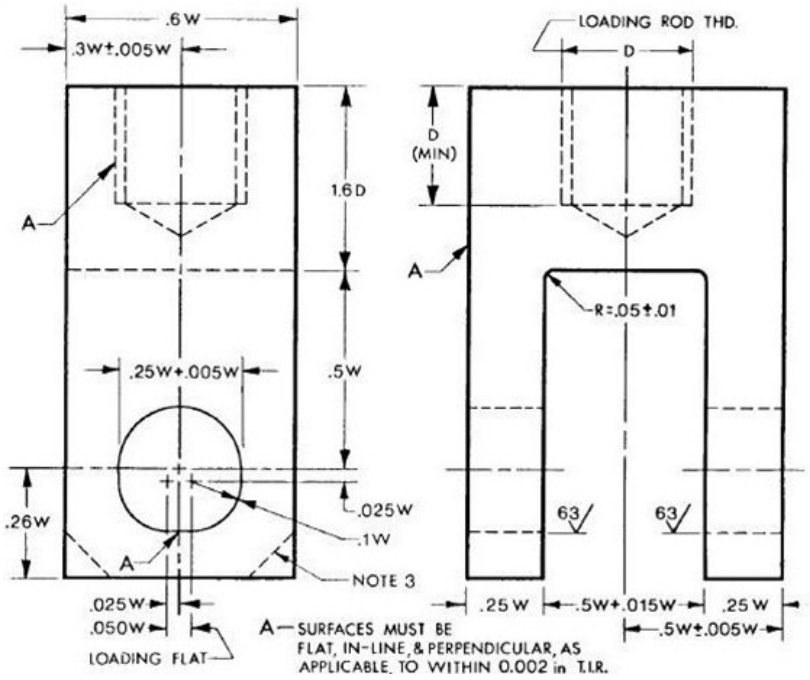

Figure 3.10: Tension testing clevises used with extension arms to allow for testing in furnace.

Controlling the load frame required the development of creep-fatigue load routines. TestWorks 4 (TW4), a proprietary software package developed by MTS, accompanied the frame to control and record experimental data. Utilizing TW4, primary control routines were designed and implemented, following the example loading patterns provided in Fig. 3.11. The routines were load-controlled, with a load rate dictated by the rise time-hold time relationship presented in Table 3.2. Tuning of the PID parameters was conducted through traditional methods and satisfactory values were implemented for each portion of the loading routine. Additionally, the PID parameters were sufficient in controlling both the loading and tensile hold periods, simplifying the tuning procedures.

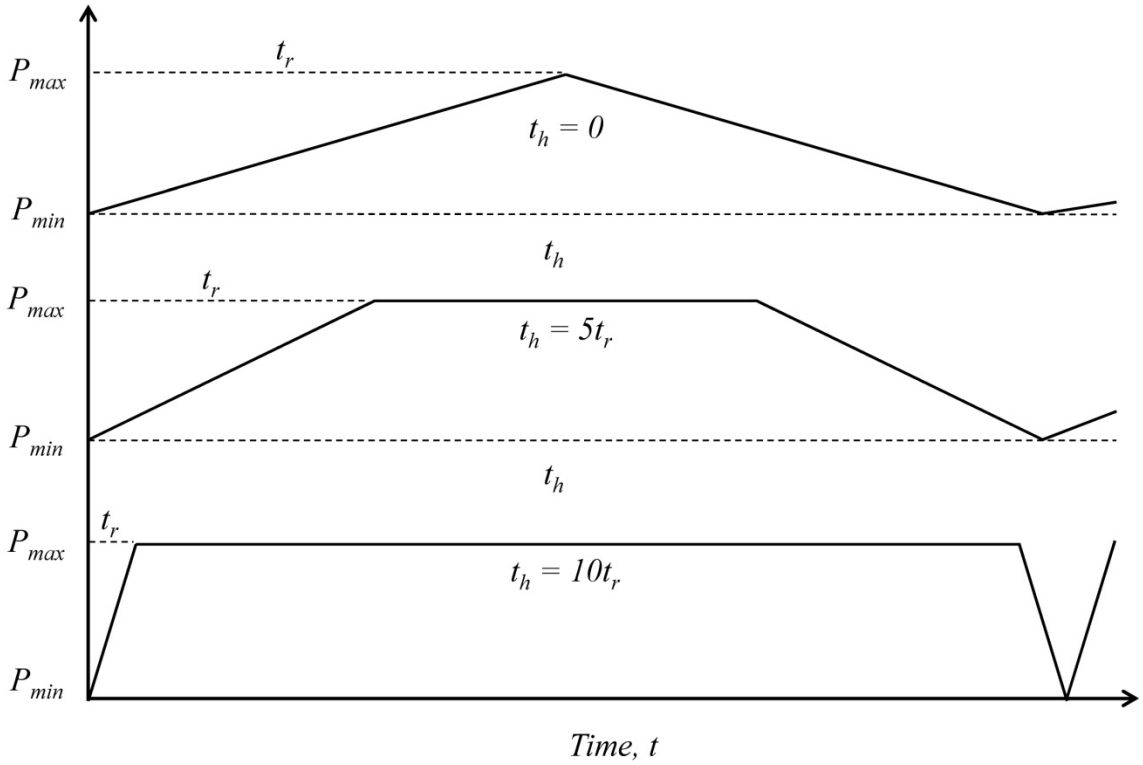

Figure 3.11: One cycle of load control waveforms used in creep-fatigue load-control routines.

An important factor in the understanding of fatigue-, creep- and creep-fatigue crack growth testing is the load ratio, *R*. Plasticity-induced closure is expected to occur at ratios of *R* less than 0.7, below which crack growth rates are expected to be slower than crack growth rates without closure. Realistically, the startup and shutdown processes involved in IGT operation are closer to zero-to-tension loading, i.e. $R = 0$. The stress ratios chosen for experimental routines were 0.05 and 0.1, as FCG and CFCG testing is simplified without having to cycle to, or through, zero loads. Rate effects were accounted for in presentation of the results of crack initiation and propagation data, as presented in Section 5.2.

Data acquisition was managed via the internal DAQ associated with the TW4 platform. Standard channels that were monitored included the load and crosshead displacement. Channels were created that allowed for the monitoring and recording of both the CMOD gage and DCPD

measurement system. By reading in the additional channels into TW4, all of the necessary, recordable measurements were captured at identical times and intervals. The use of an externally assembled DAQ, as shown in Fig. 3.7, was used to capture all recordable values in the event of a software crash. By having the redundant DAQ system, the loss of experimental data was greatly minimized.

3.4.2 Crack Mouth Opening Displacement Gage

Creep-Fatigue crack growth experimental routines require the monitoring of the load line deflection, particularly with a displacement gage [ASTM E2760-10]. Fracture mechanics specimens, like the one designed for use in this study, incorporate ridges and/or knife edges for these gages to clip into, giving rise to the pseudonym "clip gage." These gages come in a variety of configurations, based on the desired capabilities, with two major classes specifically for low- and high-temperature fracture mechanics testing.

For this experimental study, a CMOD gage (Epsilon Technology model 3548COD), was used to measure load line deflection, as shown in Fig. 3.12. Relevant specifications for this gage are provided, Table 3.8. The high temperature clip gage is capable of testing in temperatures up to 2200°F (1200°C), incorporates active cooling and conforms to all applicable ASTM standards regarding electronic monitoring devices. The gage arms were machined from alumina ceramic rods and heat shields were incorporated, enabling the high temperature use. Calibration of the clip gage was done by the manufacturer prior to shipping. Fixturing of the CMOD gage to the specimen was developed around the removable frame used by the furnace, to be discussed in Section 3.5.2. Connection to the MTS software was completed onsite, following instructions furnished by MTS.

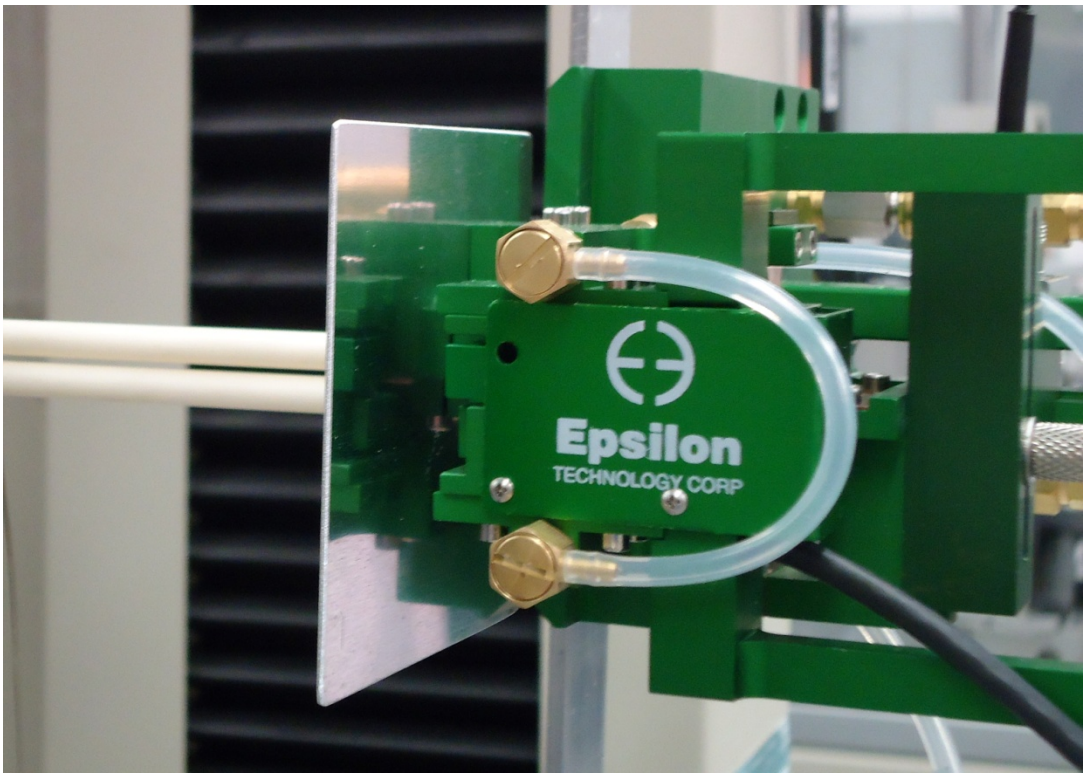

Figure 3.12: Epsilon 3548 CMOD gage with high temperature extension arms.

Table 3.8: *Epsilon Tech CMOD Gage - 3548COD.*	
Gage Length	0.200 in (5.00 mm)
Travel	+0.100 in (+2.50 mm)
Temperature Range	+71°/+2200°F (+22°/+1200°C)

Load line deflection measurements were utilized in the calculation of creep-fatigue crack growth dependent parameters, particularly in observing the force line displacement and displacement rate, V and $\dot{V}$, respectively. Total displacement can be separated into elastic, plastic and creep-time dependent contributions, when warranted and observed, i.e.,

$$V \approx V_e + V_p + V_c \,. \tag{3.2}$$

In typical CFCG experiments, outlined in ASTM E2760 [2010], the force line displacement and displacement rate, V and $\dot{V}$, are used to derive the parameters C^* and C_t. By monitoring the load

line deflection in conjunction with time, the total displacement can be divided into the individual classification and subsequently used in calculating the aforementioned parameters.

3.4.3 Direct Current Potential Drop Method

The direct current potential drop (DCPD) technique was used to monitor the crack length during experimental testing. This required the development of such a system, including a power supply, lead wire and pick-up wire selection, wire placement and signal amplification. To allow consistent data acquisition, TestWorks had a high level analog channel developed, capable of recording the voltage in real time alongside load, displacement and CMOD measurements. Together, the system had to be able to maintain a constant, stable current over the life of the specimen, allowing information on the crack initiation and propagation process to be obtained.

The power supply used in the DCPD system was a Xantrex XTR 60-14 850 Watt programmable DC power supply. The supply current was set to 3A, which resulted in voltage readings on the order of 10-100μV. Lead wire for the supply of current was the positive lead of a 0.032in (0.812mm) diameter K-type thermocouple, i.e. Chromel wire. Voltage pick-up wire was again the positive lead from a K-type thermocouple, but with a diameter of 0.01in (0.255mm). Reference leads were used in conjunction with the active pick-ups, using the same diameter Chromel wire. Wires were spot welded to specimens using an Omega TL-Weld thermocouple welder in the locations identified for C(T) specimens in ASTM E647 [ASTM E647-08$^{\varepsilon 2}$, 2008]. A specimen with DCPD and thermocouple wires welded is provided, as shown in Fig. 3.13.

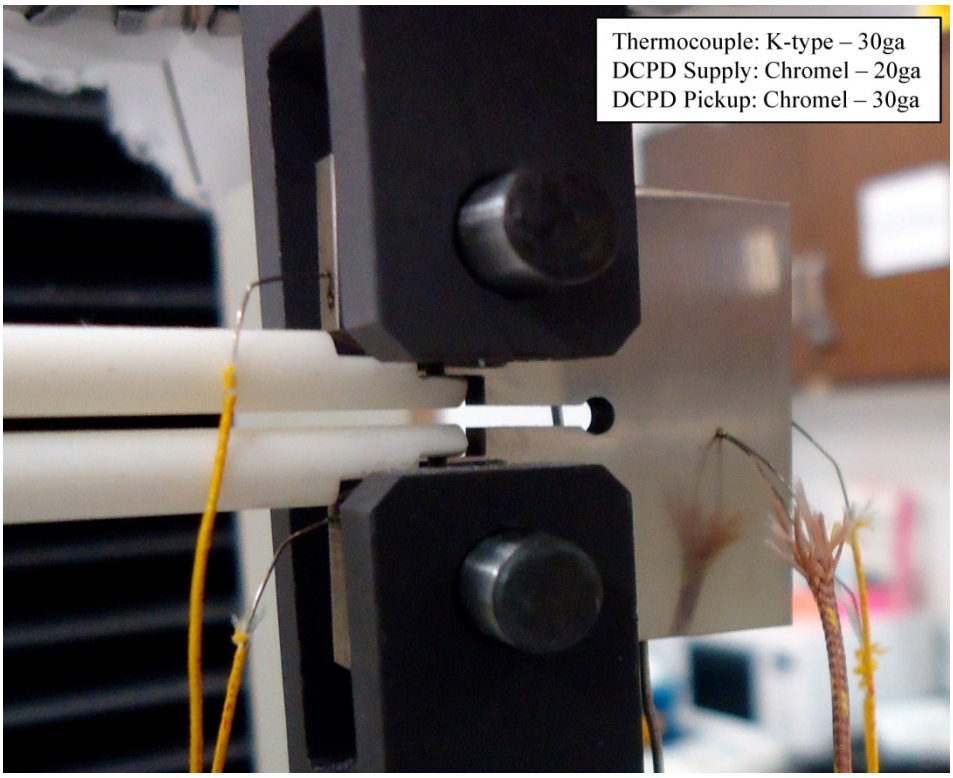

Figure 3.13: Blunt notch C(T) specimen with CMOD gage inserted and DCPD lead wires and thermocouple welded to specimen.

The active and reference voltages were read via a developed LabVIEW routine and associated NI CompactDAQ chassis. Voltage readings for the active and reference probes implemented a ±80mV range module with 24-bit resolution, having the ability to read on the μV-scale. Signal differencing and amplification (typically 1,000x) was conducted in LabVIEW, with the resulting signal output on an analog ±10V module, which was subsequently read in by TestWorks as another strain channel. This allowed for sampling and collection of data, from both the CMOD gage and the DCPD system, to be synchronized and contained within one data file. This provides the advantage of ensuring the data was sampled together and that values from one subsystem were directly related to values of other subsystems.

3.5 High Temperature Testing

A majority of the experiments performed during the course of this research involved testing within elevated temperature environments. Stress-Free oxidation testing utilized a basic laboratory furnace, whereas the creep-fatigue tests required the development of a furnace and framing fixture. Both setups were capable of reaching and maintaining a constant temperature environment. An overview of the individual components is provided.

3.5.1 Stress-Free Oxidation Testing

Stress-Free Oxidation (SFO) tests were conducted during the course of this research, as detailed in Table 3.3. Tests were conducted on samples obtained from the raw material used in producing the tensile and creep-fatigue specimens. Small specimens were cut from the remaining material, resulting in specimens similar in size and shape as those used in crack growth studies, Fig. 3.14. Following the polishing routine presented in Section 3.3, three sides of the SFO specimens were polished and the remaining sides were left in the as-machined state. Any differences between the polished and unpolished surfaces would be observed and accounted for during optical microscopy of specimens.

Experimental temperatures used were those at which the crack initiation and propagation experiments were conducted. Exposure times were determined based on the geometric mean of increasing orders of magnitude, e.g. 1, 3, 10, 30, 100 and 200 hours. The goal of the SFO experiments was to correlate any visual oxidation, as well as penetration depth, with damage accumulated during high temperature load-based tests. By conducting the SFO tests over test periods similar to the duration of creep-fatigue experiments, the effects the elevated temperature lab air had on crack growth could be observed.

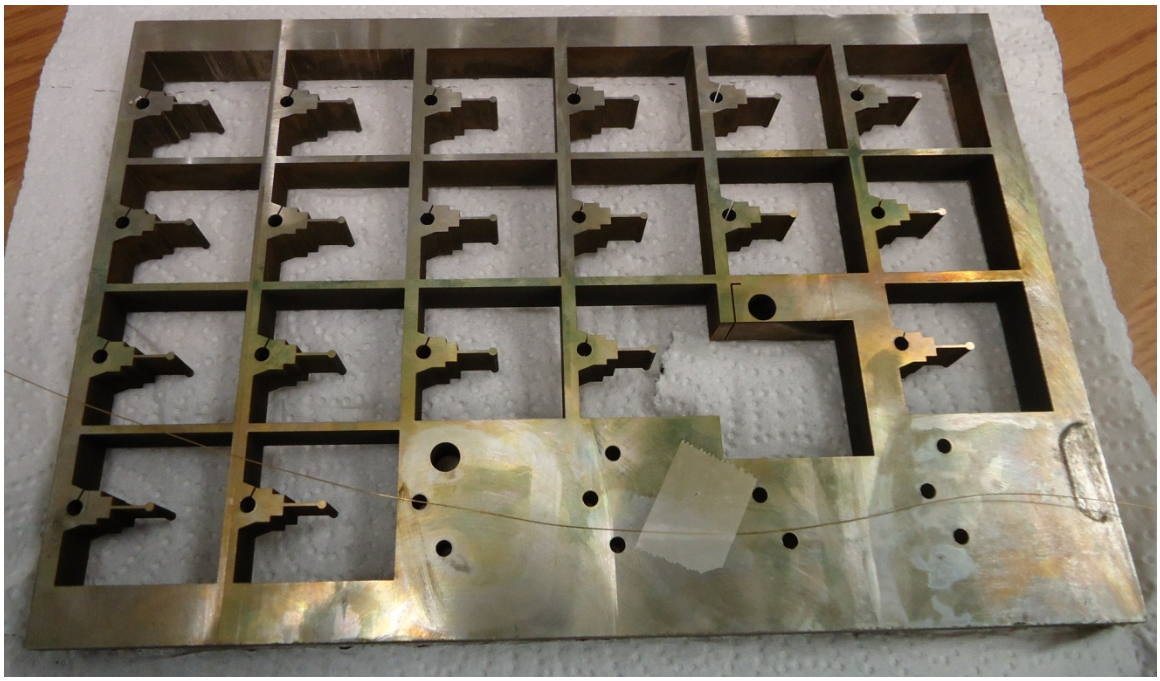

Figure 3.14: Raw material remaining from specimen machining used to obtain SFO specimens.

The furnace implemented during SFO tests was a Barnstead/Thermolyne 48000 Furnace, as shown in Fig. 3.15. Used commonly in small specimen laboratory heat treating processes, the maximum temperature of the 48000 furnace was 2200°F (1200°C). Temperature was controlled via the incorporated Eurotherm temperature controller with a single programmable set point. Prior to inserting specimens, the oven was preheated to the test temperature and allowed to maintain temperature for one hour. Allowing the oven to "settle" provided for a minor fluctuation in temperature as specimens were inserted, ensuring that the temperature was uniform throughout the duration of the test. Upon reaching maximum exposure times, individual specimens were removed and air cooled. Microscopy of tested specimens was then completed, which processes will be discussed in Section 3.6.

Figure 3.15: Barnstead Thermolyne 48000 furnace used in SFO tests.

3.5.2 Creep-Fatigue Environmental Chamber and Frame

The MTS Insight 5 utilized in the creep-fatigue experiments is commonly used for room temperature testing. As such, a portable, standalone frame and furnace were developed and implemented for this research, as shown in Fig. 3.16. Major components of the furnace include the frame, resistance band heater and temperature controller. Together, the components are capable of reaching temperatures as high as 1400°F (760°C) and maintaining better than a 1% deviation in temperature with proper insulation added to the furnace.

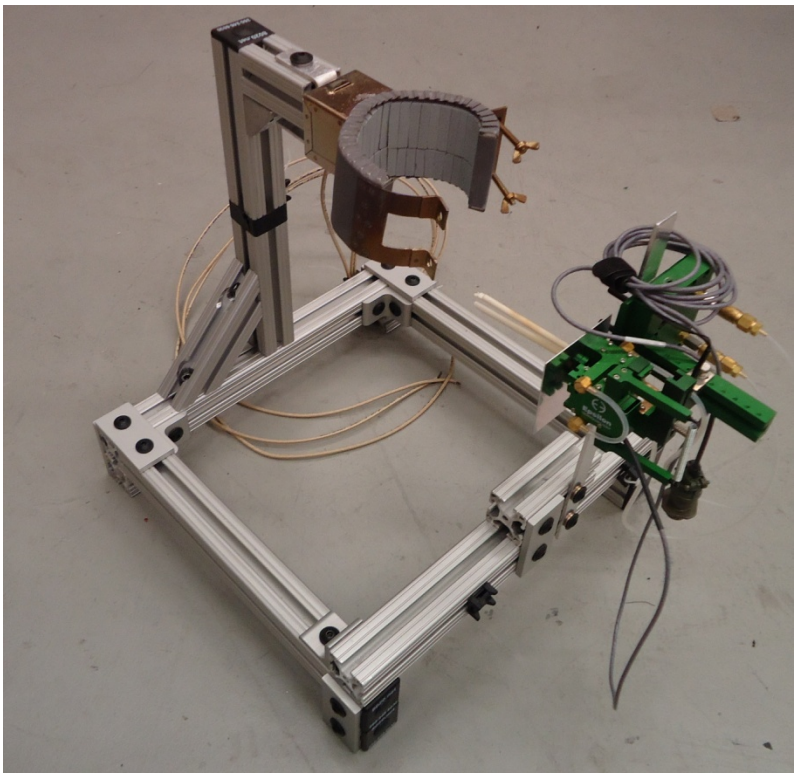

Figure 3.16: Custom 80/20 frame used to position CMOD gage and ceramic band heater.

The portable frame was constructed out of 80/20 aluminum framing, as shown in Fig. 3.16. Adjustments could be made in the X, Y and Z directions, allowing for optimum positioning of the furnace. In addition to fixturing the furnace, the frame also served as an attachment point for the CMOD gage. Custom brackets were designed that secured the CMOD gage to the frame and provided an adjustable platform to move the gage around the specimen and furnace. Upon removing the wires from individual components, e.g. power, thermocouples, etc., the frame was portable and could be transferred to various frames in the future.

The furnace used to heat the specimen was an Industrial Heater Corp. ceramic band heater, model B74772. Maximum achievable temperatures were dictated by the internal components, which had a maximum continuous-use operating limit of 1400°F (760°C). Relevant geometrical concerns are provided, Table 3.9. The extensometer slot had to be cut in

the flange to allow for the CMOD gage to be attached to the specimen. Heat containment at the top and bottom of the band heater was achieved by flexible ceramic insulation, with a maximum continuous-use operating temperature of 2150°F (1180°C). In addition to preventing heat loss from the furnace, the insulation also provided useful in keeping surrounding equipment, i.e. the load cell, cool and away from the heat.

Table 3.9: *Industrial Heater Corp. B74772 Heater.*	
Inner Diameter	2.25 in (57.2 mm)
Outer Diameter	3.00 in (76.2 mm)
Height	2.50 in (63.5 mm)
Extensometer Slot	1.00 in (25.4 mm)
Electrical Rating	500 W and 240 V

Temperature was controlled via a BCS Hot Box furnace controller. This particular unit contained a single channel controller with internal PID controls. By default, the module ran a "learning cycle" used to tune the initial parameters to be used by the PID. Upon completion of the learning process, PID parameters were automatically implemented that provided a stable response in temperature control with minor overshoot and steady, long-term control. Temperature was monitored via a K-type thermocouple welded to the surface of the specimen. The thermocouple was thermally- and electrically-shielded to prevent any misreading due to elevated temperatures and DCPD lead wires.

With all of the components assembled, including the DCPD and furnace setups, the creep-fatigue experimental frame was capable of high temperature crack initiation and growth studies, Fig. 3.17. Depending on the type of load waveform, standard FCG and CCG tests could be conducted, as well as more complex CFCIG experiments. Upon test completion, microscopy was used to provide additional qualitative data.

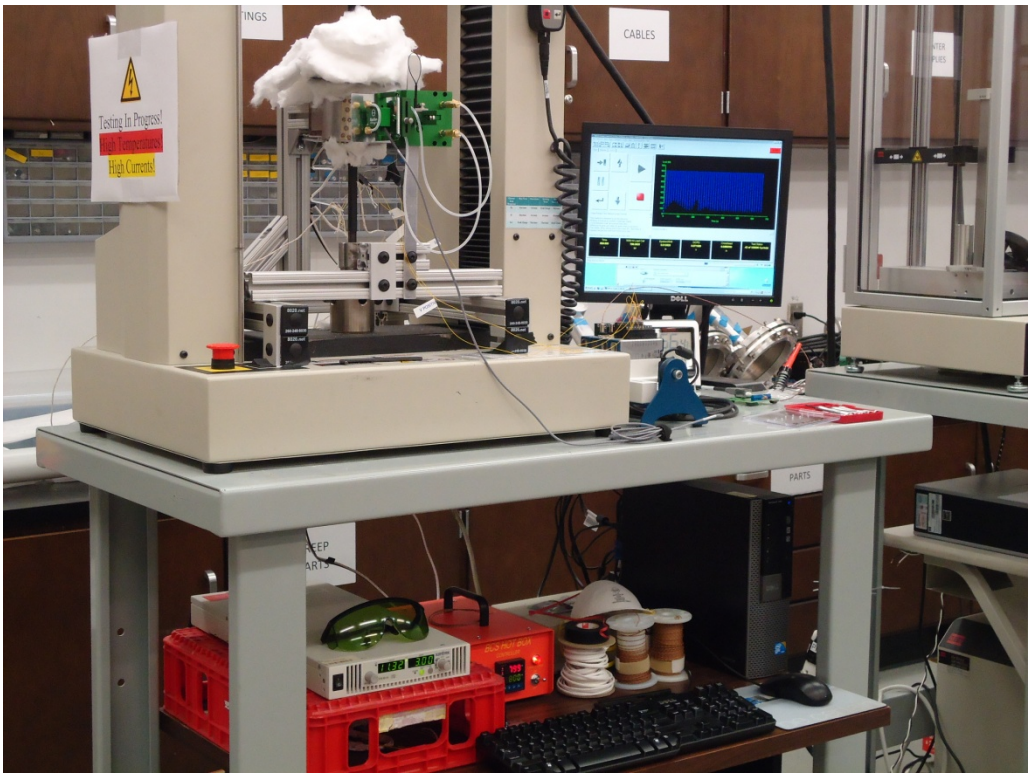

Figure 3.17: Complete experimental setup, including CMOD, DCPD system and furnace controller.

3.6 Metallurgical Analysis

Metallurgical analyses were conducted on the SFO specimens and fractured tensile and blunt notch C(T) specimens. Microstructure and oxidation depth within specimens was observed via optical microscopy, whereas fracture surfaces and modes of fracture were analyzed via scanning electron microscopy (SEM). Optical microscopy was conducted at the MPCL, utilizing the setup shown in Fig. 3.18, and scanning electron microscopy was conducted at MCF.

Figure 3.18: Optical microscopy center at MPCL.

3.6.1 Optical Microscopy

Optical microscopy furnished high-resolution images of the test specimens, as well macroscopic views of fracture surfaces. Two microscopes were employed, with one being a digital microscope and the other being a traditional metallurgical microscope with digital camera attachment. The digital microscope was primarily used for macroscopic fracture surface images, whereas the metallurgical microscope was used in characterizing the microstructure, as well as to measure oxide penetration depth on SFO and blunt notch C(T) specimens.

The digital microscope employed was a DinoLite AM7013-MZTS with a polarizing lens. This particular microscope had a 5MP digital camera sufficient up to 240x magnification making it ideal for general purpose imaging. The polarizing lens allowed for high resolution images without much of the glare associated with macroscopic imaging of metallic specimens. No preparation of samples was required for use with the DinoLite, making it suitable for macroscopic imaging of fracture surfaces.

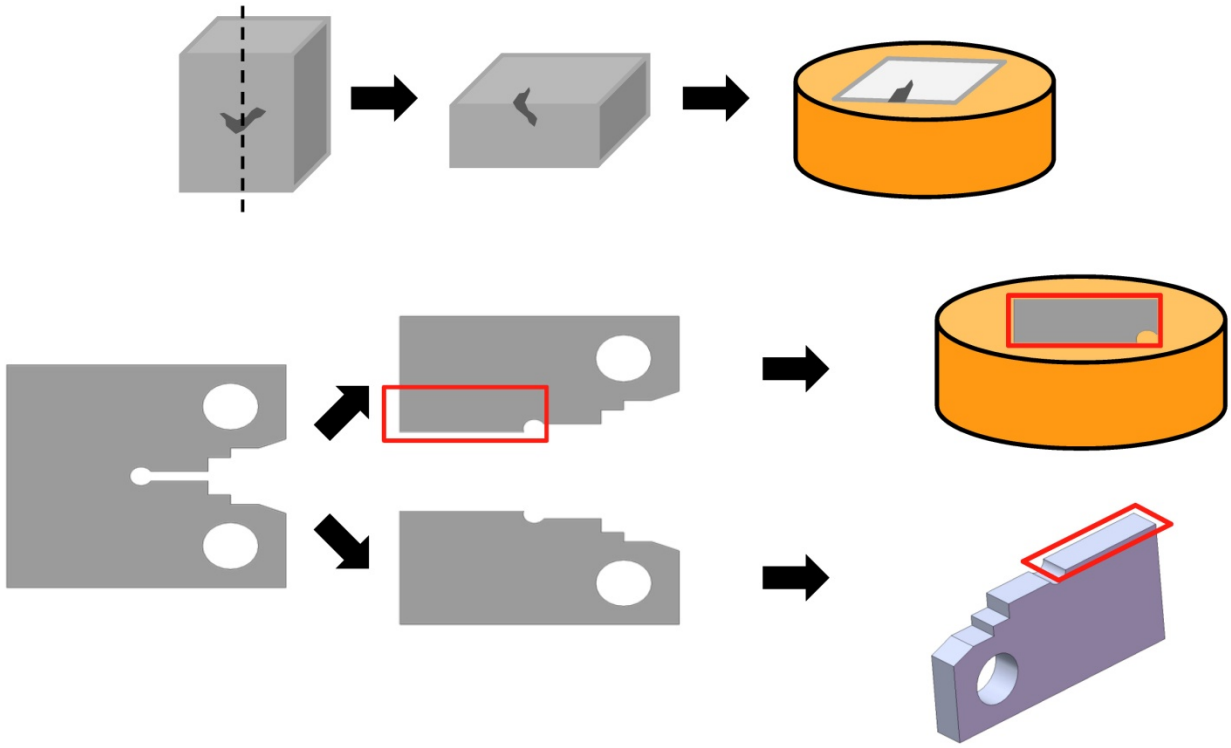

Figure 3.19: Sectioning procedures used to mount, polish and inspect SFO (top) and creep-fatigue (bottom) specimens under a metallographic microscope.

Microscopic metallurgical observations required the sectioning and mounting of specimens. Key features, such as cracks in the surface of the material, were identified as areas of interest. Both stress-free oxidation and creep-fatigue specimens were then sectioned, mounted and polished, based on the areas of interest, as shown in Fig. 3.19. The mount material implemented was a LECO epoxy kit, namely the QUICK-CURE EPOXY KIT. The cold curing process set in an hour and upon curing, the mounted specimens were polished, utilizing the same polishing procedure outlined in Section 3.3

Observation of the grain structure required the use of a chemical etchant prior to viewing sectioned specimens. Following sectioning and mounting, prepared surfaces were etched using Kalling's etchant solution. The constituents of the chemical etchant are provided, Table 3.10. The etchant is commonly used in analysis of austenitic stainless steels, making it useful in the

study of SS304 (LECO, 2012). Upon polishing and etching, specimens were observed via the metallurgical microscope.

Table 3.10: *Kalling's Etchant Composition*

Component	**Amount**
$CuCl_2$	5 g
HCl	100 ml
Ethyl Alcohol	100 ml
Distilled Water	100 ml

Observations on the microscopic scale were performed on a UNITRON metallurgical microscope. Images were recorded via an attached Leica EC3 3.1MP digital camera. Utilizing a standard C-mount, the Leica camera was affixed to the eyepiece of the metallurgical microscope. Measurements of oxide depth and grain size were made with the related software for the camera. Based on the objective selected, the image was calibrated and measurements were easily made on screen, in real time.

3.6.2 Scanning Electron Microscopy

Scanning electron microscopy was primarily utilized in the fractographic analysis of CFCIG specimens. Upon fracturing of specimens, an SEM was used in characterizing the mode of fracture, the extent of secondary cracking and to measure fatigue striations. Measurement of the striation spacing was useful in confirming the crack length and *da/dN* measurements obtained via CMOD and DCPD methods. The SEM employed in this investigation was a JEOL JSM-6480 with an accelerating voltage 20kV and maximum resolution of 30-50nm, depending on the selected vacuum mode. Typical magnification was between 1,000-1,500x and provided sufficient resolution to identify the key areas of interest. Coupled with the numerical data, the qualitative imaging tools provided invaluable assistance in the development of the crack initiation and propagation models.

3.7 Experimental Data Post Processing

Post-processing of data obtained from experimental tests required the development of numerical routines to reduce the raw data. During the reduction process, vital fracture mechanics parameters were calculated, enabling faster post-processing of large sets of data. Separate routines were developed to curve-fit the proposed creep-fatigue crack initiation and propagation model. In addition to the reduction of data, routines were developed that produced user-friendly files for data presentation. An overview of the routines, as well as the languages used, is provided.

Experimental data obtained from tensile tests required no data reduction and minimal post-processing. The post-processing involved standard "toe compensation" and fitting the linear portion of the tensile test to determine the elastic modulus, as per the methods outlined in E8 and E21 [ASTM E8/E8M-09; ASTM E21-09]. Other key parameters, such as the yield and ultimate tensile strengths were readily obtained from the produced stress-strain curves. Values obtained were subsequently used in CFCIG calculations, as necessary, detailed further in Section 5.2.

Creep-Fatigue data reduction was necessary to analyze the data obtained from each experiment. To reduce the data, a custom Fortran routine was developed to reduce the data outputted from the data acquisition system. The routine would read in all of the data outputted from the DAQ and calculate key components parameters, such as minimum, maximum, average load-line displacement, load-line displacement rates, DCPD voltages, etc. Additionally, a routine was developed within Microsoft Excel to search for all values for a given cycle, allowing for the data to be selected and manipulated, as needed, on a cycle-by-cycle basis.

Creep-Fatigue crack growth rates were calculated based on a ΔJ versus *da/dN* approach, as outlined by [Dowling and Begley, 1976]. For deeply-notched tensile specimens, the value of ΔJ is approximated by the area under the rising load versus load-line displacement curve, i.e.,

$$\Delta J = \frac{2}{B(W-a)} \int_{\delta_i}^{\delta_f} \Delta P \mathrm{d}\delta \,, \tag{3.3}$$

where B is the specimen thickness, W is the width, a is the crack length, ΔP is the load range and δ_i and δ_f are the initial and final load-line deflections, respectively. For each cycle, 4th order polynomials were fit to the load versus load-line displacement curve, which typically resulted in fits with an r^2 value greater than 0.99. The resulting fit was integrated using Mathcad, thus providing the area under the curve, shown previously in Fig. 2.16, and furnishing the value of ΔJ. In the event LEFM methods were valid, i.e., very limited amounts of cyclic plasticity observed, ΔK values were approximated [Dowling and Begley, 1976], e.g.

$$\Delta K = \sqrt{E \Delta J} \,. \tag{3.4}$$

By using the Excel spreadsheet to pull individual cycle data, calculation of the cyclic crack tip parameters was semi-automated and straightforward.

In addition the method outlined for generating crack growth curves, a fitting routine was developed in Fortran based on the polynomial fit method. The fitting routine was modeled after the Basic programming language FCG data reduction routine provided in E647, provided in Appendix B [ASTM E647-08$^{\varepsilon 2}$]. Furnished in an older language, modifications and updates had to be made to the syntax to conform to standards of a current Fortran compiler and to calculate crack growth rates based on ΔJ, as opposed to the ΔK calculation within the original routine. By reading in data from the modified data reduction program, the routine would then calculate the average crack growth rates, accepted as a common practice within the ASTM standard for LEFM

FCG. The sample input and output furnished in E647 was replicated utilizing the updated curve fitting program using ΔK calculation within the original routine, and is also provided in Appendix B.

Following the data reduction routine, curve fitting was necessary to establish the constants in the proposed CFCIG model, outlined in Section 5.2. Utilizing the freeware program Eureqa from Cornell Creative Machine Labs, analytical models and constants for potential crack initiation and propagation models were parametrically determined [Schmidt and Lipson, 2009]. This software is used in finding the relationship between experimental data sets by taking the partial derivatives between the variables in test parameters and attempting to fit equations to the physical invariance. By supplying crack growth rates, as well as any variable that may affect those rates, Eureqa would search for applicable analytical models to fit the data. In the event that an analytical model was chosen, Eureqa was then used to optimize the constants of the model, by parametrically altering the constants, in effort to increase the R^2 goodness of fit for the experimental data. By implementing this powerful software, development of constant optimization routines were avoided and reduced the number of iterations required to optimized the constants used in any proposed analytical models.

3.8 Data Management and Organization

Throughout the course of the experimental investigation, a large amount of data was obtained. Without reduction, the raw data files required several gigabytes of hard drive space. Further reduction and manipulation produced additional data files, as well as high quality image files. In the event that the data is required for future investigations, archival of all of the obtained and generated files was a necessity. As such, the data management, including long term storage and organization, was a topic of concern during the study.

To address the storage issue, an external hard drive (1 TB capacity) was acquired and used for data storage. The advantage of the external drive was the storage capacity, portability and ability to password protect experimental data. A convenient file structure was developed, based on the alloy, type of test and test temperatures/environments. The structure provided a format for future storage of test data from experiments conducted within the research group. By laying out the framework for data management, a useful, convenient and centralized method for storing test data was developed and implemented.

CHAPTER 4
EXPERIMENTAL RESULTS AND MICROSCOPY

Several forms of mechanical experiments were conducted during this investigation to analyze the creep-fatigue behavior of a notched component. A majority of the tests were intended solely to be used in the development of the proposed coupled crack initiation and propagation models. Additional tests were conducted to determine the material properties for the specific batch of material and the orientation of specimens used during the investigation. Room and elevated temperature tests were conducted, with the emphasis on high temperature experiments, as the intended end user is to be interested in crack initiation and propagation in elevated temperatures. Results are presented in order of the test type, i.e. tensile, stress-free oxidation and creep-fatigue, with relevant microscopy for each contained within individual sections. Complete experimental data sets and microscopy for individual specimens are located in Appendix C.

4.1 Tensile Test Results

Elastic and tensile properties for the selected orientation and batch of material were determined from standard tensile tests, as per ASTM E8 and E21 [ASTM E8/E8M-09; ASTM E21-09]. Tensile tests were conducted at 68°F (20°C), 600°F (315°C) and 800°F (427°C) at a rate of 0.2in/in/sec (0.2mm/mm/sec). Mechanical loading was imposed after approximately a 15 minute saturation period, in which the specimen was allowed to obtain a stable temperature reading, as reported via the attached thermocouple. Selected results are provided, Table 4.1, as well as the stress-strain curves for the tests, Figs. 4.1 and 4.2. The curves are split into the full range of testing, Fig. 4.1, for ultimate strength and rupture properties, and an expanded view

incorporating the Ramberg-Osgood approximations, Fig. 4.2, useful in capturing the elastic modulus and yield strength.

Table 4.1: *Material properties obtained from tensile tests.*

Specimen	**Temperature, *T*** °F (°C)	**Elastic Modulus, *E*** Msi (GPa)	**0.2% Yield Strength, $\sigma_{0.2}$** ksi (MPa)	**Ultimate Strength, σ_{uts}** ksi (MPa)	**Rupture Strain, ϵ_f** (%)	**Strength Coefficient, *K*** ksi (MPa)	**Strain Hardening Exponent, *n***
Ten1	68 (20)	28.2 (195)	66.5 (458)	101.1 (696.9)	58.4	99.1 (683)	0.0687
Ten2	600 (315)	25.1 (173)	43.9 (303)	71.56 (493.4)	32.8	78.0 (538)	0.1000
Ten3	800 (427)	25.6 (176)	40.1 (277)	67.02 (462.1)	30.9	72.8 (502)	0.1050

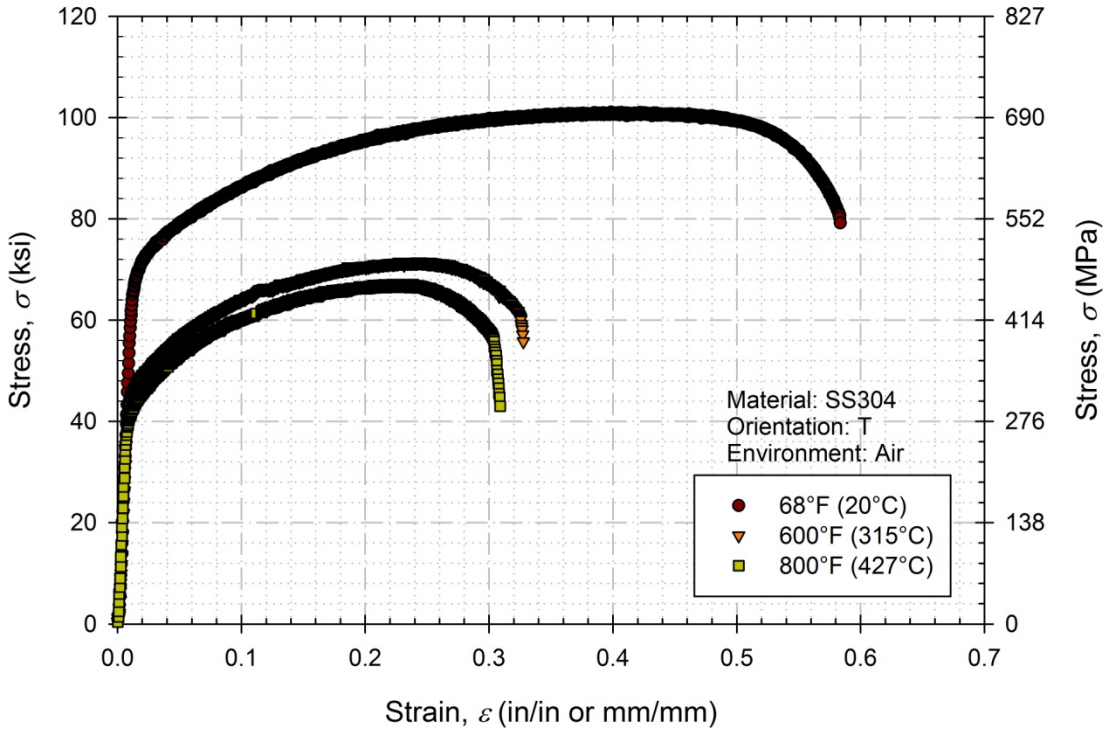

Figure 4.1: Full range stress-strain curves for room and elevated temperatures.

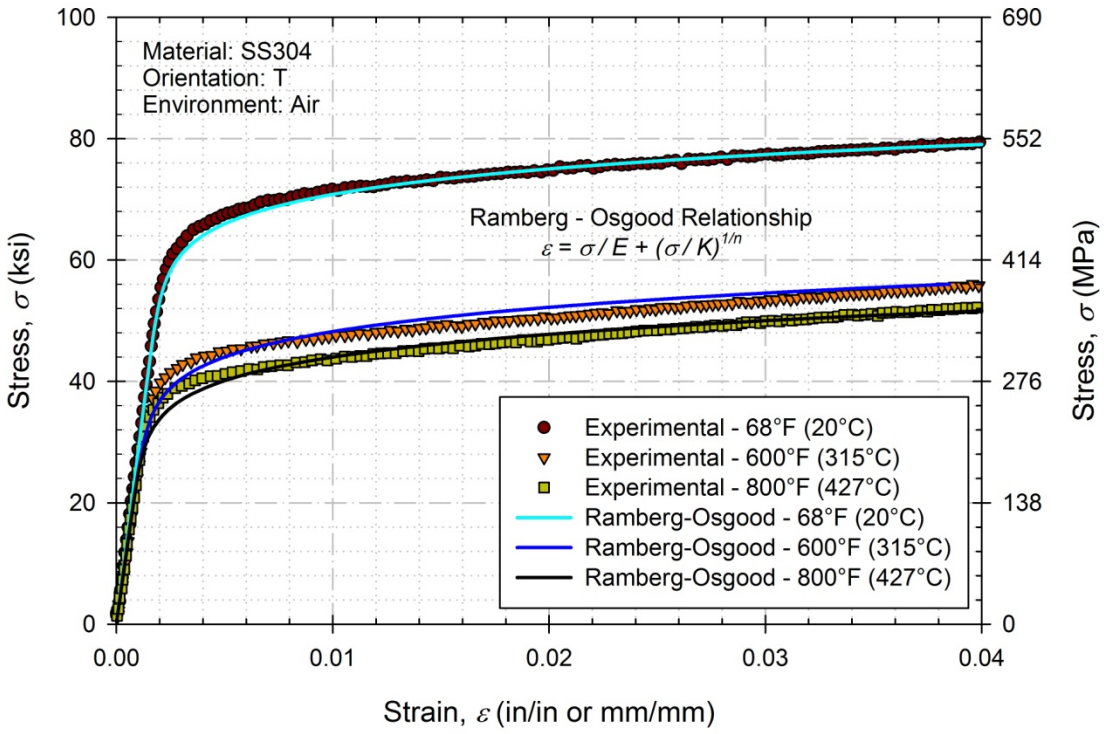

Figure 4.2: Expanded view of the stress-strain curves in the low strain regime with fitted Ramberg-Osgood approximation.

In relation to the published data in Section 2.4.1, several differences are observed. At all three temperatures, the strength is noticeably higher, with an ultimate strength 20% greater than that of referenced data for room temperature. The difference at higher temperatures is less pronounced, with a 12% and 11% increase in strength over data published for 600°F (315°C) and 800°F (427°C), respectively. Yield strength differences were more significant, with nearly a 100% increase for both elevated test temperatures. The strength differences could be related to small differences in chemistry, the orientation of the material used in published data, different heat treatments and different forming processes, amongst other contributing factors.

Noticeable differences in the rupture strain are readily observed, as well. For all three temperatures, the rupture strain obtained from the plate is roughly 40% less than referenced data. It is expected the literature data was obtained from rod stock, which has an elongated grain

structure in the direction of load application during a tensile test. The tensile specimens used in this study have a shortened grain orientation in the load application direction, providing less stress carrying capability. This is expected, as orientation effects are widely acknowledged and test standards identify the orientation to conduct tests, e.g. [ASTM E399].

The elastic modulus is observed to decrease as the test temperature increases, as was expected. From room temperature to the maximum test temperature of 800°F (427°C), a 11% reduction in the elastic modulus was observed. Again, this was expected, as softening of the material occurs at elevated temperatures. The elastic modulus for both the 600°F (315°C) and 800°F (427°C) were nearly equivalent, signifying that the stiffness of the material is not greatly reduced between the two elevated temperatures.

A major result from the tensile tests indicated that the material was much stronger than material data that was used in the design of the blunt notch C(T) specimen. Tensile data obtained and utilized in the design phase, as presented in Section 2.4.1, exhibited a yield strength of nearly half that of the material used in this investigation at all test temperatures. Further discussion on the impact of the higher strength of the subject steel on the specimen dimensions will be provided in Section 4.3.

Not only were the tensile results useful in characterizing the elastic and plastic properties for the material, the experiments dictated the loads to be used in the creep-fatigue experiments on the modified specimens. As elastic and plastic notch tip responses can be accounted for via fracture mechanics techniques, loads were tailored to be around the experimentally-obtained yield strength at the respective temperatures. This allowed for finer control over the fracture mechanics-based experiments and reduced the number of specimens required for testing.

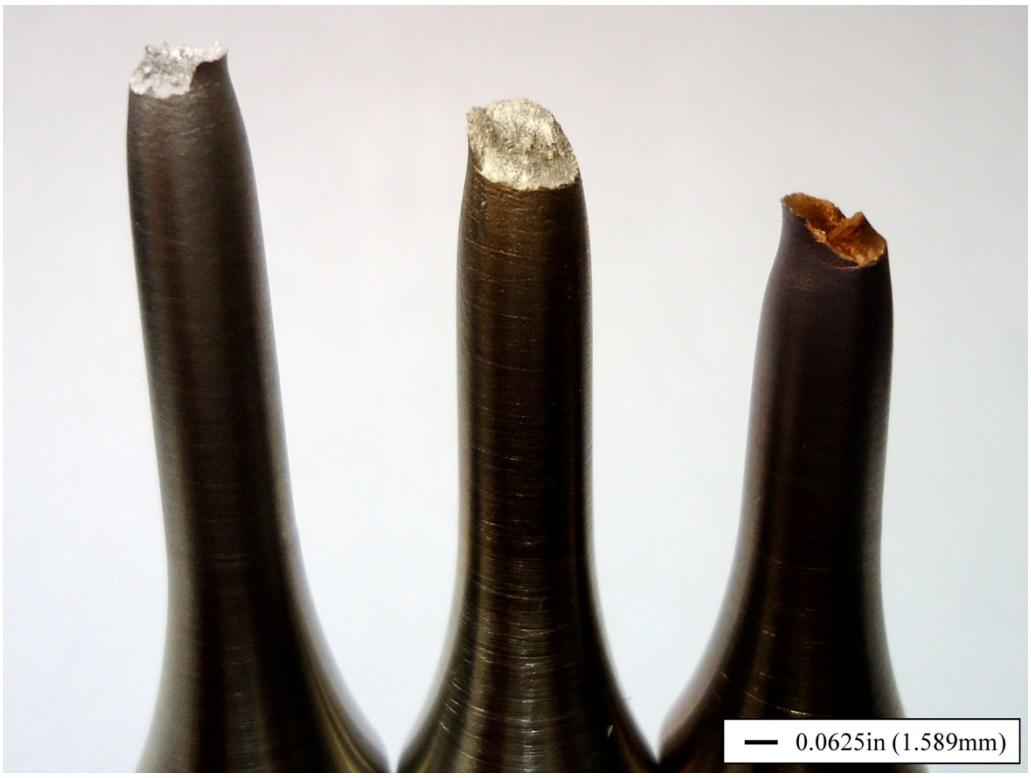

Figure 4.3: Tensile specimens tests at test temperatures of (left) 68°F (20°C) (center) 600°F (315°C) and (right) 800°F (427°C).

Macroscopic images of the tensile specimens conducted at room and elevated temperatures are provided, as shown in Fig. 4.3. Individual fracture surfaces at each temperature are provided in Figs. 4.4-4.6. Fracture surfaces of all tensile specimens were observed to display ductile failure features, with typical cup-and-cone fracture and extensive necking. Failures were contained within the gage section, mostly around the center of the specimen, as expected in standard tensile tests. No initiation of fractures were observed to occur at the location of the thermocouple weld, eliminating the potential for skewed or premature failures due to a stress concentration or heat affected zone as a arc weld.

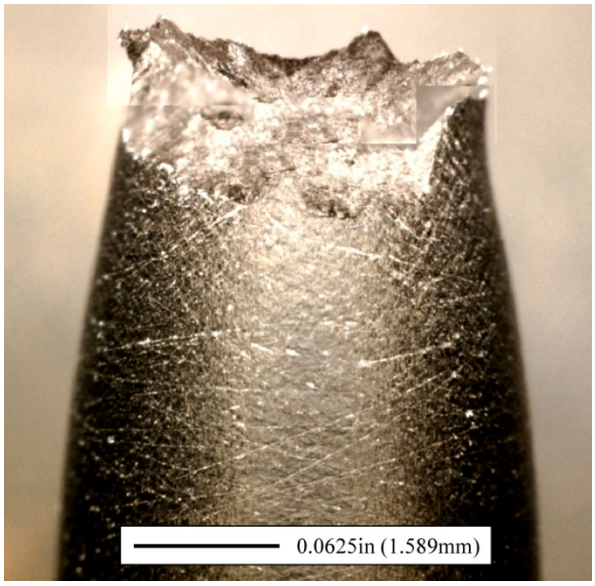

Figure 4.4: Fracture surface of tensile specimen, Ten1, tested at 68°F (20°C).

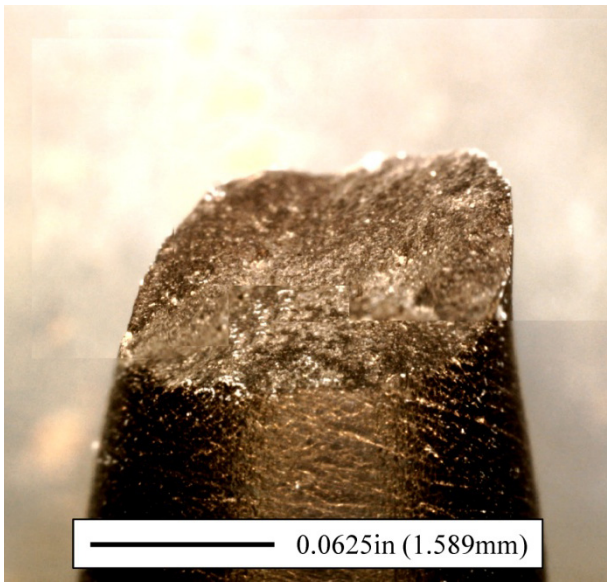

Figure 4.5: Fracture surface of tensile specimen, Ten2, tested at 600°F (315°C).

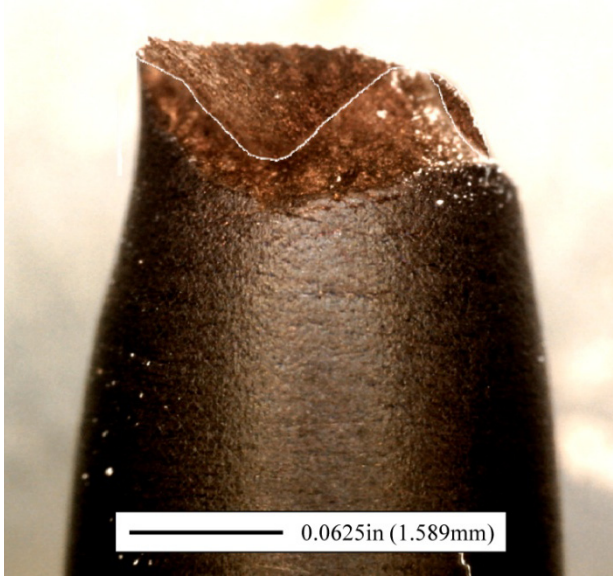

Figure 4.6: Fracture surface of tensile specimen, Ten3, tested at 800°F (427°C).

The main difference between the three tensile specimens is the color tint observed on the surface of each specimen, as observed in Fig. 4.3. For the room temperature test, the fracture surface appears to be a dull gray, approximately the same color as the remainder of the specimen. The surface of Ten2, tested at 600°F (315°C), has a straw-yellow appearance whereas the surface of Ten3, 800°F (427°C), has a reddish-brownish appearance. Color tint of the surface of stainless steel has been related back to the temperature of the environment; however, it was noted that due to chemistry variations and processing of the material, this can vary widely. The colors of the surfaces observed in this investigation correlate with the experimental data on the same alloy exposed to the test temperatures for 1 hour [Labanowski and Glowacka, 2011]. Given the small amount of time of exposure, approximately 15 minutes for saturation and 10 minutes for test completion, the color tint was used as a validation that the actual temperatures were those desired.

No additional microscopy was conducted on the tensile specimens, as the primary function of the tensile tests was to provide the monotonic material properties of the subject plate used to obtain the creep-fatigue specimens. The main qualitative contribution was in the validation of the experimental test temperatures, as judged by the color tint on fracture surfaces.

4.2 Stress-Free Oxidation Test Results

Stress-free oxidation experiments were conducted, as outlined in Section 3.5.1, to assess the extent of which oxidation affected the crack initiation and propagation behavior at the elevated temperatures. Small rectangular pieces were machined from the scrap material and polished following the routine Section 3.3. Upon removal of specimens from the furnace, specimens were allowed to cool in lab air conditions in allocated sections, ensuring the containment of any flaking of scales, if applicable. An overview of all specimens, post mounting and polishing, is provided in Fig. 4.7.

Under the metallurgical microscope, polished surfaces were observed for both test temperatures, provided in Figs. 4.8 and 4.9**.** In both cases, no appreciable oxide layer of any depth was observed, with any oxide depths expected to on the order the micron or sub-micron level. Observation of both the polished side and three unpolished sides of each rectangular specimen, resulted in undistinguishable levels of oxidation. The implication from the stress-free oxidation tests, in which no oxidation was observed, is that oxidation will not have a significant role in the initiation and propagation of cracks under the experimental test environments or that any appreciable oxidation observed on fracture specimens will be stress-induced. The observation of fracture surfaces and sections of specimens subjected to creep-fatigue tests will indentify which of the two implications is relative to the current investigation and dictate whether or not oxidation terms will be present in the proposed model.

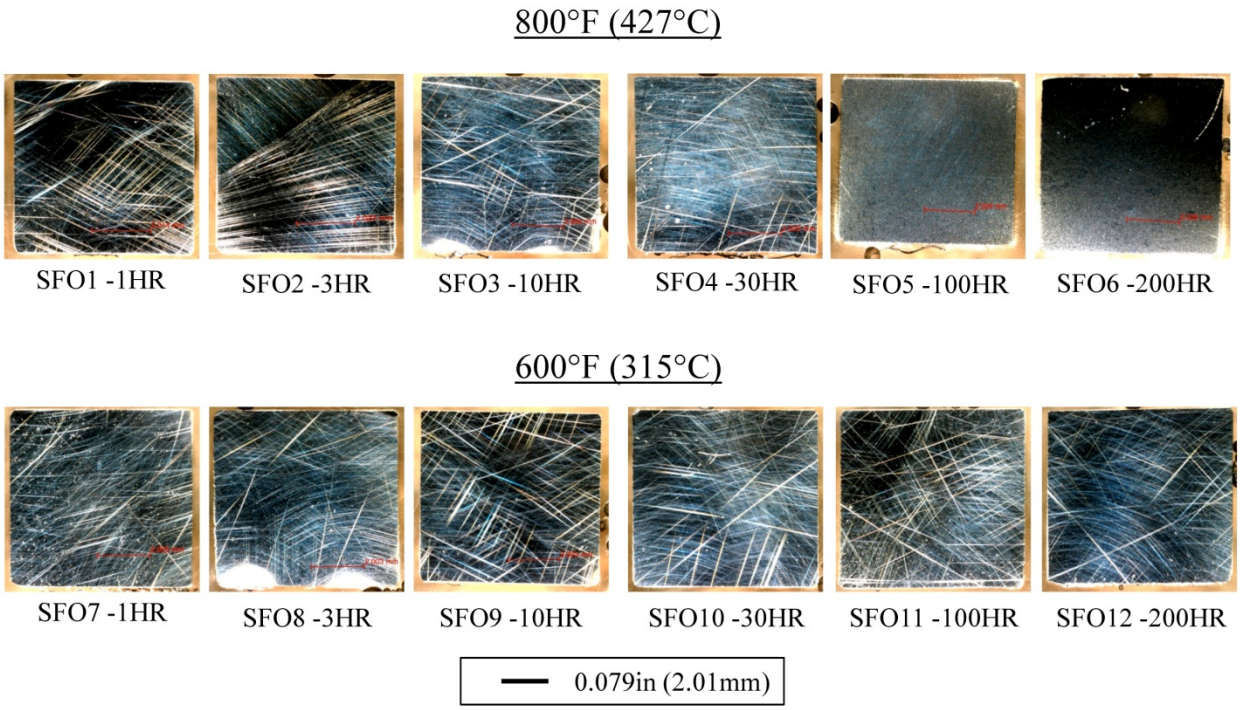

Figure 4.7: Overview of SS304 Stress-Free Oxidation specimens.

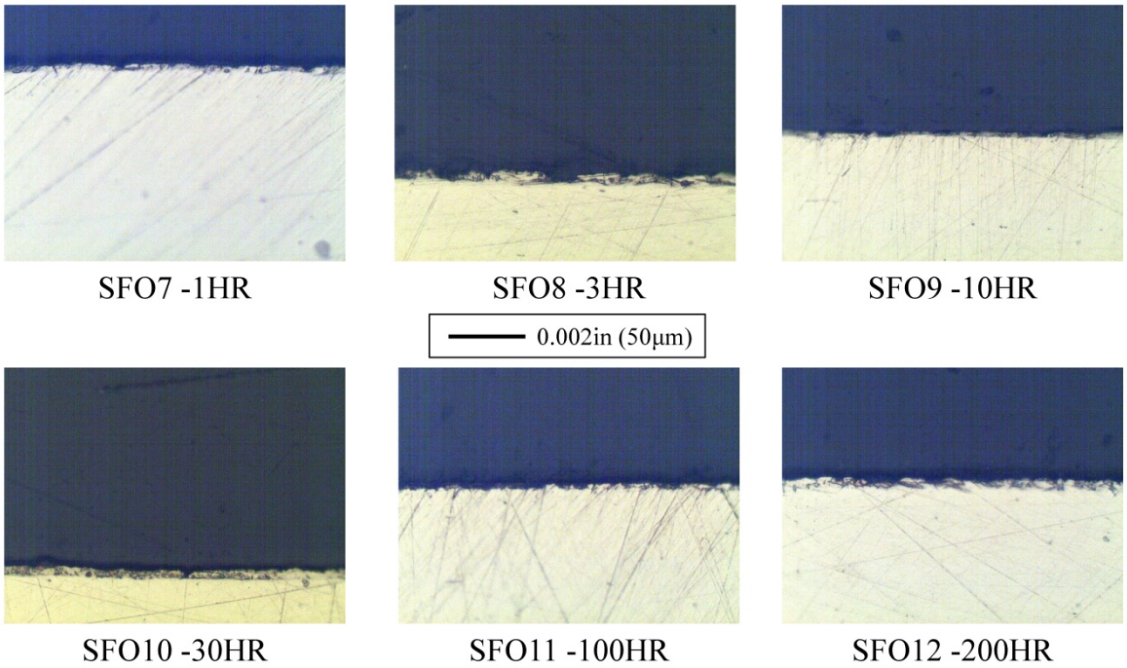

Figure 4.8: Stress-free oxidation specimens tested at 600°F (315°C).

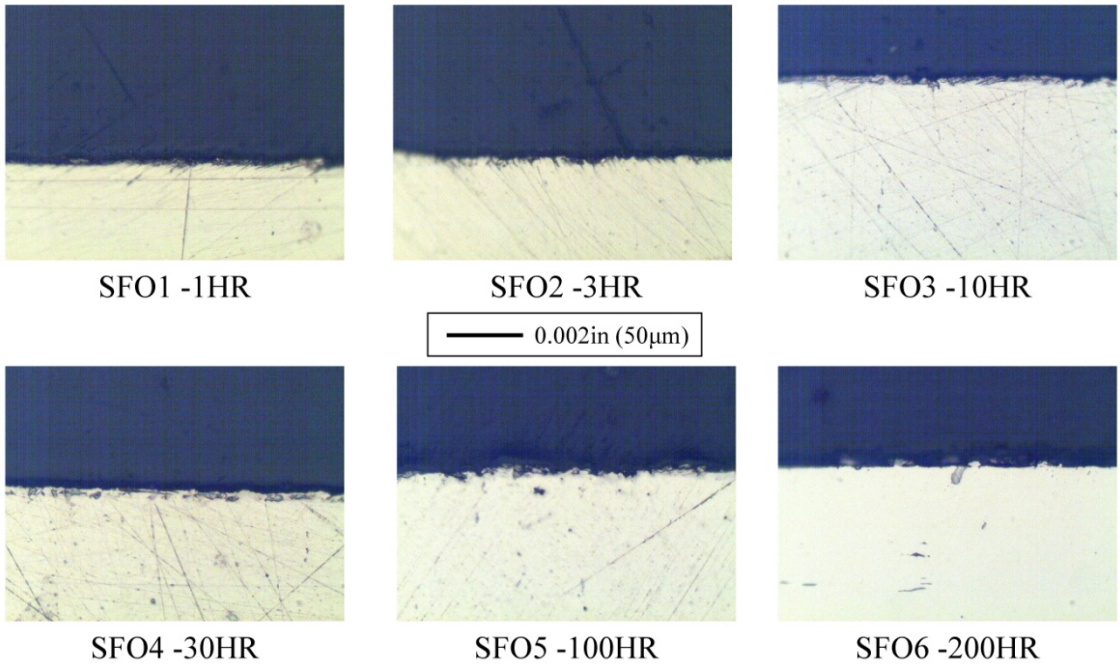

Figure 4.9: Stress-free oxidation specimens tested at 800°F (427°C).

4.3 Creep-Fatigue Simulation and Test Results

Creep-Fatigue experiments were conducted at elevated temperatures of 600°F (315°C) and 800°F (427°C), as chosen due to relevance to the service conditions of stainless steel. Various parameters were controlled during the course of each test, as outlined in Section 3.1 and Tables 3.1 and 3.2, with a list of completed experiments provided, as in Table 4.2. Deviations in the proposed and completed test matrix will be discussed in Section 4.2.3. All tests were conducted utilizing load control, with the load waveforms utilized provided in Fig. 4.10. Main aspects include load hold-time to rise-time ratios of 1, 5 or 10 and load hold periods of 2, 10, 20, 50 and 100s. Applied loads were chosen based on results from the tensile tests, as well as numerical monotonic simulations of the developed creep fatigue-specimen. Physical monitoring

devices included a load-line CMOD gage, DCPD crack length measurement system and standard load frame channels, i.e. load and displacement monitors.

Table 4.2: *Completed experimental test matrix, including failure cycle and final crack length.*

Specimen	**Temperature, T** °F (°C)	**Max Load, P** lbf (kN)	**Load Ratio R**	**Rise Time, t_r** (s)	**Hold Time, t_h** (s)	J_1 lbf/in (N/mm)	ΔJ_{stab} lbf/in (N/mm)	**Failure Cycle, N_f**	**Final Crack Length, a_f** in (mm)
BN1	600 (315)	825 (3.67)	0.1	2	2	140.9 (24.68)	53.96 (9.450)	6068	0.6621 (16.82)
BN2	800 (427)	800 (3.56)	0.1	2	2	214.2 (37.51)	52.83 (9.252)	3980	0.6424 (16.32)
BN3	800 (427)	800 (3.56)	0.1	2	20	227.5 (39.84)	51.12 (8.952)	5212	0.6426 (16.32)
BN4	800 (427)	800 (3.56)	0.1	10	100	228.4 (39.99)	50.15 (8.783)	5194	0.6395 (16.24)
BN5	800 (427)	800 (3.56)	0.1	2	10	234.9 (41.12)	54.62 (95.65)	3485	0.6337 (16.09)
BN6	800 (427)	800 (3.56)	0.1	10	50	193.1 (33.82)	51.87 (9.084)	4415	0.6584 (16.72)
BN7	800 (427)	800 (3.56)	0.05	2	20	212.2 (37.16)	56.88 (9.961)	3939	0.6372 (16.19)
BN8	800 (427)	800 (3.56)	0.05	10	100	227.8 (38.89)	58.34 (10.22)	3144	0.6447 (16.38)
BN9	800 (427)	800 (3.56)	0.05	2	10	202.3 (35.43)	59.21 (10.37)	3983	0.6587 (16.73)
BN10	800 (427)	800 (3.56)	0.05	10	50	227.6 (39.86)	59.47 (10.42)	3535	0.6416 (16.30)
BN11	600 (315)	825 (3.67)	0.1	2	20	163.7 (28.67)	50.88 (8.910)	5927	0.6375 (16.19)
BN13	600 (315)	825 (3.67)	0.1	2	10	140.6 (24.62)	53.69 (9.403)	6718	0.6449 (16.38)
BN14	600 (315)	825 (3.67)	0.1	10	50	181.6 (31.80)	55.58 (9.734)	6324	0.6487 (16.47)
BN15	600 (315)	825 (3.67)	0.05	2	20	121.1 (21.21)	60.40 (10.58)	5623	0.6636 (16.85)
BN17	600 (315)	825 (3.67)	0.05	2	10	178.2 (31.21)	61.37 (10.75)	3498	0.6443 (16.36)
BN18	600 (315)	825 (3.67)	0.05	10	50	184.6 (32.33)	60.87 (10.66)	5758	0.6392 (16.24)
BN19	800 (427)	800 (3.56)	0.05	2	2	325.5 (57.00)	59.15 (10.36)	3337	0.6166 (15.66)
BN20	600 (315)	825 (3.67)	0.05	2	2	127.1 (22.26)	56.27 (9.854)	5905	0.6561 (16.66)

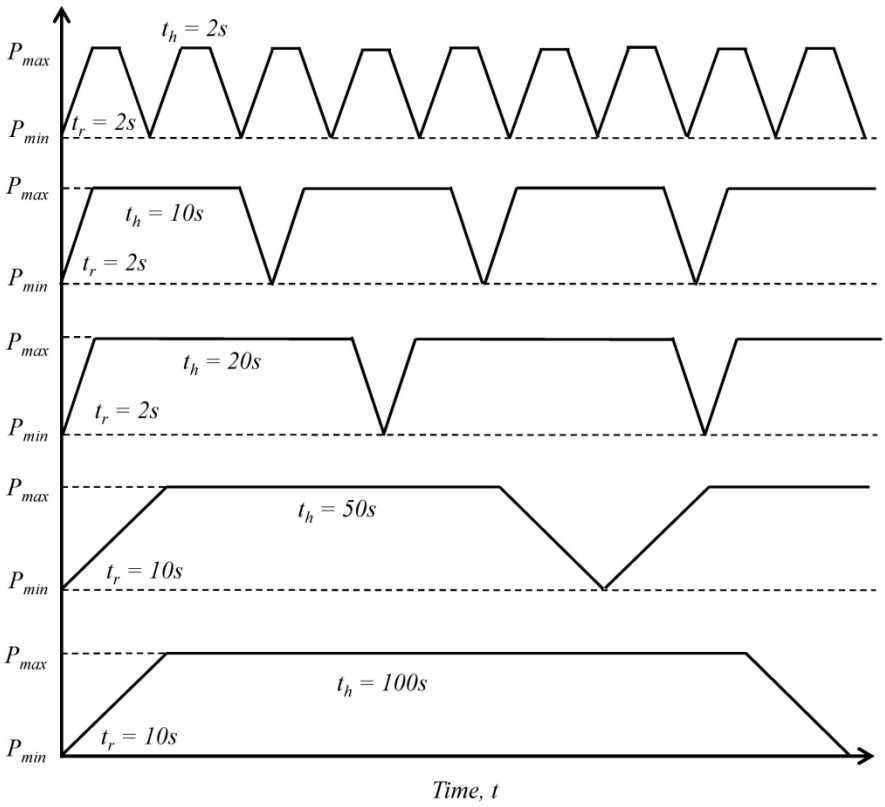

Figure 4.10: Load waveform used during crack initiation and propagation experiments.

As the investigation focused around the ability to impart significant amounts of plasticity at the notch tip, modifications needed to be made to the specimen to ensure that plasticity-inducing loads could be obtained at the notch using the MTS Insight 5kN load frame implemented. This was a direct result of to the stronger batch of material that specimens were obtained from and required a reduction in the specimen thickness to properly test using the desired load frame. After sectioning a dummy specimen to reduce the thickness and experimentally testing at room temperature, coupled with numerical simulation results, a thickness of 0.15in (3.81mm) was chosen. Specimens were then sectioned down to the new thickness through both milling and wire EDM processes. Using the new thickness, stresses above the yield strength could readily be obtained without over-exerting the load frame.

In addition to the physical experiments, numerical simulations using ANSYS were conducted to simulate the response of the material at test temperatures. The following sections are divided into three respective sections, including numerical simulation, creep-fatigue crack initiation, creep-fatigue crack propagation results and microscopy.

4.3.1 Monotonic Numerical Simulations

Monotonic numerical simulations were conducted on one half of a replicated creep-fatigue specimen used in the experimental portion of this study. A multilinear kinematic (MKIN) hardening model was used, utilizing the monotonic properties provided in Section 4.1. The MKIN model required the input of several data points from the temperature dependent stress-strain curves. To ensure accurate capturing of the material response, large strains were included for each temperature, as outlined in Table 4.3 and shown in Fig. 4.11. By including large strain, no extrapolation of stress or strain was necessary, providing confidence in the results based on the material model.

Table 4.3: *Stress-strain values used in MKIN material model for 600°F (315°C) and 800°F (427°C).*

600°F (315°C)		**800°F (427°F)**	
Strain, ϵ_v %	**Stress, σ_{vv}** ksi (MPa)	**Strain, ϵ_v** %	**Stress, σ_{vv}** ksi (MPa)
0.15	35.289 (243.31)	0.15	34.126 (235.29)
0.50	45.397 (313.00)	0.50	41.710 (287.58)
8.00	62.970 (434.16)	8.00	57.818 (398.64)
23.40	71.389 (492.201)	23.40	67.010 (462.02)

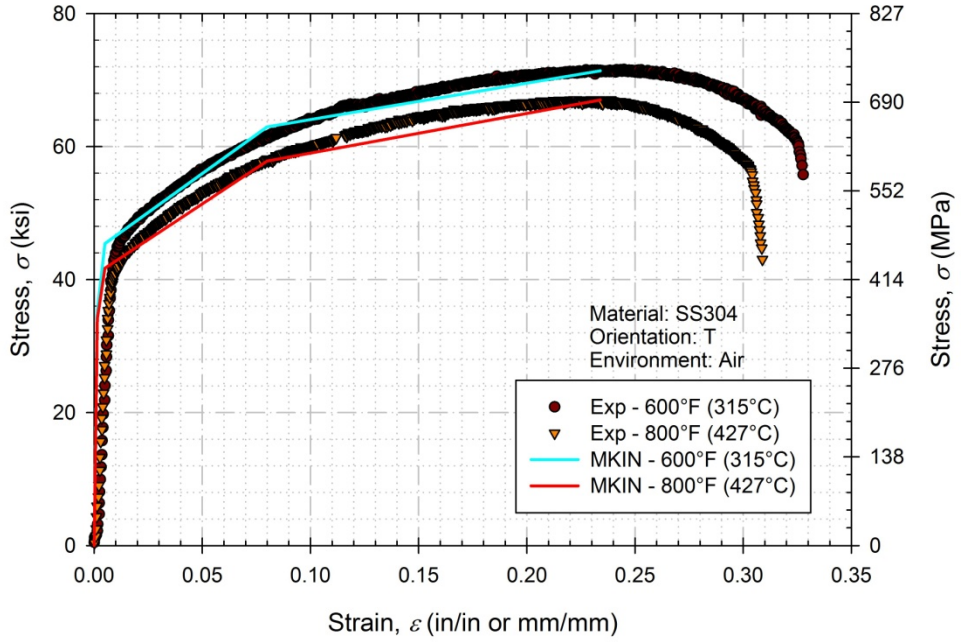

Figure 4.11: Correlation of material model used in FEA simulations with experimental tensile data at elevated temperatures.

Automatic meshing of the simulated component was conducted using standard 3D 20-noded tetrahedral elements. A total of 6,359 Solid186 elements with 10,230 nodes were generated, with mesh refinement at the blunt notch tip, as shown in Fig. 4.12. Boundary conditions were applied to the symmetry surface, with zero displacements prescribed in the vertical direction along the surface and vertical and horizontal directions at the intersection of the symmetry line and back face of the specimen. The latter condition was to ensure rigid body motion was constrained and not a factor in simulations. One half of the load pin hole was modeled, allowing for a pressure to be applied to the surface that was representative of a load imparted by the load pin. Loads were chosen that would result in similar behavior at the notch, which was dependent upon the temperature at which the simulation was replicating.

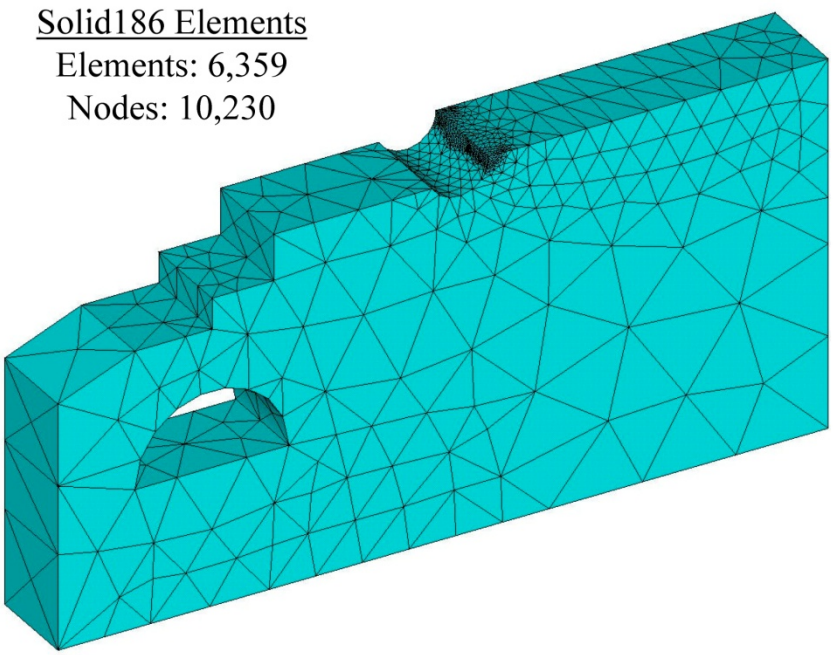

Figure 4.12: One half of a creep-fatigue specimen used in numerically simulating the response of the material under a monotonic load.

Finite element simulations provided the results for three main areas of interest: the stress and strain response along the notch tip, the stress distribution along the symmetry plane and the approximate *J*-integral at the notch tip. First, the stress and strain response along the notch tip provided an estimate of the actual stress and strain at the root of the notch tip. Secondly, the distribution of stresses along the symmetric plane was used in calculating the stress gradient, χ, at the notch tip. Finally, the approximate *J*-integral for the notch tip geometry was used to correlate with the physical experimental measurements. Simulation results at 600°F (315°C) and 800°F (427°C) are provided for a single load case at each temperature, shown in Table 4.4, with stress and plastic strain responses provided in Figs. 4.13 and 4.14.

Table 4.4: *Numerical results for 600°F (315°C) and 800°F (427°C) simulations subjected to a 800lbf (3.56kN) and 825lbf (3.67kN) load, respectively.*

Temperature, *T* °F (°C)	**Average Notch Stress, σ_n** ksi (MPa)	**Maximum Notch Stress, σ_n** ksi (MPa)	**Average Notch Strain, ϵ_n** (%)	**Load-Line Deflection, δ** in (mm)	χ in^{-1}, mm^{-1}	***J-Integral, J*** lbf/in (N/mm)
600 (315)	65.68 (452.9)	70.84 (488.4)	6.4	0.0164 (0.4166)	3.03	179 (31.3)
800 (427)	62.20 (428.8)	67.01 (462.0)	6.1	0.0154 (0.3912)	3.14	164 (28.7)

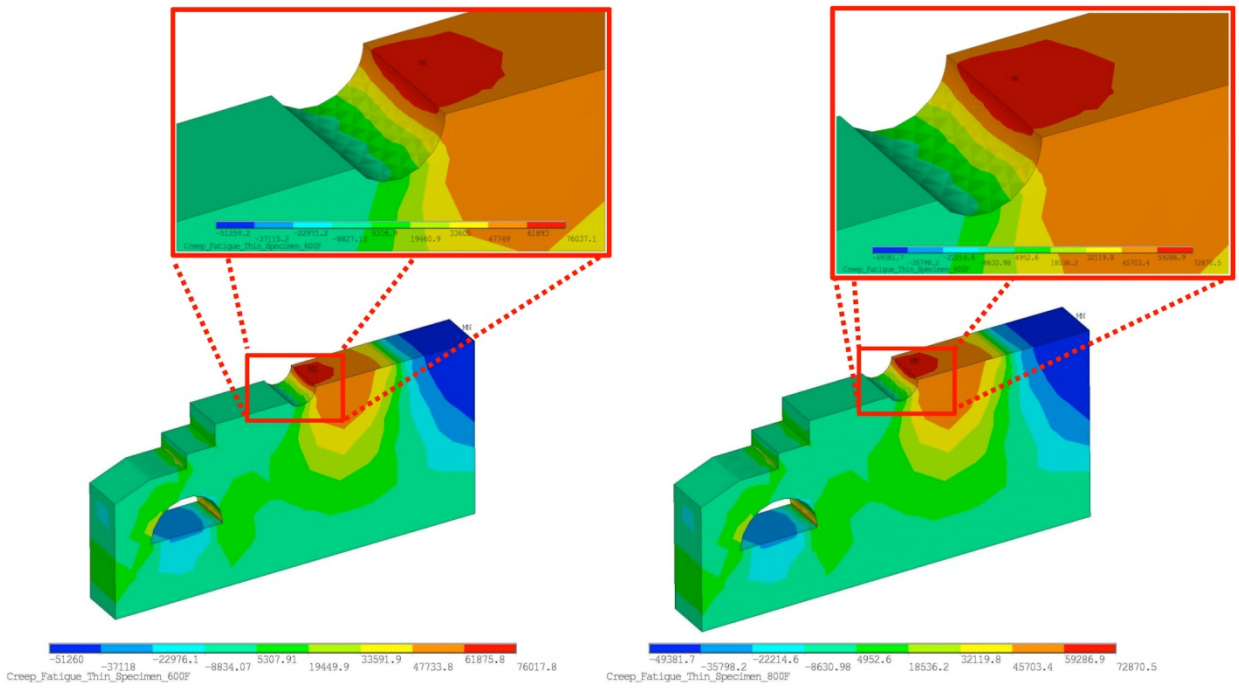

Figure 4.13: Simulated stress distribution along the notch tip for 600°F (315°C) and 800°F (427°C) simulations subjected to a 800lbf (3.56kN) and 825lbf (3.67kN) load, respectively.

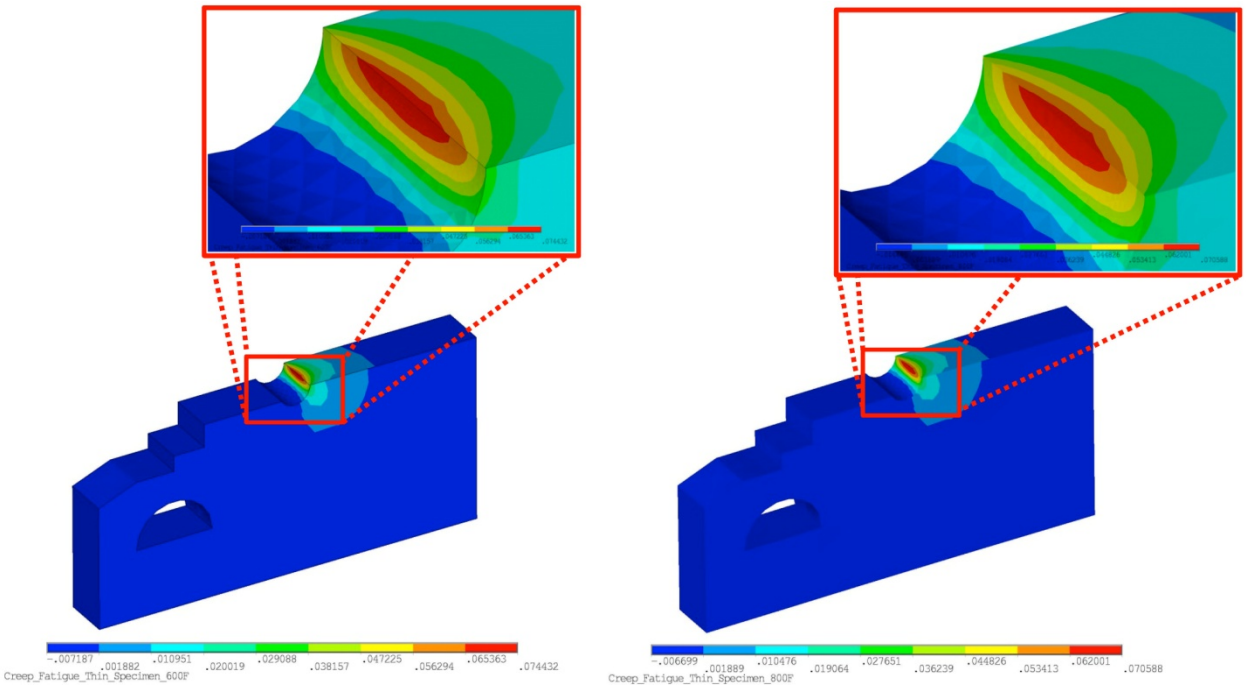

Figure 4.14: Simulated plastic strain distribution along the notch tip for 600°F (315°C) and 800°F (427°C) simulations subjected to a 800lbf (3.56kN) and 825lbf (3.67kN) load, respectively.

The response of the material in Fig. 4.13 for both temperature and load cases reveal a similar predicted behavior. For both cases, a stress state that has a higher stress in the mid-section of the specimen is observed. The increase in stress relates to the stress state throughout the thickness, particularly the plane-strain state in the center of the specimen. As the side of the specimen is approached, the stress state becomes more of a plane-stress scenario, resulting in a lower stress. Maximum stresses are observed in the vicinity of the notch, with maximum stresses for simulations at 600°F (315°C) and 800°F (427°C) of 70.8ksi (488MPa) and 67.0ksi (462MPa), respectively. Additionally, the load-line deflection for both cases is reported at the attachment location of the CMOD gage, with values of 0.0164in (0.4166mm) and 0.0154in (0.3912mm), respectively. Plastic strains were observed throughout the width and thickness of the specimen, as in Fig. 4.14, necessitating the use of EPFM parameters in the crack initiation

and propagation models. As a result, the explicit calculation of the plastic zone size was not considered in the results.

In simulations at both temperatures, the stress and strain distribution along the notch was observed to vary as a function of position on the notch, as shown in Fig. 4.15. Stress values corresponding to the principal direction, i.e. vertical direction, were dominant throughout all simulations, as would be expected given the geometry and load application direction. Elastic and plastic strain distributions followed a similar suit, with peak strains occurring in the middle of the specimen, shown in Fig. 4.16. Considering the thickness of the test specimen, in particular the violation of plane-strain conditions based on the modified specimen thickness, variation along the notch tip is expected.

The stress gradient was calculated for both monotonic cases, based on the relationships presented in Section 2.1.1.2. Stress values in the principal direction, i.e. vertical direction, along the surface of symmetry and the mid-plane of the specimen were extracted, as shown in Fig. 4.17. Simulations predicted a peak stress approximately 0.02in (0.51mm) in from the edge of the notch. In the cases presented in Fig. 4.17, a 6% and 5% increase in stress was observed for simulations at 600°F (315°C) and 800°F (427°C), respectively. This can be attributed to a mesh dependency, where further refinement of the mesh at the notch could potentially achieve less variation within this region. To calculate χ, the average of stress values in the 0.02in (0.51mm) vicinity of the notch was obtained and used as the maximum stress value in Eq. (2.10). Using this technique, the values of χ for both test temperatures were within 3.5%, as the loads applied for the respective temperatures were such that similar notch tip conditions would be achieved, regardless of the test temperature.

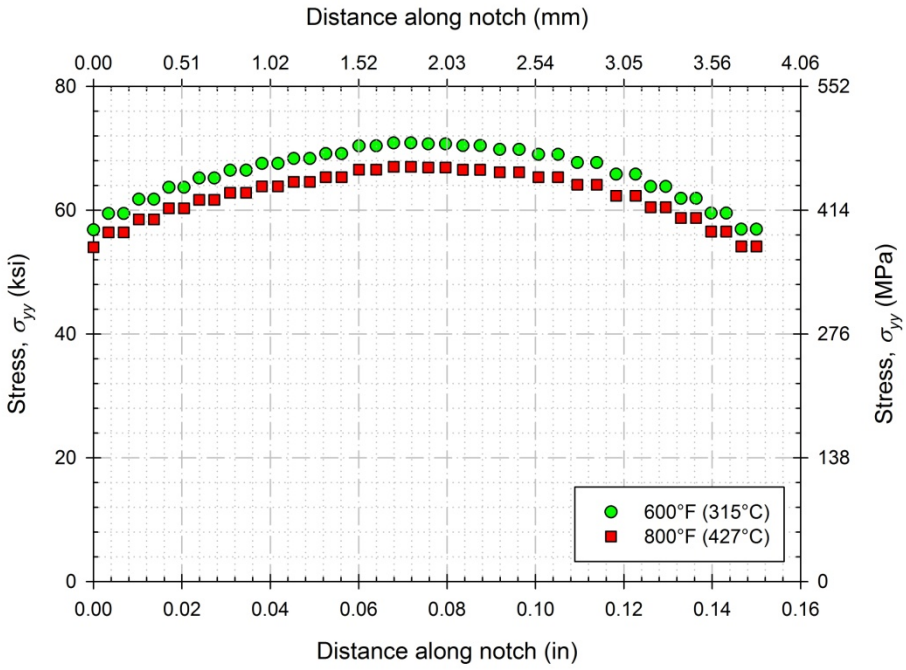

Figure 4.15: Stress values, in y-direction extracted along the length of the notch tip for 600°F (315°C) and 800°F (427°C) simulations subjected to a 800lbf (3.56kN) and 825lbf (3.67kN) load, respectively.

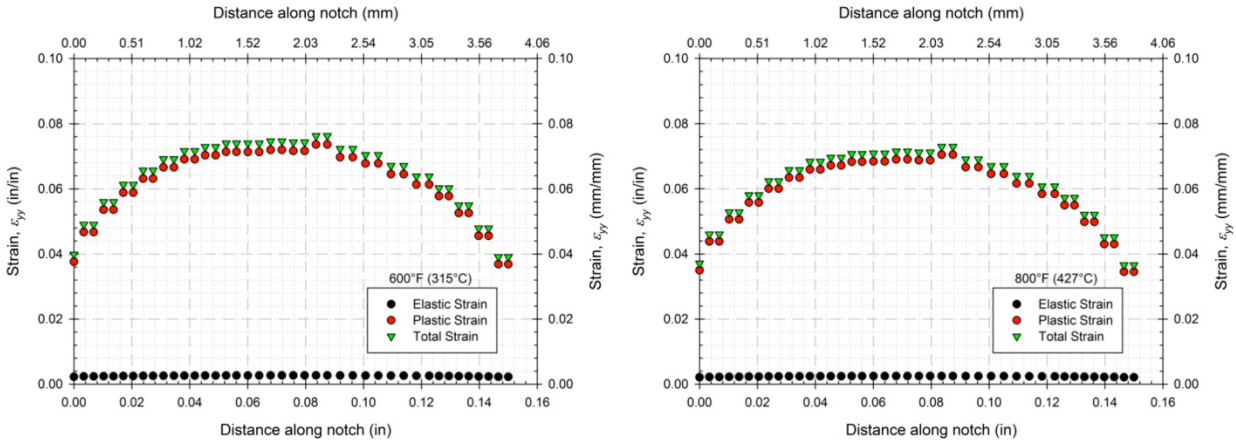

Figure 4.16: Strain values, in y-direction, extracted along the length of the notch tip for 600°F (315°C) and 800°F (427°C) simulations subjected to a 800lbf (3.56kN) and 825lbf (3.67kN) load, respectively.

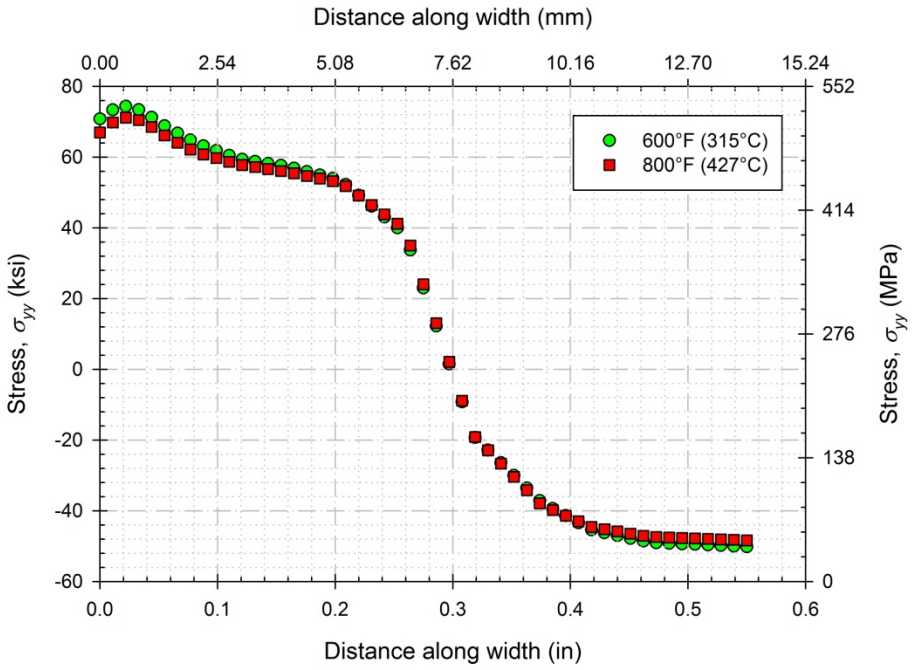

Figure 4.17: Simulated stress distribution through the width and mid-plane of the creep-fatigue specimen used in calculating χ for 600°F (315°C) and 800°F (427°C) simulations subjected to a 800lbf (3.56kN) and 825lbf (3.67kN) load, respectively.

The *J*-integral calculation around the notch was conducted using the CINT command within ANSYS. This command utilizes the *J*-integral calculation for 3D volumes by conducting a volume integral over area of interest, as shown in Fig. 4.18. Here, the blocks represent the elements used in an arbitrary mesh, with the crack visualized as the separation of the elements. Blocks denoted by the varying colors are the volumes over which the integral is evaluated. Using the elastoplastic material model, nonlinear behavior in the stress and strain response is accounted for via the strain energy density, *W*, and used in the calculation of *J* over the selected domain. Although a crack was not explicitly modeled, several contour integrals can taken around the area of interest and provide the *J* approximation for the given geometry and load, provided a linear set of nodes exist at the intended crack location. As the *J*-integral can be calculated through multiple contours, the number of contours is typically chosen based on the geometry and refinement of nodes along the location.

$$J_i = \iiint_{V_i} W dy - \mathbf{T}\frac{\partial \mathbf{u}}{\partial \mathbf{x}} dV \qquad \text{where} \qquad W = \int_0^{\varepsilon} \boldsymbol{\sigma} d\boldsymbol{\varepsilon}$$

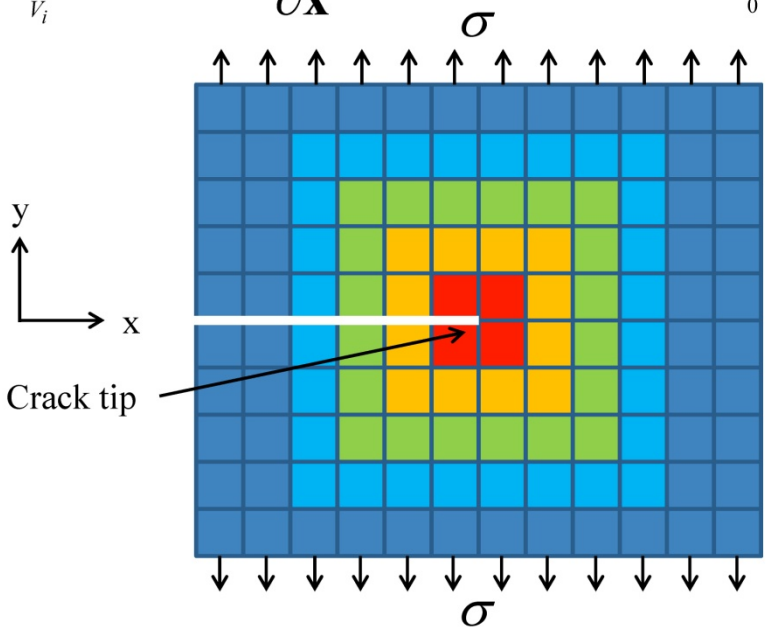

Figure 4.18: Method of J-integral calculation for increasing number of contours for a 3D simulation in ANSYS.

Provided the geometry, level of refinement in the notch tip area and ANSYS example files, a number of 6 contours were chosen to be calculated [ANSYS, 2010]. The mid-plane average of the *J*-integral for the 6th contour is reported in Table 4.4, with a maximum value of 180lbf/in (31.3N/mm) for 600°F (315°C) and 164lbf/in (28.7N/mm) for 800°F (427°C) simulations. The maximum value is chosen, as values reported were averaged over all elements used in calculating the *J*-integral. Values were observed to decrease as distance from the mid-plane of the specimen increased, similar to the stress response along the notch tip, as shown in Fig. 4.19. Simulations did not include a hold period, to allow for relaxation and further displacement of the specimen, thus it is to be expected that the values obtained for *J* approximations in experiments with tensile hold periods will be greater. A comparison of experimental and numerical results will be provided in Section 4.2.2.

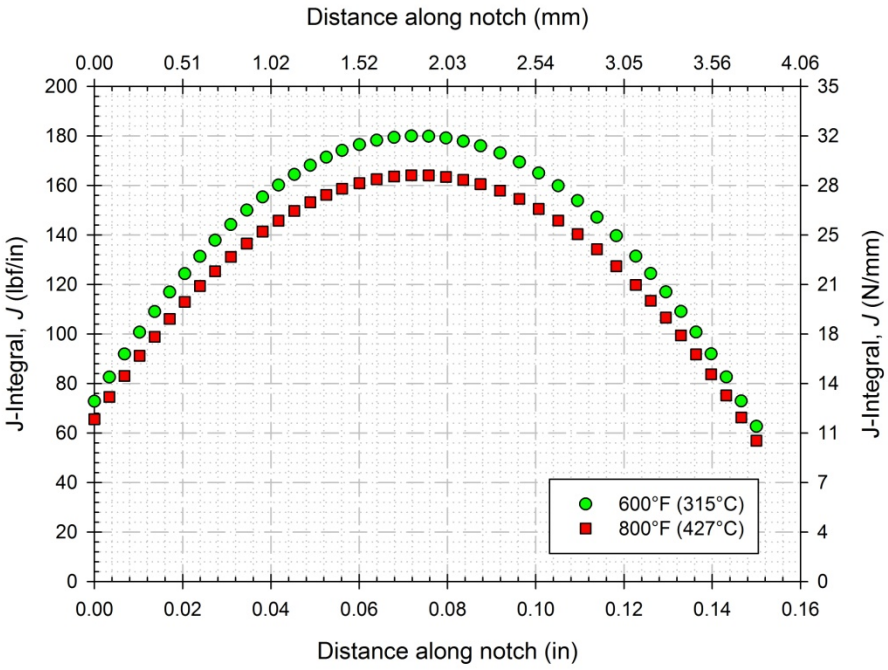

Figure 4.19: Calculation of *J*-integral at the notch tip through the thickness of the simulated specimen in ANSYS.

4.3.2 Comments on Experimental Data

Prior to providing the formatted results and microscopy regarding crack initiation and propagation, general comments regarding the test matrix and raw data is necessary. Deviation in the test matrix proposed in Chapter 3 was necessary, as was redefining some of the experimental conditions. General trends were observed during the course of the experimental investigation, with levels of commonality between all experiments, e.g. maximum load-line deflection versus cycle. An overview of generalities amongst test specimens is provided here.

Deviation from the proposed test matrix in Table 3.2 in Section 3.1 is observed, when compared to the set of experiments conducted in Table 4.2. The notable changes are the change in conditions for specimens BN1 and BN2, the absence of BN12 and the incomplete data set for BN16. The conditions for BN1 and BN2 were modified in order to capture the fatigue-dominated crack initiation and propagation at elevated temperatures, while tests were conducted

with load rise and hold times equivalent. Specimens BN19 and BN20 were extensions of BN1 and BN2, with the exception of the load ratio, which was reduced to $R = 0.05$.

During all crack initiation and propagation experiments, a significant amount of plasticity was observed, in particular during the first load, as shown in Fig. 4.20. Upon initial loading of the specimen, plastic strains accumulate at the notch tip, resulting in permanent set in the material at the notch. Upon subsequent loading, this effect was greatly diminished, with the softening of the material in the notch vicinity completed within the first fifty cycles of the test, as shown in Fig. 4.21. This behavior is representative of structures that may have sharp notches or concentrations, in which the material relaxes and the response upon further cycling is linear, such as a component exposed to a thermomechanical load under fixed boundary conditions. Furthermore, the Figs. 4.20 and 4.21 were used in calculating both J_1 and ΔJ, based on the method outlined in Section 3.7, shown in Fig. 4.22.

The overall amount of plasticity observed in experiments was extensive, as observed by the evolution of the load versus load-line deflection response for the entirety of a test, provided in Fig. 4.23. Excluding the first and last few cycles of a test, however, the amount of cyclic plasticity was small. A result of the of the small cyclic plasticity is that approximations to ΔK could be made, as in [Dowling and Begley, 1976]; however, due to the existence of hold periods and overall plasticity observed, such an approximation was not made in this investigation and will be addressed further in Section 6.3. The choice was further aided by the physical appearance of the tested specimens, to be detailed in Section 4.3.5.

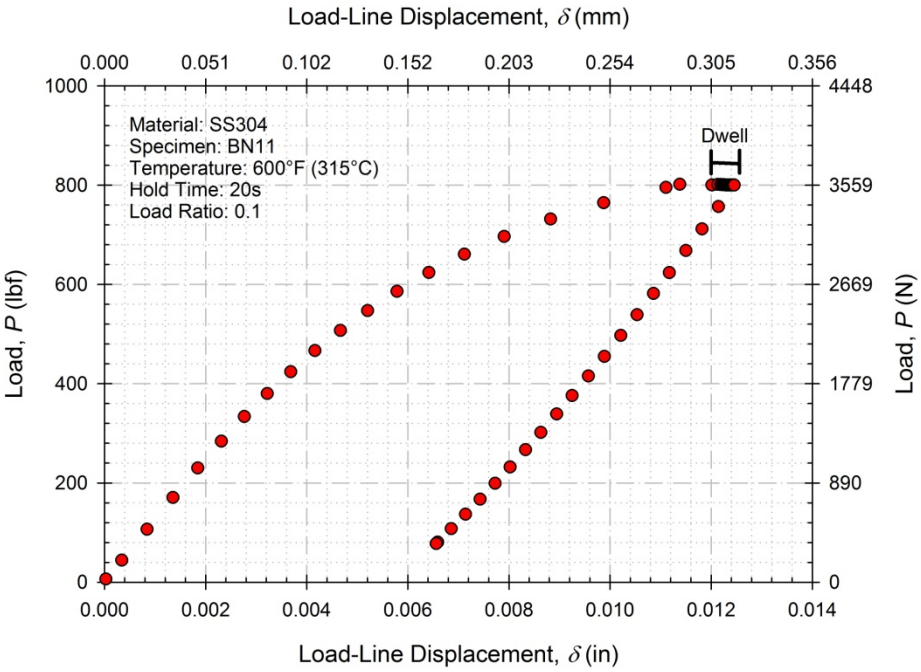

Figure 4.20: Nonlinear behavior in the load versus load-line displacement curve for the first cycle of a CF specimen, BN11.

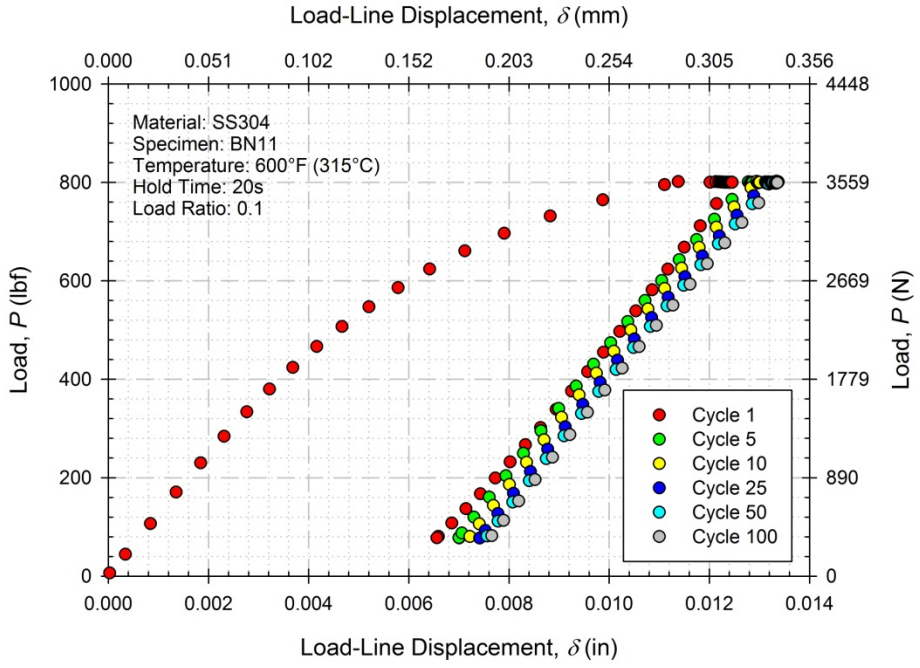

Figure 4.21: Example of the load versus load-line displacement for the first one hundred cycles of a specimen, BN11, in Fig. 4.20.

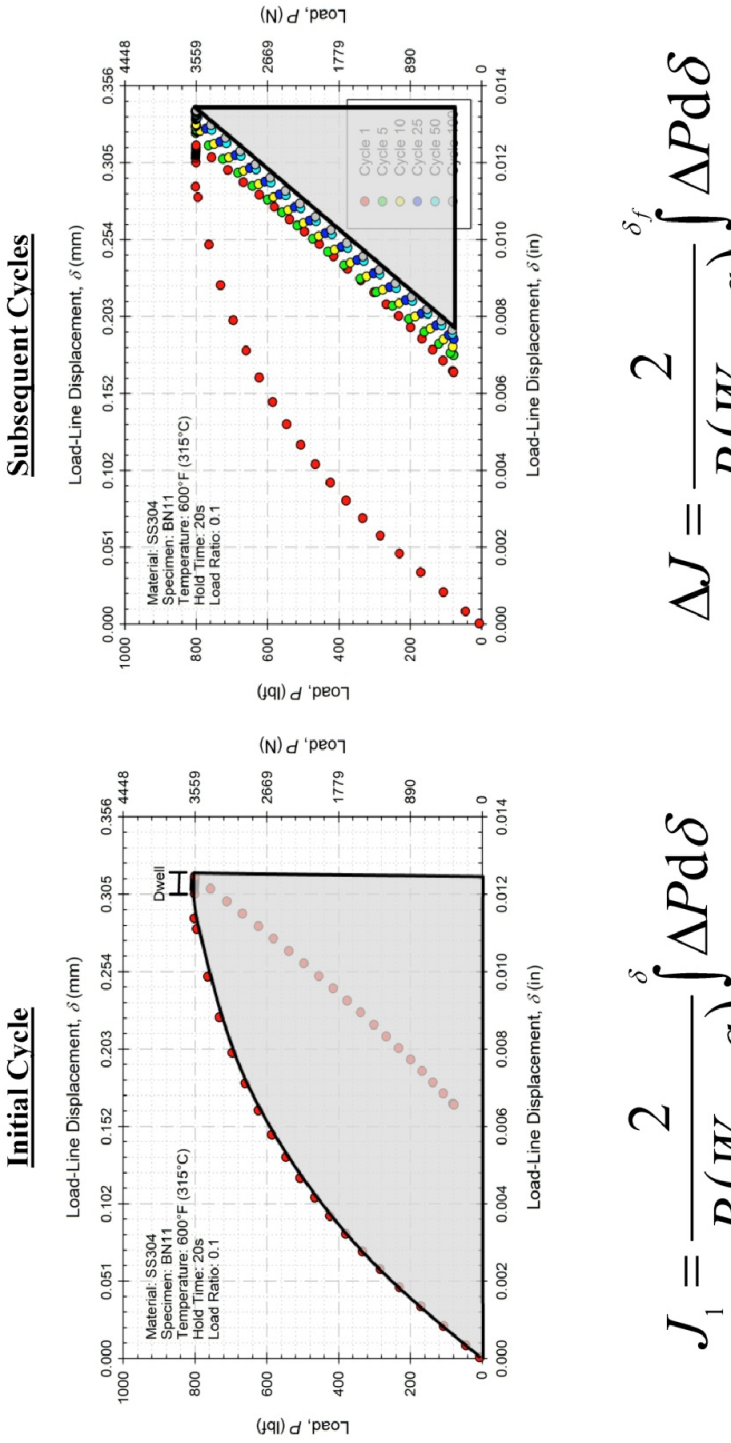

Figure 4.22: Method of calculating J_1 and ΔJ for C(T) specimens, based on method of [Dowling and Begley, 1976].

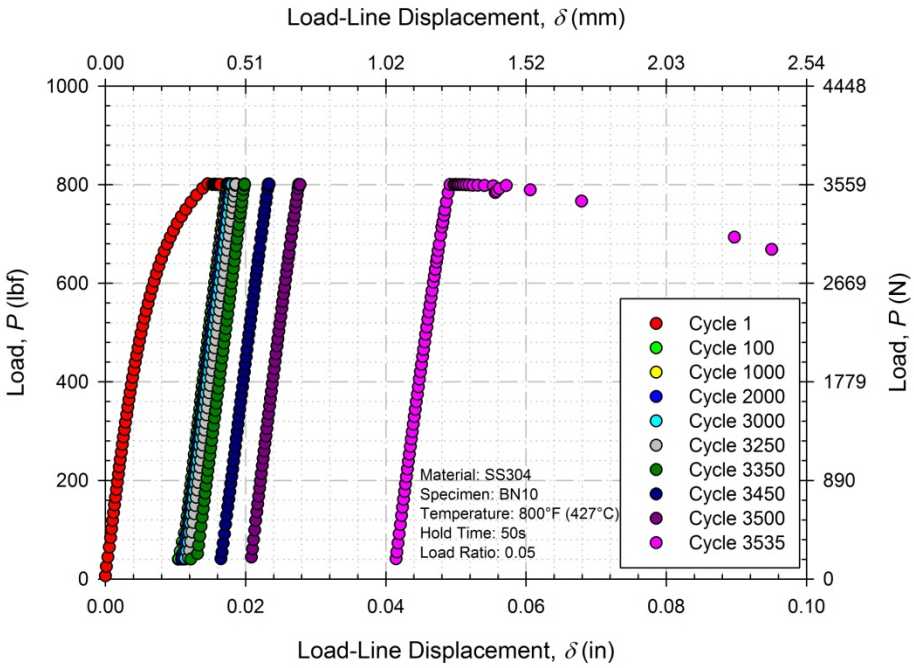

Figure 4.23: Example of the load versus load-line displacement for the entirety of a test during CFCIG experiments, with data from BN10 with 50s tensile hold.

Maximum load-line deflection versus cycle number for a selected specimen is provided, shown in Fig. 4.24. During the initial 50-100 cycles, all softening of the material is completed and stable cycling continues until later stages of the specimen life. All specimens displayed a similar behavior, with initial softening, a stable region and then growth due to the extension of cracks and plasticity. Increases in the load-line deflection observed in all test specimens were assumed to be attributed to relaxation of the material in early cycles and general plasticity/overload in late life cycles, which is to be confirmed via microscopy in Section 4.3.5. The maximum load-line deflection was subsequently used in select crack initiation prediction methods, outlined in the following section, as it provided for a convenient and stable platform for such methods.

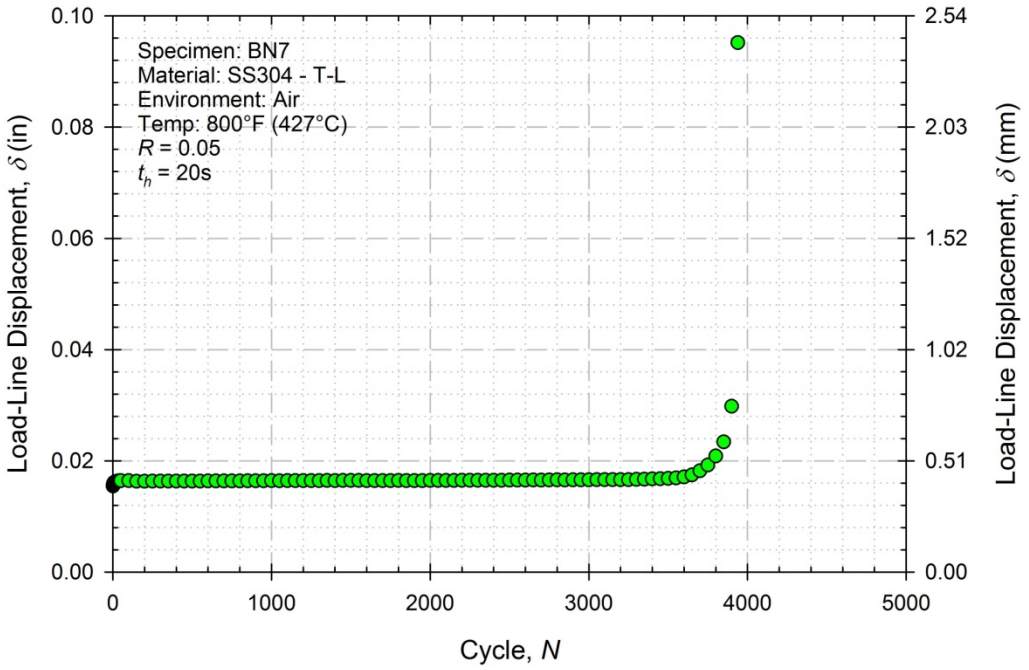

Figure 4.24: Example of the maximum load-line deflection versus cycle for an entire test, e.g. BN7.

Crack lengths were monitored via the DCPD system developed during the course of the investigation, as outlined in Chapter 3. Upon the initiation of a crack, the drop in potential voltage as the crack grew was observed and related to the crack length using ASTM standard methods, as shown in Fig. 4.25. Cracks are observed to propagate in a linear fashion for the first several hundred cycles of crack growth, during which plane-strain conditions are expected. Subsequently, cracks were observed to grow in a nonlinear fashion, during which plane-strain conditions were not expected, necessitating the use of EPFM parameters. All specimens detailed within this investigation displayed identical behavior, providing confidence in the crack monitoring system.

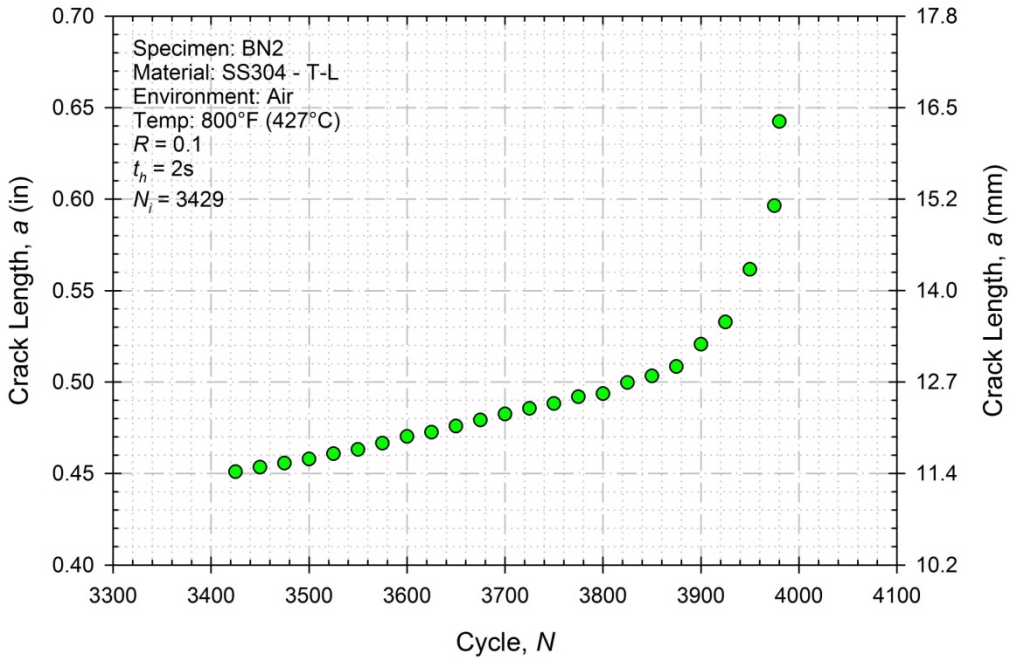

Figure 4.25: Example of the crack length as a function of cycle count, calculated from the DCPD monitoring system.

Loss of specimen data was uncommon during the experimental investigation; however, approximately 3-4 tests and data sets were compromised and unable for analysis. One particular case, while conducting the experiment on BN16, a power loss occurred 3.5 days into the test. This resulted in a loss of communication between the controller and load frame, subsequently placing the specimen under a compressive load of 850lbf (3.78kN). Upon restoring communication and resetting the software, the CMOD displacement was less than the last recorded cycle prior to power failure, leading to the decision to disqualify the data, as the cyclic plasticity was reversed based on the large compressive force. The choice to avoid conducting a replica of BN16, as well as conducting BN12, was made in favor of the additional tests at the conditions for BN19 and BN20. As the saturation of the first cycle J was observed, to be outlined in the following section, it was argued that a similar trend would be observed for the

longer tests and data would be more useful aimed at capturing the effect that a load rise-hold time ratio of 1 would have on the life of specimens.

4.3.3 Crack Initiation Results

The initiation of cracks is typically dependent on the type of test being conducted and the initiation criterion, e.g. [Piques et al., 1986; Davies, 2009; Lazzarin et al., 1997]. For this investigation, cracks were determined to be initiated using three different criteria. The methods included (1) observing a 10% increase in the CMOD gage displacement or a 10% drop in the DCPD monitoring system, (2) bisection of the steady-state and unstable slopes in the CMOD displacement and (3) bisection of the steady-state and unstable slopes in the derivative of the CMOD displacement with respect to the change in cycle count. Individual methods of determining the initiation life are presented in further detail, with the results of the each method provided in Table 4.5. Upon initiation, a crack of 0.001in (0.025mm), in addition to length of the initial notch of 0.450in (11.43mm), was the assumed crack length which subsequent crack propagation predictions would use as the initial crack length. The arbitrary length was chosen for this investigation, as it provided a lower asymptotic value for Stage I crack growth and subsequent predicted crack growth rates aligned with experimentally obtained crack growth rates, as viewed on fracture surfaces during post-mortem fractography.

Table 4.5: *Crack initiation life based on the three individual initiation criteria.*

Specimen	N_i 10%	N_i 20-10	N_i 50-20
1	4950	5588	5237
2	3450	3650	3429
3	4275	4767	4480
4	4825	4803	4474
5	3025	3189	2970
6	2675	4002	3777
7	3575	3612	3388
8	2825	2892	2692
9	3450	3663	3425
10	3275	3252	3025
11	5275	5454	5080
13	5787	6185	5794
14	5025	2791	5443
15	4925	5192	4820
17	3025	3183	2969
18	4425	5276	4910
19	2625	3068	2860
20	4875	5435	5089

Crack initiation based on a 10% increase in the CMOD displacement or 10% decrease in the DCPD reading was the most straightforward crack initiation criterion. By plotting the CMOD or DCPD reading over the entirety of the test, a 10% increase or decrease, respectively, was readily calculated, as shown in Fig. 4.26. The value at which the initial reading was taken corresponded to the reading at cycle 50 for each test. This provided a stabilized reading, as the displacement and voltage readings had reached a steady-state value, after initial softening of the material had completed. From there, once a 10% increase or decrease was observed in either of the signals, cracks were assumed to be initiated, with the results provided in Table 4.5.

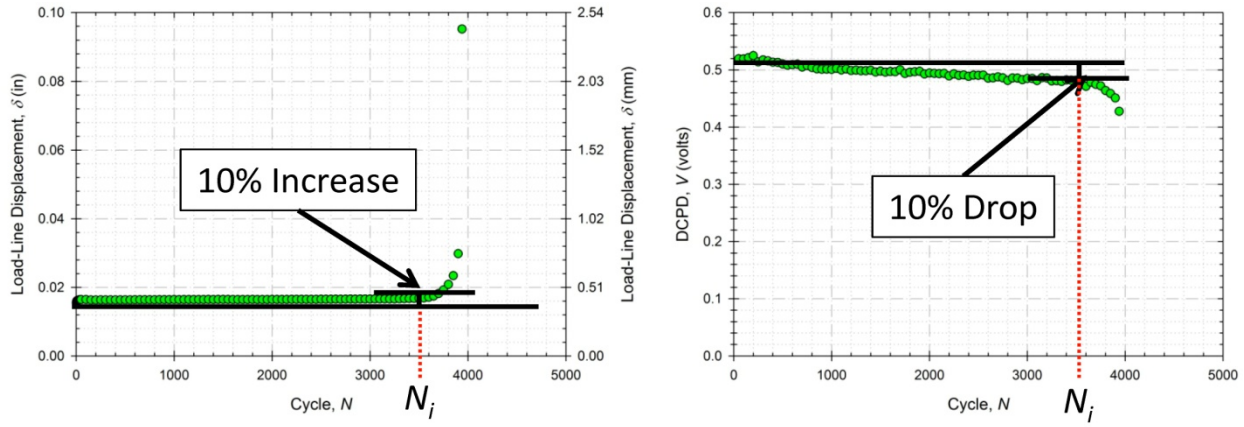

Figure 4.26: Example of crack initiation determination based on a 10% increase or decrease of the CMOD or DCPD measurement, respectively.

The remaining two crack initiation methods involved the use of a bisection method that fit straight lines to the slope of the steady-state and unstable portions of a measurement reading. The two generated lines would then intersect at a particular point, creating an angle between the two lines. This angle was then bisected with a third line that would bisect the previous angle in half and intersect the experimental data curve. The corresponding cycle at which the third generated line intersected the data was then the cycle at which crack initiation was assumed. An example of this method is provided, shown in Fig. 4.27. The two measurements that utilized this method were the CMOD gage displacement and the derivative of the CMOD gage displacement with respect to the change in cycles. Results based on this criterion for both the bisection of the steady-state and unstable slopes in the CMOD displacement and bisection of the steady-state and unstable slopes in the derivative of the CMOD displacement with respect to the change in cycle number are provided, Table 4.5.

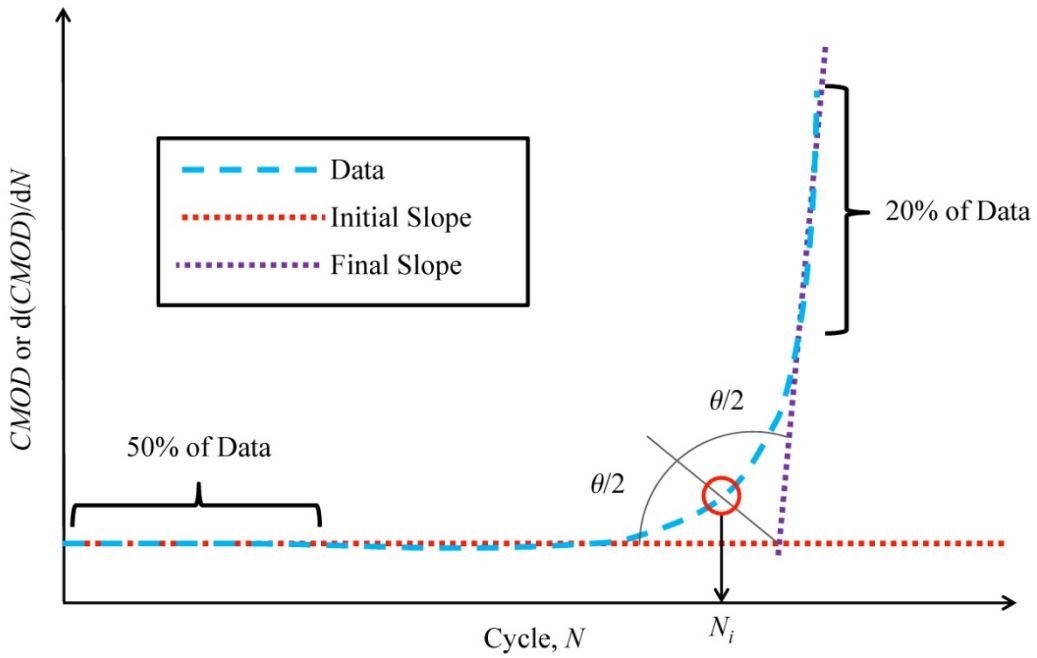

Figure 4.27: Example of crack initiation determination based on the bisection method utilizing the slopes of the steady-state and unstable portions of the (left) CMOD gage displacement or (right) the derivative of the CMOD gage displacement with respect to the change in cycles.

Determination of the initiation criterion to be used involved the comparison of the assumed crack initiation cycle with the total number of cycles to failure. Using a goodness of fit regression, regression lines were generated for each crack initiation scenario, with results provided in Fig. 4.28. It was observed that the method of crack initiation involving the derivative of the CMOD gage displacement with respect to the change in cycles provided the most consistent relationship between approximated crack initiation cycles and the number of cycles to failure. Failure was assessed to be the cycle at which ductile tearing dominated and maximum load-line deflection was observed in the CMOD gage. Based on these results, crack initiation was based on the bisection method of the derivative of the CMOD gage displacement with respect to the change in cycles, subsequently labeled the *dCMOD* method.

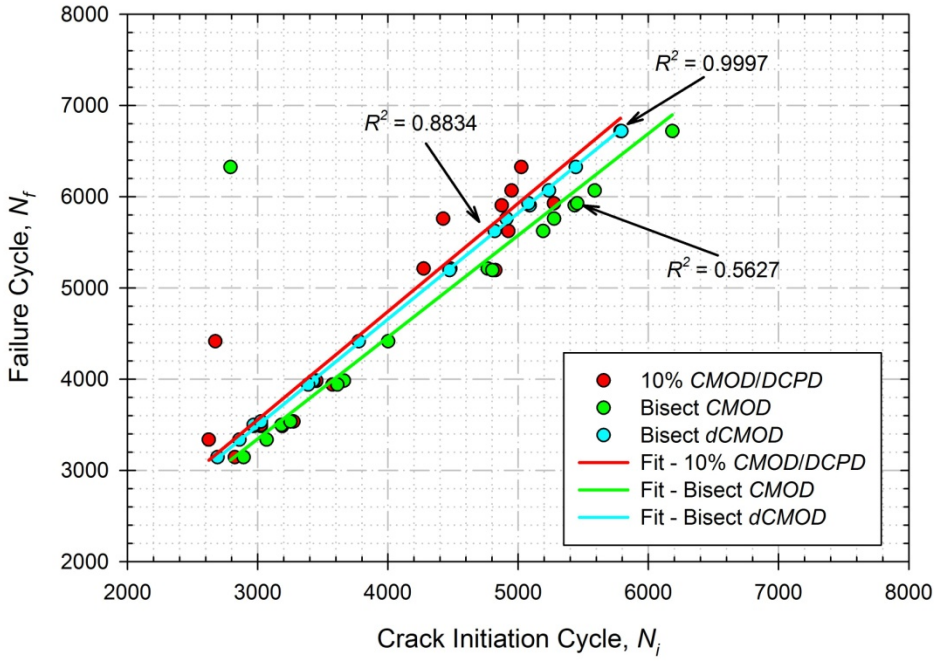

Figure 4.28: Comparison of the crack initiation cycle to failure cycle for all specimens using the three different crack initiation criterions.

Saturation of the approximated value of J for the first cycle, J_1, was observed based on the tensile hold period, with the exception of one outlier, as shown in Fig. 4.29. As the hold time in experiments was increased, the minimum value of J_1 was observed to trend higher towards an upper limit, which is dependent on the maximum load of tests and the extent of relaxation of the material during the initial cycle hold period. The identification of an upper limit suggests that accelerated experimental routines, in which abbreviated hold periods are used to replicate longer exposure times in service, can be developed. By identifying an upper limit, investigators are able conduct experiments in which excessively long hold periods can be avoided. This results in the ability to conduct shorter tests, driving the financial burden of testing down, potentially leading to additional testing being conducted with additional parameters of interest.

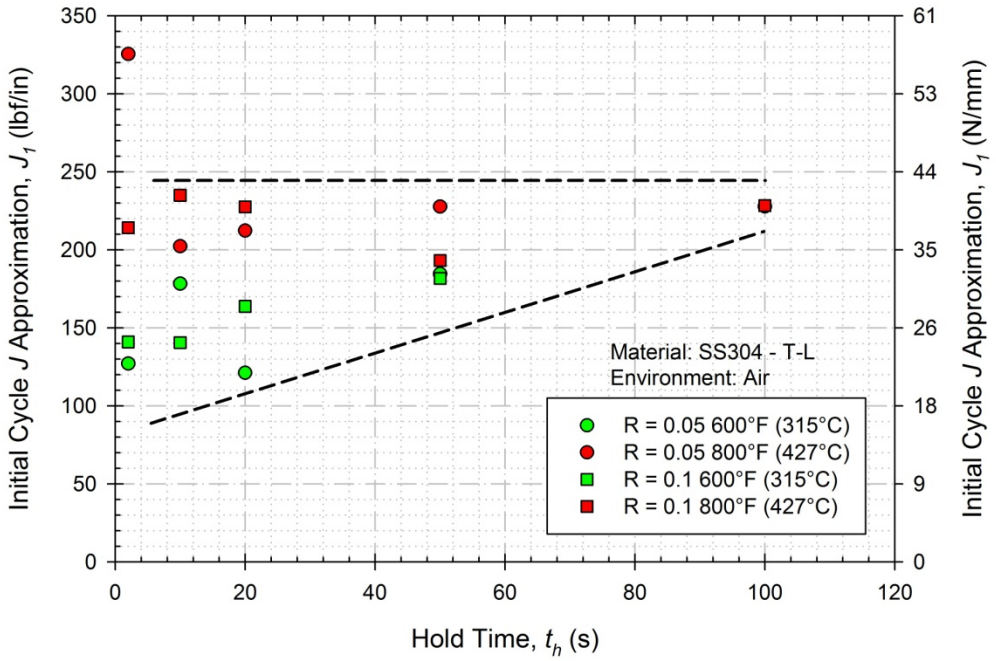

Figure 4.29: Saturation of the calculated *J* for the first cycle based on the tensile hold period during experiments.

The saturation of a consistent J_1 for the two temperatures is apparent in Fig. 4.29. The tests conducted at a higher temperature have a higher level of saturation, as well as a higher initial J_1 approximation. Temperature dependency can be argued; however the increased J_1 approximation for identical conditions outside of temperature could also be used to account for the temperature dependency without explicitly including a temperature-based component. The saturation is expected to be dependent on the level of *J* imparted on the specimen, therefore a few exploratory tests would be necessary to determine the saturation limit; however, once it is defined, subsequent experiments can utilize the existence of the upper limit.

In the case of the outlier, BN19, a higher-than-expected first cycle load was imparted, due to a software malfunction in relation to the PID controls. The maximum load imparted on this specimen was visually observed to exceed the desired 800lbf (3.56kN); however, the software did not capture the value in the exported data. With this data point removed, the

saturation is still expected for the particular load case employed in this investigation, as all other specimens indicate such a plateau observed.

Crack initiation was observed to be primarily dependent upon the load ratio, R, and approximated value of J approximation for the first cycle, J_1, as shown in Figs. 4.30 and 4.31. As the load ratio increased from $R = 0.05$ to $R = 0.1$, the number of cycles required to generate a crack increased, as in Fig. 4.30. Temperature appears to have an effect on the number of cycles to crack initiation; however, as with the saturation of J_1 in Fig. 4.13, the value obtained for J increases at the higher temperature, therefore taking into account the temperature dependency, as shown in Fig. 4.31. A larger load ratio implies a smaller stress range at the notch tip, thus a larger number of cycles is expected to generate a crack. Essentially, this relates back to the traditional S-N or ϵ-N diagrams for fatigue life analyses, in which smaller ranges result in longer lives of components. Ignoring the mean stress effect, as little difference in the initial cyclic J value is observed, this is the effect that is observed within the initiation lives, with respect to the load ratio.

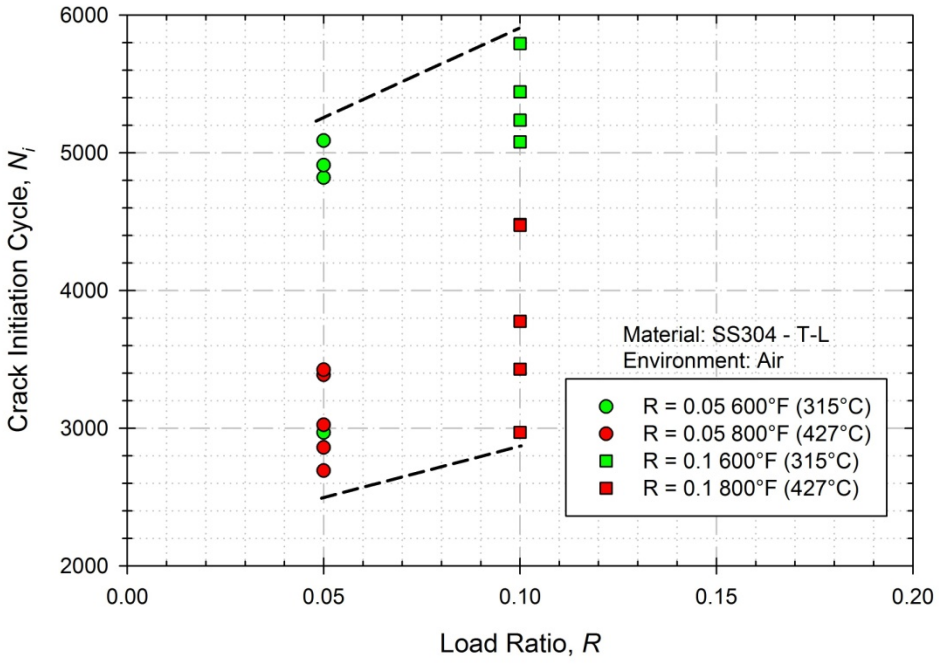

Figure 4.30: Load ratio effect on the crack initiation, in which the lower load ratio produced a shorter life to crack initiation.

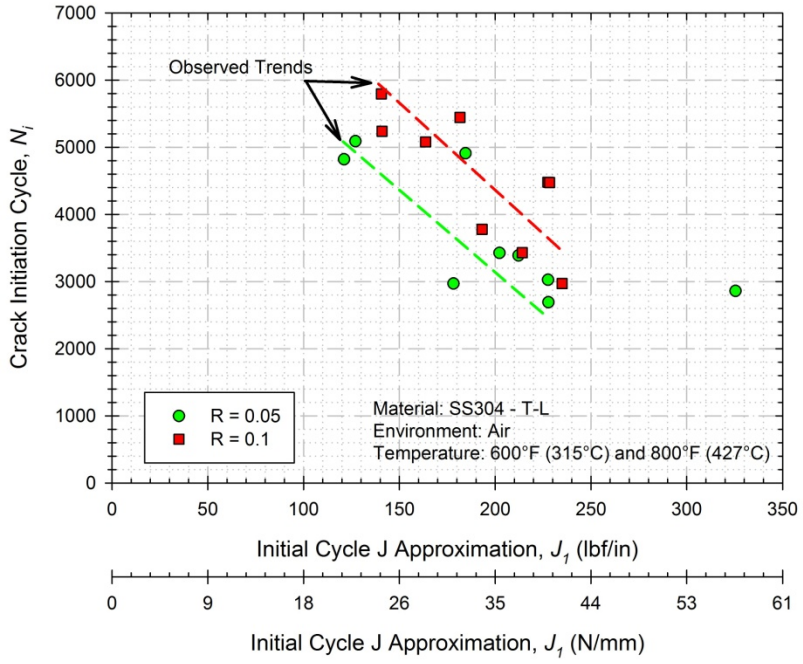

Figure 4.31: Crack initiation based on the calculated J for the first cycle at the two load ratios implemented in experimental routines.

When comparing the approximated value of J for the first cycle to the number of cycles to crack initiation, an increase in the load ratio results in a larger J approximation for the same number of cycles at the lower load ratio, as in Fig. 4.31. A trend is also reported, as shown as a solid line, representing the observed behavior in regards to the number of cycles to crack initiation. The approximation of J_1 depends upon the specimen, the measured displacement, the load and the hold time. Regarding the values reported within Table 4.2 for the experimentally obtained J_1 value, the numerical results are within expectation. Experimental values of J_1 are observed to be greater than numerical predictions, as numerical simulations did not incorporate a hold time. By incorporating a more complex material model into numerical simulations, the hold time effects can be accounted for and values of J_1 are expected to correlate very well with experimental data.

An additional test that replicated the conditions of BN17 was conducted with a load ratio of R = 0.4; however, the test was interrupted prior to crack initiation. Test conditions were identical to BN17, i.e. 600°F (315°C) with a hold time of 10s; however, after completing 5,880 cycles, no crack initiation was observed. Using all three methods to determine crack initiation were unsuccessful, as the load-line displacement at cycle 1427 and 5880 was approximately 0.0103in (0.2616mm). The lack of crack initiation within this specimen confirms the assertion that as the load ratio decreases, the number of cycles to crack initiation decreases, as a result of the lower cyclic stress-strain range. Further analysis regarding this specimen is provided in Section 6.2.

Combined, the initial J approximation, J_1, and the load ratio, R, at which tests were conducted were observed to have a significant impact on the number of cycles to crack initiation.

4.3.4 Crack Propagation Results

Propagation of cracks from the assumed initial length of 0.451in (11.45mm), as determined in the previous section, was observed at various rates due to a variety of factors. Main factors affecting the rate at which cracks propagated include the temperature, load (or stress) ratio and the characteristics of the load waveform. Crack growth rates were intended to be calculated based on the incremental polynomial fitting routine developed and outlined in Section 3.7 utilizing ΔJ; however, the alternative secant method furnished in ASTM E647 was utilized [ASTM E647-08$^{\varepsilon 2}$]. The deviation from the incremental polynomial fitting method was necessary, as the limited amount of crack growth exhibited in the specimens resulted in the polynomial routine providing ΔJ values much lower than experimentally observed values. As such, the secant method was employed, more accurately capturing the crack growth per cycle based on the experimentally obtained ΔJ values.

Late stage crack growth rates, within the last 50 cycles of a given test, are likely to be reported at slower rates than actually observed within the specimens. Limited by the software at which data acquisition rates would successfully capture data, some specimens had 30-40 cycles between the failure cycle and the previous complete cycle data point. In this event, the curvature of the crack growth curve in Stage III growth does not have the typical asymptotic behavior, as the secant method averages growth over the period between measurements. Experimental data which had 5-10 cycles between the failure cycle and previous cycle show the typical behavior, validating the claim that the behavior is as expected, but underreported due to the software sampling limitations. More information regarding this behavior will be discussed in Section 5.2.2.

The following sections will highlight the crack growth rates of various specimens at the different test conditions. Experimental data will be duplicated in each section, based on the experimental test condition being presented. Subsequent observations regarding the behavior of the material and experimental test conditions not directly related to the highlighted test condition will be presented as a summary. All experimental data, including the load waveform, rise time and hold time conditions, and individual crack growth curves, is provided in Appendix C.

4.3.4.1 Temperature-Dependency of Crack Growth Rates

Cumulative crack growth curves, based on growth per cycle, at 600°F (315°C) and 800°F (427°C) are provided, as shown in Fig. 4.32. A total of 18 specimens are represented, with 8 experiments at 600°F (315°C) and 10 experiments at 800°F (427°C). Crack growth curves are presented without regard to the load ratio or the tensile hold period.

As in standard fatigue crack growth experiments, the temperature is expected to result in an increase in the crack growth rates, as in [James and Schwenk, 1971; ASM, 1986]; however, no definitive distinction between the two temperatures is apparent when utilizing EPFM parameters. This is attributed to the similarity in behavior at the two test temperatures and the change in maximum load that each test temperature was conducted at, in which the lower temperature tests had a higher maximum load. Maximum loads were chosen for each temperature in a manner that would result in similar notch tip conditions for all specimens, irrespective of temperature. By providing a consistent notch condition regardless of temperature, it was expected that the influence of other crack growth rate modifying parameters would be exaggerated.

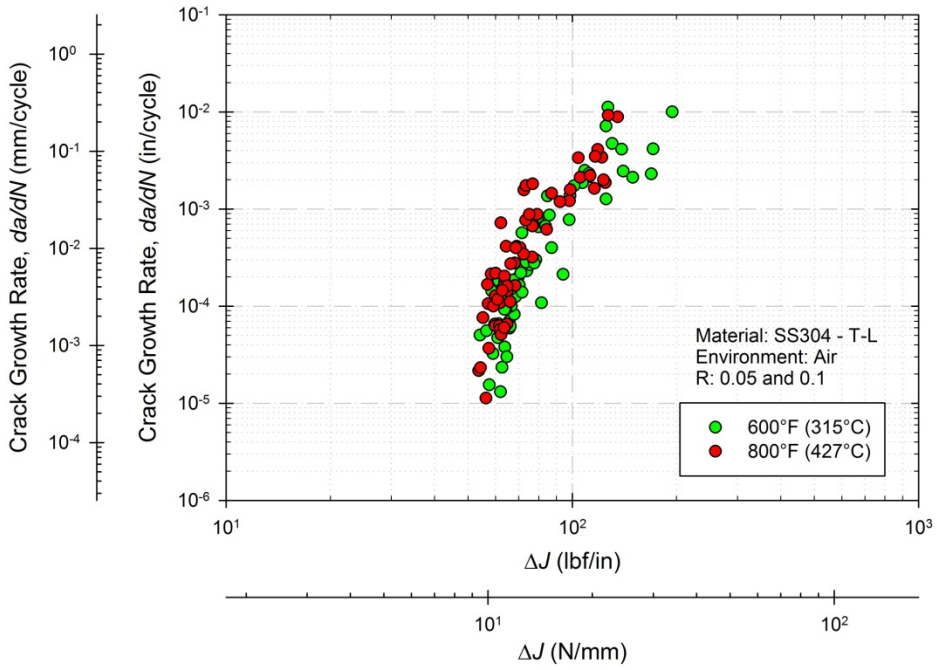

Figure 4.32: Crack growth rate curves at 600°F (315°C) and 800°F (427°C).

4.3.4.2 Load Ratio Effect of Crack Growth Rates

Cumulative crack growth rate curves, based on growth per cycle, at load ratios of 0.05 and 0.1 are provided, as shown in Fig. 4.33. A total of 18 specimens are represented, with 9 experiments cycled at *R* of 0.05 and 9 experiments cycled at *R* of 0.1 load ratios. Crack growth curves are presented without regard to the test temperature or the tensile hold period.

Irrespective of the temperature, hold time or rise time, as the load ratio was increased, the trend was that the crack growth rate curve shifted left, resulting in a lower ΔJ required to grow cracks at the same rate. This effect was expected, as the rate of crack propagation has been experimentally proven to be dependent on the load ratio implemented during testing relating back to the amount of crack closure, e.g. [Forman et al., 1967; Elber, 1971; Yamada and Newman, 2009]. The small increase in load ratio, which related to approximately a 40lbf (178N) difference in minimum loads, was large enough to observe the effect the load ratio has on crack propagation rates subjected to the load waveforms implemented in this study. The difference in

crack growth rates based on the load ratio necessitates that the proposed model has a dependency on the load ratio, used to accelerate crack growth rates at higher load ratios.

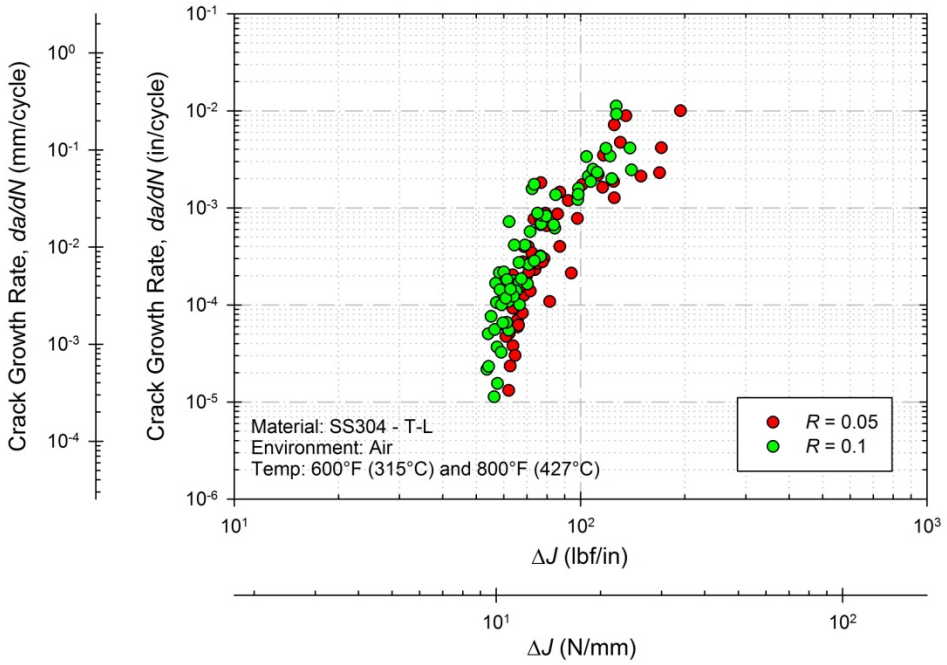

Figure 4.33: Crack growth rate curves for load ratios of $R = 0.05$ and $R = 0.1$ at both test temperatures.

4.3.4.3 Rise Time and Hold Time Dependency on Crack Growth Rates

Cumulative crack growth curves, based on hold time, conducted at both temperatures are provided, as shown in Fig. 4.34. A total of 18 specimens are represented, with 4 experiments incorporating a tensile hold period of 2 seconds, 4 with a tensile hold period of 10s, 4 with a tensile hold period of 20s, 4 with a tensile hold period of 50s and 2 with a tensile hold period of 100s. Crack growth curves are presented without regard to the test temperature or the load ratio.

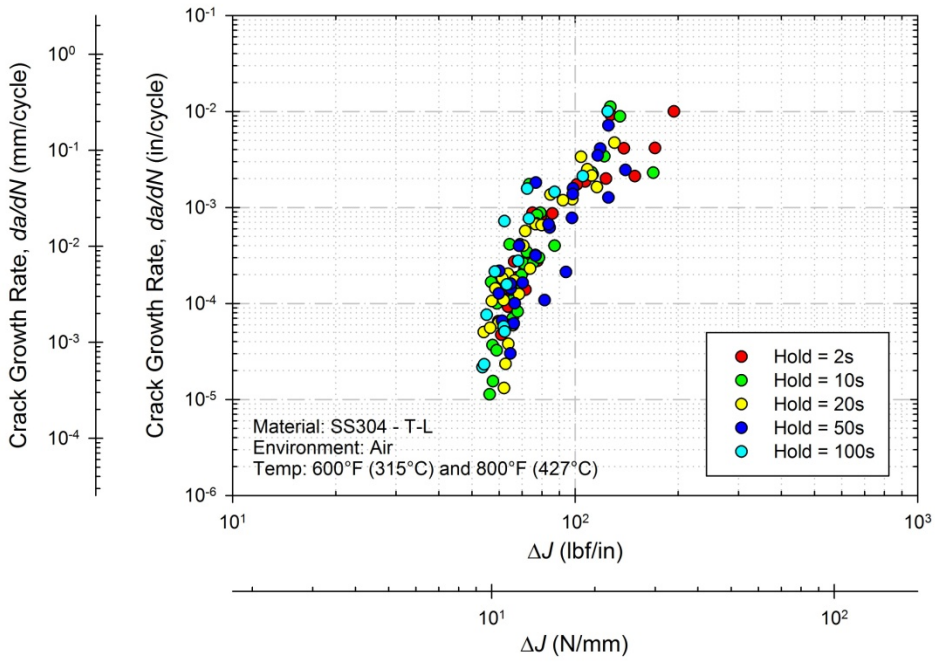

Figure 4.34: Crack growth rate curves based on the duration of a positive tensile hold period for both test temperatures.

Inspection of the crack growth curves based on the positive tensile hold yields little to no clear differentiation between the data sets. Initially, it was thought that the temperatures and the loads would result in accelerated crack growth rates for longer hold periods, in terms of growth per cycle, which would be clearly discernible. The affect of hold time on the creep-fatigue crack growth rates was expected to shift the curves to the left, similar to the affect raising the load ratio, R, has on crack growth rates. A proposed explanation is that the method of calculating ΔJ, based on integrating the load versus load-line displacement, readily captures the affects of hold time, as any additional displacement due to longer hold times is captured by the bounds of the integration. The total area under the curve is calculated, thus taking additional displacements due to hold period crack extension into account.

In addition to the hold time-based crack growth rate curves, rates were inspected based on the ratio between the load rise and hold time, as shown in Fig. 4.35. Again, a clear distinction

between experiments with hold-rise time ratios of 1, 5 and 10 was not readily achieved. The lack of correlation is proposed to be similar to the assessment that the *J* calculation inherently includes the affects of hold time on the crack growth rates. Any notable affects based on the rise-hold time ratios are accounted for in the calculation of *J* and remains dependent on the applied load ratio.

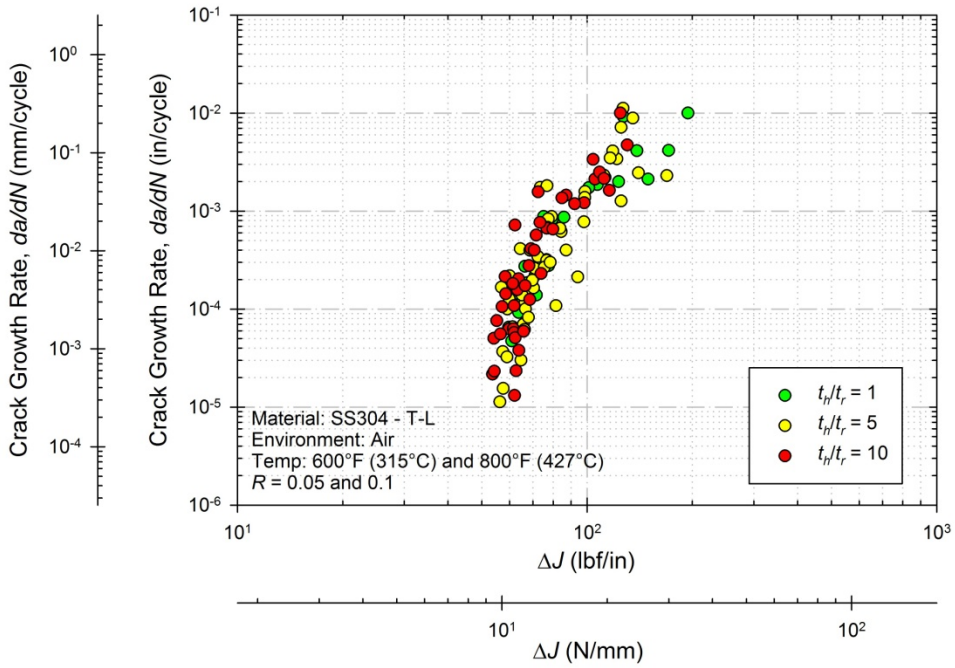

Figure 4.35: Crack growth rate curves based on the ratio of the load rise time to hold time.

4.3.5 Microscopy

Creep-fatigue specimens, including surfaces and through-thickness sections, were observed utilizing various forms of microscopy. General images of the overall specimen post-test were captured via the DinoLite and with a standard digital camera, whereas sectioned and polished samples were observed with the Leica metallurgical camera and fracture surfaces were viewed under the JEOL SEM. As such, the following microscopy results are divided into optical and scanning electron microscopy sections.

4.3.5.1 Optical Microscopy

Creep-fatigue specimens were viewed under various magnifications using both the DinoLite and Leica digital microscopes. Upon the completion of an experiment, specimens were photographed prior to separation and crack length measurements, as shown in Fig. 4.36. An overview of the crack profiles along the root of the notch, for all specimens, is provided, as shown in Fig. 4.37. Upon separation of specimens, fracture surfaces were imaged, with an overview of all specimens provided in Fig. 4.38.

Large scale plasticity was visibly noted in all of the test specimens, regardless of test temperature or hold time, with an example provided in Fig. 4.39. The presence of extensive plasticity serves to validate the large deflections measured by the CMOD gage throughout the duration a single test, as shown in Fig. 4.23. A majority of the deflection was obtained during the last cycle of the test, as the crack began to grow unstably into the ductile tearing regime. Cracks were not allowed to propagate through the entirety of the specimen width, as the experimental routine was set to stop upon reaching the physical limit on the CMOD gage, which in this case was 0.1in (2.54mm). After reaching the hardware limit, the test was completed, the load was removed and the furnace was turned off.

Prior to separation, several specimens were observed to have some extent of secondary cracking at the notch root, e.g. BN9 and BN18 in Fig. 4.37. A loose trend relating to the observed *J*-integral calculated for the first cycle was noted. Some specimens with a larger value of J_1 exhibited a singular dominant crack, e.g. BN5, whereas specimens with lower values were prone to multiple crack locations at the notch tip, e.g. BN15, as shown in Fig 4.40**.**

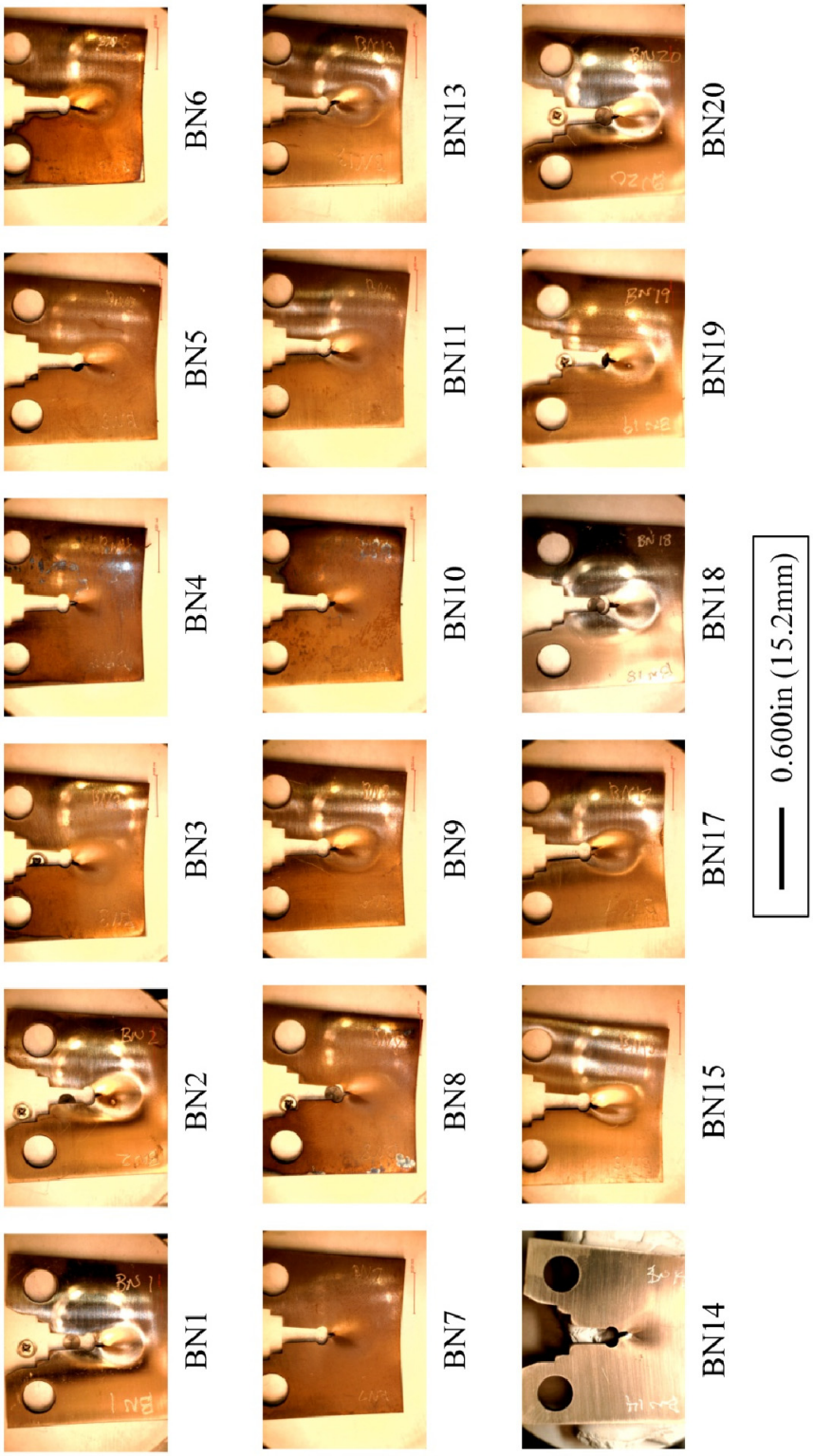

Figure 4.36: Overview of blunt notch C(T) specimen notch roots prior to separation of specimens.

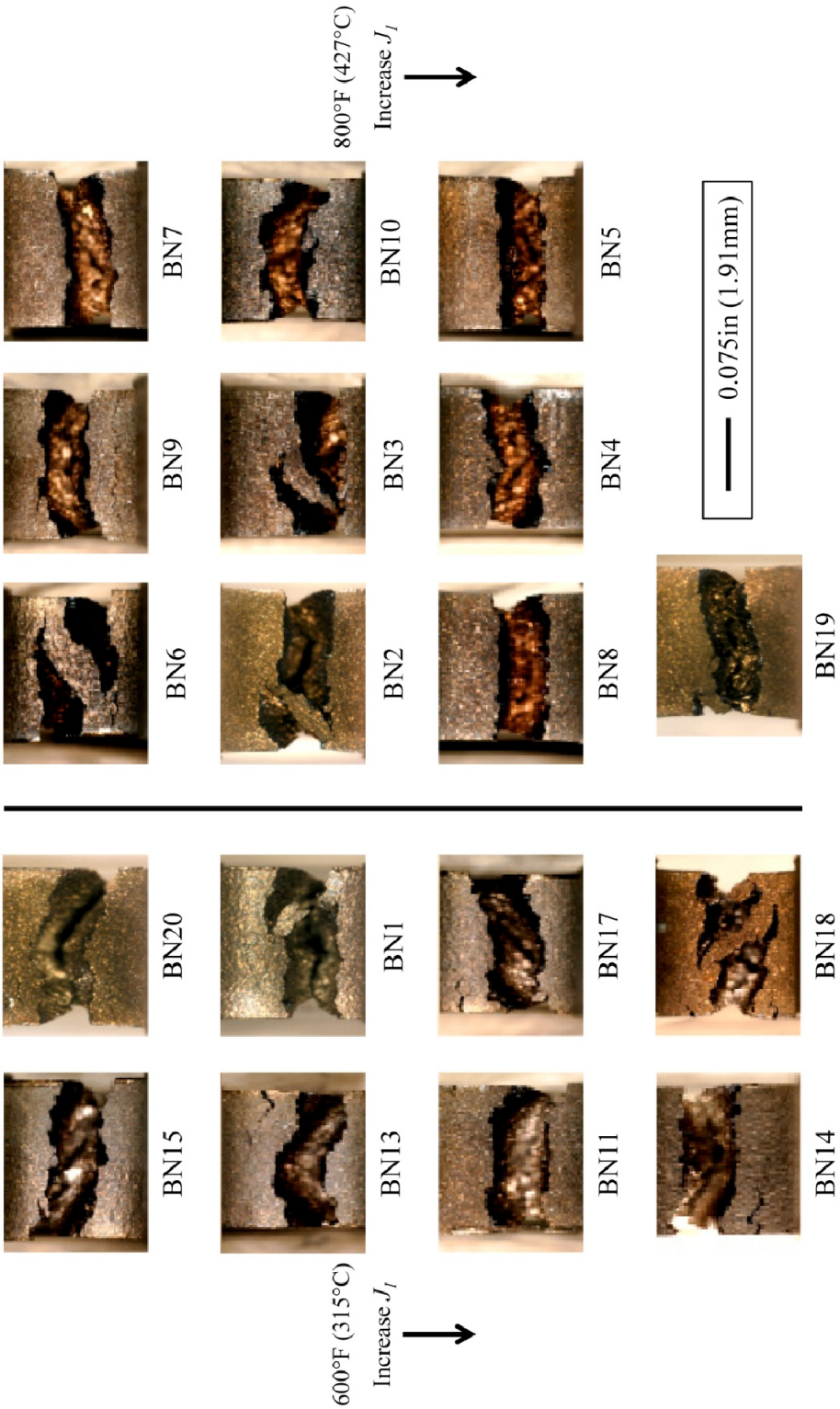

Figure 4.37: Overview of crack profiles for all blunt notch C(T) specimens prior to separation of specimens.

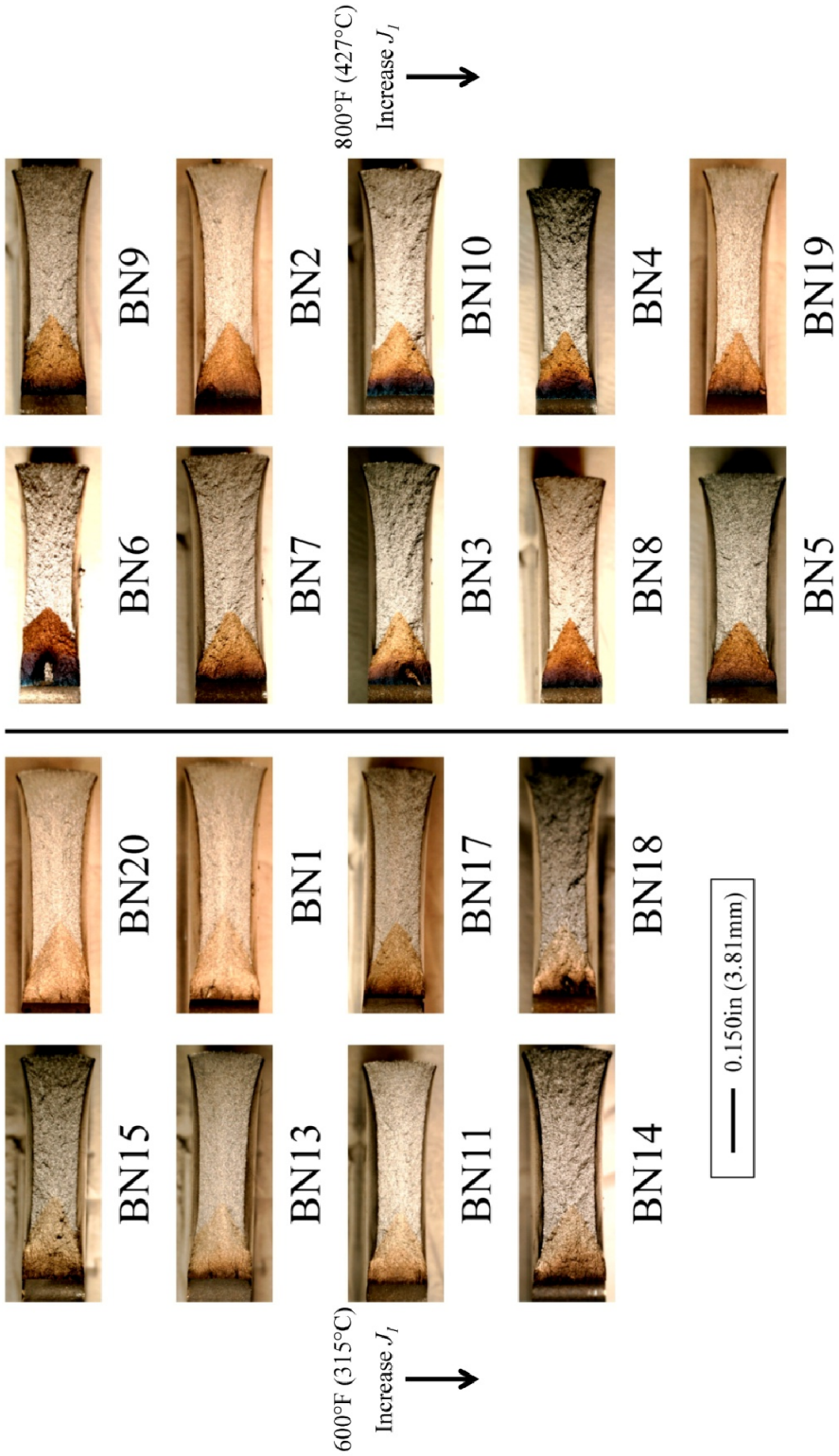

Figure 4.38: Overview of fracture surfaces of C(T) specimens upon separation of specimens

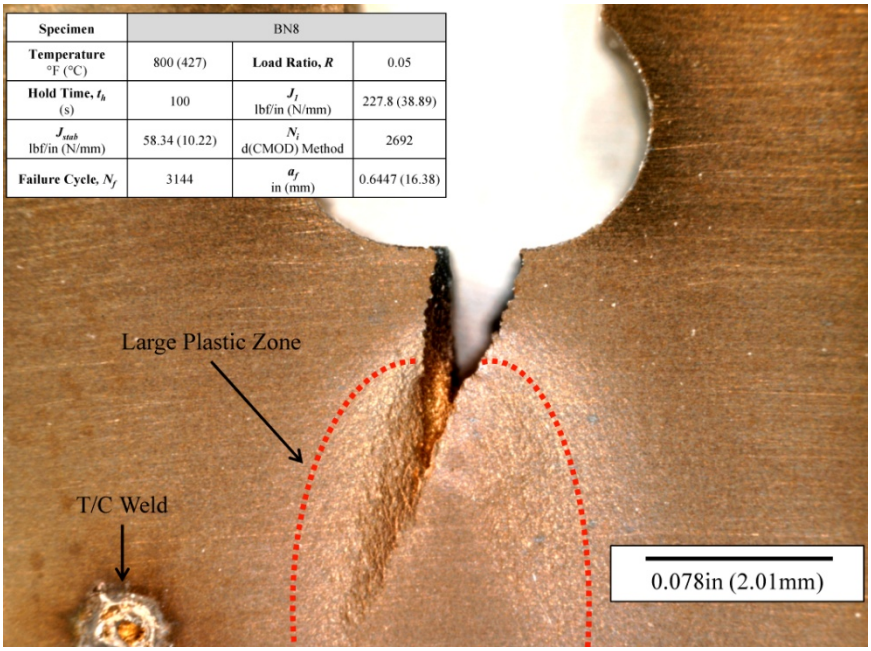

Figure 4.39: Example of the large scale plasticity observed during the duration of a single creep-fatigue experiment.

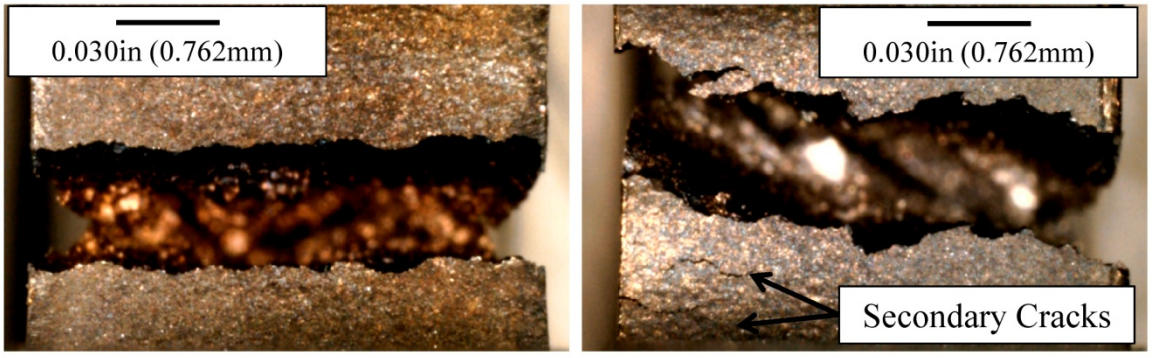

Specimen	BN5		
Temperature °F (°C)	800 (427)	Load Ratio, R	0.1
Hold Time, t_h (s)	10	J_I lbf/in (N/mm)	234.9 (41.12)
J_{stab} lbf/in (N/mm)	54.62 (95.65)	N_i d(CMOD) Method	2970
Failure Cycle, N_f	3485	a_f in (mm)	0.6337 (16.09)

Specimen	BN15		
Temperature °F (°C)	600 (315)	Load Ratio, R	0.05
Hold Time, t_h (s)	20	J_I lbf/in (N/mm)	121.1 (21.21)
J_{stab} lbf/in (N/mm)	60.40 (10.58)	N_i d(CMOD) Method	4820
Failure Cycle, N_f	5623	a_f in (mm)	0.6636 (16.85)

Figure 4.40: Extent of secondary cracking for a specimen with a (left) high initial *J*, as in BN5 and a (right) low initial *J*, as in BN15.

The calculation of *J* related back to the level of plasticity, as additional deflection in the load-line displacement due to plasticity. It is proposed that specimens with the higher value of initial *J* more evenly concentrated the stresses around the notch tip, resulting in a larger stress concentration at the root of the notch. By relaxing out the stress at other regions around the notch tip, sufficient conditions for crack initiated were focused directly at the root of the notch.

Separation of the specimens revealed the fracture surfaces and, upon viewing under the digital microscope, crack lengths were able to be measured. Due to the elevated temperatures, heat tints were highly visible for both 600°F (315°C) and 800°F (427°C), e.g. BN17 and BN9, respectively, shown in Fig. 4.41. Using the heat tint on the surface as a reference, crack lengths were readily measured, using the tip of the heat tint as the maximum length. Additionally, the heat tints served to validate the test temperatures at which tests were conducted, with color bands similar to those found in literature for the test temperatures used in this investigation.

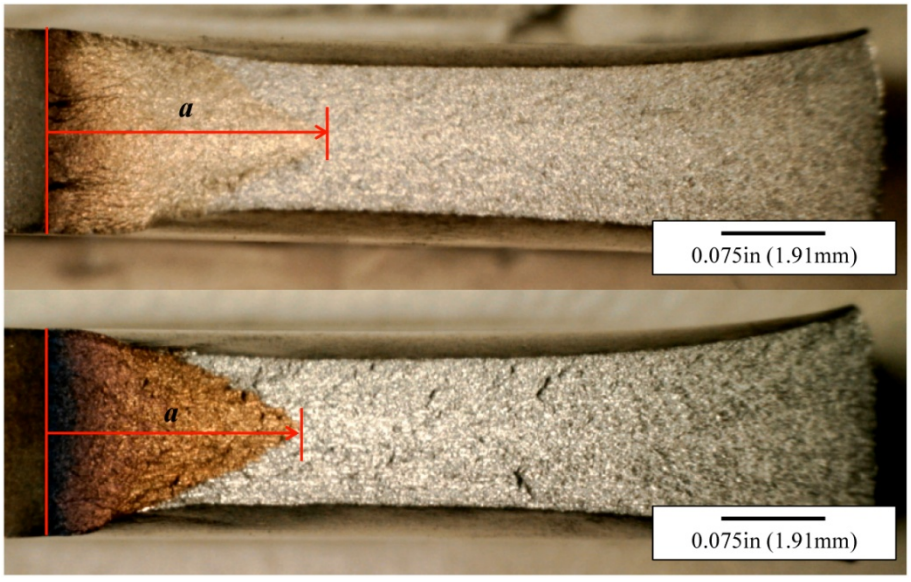

Figure 4.41: Heat tint observed on specimens exposed to (top) 600°F (315°C) and (bottom) 800°F (427°C).

Fracture surfaces within the heat tinted area, i.e. the region of crack initiation and propagation, were predominantly flat, with minimal deviation from the plane normal to load application. The absence of shear lips within this region provides evidence that plane strain conditions prevail at the notch tip and for the majority of crack propagation. A transition is readily observed, in that extensive shear lips dominate towards the end of life, as shown in Fig. 4.42. Although the specimen thickness violates the standard thicknesses outlined in ASTM standards for fatigue and creep-crack growth experiments, states of plane-strain crack growth are present. In the event EPFM crack growth data is unavailable, using the approximation of LEFM parameters from EPFM parameters, i.e. Eq. (3.4), is warranted for the current load and environment combination.

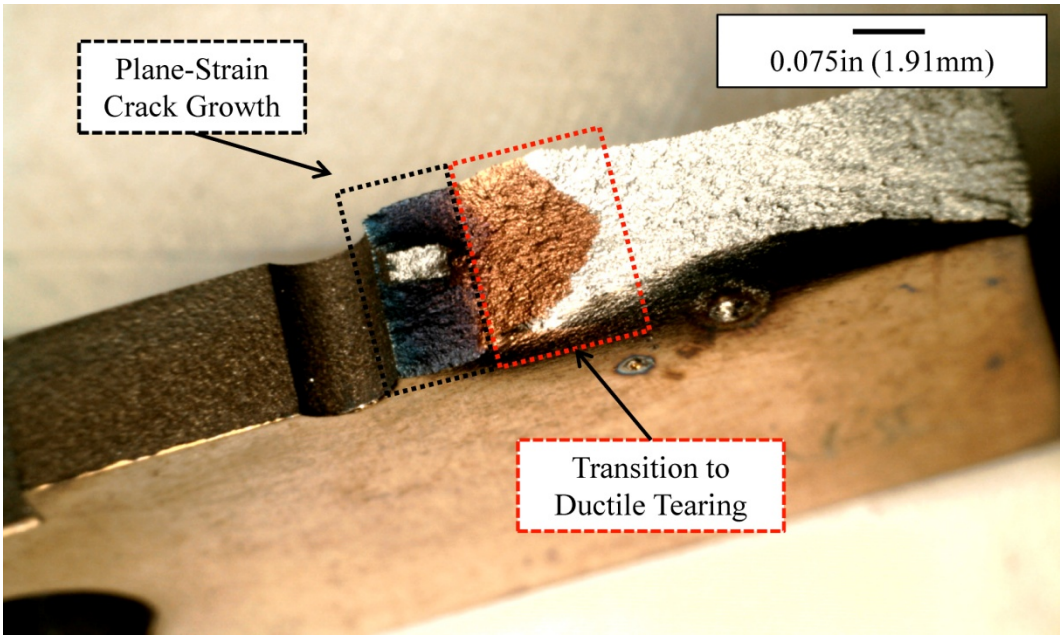

Figure 4.42: Transition from plane-strain crack growth to extensive plasticity and ductile tearing.

Selected specimens were sectioned through the thickness and subsequently mounted, polished and etched. Kalling's reagent, provided in Table 3.10, was the solution that was to be used to etch specimens; however, after immersion and submersion in the mix, no etching was achieved. Additionally, chromic acid (CrO_3) and electrical potentials (6V) were unsuccessfully employed. Ultimately, a final polish with a 1μm pad and oxide polishing suspension (OPS) successfully etched specimens, revealing grain structures consistent to structures observed in literature, e.g. Fig. 2.30, as shown in Fig. 4.43. Cracks were observed to initiate at the surface of the specimen, in the vicinity of the notch and no initiation was observed originating from carbide clusters.

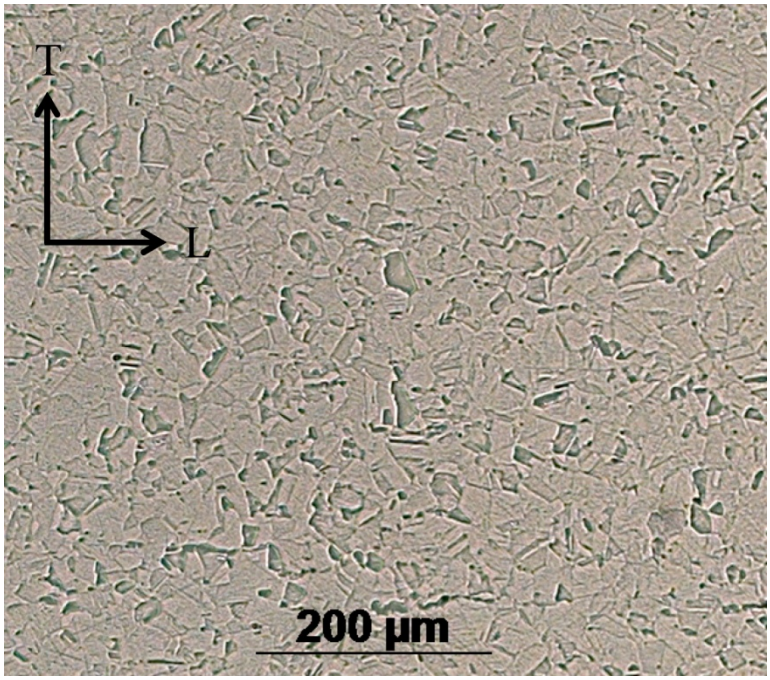

Figure 4.43: Grain structure of the subject SS304 used in this investigation.

As mentioned previously, several specimens had multiple crack initiation locations along the root of the notch, as observed in Fig. 4.37. One specimen, BN9, displayed a large crack through the thickness of the sample, penetrating approximately 0.39in (1mm) into the specimen, as shown in Fig. 4.44. More tortuous crack morphologies were observed, as in the case of BN3, with a section revealing additional secondary cracking at the notch, as shown in Fig. 4.45. The existence of secondary cracks was not limited to specimens with lower tensile hold periods, as tests conducted with holds of 100s revealed, to some extent, as shown in Fig. 4.46. The multiple cracks observed within the investigation are a result of the fatigue damage during tests and no measurable internal cracking, indicating significant creep contributions, was noted.

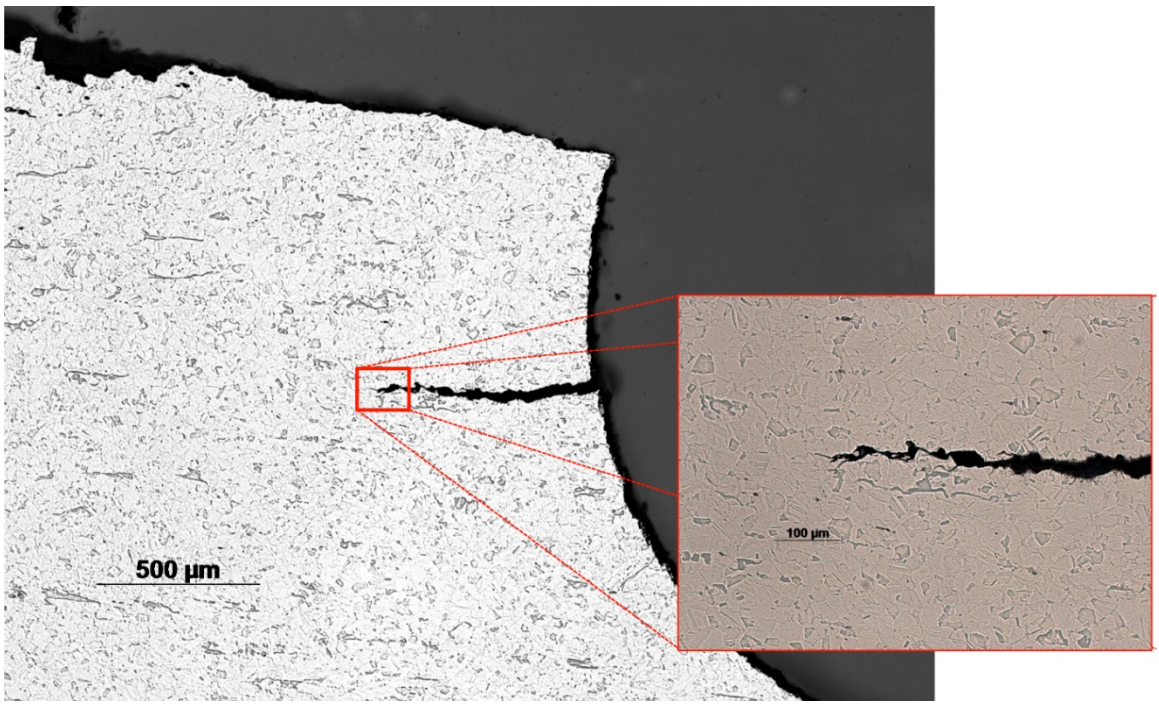

Figure 4.44: Large secondary crack observed in the notch root of specimen BN9, subjected to a temperature of 800°F (427°C) with a tensile hold period of 10s.

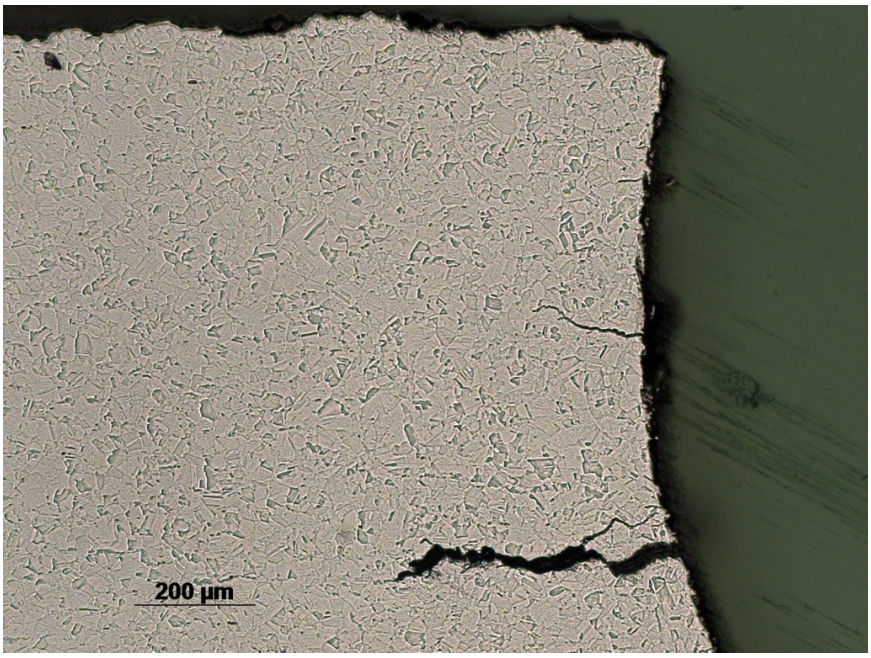

Figure 4.45: Competing dominant cracks observed near the center of the notch root in specimen BN3, subjected to a temperature of 800°F (427°C) with a tensile hold period of 20s.

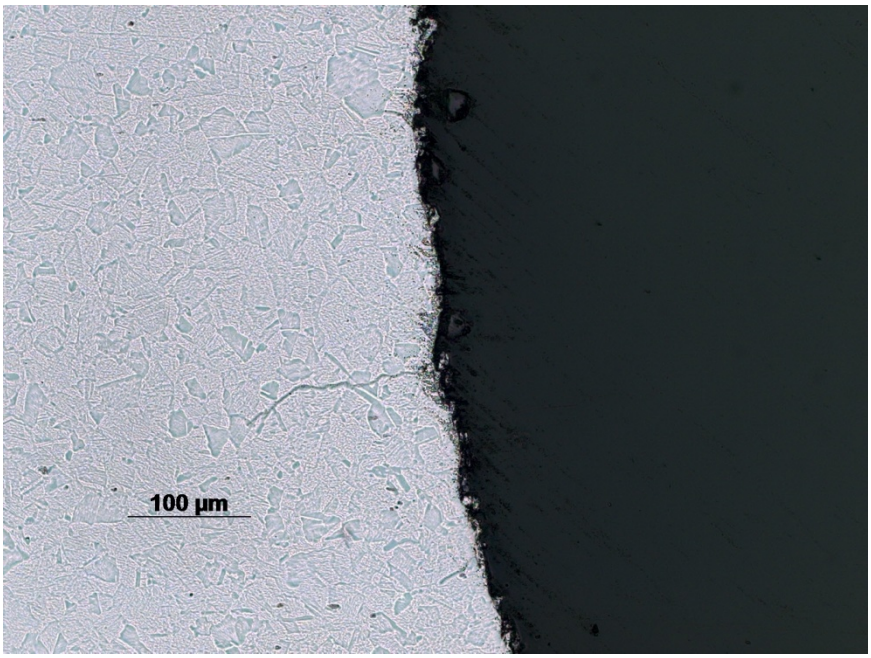

Figure 4.46: Secondary crack observed in the root of a notch for specimen BN8, subjected to a temperature of 800°F (427°C) with a tensile hold period of 20s.

Crack surface morphologies were mostly consistent along all specimens tested with various hold periods, as shown in Fig. 4.47. Dominant cracks were observed to result in surfaces that were perpendicular to the applied loading direction, as expected. Secondary cracking was observed in all cases along the surface of fracture specimens. As noted in the SFO experiments, no appreciable oxide layer was observed on either the main or secondary cracks. The temperatures employed within this investigation were not significant enough to contribute to either internal void or oxidation formation.

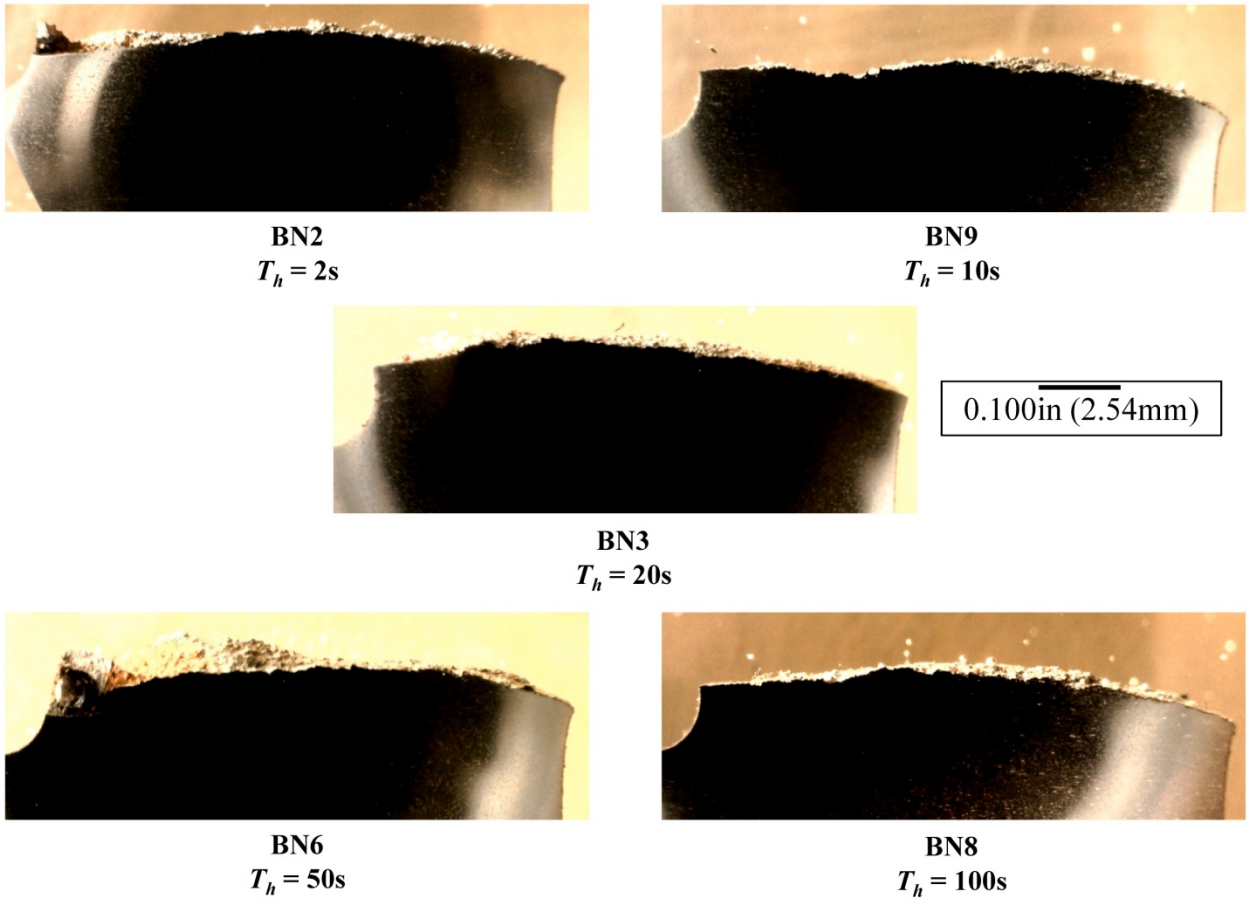

Figure 4.47: Crack surfaces of specimens tested at 800°F (427°C) with hold periods of 2, 10, 20, 50 and 100s.

From the optical microscopy, it was observed that the dominant failure mechanism, of all specimens, was due to fatigue-based processes. Cracks were observed to initiate at multiple locations along the surface of the notch; with no substantial subsurface cracking observed. The lack of internal voids and oxide formation on fracture surfaces, or any surface, eliminates the necessity to include such terms in the proposed crack initiation and propagation model of Chapter 5.

4.3.5.2 Scanning Electron Microscopy

Fracture surfaces of selected specimens were observed under the SEM, with primary goals of distinguishing the modes of fracture and observing striations as a result of the cyclic loading. An overview of fracture surfaces is furnished for temperatures of 600°F (315°C) and 800°F (427°C), shown in Figs. 4.48 and 4.49, respectively.

Major differences in the general appearance of fracture surfaces of specimens tested at the two elevated temperatures were not readily observed. The fracture surfaces, for all specimens in Figs. 4.48 and 4.49, exhibit flat surfaces near the notch where cracks were grown, as a result of the imposed creep-fatigue loading. As noted in the previous section, cracks were observed to initiate at the root of the notch in the desired location. In some cases, e.g. BN6, competition among crack initiation locations eventually lead to coalescence and one single dominant crack, with a large portion of material left in the wake of the dominant crack. Fatigue striations were observed on both the top and underside of the flakes, with striations of equal spacing, as shown in Fig. 4.50.

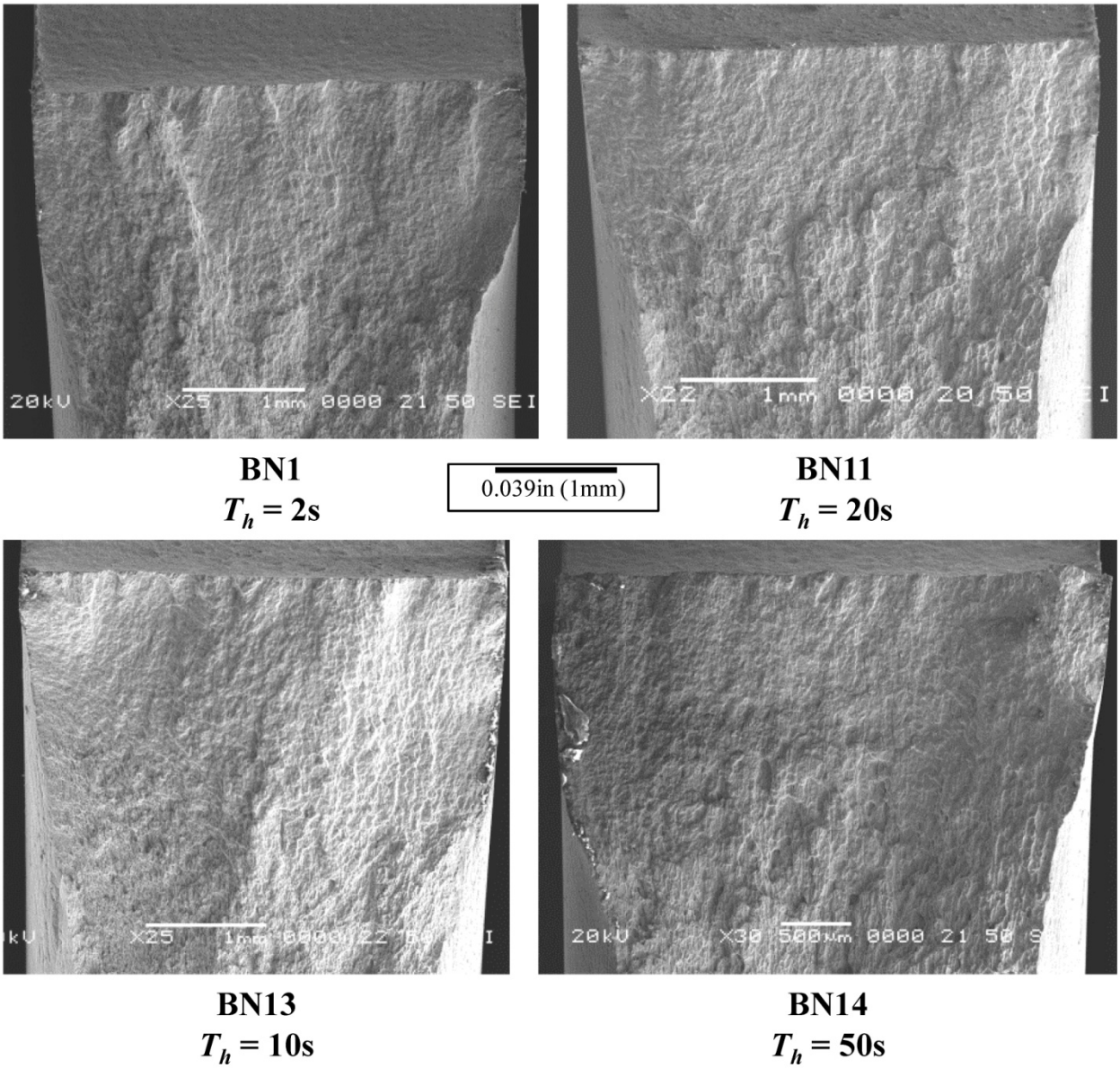

Figure 4.48: Sample fracture surfaces of specimens tested at 600°F (315°C) as viewed under the SEM.

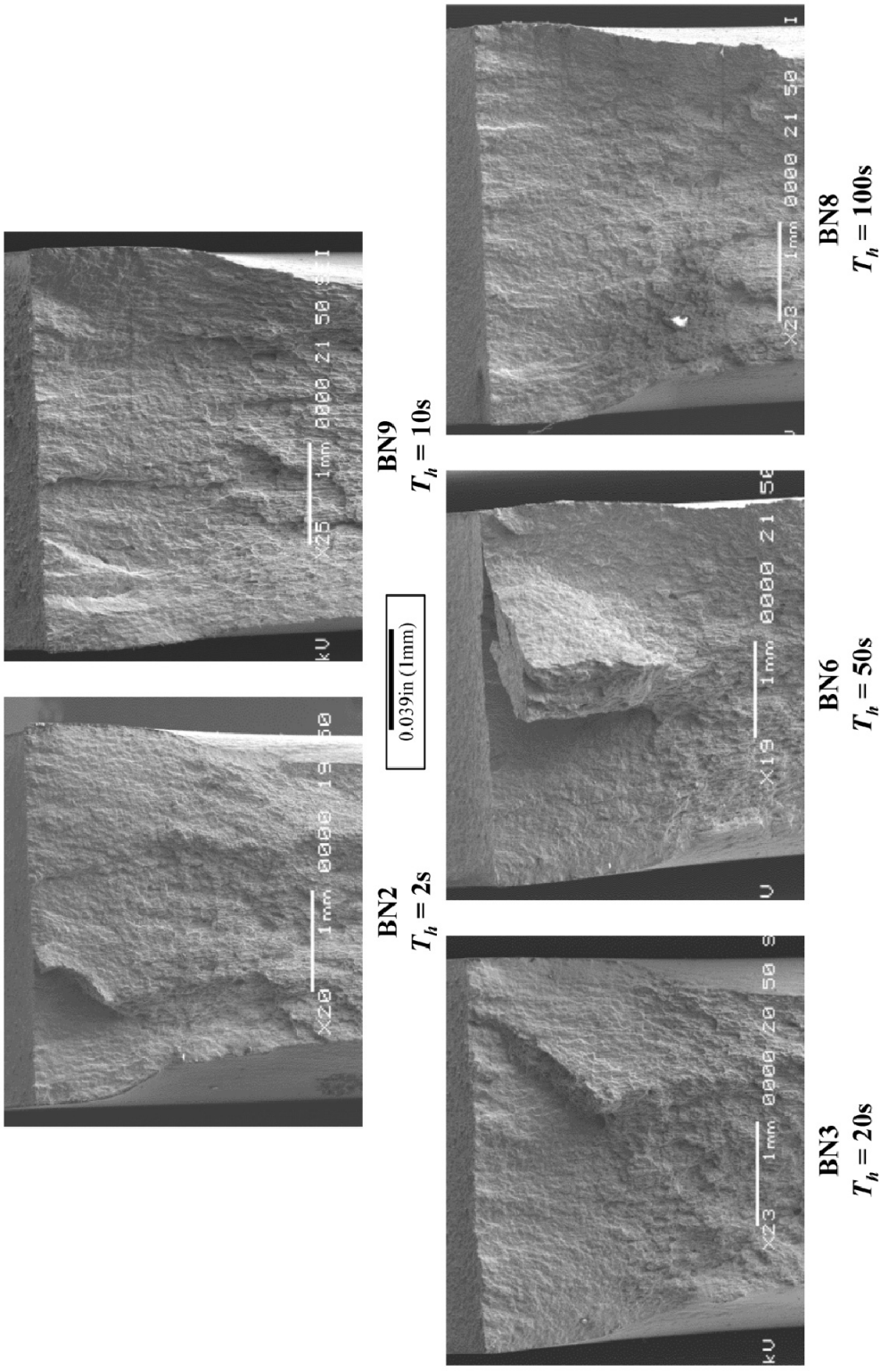

Figure 4.49: Sample fracture surfaces of specimens tested at 800°F (427°C) as viewed under the SEM.

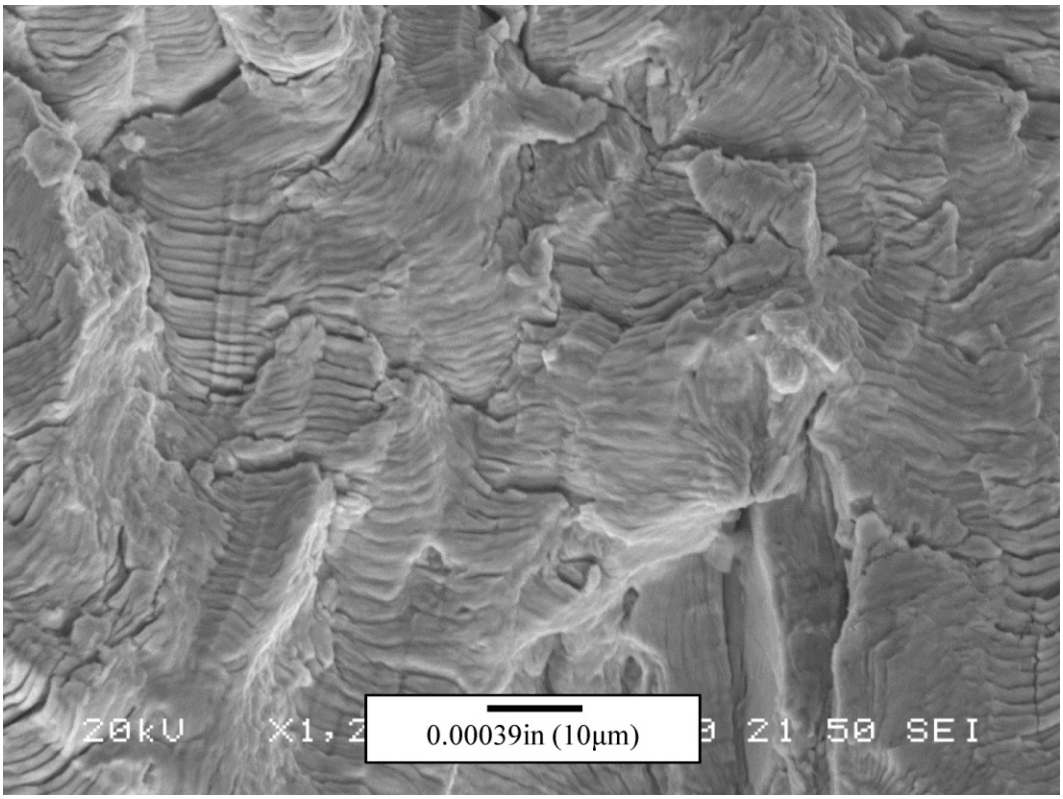

Figure 4.50: Fatigue striations on the surface of large flake observed on fracture surface of BN6.

A transition is observed from the creep-fatigue dominated regime to a regime of ductile tearing, e.g. the surface of BN11, shown in Fig. 4.51. Upon further magnification in this region, the presence of both creep-fatigue striations and the introduction of ductile dimples confirm that there exists a transition of failure mechanism toward the end of the life of the specimen. This is expected, as the crack length begins to extend to lengths that will result in instability and ductile tearing. These regions, which correlated with the digital microscopy, also served to confirm the crack lengths, as measured in Section 4.2, ensuring that accurate crack measurements were achieved.

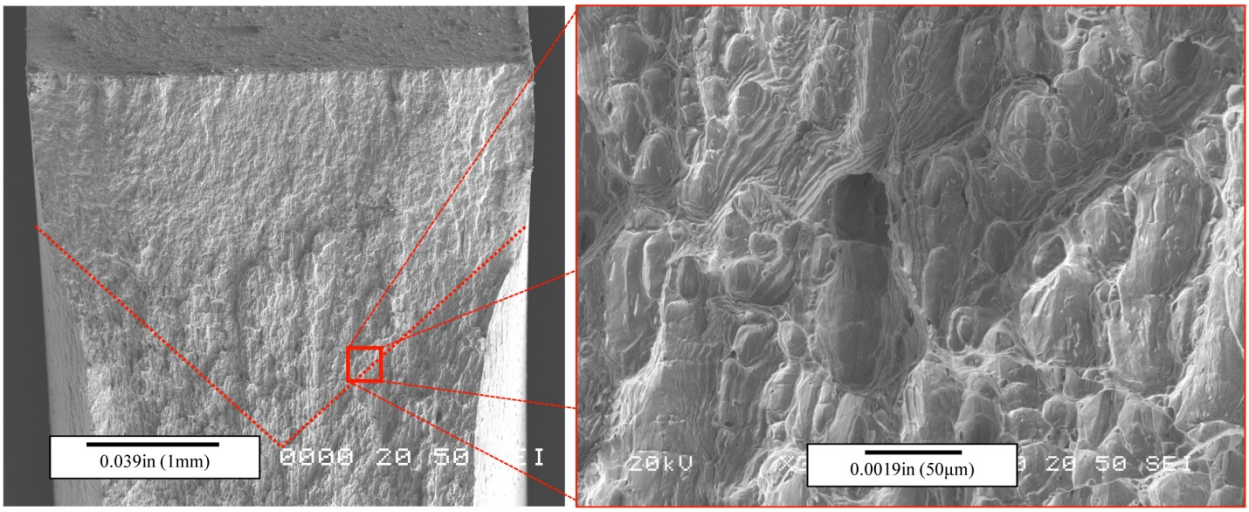

Figure 4.51: Transition region (left) from crack growth to ductile tearing on BN11 tested at 600°F (315°C) with a tensile hold of 20s, with a magnified view provided (right).

Striation spacing was directly measured on the surface of specimens in both the early and mid stages of crack growth, shown in Figs. 4.52 and 4.53. In the early stages of crack growth, striation spacing was typically 0.00001in (0.254µm) and mid-life striations on the order of 0.0001in (2.56µm) to 0.0006 (15.2µm). In both cases, the spacing correlated with the crack growth rates obtained in Section 4.2 for Stage I and II crack growth rates. Late stage crack growth was observed to transition from creep-fatigue failure to ductile tearing, as noted previously, resulting in larger than anticipated crack growth rates. The observation of the spacing and transition to ductile tearing towards the end of the crack length confirm that larger than normal crack growth rates are present, as a result of the addition of extensive plasticity occurring.

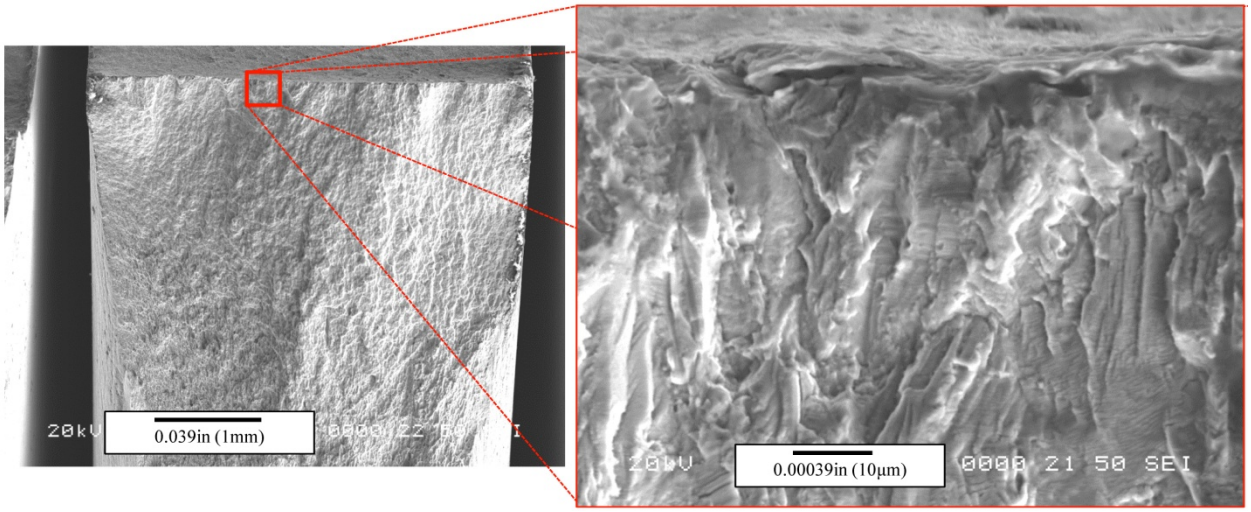

Figure 4.52 Stage I crack growth striations in vicinity close to the notch, shown on BN13 tested at 600°F (315°C) with a tensile hold of 20s, with a magnified view provided (right).:

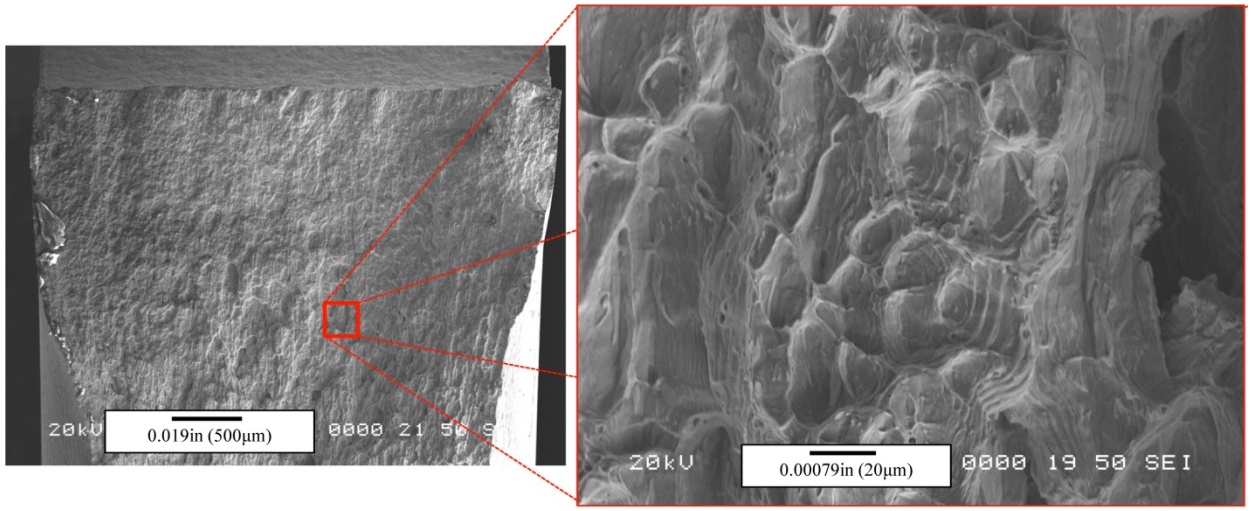

Figure 4.53: Stage II-III crack growth striations near the end of the crack, shown on BN14 tested at 600F (315C) with a tensile hold of 50s, with a magnified view provided (right).

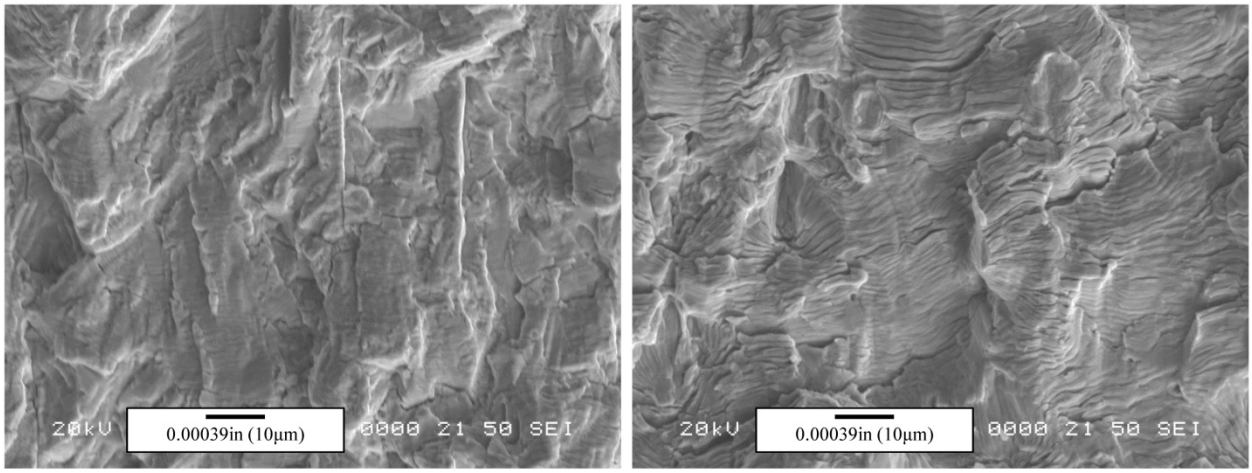

BN11
T_h = 20s

BN9
T_h = 10s

Figure 4.54: Extensive secondary crack observed on fracture surfaces of specimens subjected to (left) 600°F (315°C) and (right) 800°F (427°C).

In all cases, extensive secondary cracking was observed on the fracture surfaces, e.g. Figs. 4.50 and 4.54. No trend regarding the hold time or temperature was observed to affect the extent of secondary cracks. Secondary cracks were not observed to result in deviation of the crack path, as main crack surfaces were predominantly perpendicular to the loading direction. They are not expected to play a significant role in the fracture of specimens, as both the SEM images and sectioned metallurgical images revealed insignificant depths without the presence of oxidation.

Ultimately, the microscopy provided in this section helped to validate and confirm the numerical results presented in Section 4.2. Multiple crack initiation locations were observed on the notch of several specimens; however, one single crack dominated during crack growth. Oxidation and creep effects were not readily observed to affect crack initiation or crack growth. Extensive plasticity was observed towards the end of the life, as confirmed by SEM imaging, revealing the transition from crack growth to ductile tearing. All the experimental results

provided within this chapter, including numerical, experimental and optical, were considered and useful in the model develop and correlation provided in the following chapter.

CHAPTER 5
CREEP-FATIGUE MODEL CORRELATIONS

The development of the proposed crack initiation and propagation models required several key components to accurately fit the experimentally obtained data. In this chapter, the motivation for such a model based on EPFM parameters, the presentation of the proposed models and the parameter and constant determination will be detailed. An emphasis will be placed on the parameter and constant determination process, as this tends to be a problematic step in implementing any type of constitutive model, whether mechanistic or phenomenological in nature. With the constants for the proposed model developed, the correlation with the experimental data will be presented.

5.1 Motivation

The ability to predict the life of a component subjected to cyclic loading at elevated temperatures is vital to a number of industries. As designs become more complex, the level of analyses required to evaluate a structure have increased. The widespread use of advanced finite element software packages have enabled designers to provide a level of analysis that could not have been achieved a few decades previous. Critical components in the nuclear, power generation and transportation sectors that are subjected to conditions that promote crack initiation and propagation have benefitted from the technological advancements.

In terms of crack analyses, several options are available to analyze the initiation and growth of cracks subjected to a myriad of loading conditions, as outlined in Chapter 2 and among several others. When fatigue loading is dominant, analytical models like the Paris law, Forman equation or the more complex NASGRO equation are adequate during linear elastic conditions. If creep is the dominant deformation mode, creep crack growth analyses related to

the C^* approach are sufficient. When a combination of mechanisms is expected to have an influence, the creep-fatigue crack analyses in Section 2.3 are applicable. A multitude of laws have been developed and applied successfully to experimental and industrial applications, e.g. [Saxena et al., 1981; Yoon (I) et al., 1993; Zhang et al., 2012]; however, the models are not without limitations and some require sophisticated parameter determination approaches.

A main limitation to these approaches is the requirement of a pre-existing crack in a component. In certain components, such as a blade in a gas turbine, the length of pre-cracks used in analytical models may be longer than the allowable length for a crack in a physical component. As such, creep-fatigue crack propagation models may not be adequately suited to capture the response of the material at the given crack length scale, with transitions from short crack to long crack occurring varying upon investigations, e.g. 0.02in (0.5mm) [Furuya and Shimada, 1984] or between 0.04 – 0.16in (1-3mm) [Sansoz et al., 2001]. It is desirable that the parameters used to determine crack initiation be subsequently used in the crack propagation analysis, bridging the gap between the two regimes. Furthermore, the approach needs to incorporate parameters that can be readily calculated using standard approaches, such as finite element analysis simulations using elastic-plastic material models.

With the limitation to pre-existing cracks, it is desired to have a model, or combination of models, which implement similar parameters that can be used to predict the initiation, as well as the propagation, of cracks subjected to creep-fatigue loading. Using finite element software running elastic-plastic material models, such as the Chaboche or MATMOD models of Section 2.3.2, the goal is to enable a structural analyst to calculate basic values within FEA software that can readily be used in the life prediction stages. Traditional FEA software is readily suited to calculate the J-integral, based on the framework of the FEM and the J-integral development,

lending itself to be a prime candidate parameter for use in initiation and propagation studies. Furthermore, the ability to have a simplistic model that allows for easy determination of material constants required to predict life is a main goal. It is the consideration of these motivating factors that led to the development of the proposed crack initiation and propagation models for creep-fatigue loading conditions.

5.2 Crack Initiation and Crack Propagation Model Development

The crack initiation and crack propagation models were split into two separate but coupled models, as necessitated by the data. Using approximations of the standard EPFM parameter J and ΔJ, as well as vital test control variables, e.g. R, both crack initiation and propagation was readily captured. The models presented are phenomenological in nature, not taking into consideration the physical mechanisms occurring within the material; however, rarely is the material condition of a component fully characterized during operation. As such, phenomenological models, like those presented here, are valid and necessary for practical applications.

5.2.1 Creep-Fatigue Crack Initiation Model

When developing the crack initiation model, several influencing factors were considered and scrutinized. Relationships between the test temperatures, load ratio, rise time, hold time and notch tip stress-strain modifying parameters were sought. Of all the influential factors observed, the most prominent factors observed to correlate with the number of cycles to crack initiation were the load ratio and the approximation of J for the initial loading cycle, as shown in Figs. 4.14 and 4.15. Temperature was found to be inconsequential, as the softening at higher temperatures was accounted for in the calculation of J as additional softening was accounted for

through the additional load-line displacement. Using Fig. 4.15, a general trend was fit over the experimental data for each load ratio, as shown in Fig. 5.1.

To reproduce the trends observed in Fig. 5.1, a balance was desired to adequately capture the experimental behavior, yet maintain a form that was easily understood and implemented. Power law-based analytical modes, e.g. Paris Law, are commonly used in phenomenological models, as the ability to replicate experimental behavior with limited complexity is achieved. Therefore, implementing a power law, the proposed creep-fatigue crack initiation model is furnished,

$$N_i = \frac{D}{\left(J_1\right)^p \left(1-R\right)^q}, \tag{5.1}$$

where J_1 is the approximated J-integral calculated from the initial load cycle, N_i is the number of cycles to crack initiation, R is the load ratio and D, p, and q are fitting constants. Equation (5.1) requires material constant determination, to be outlined in Section 5.3, in addition to the calculation of J_1 and N_i from experimental data. Correlations of Eq. (5.1) with experimental data will be provided in Section 5.4.

The main assumption of the model proposed in Eq. (5.1) is that the presence of a notch constitutes a crack-like feature. In the experimental portion of this investigation, crack initiation was observed to occur at the root of the notch, providing the necessary condition for Eq. (5.1) to be applicable. No constraints were applied in regards to max crack length or the load type, as the crack length is to be defined during the experimental portion and the load is inherently taken into account by the calculation of the proposed J_1 approximation. It is intended that this value of J_1 be calculated via FEA, as analytical solutions may be challenging for typical life analyses. Extension of this model to smooth or other experimental geometries will require the use of appropriate specimen geometries, capable of observing initiation and small crack propagation.

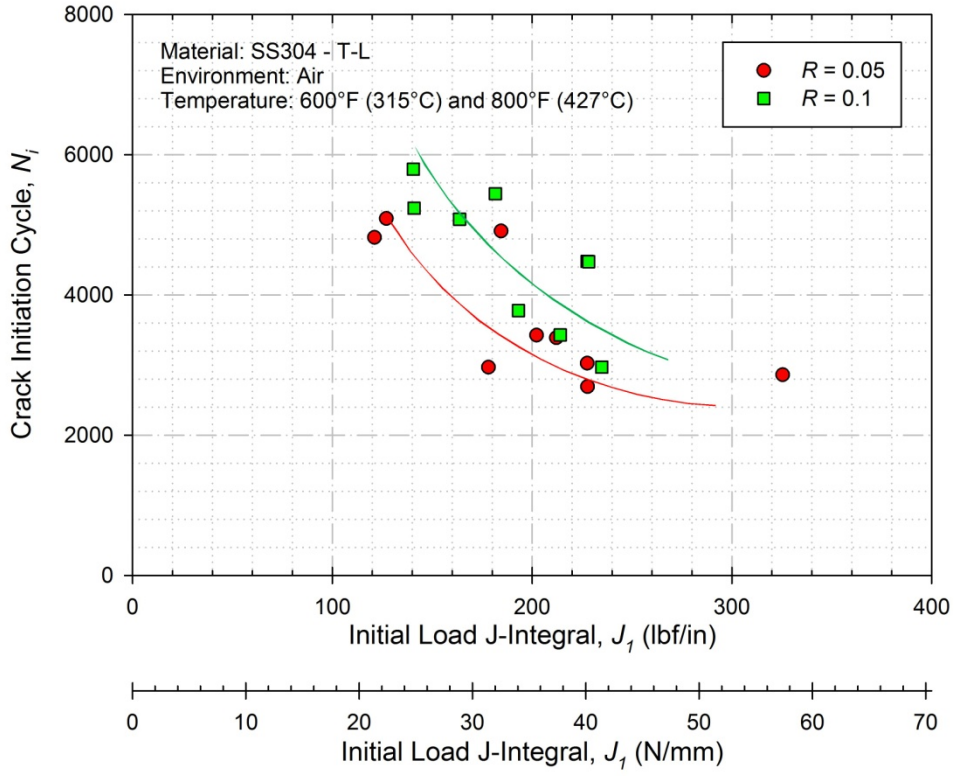

Figure 5.1: Effects of load ratio, *R*, on the observed and simulated crack initiation of SS304.

It is observed that neither the stress gradient nor the radius of the blunt notch is accounted for in Eq. (5.1). The stress gradient required a fair amount of post processing, as well as several iterations of finite element meshes to achieve nodes at locations needed to calculate the gradient. By using *J*-integrals, the FEA software automatically calculates over the desired number of contours, simplifying the process of the analyst. The notch radius was not accounted for, as all of the specimens used in this investigation utilized the same radius notch. Inclusion of the radius would have essentially resulted in another constant, which the value of *D* accounts for. Future work including the variation of the notch root radius will be provided in Chapter 8.

The main advantage to implementing Eq. (5.1) in crack initiation life estimation analyses is the simplicity of the requisite parameters. Upon completing experimental testing and constant determination for a given material, merely calculating the approximated value of J_1 at a crack-

like location within an elastic-plastic FE simulation has the ability to predict the number of cycles to crack initiation. In most cases, the load ratio would be nearly zero depending on the extent of plasticity, as in the case of a "peaker;" however, crack initiation predictions can readily be made at any load ratio experimental data has been obtained for set load conditions. While the length of the crack that defines initiation is open to interpretation, Eq. (5.1) is adaptable to any length as defined by the investigator. Predictions using the proposed crack initiation model will be provided in the following chapter.

5.2.2 Creep-Fatigue Crack Propagation Model

The proposed creep-fatigue crack propagation model, similar to the proposed crack initiation model, follows suit in that a power law behavior is noted. Incorporating multiple terms to account for the three stages of crack growth observed within this investigation, the proposed model is provided, i.e.,

$$\frac{da}{dN} = \frac{C\left(1-\frac{\Delta J_{stab}}{\Delta J}\right)^{a}}{\left(\Delta J\right)^{b}\left[\left(1-R\right)J_{c}-\Delta J\right]^{c}}, \tag{5.2}$$

where ΔJ_{stab} is the threshold-like asymptote for Stage I creep-fatigue crack growth, ΔJ is the cyclic J-integral, J_c is the critical-like asymptote for Stage III creep-fatigue crack growth, R is the load ratio, and C, a, b and c are fitting constants. Each term with an exponential is targeted to capture a particular stage of crack growth, to be discussed further. Implementing Eq. (5.2) into crack growth, the creep-fatigue crack growth behavior observed is readily simulated, as shown in Fig. 5.2.

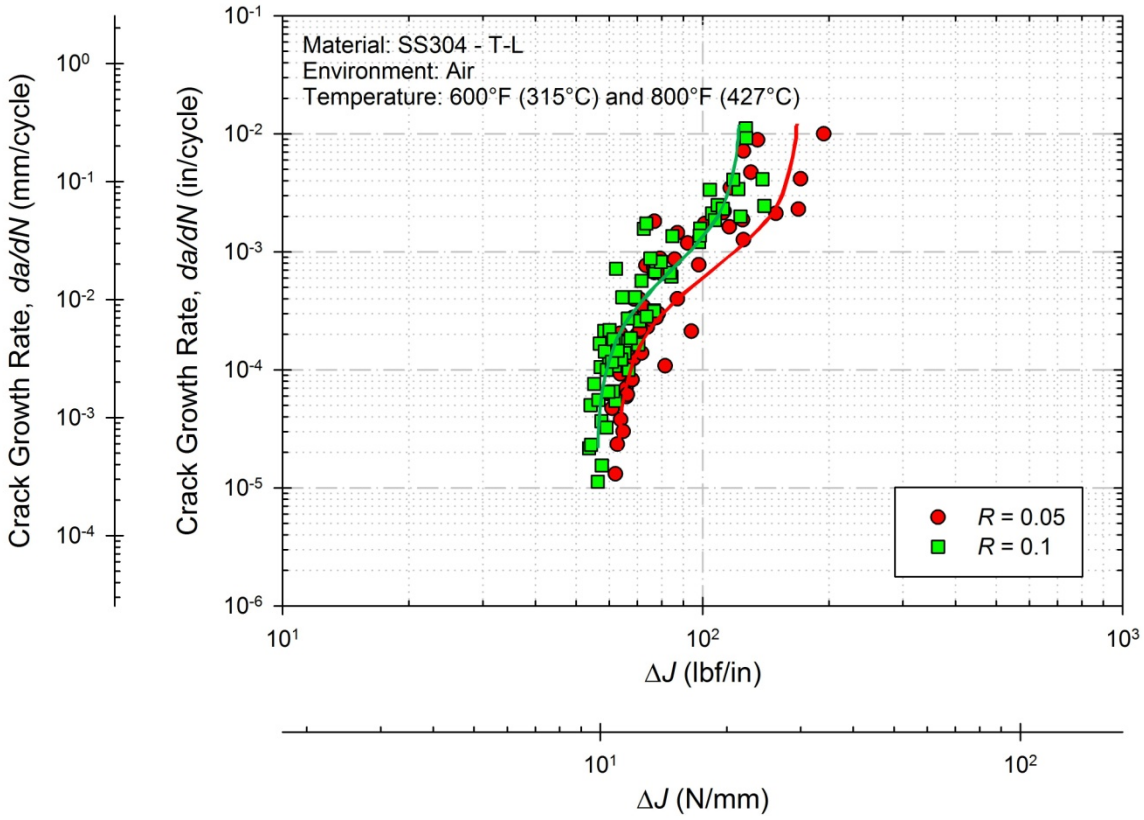

Figure 5.2: Observed and simulated crack propagation of SS304 under creep-fatigue conditions.

Model development began with the Stage II crack growth, i.e. the linear portion of crack growth on a log-log scale. As pioneered by Paris for LEFM parameters, the crack growth rate per cycle was observed to be a function of the cyclic EPFM *J*-integral [Paris et al., 1961], i.e.,

$$\frac{da}{dN} \propto C\left(\Delta J\right)^{b}. \tag{5.3}$$

To incorporate the increased rates of Stage III crack growth, the load ratio, R, and the critical-like asymptote J_c for instability was incorporated, similar to [Forman et al., 1967], i.e.,

$$\frac{da}{dN} \propto \frac{1}{\left[\left(1-R\right)J_c - \Delta J\right]^{c}}. \tag{5.4}$$

Stage I crack growth rate dependencies incorporated the threshold-like asymptote ΔJ_{stab}, similar to [NASGRO, 2012], i.e.,

$$\frac{da}{dN} \propto \left(1 - \frac{\Delta J_{stab}}{\Delta J}\right)^{a}. \tag{5.5}$$

The final form of the proposed crack growth model, as shown in Eq. (5.2), is a combination of Eqs. (5.3-5.5), which is capable of simulating the creep-fatigue crack growth rates in materials subjected to elastic-plastic loads.

Two of the parameters in the proposed model, ΔJ_{stab} and J_c, are plastic variations of the threshold stress intensity factor, K_{th}, and the critical or plane-strain fracture toughness, K_c, respectively. In LEFM, the K_{th} is an experimentally obtained minimum value at which cracks are not expected to propagate when ΔK is below. The plastic variation presented here, ΔJ_{stab}, is the approximate to the cyclic J-integral at which the un-cracked component is subjected. It is not a threshold below which cracks do not grow; rather, it is a parameter that relates to the stress and strain at the blunted notch, from which subsequent CF crack propagation predictions use as the initial ΔJ. By implementing this into Eq. (5.2), the asymptotic behavior and faster crack growth rates for small cracks can accurately be modeled.

Accelerating the crack growth rates closer to the instability region, J_c is the plastic variant of the critical stress intensity or the plane-strain fracture toughness, K_c or K_{Ic}, respectively. Under LEFM crack growth analyses, this parameter serves as the asymptote for crack growth rates with respect to ΔK and is the measured instability for the material. In the elastoplastic analysis conducted, a plastic variation of this value, J_c, is used in a similar manner. As the value of ΔJ approaches the value of J_c, crack growth rates are observed to increase at an increasing rate. By incorporating this value in Eq. (5.2), the acceleration of crack growth rates is captured.

Accurate replication of the experimental data utilizing Eq. (5.2) requires the determination of material constants. As with all mechanical models, either mechanistic or phenomenologically-based, the constants will be dependent upon the material and environment.

In the current state, neither Eqs. (5.1) or (5.2) are temperature dependent, as the approach taken eliminated the temperature dependency. Regardless, both of the proposed models require the estimation of constants.

5.3 Parameter and Constant Estimation

Two approaches to parameter and constant determination were utilized in this investigation. The first approach employed the use of Microsoft Excel, in particular the Solver tool, and the second used the software Eureqa, as overviewed in Section 3.7. Both methods involved the optimization of constants through similar methods, with various levels of user input required.

Microsoft Excel enables optimization through the use of the Solver add-in tool. By targeting a cell, the value within that cell can be minimized, maximized or set to obtain a predetermined value by varying values in other cells. For this investigation, Solver was used to minimize the sum of the squared error between actual and predicted crack initiation and crack propagation models. The crack initiation model required the use of four columns, containing the values of J_1, N_i, R and $N_{i,pred}$, with the constants D, p and q in separate cells. The crack propagation model required the use of six columns, containing the values of ΔJ_{stab}, ΔJ, J_c, R, da/dN and da/dN_{pred}, with constants C, a, b and c in separate cells. For each optimization, an additional column containing the square of the error between actual and predicted values was added, based on the predicted values furnished for the current constants used in each model.

Initial constant determination was obtained using a trial-and-error process. The sum of the squared error was minimized by manually changing the values of the constants in the respective cells. Once a fit was achieved that resembled the experimental data, the Solver add-in was used to parametrically optimize the constants. In some cases, the number of iterations, the

tolerance and the degree of precision were altered, assisting in refinement of the fit. Upon obtaining a set of constants that were satisfactory, one constant was changed to a random number and the optimization routine was repeated. This was a necessary step in obtaining "nice" constant values, as the Solver does not find global minimums, only local minimums. A schematic of the constant determination using the Microsoft Excel Solver add-in is provided, shown in Fig. 5.3.

Utilizing the software Eureqa, initial and optimized constant determination was more automated. As with the use in Excel, columns with the test parameters and experimentally obtained values were input into the spreadsheet. Next, data manipulation was an option, e.g. excluding outliers, normalizing data, etc.; however, no manipulation of the data was conducted. Next, the form of the equation was input, leaving the values represented as material constants as unknown functions to be parametrically determined. A multitude of options for optimizing were available, with the R^2 goodness of fit chosen. Using the routine outlined in Section 3.7, the analyses were run, providing fully-optimized constants without the need for initial constant determination. A schematic of the constant determination using Eureqa is provided, as shown in Fig. 5.4.

Both methods provided satisfactory material constant determination routines. As opposed to using Microsoft Excel, Eureqa provided a stable optimization routine that excluded the initial constant determination process. By eliminating the initial constant determination process, a significant time savings was observed. Along with the global optimization routine that Eureqa employed, it was chosen as the method of constant determination for this investigation, with constants provided in Tables 5.1 and 5.2.

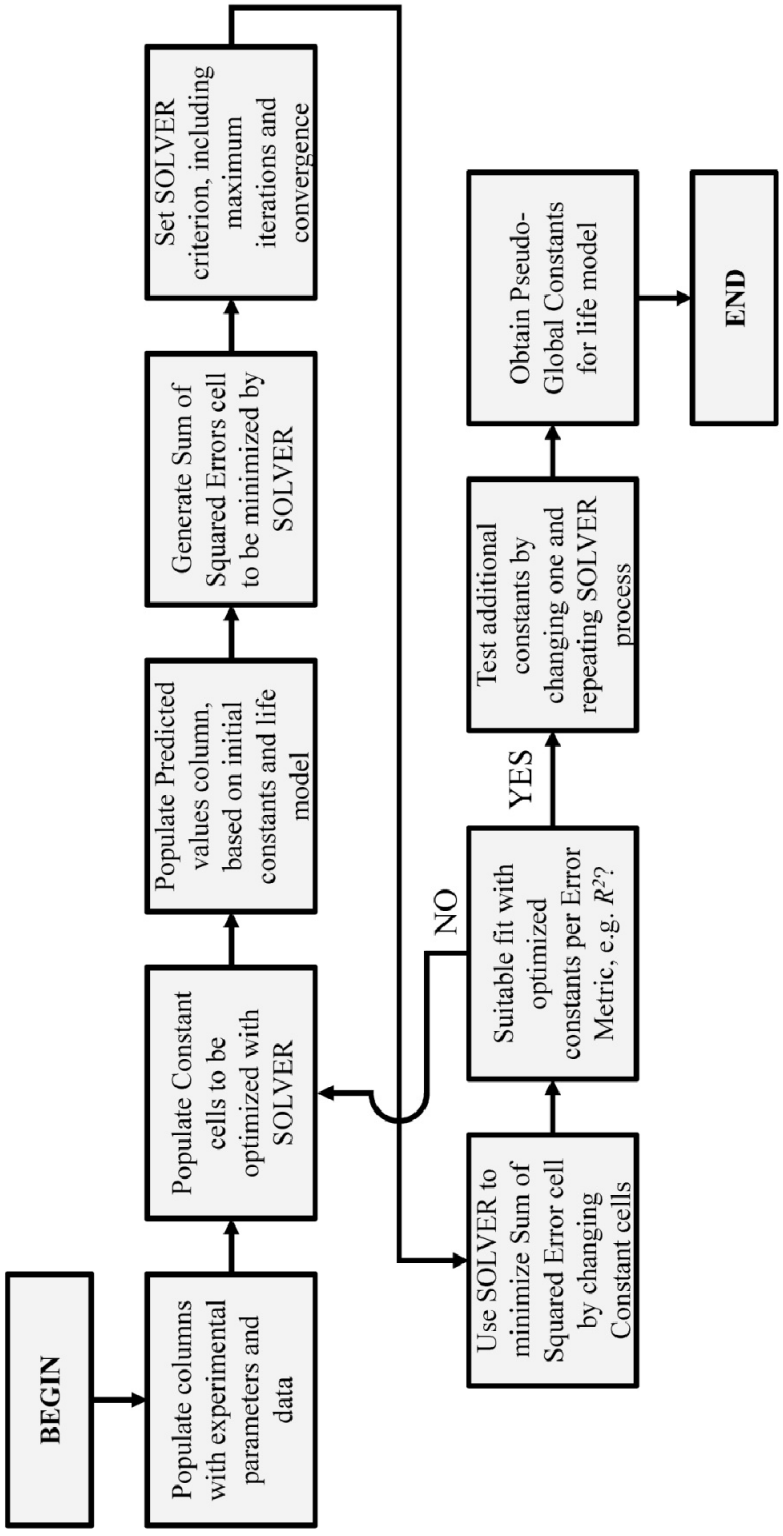

Figure 5.3: Schematic of constant determination using the Microsoft Excel approach.

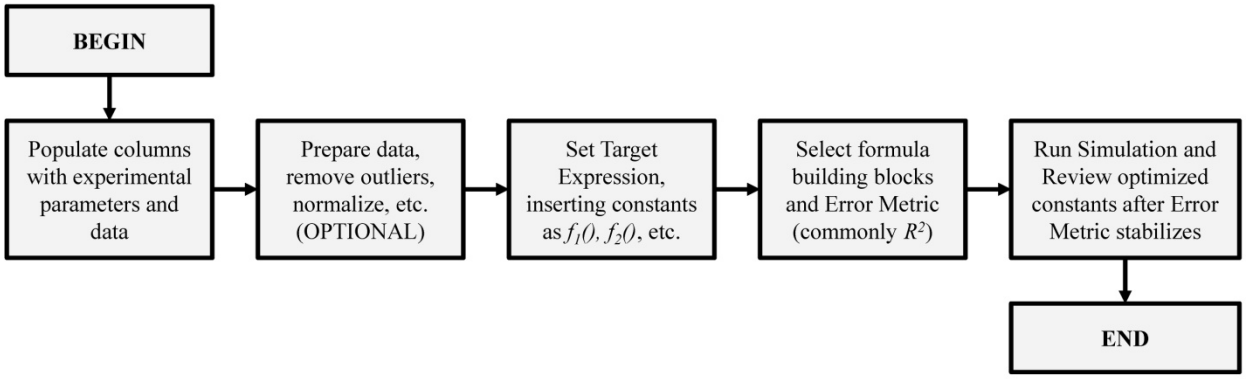

Figure 5.4: Schematic of constant determination using the Eureqa approach.

Table 5.1: *Optimized Creep-Fatigue Crack Initiation Model Constants*		
D	***p***	***q***
128894	0.719454	4.04939

Table 5.2: *Optimized Creep-Fatigue Crack Propagation Model Constants*				
C	***a***	***b***	***c***	J_c
281.124	2.08283	1.07662	1.07899	240

5.4 Crack Initiation and Crack Propagation Model Correlations

Implementing the constant estimation and optimization routine provided in Section 5.3, the proposed creep-fatigue crack initiation and propagation models in Eqs. (5.1) and (5.2) were correlated with the experimental results obtained in Section 4.2, as shown Figs. 5.5 and 5.6, respectively. Comparisons of the actual versus predicted values for all crack initiation and crack propagation rates are provided, as shown in Figs. 5.7 and 5.8, respectively. Experimental and predicted data is provided based on the stress ratio, regardless of temperature or incorporated hold time, utilizing the constants in Tables 5.1 and 5.2.

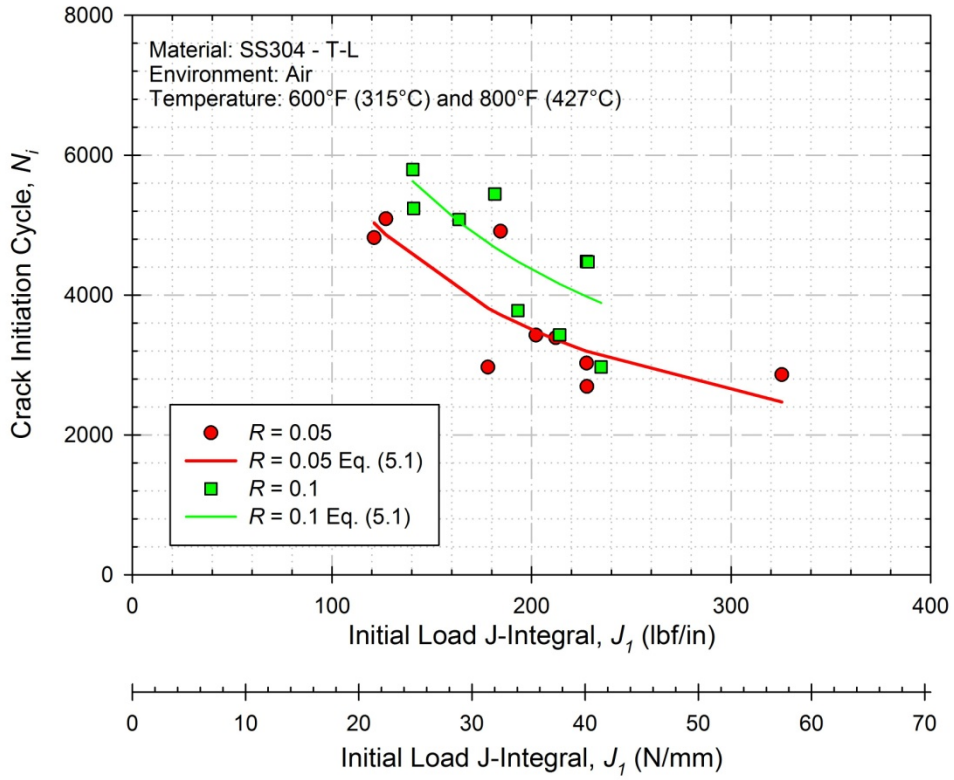

Figure 5.5: Experimental and predicted crack initiation results using the proposed creep-fatigue crack initiation model.

The number of cycles to crack initiation is observed to be dependent upon J corresponding to the initial load cycle, J_1, and the load ratio, R, at which subsequent cycling is conducted, in addition to three material constants. As the stress ratio decreases, more closely replicating the actual mechanical cycle of a gas turbine cycling on and off, the sum of the squared error was observed to decrease 17.1% for tests conducted at the lower load ratio. Maximum error between the predicted cycle to initiation and the actual cycle to crack initiation was observed to be 30.9% with an average percent difference of 2.9%. Several predictions are observed to coincide directly with the actual initiation cycle, e.g. Specimens BN7 and BN11. No "sampling" of the data was conducted, in which tests suspected of being an outlier or unsubstantiated were removed.

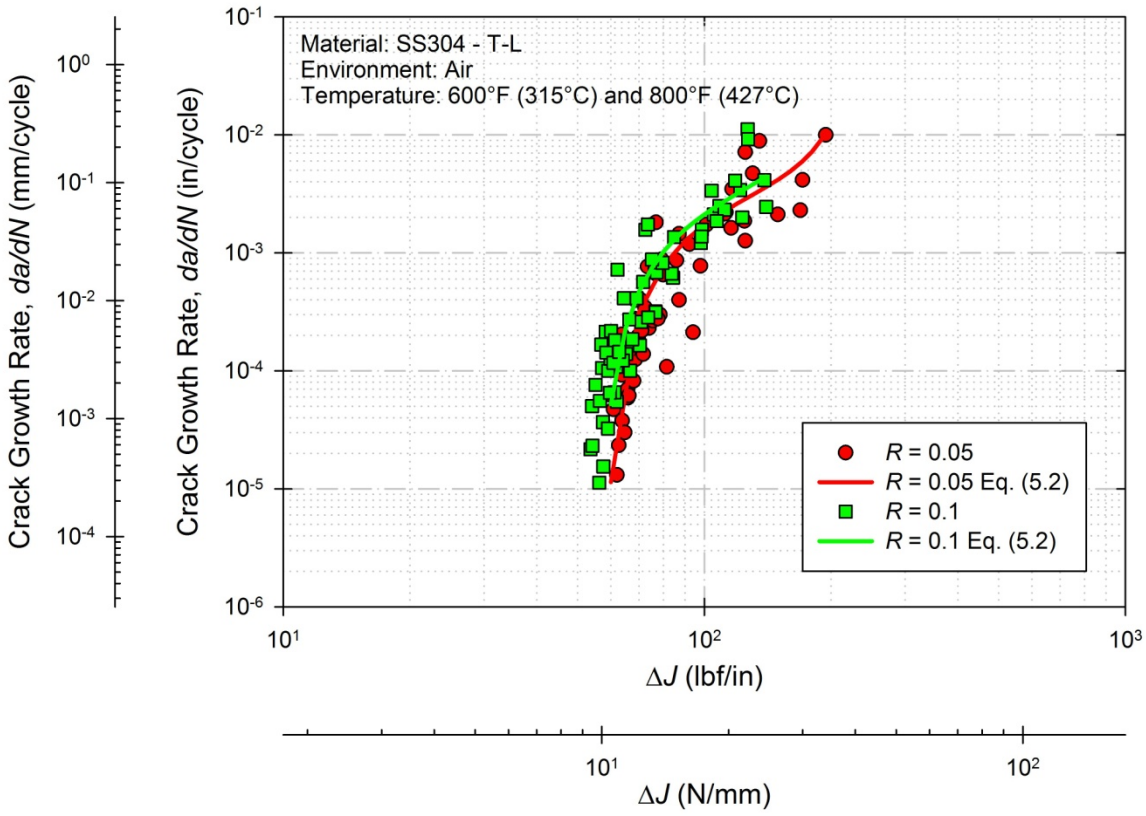

Figure 5.6: Experimental and predicted crack propagation results using the proposed creep-fatigue crack propagation model.

Crack propagation rates were observed to be dependent upon a number of factors, including ΔJ, ΔJ_{stab}, J_c and R, as well as four material constants. As with the initiation model, as the load ratio decreases, the sum of the squared error was observed to decrease by 18.6% for tests conducted at the lower load ratio. On a percentage basis, the comparison of actual versus predicted crack growth appears large, due to the small orders of magnitude; however, all predicted values were within an order of magnitude of experimental values. The largest differences were noted for growth rates in the late-Stage II/Stage III regimes, which is attributed to the sampling rate of data, previously addressed in Section 4.2. Additionally, no "sampling" of the data was conducted, in which tests suspected of being an outlier or unsubstantiated were removed.

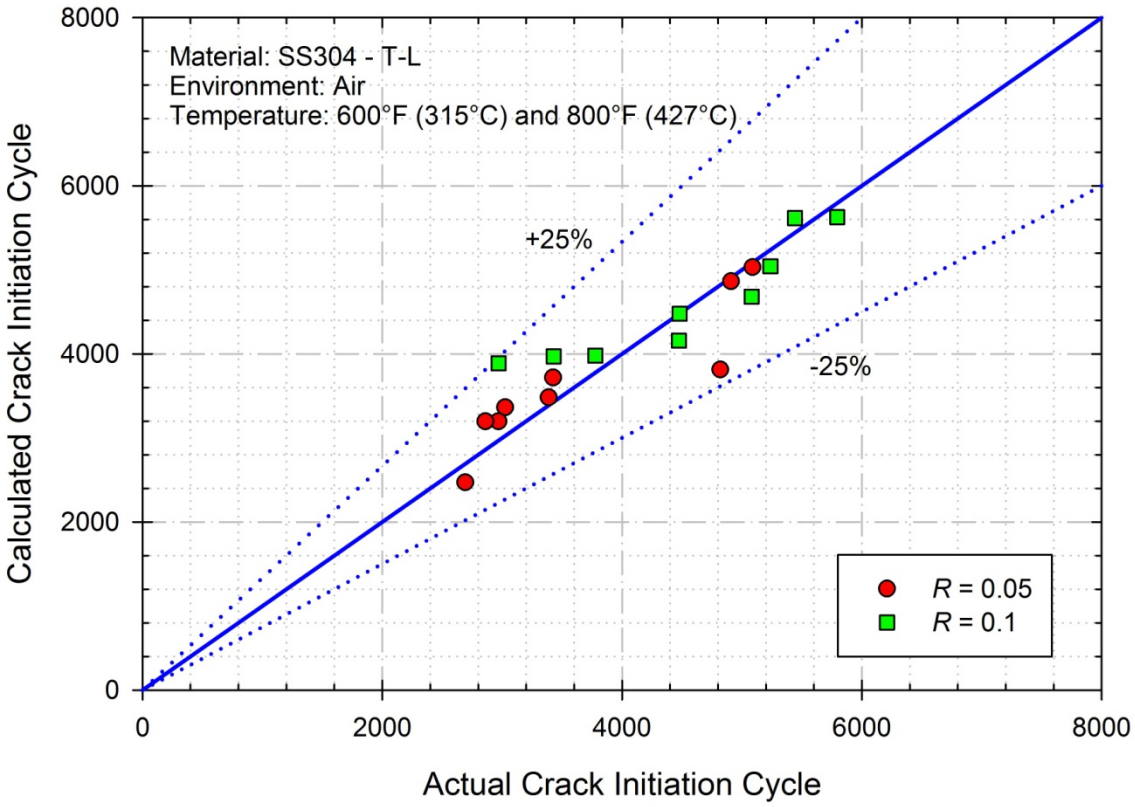

Figure 5.7: Correlation of crack initiation life using the proposed creep-fatigue crack initiation model on SS304 at 600°F (315°C) and 800°F (427°C).

Both crack initiation and propagation models predict and replicate the experimental data to a degree with limited amounts of variability, as shown in Figs. 5.7 and 5.8. In Fig. 5.7., the correlation for crack initiation cycle includes error bars that are a factor of plus-minus 25%, whereas Fig. 5.8 regarding crack growth rates includes error bars that are factor of plus-minus two. Using the R^2 error metric, the crack initiation model has a value of $R^2 = 0.705$ and the crack propagation model has a value of $R^2 = 0.913$. Model correlation coefficients with the experimental data for both the initiation and propagation models were observed to be 0.840 and 0.891, respectively.

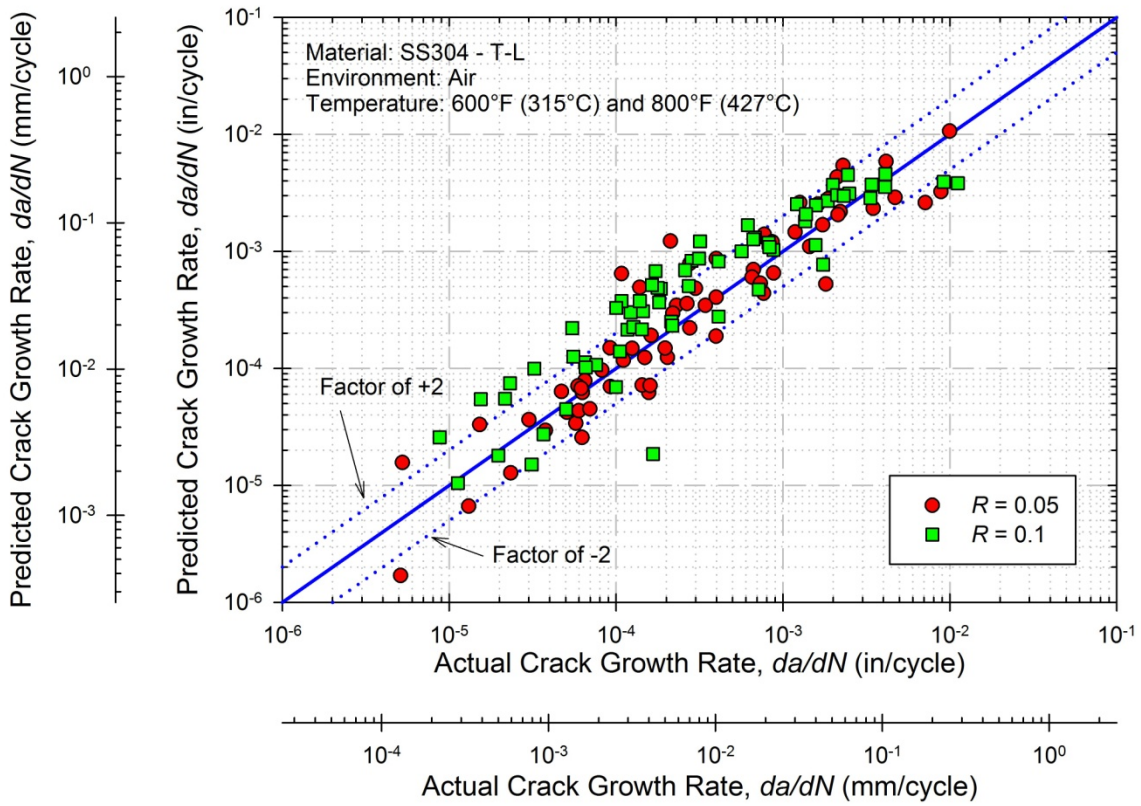

Figure 5.8: Correlation of crack propagation rates using the proposed creep-fatigue crack propagation model on SS304 at 600°F (315°C) and 800°F (427°C).

As observed in the application of current models, the scatter in data is common even with models that utilize more complex formulations and require more parameters to furnish predictions. This scatter can be related back to the experimental data and the constants used to fit the data. The affect of varying the constants, for both the initiation and propagation models, is observed as a hypothetical situation represented by the dotted lines, shown in Fig. 5.9. For the optimized set of constants, crack growth rates were observed to be non-conservative towards the end of life, as shown in Fig. 5.8. This is a direct result of the sampling rate limitation of the software, as noted in Section 4.2.3. Ultimately, a balance of simplicity and accuracy is maintained using both the proposed initiation and propagation model, in which conservative life predictions can be made by simply multiplying by a standard factor.

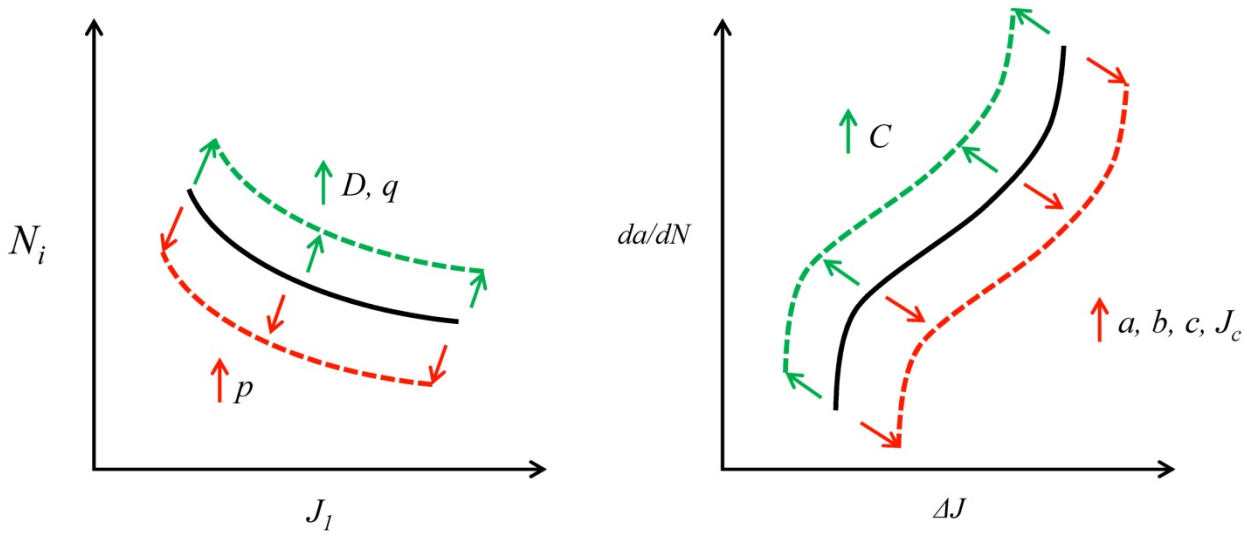

Figure 5.9: The affect of constants on predicted behavior used in the (left) crack initiation and (right) crack propagation models.

The main advantage to the proposed creep-fatigue crack initiation and propagation models is in the simplicity of the approach. Crack initiation for tests at different temperatures and incorporating various hold times was able to be predicted based on the approximation of J for the initial load up. The model allows the user to define the initiation criterion, whether it is through load-drop techniques, DCPD monitoring systems, or other suitable crack measurement methods. Once a crack has initiated, the subsequent creep-fatigue crack propagation model is capable of predicting crack growth rates in the presence of elastic or plastic stress fields ahead of the crack tip for any length of crack under investigation.

A method of implementing the proposed model into design, incorporating elastic-plastic finite element analyses, will be provided in the following chapter.

CHAPTER 6
CREEP-FATIGUE MODEL IMPLEMENTATION

The proposed creep-fatigue crack initiation and propagation models are intended to be used during the design and assessment of structural components subjected to creep-fatigue conditions. When assessing a component that has been exposed to service conditions, the creep-fatigue crack propagation model can be implemented in remaining-life evaluations, much in the same way that traditional crack growth analyses are conducted. Proposed methods of implementation, for both the initiation and propagation models are included, as well as the capabilities and limitations of the current form of the models.

6.1 Implementation of Creep-Fatigue Model

The intended application of the creep-fatigue crack initiation model requires the use of an elastic-plastic finite element simulation. A material model must be selected and can be either a standard model within the software package or a custom user-developed model. Suitable constitutive material models include a multilinear kinematic hardening (MKIN) or a viscoplastic model, e.g. Chaboche or MATMOD models. By implementing an advanced material model with plasticity, the behavior can be accurately simulated after softening or hardening effects, establishing the baseline for the ΔJ_{stab} parameter used in the crack propagation model.

Locations with a significant stress concentration and the potential for yielding upon initial loading, such as the transition from a blade platform to the blade, shall be modeled and meshed with suitable refinements. By refining around the location of interest, a smaller deviation in the contour integral calculations is expected. Although the *J*-integral is theoretically path-independent, when carrying out elastic-plastic analyses, some dependency is observed. To minimize the amount of variation, simple simulations should be run with various levels of

refinement at the key area. As the values obtained from the *J*-integral converge, a suitable mesh has been achieved and full simulations should be conducted.

With the appropriate boundary conditions applied to the model, simulations should be conducted to simulate the response after the first cycle. Obtaining the value of the approximate *J*-integral around the area of interest, crack initiation estimations can be made from this value and the load ratio of subsequent cycling. Crack lengths that define crack initiation are to be defined by the user, as it will depend on the monitoring technique, the resolution of the monitoring devices and/or a standard length defined by the governing body of the investigator. This is to be set prior to structural assessment analyses, in particular, during the experimental investigation and subsequently used in the material constant determination process. With the model calibrated to the material and a fixed length defining initiation, the number of cycles to crack initiation is readily calculated, outlined in Fig. 6.1.

Component geometries, such as the arbitrary body presented in Fig. 6.1, that contain features and geometrical discontinuities are of primary interest, as highlighted in the red in (1). To make a *J*-integral approximation, nodes must be placed along a line placed at the probable location of crack initiation, as in (2). Upon conducting preliminary mesh studies, the level of refinement of nodes and elements at the location must be sufficient enough to not provide highly sensitive contour integral calculations, shown in (3). Upon reaching a suitable refinement with little mesh dependency, appropriate boundary conditions and tractions should be applied to the model and the FEA shall be conducted, including the *J*-integral calculation, as in (4). Comparison of the values for several contours shall be conducted, and upon achieving a small deviation between reported *J* values for subsequent contours, crack initiation can be predicted using the proposed crack initiation model.

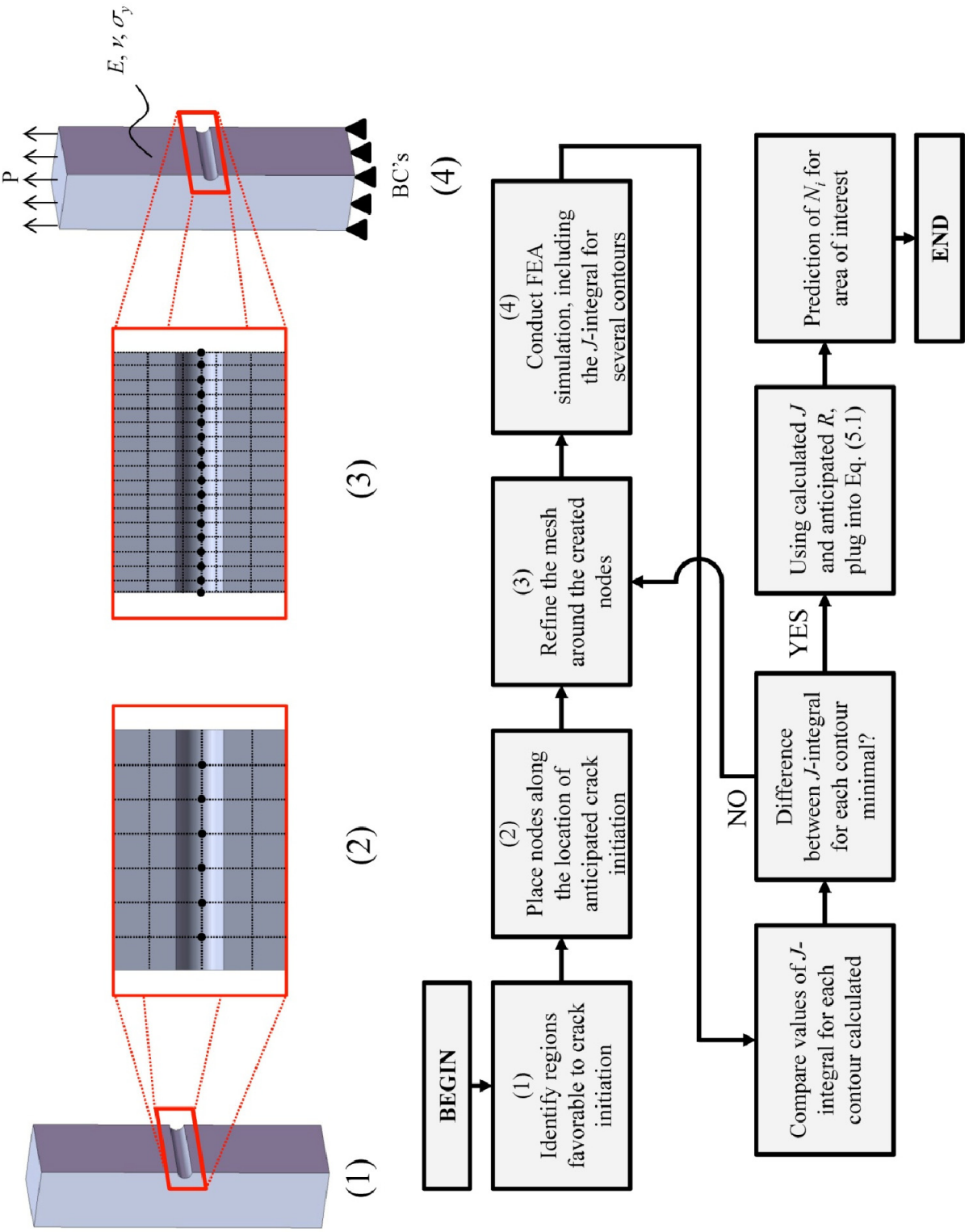

Figure 6.1: Schematic of suggested implementation routine for the proposed crack initiation model.

Crack propagation analyses can be completed in a number of fashions, ranging in levels of complexity. Following the initiation of a crack, a quick approximation to determine the number of cycles until failure is to integrate the proposed model in Eq. (5.2) between the current crack length and the critical crack length. This is likened to the effect of using a Paris law for Stage II crack growth to simulate the accumulation of length over all stages of crack growth. This method, while straightforward and fast, will ultimately lead to an over approximation in life, as it does not take into account the increase in crack growth rates as the value of ΔJ increases with increasing crack lengths. As such, an iterative process to determining the remaining life is necessary.

To achieve a more accurate, conservative approach, a multistep process is suggested, as outlined in Fig. 6.2. First, calculation of the approximate J for the initial crack length is to be done. Using the initial length, the approximate ΔJ value and the load ratio, the crack growth rates are to be summed over a set of cycles, e.g. 100-200 cycles for early stages of crack growth. Following, the initial crack length is to be extended by the total Δa as a result of the growth over the set of cycles and a new value of ΔJ is to be obtained. Again, the corresponding crack growth rate for this value of ΔJ is to be obtained and the summation of crack growth rates should be done. This process is to be repeated until nearing the critical crack length of the subject material, in which the number of cycles in a set in which Δa is approximated over should be decreased to accurately account for the transition from Stage II to Stage III crack growth. Conducting an iterative crack propagation study, like that of Fig. 6.2, will provide more accurate total life predictions with the lesser probability of being non-conservative.

Figure 6.2: Schematic of suggested implementation routine for the proposed crack propagation model.

6.2 Creep-Fatigue Model Extrapolations

In this section, predictions furnished by the creep-fatigue crack initiation and propagation models will be provided based on hypothetical situations. By starting with a baseline test case, key parameters used in Eqs. (5.1) and (5.2) will be varied in order to test the robustness of the model, as well as identify any potential issues regarding the constants. The goal of this section will be to provide the end-user an idea of what manipulations can be successfully made to the model without compromising the intended life predictions. Such an analysis of proposed models was absent in the literature review of Chapter 2, further providing the need for such exploratory predictions.

The benchmark conditions for which further predictions are compared on is an average of the data obtained for tests conducted at 800°F (427°C), as provided in Table 6.1. By averaging over the experiments, predictions are able to be compared the back to the experimentally obtained data, providing a physical root for predictions. The material constants used in predictions are the constants optimized for the data in this investigation, provided in Tables 5.1 and 5.2. In Chapter 4 and 5, it was observed that both the temperature and hold time are incorporated by the EPFM approximations utilized within this investigation, therefore predictions are made based on the influencing factors, namely the load-based EPFM parameter approximations and the load ratio.

Table 6.1: *Benchmark parameters used in the crack initiation and propagation models used to correlate with predictions.*

Trial	**Temperature, T** °F (°C)	**Load Ratio, R**	**Rise Time, t_r** (s)	**Hold Time, t_h** (s)	J_1 lbf/in (N/mm)	ΔJ_{stab} lbf/in (N/mm)	**Final Crack Length, a_f** in (mm)
800B	800 (427)	0.05	10	50	229 (40.1)	55.3 (9.69)	0.6415 (16.29)

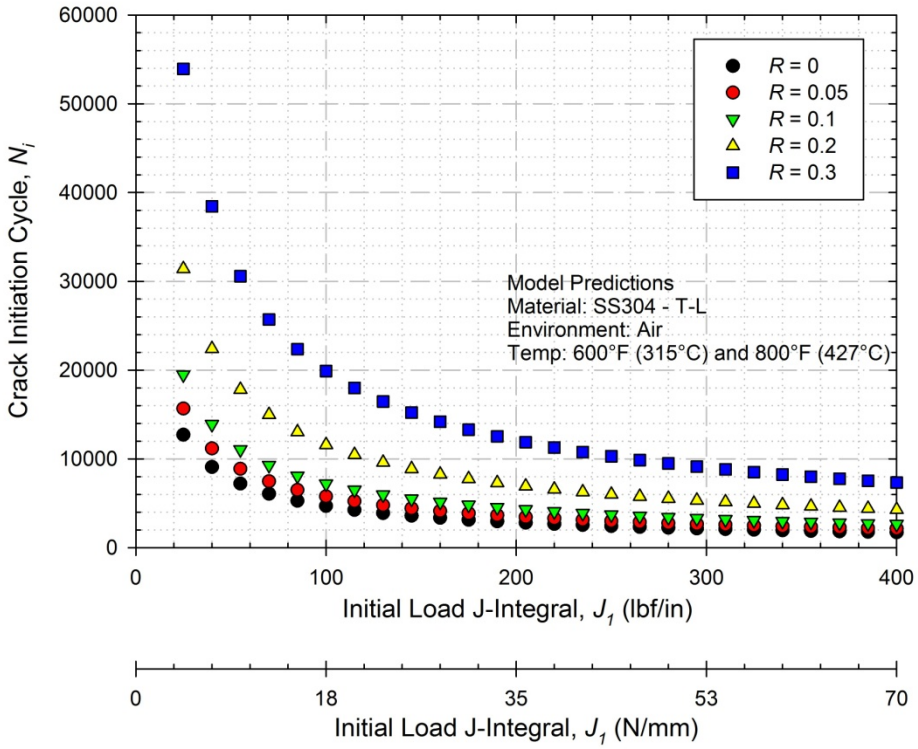

Figure 6.3: Predictions of crack initiation cycle based on various J_1 and R values.

Crack initiation was observed to be primarily dependent upon the first cycle J-integral approximation, J_1, and the load ratio at which subsequent cycling is conducted. Starting with the baseline case, a series of crack initiation cycle predictions are furnished, as shown in Fig. 6.3. The value of the first cycle J-integral approximation is varied from 40.0lbf/in (7.01N/mm) to 400lbf/in (70.1 N/mm) and at load ratios between 0 and 0.3. As intended, as the level of plasticity observed in the initial cycle increases, the number of cycles to crack initiation decreases. The effect of the load ratio is observed to increase the number of cycles to crack initiation as the load ratio increases. The increase in load ratio results in a lower alternating stress at the notch, requiring more cycles to generate a crack.

At the lower and upper bounds provided in Fig. 6.3, differences in the predictions are readily observed. When the level of plasticity on the first cycle is minimal, i.e. a low value of J_1,

the number of cycles to crack initiation increases rapidly for all load ratios. Essentially, the cycling at the crack-like feature is no longer loaded in a manner that results in substantial flow of the material around the notch. By remaining in an elastic regime, the predictions furnished from the crack initiation model break down, as the model requires an appreciable extent of plasticity at the notch, as measured by the area under the load versus load-line displacement curve for the first cycle. On the contrary, as the level of J_1 increases, and thus the extent of plasticity at the notch tip during the initial loading, regardless of the load ratio, the cycles to crack initiation decreases and all curves trend to a lower asymptote.

The function of the constants within the crack initiation model have the ability to shift the initiation cycle curves up or down, left or right, based on the experimental data. By increasing the proportional constant D by a factor of 25%, the predictions are observed to shift upwards, resulting in the same percentage increase in the predicted number of cycles to crack initiation. More pronounced changes in the behavior of the curve are obvious when the exponentials are changed. Setting the J_1 exponent, p, to unity, a significant amount of life to crack initiation is reduced, with cycles to crack initiation around 500 for ranges of J_1 in this study, as shown in Fig. 6.4. By modifying the load ratio exponent, q, to unity, small shifts in the curve are observed, as the significance of the cycling with different responses at the notch tip are less pronounced, as shown in Fig. 6.5. In these cases of modifying the constants, the trend in behavior is still observed and no breakdown of the model is observed.

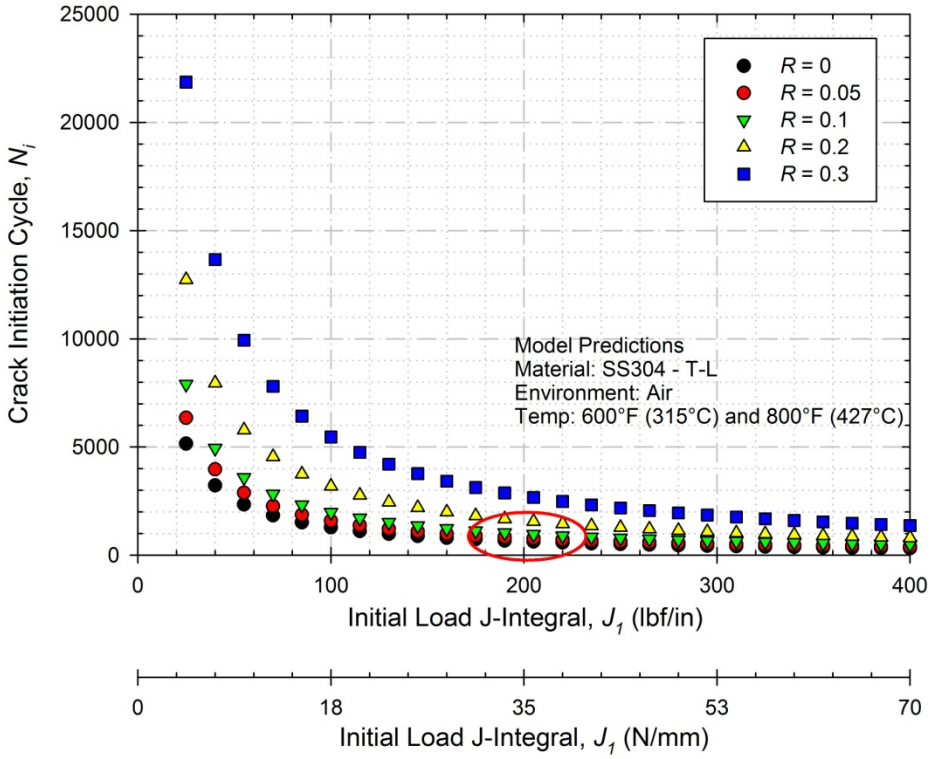

Figure 6.4: Effect of modifying the J_1 exponent, p, to unity on the predicted number of cycles.

The method of experimentally calculating the approximate J_1 value inherently accounts for deformation during the hold period, as any elongation during the initial load cycle is readily captured. This behavior in the elongation can be due to either the hardening/softening of the material or primary creep, if the temperature and stress are sufficient for those conditions. Furthermore, an increase in temperature should decrease the cycles to initiation, as well as the stiffness of the material, resulting in more deflection measured along the load line. By measuring the load-line deflection and integrating over the entire load versus load-line deflection curve, valid approximations can be made, without adding the complexity of a hold time or temperature dependency on the cycles to crack initiation prediction.

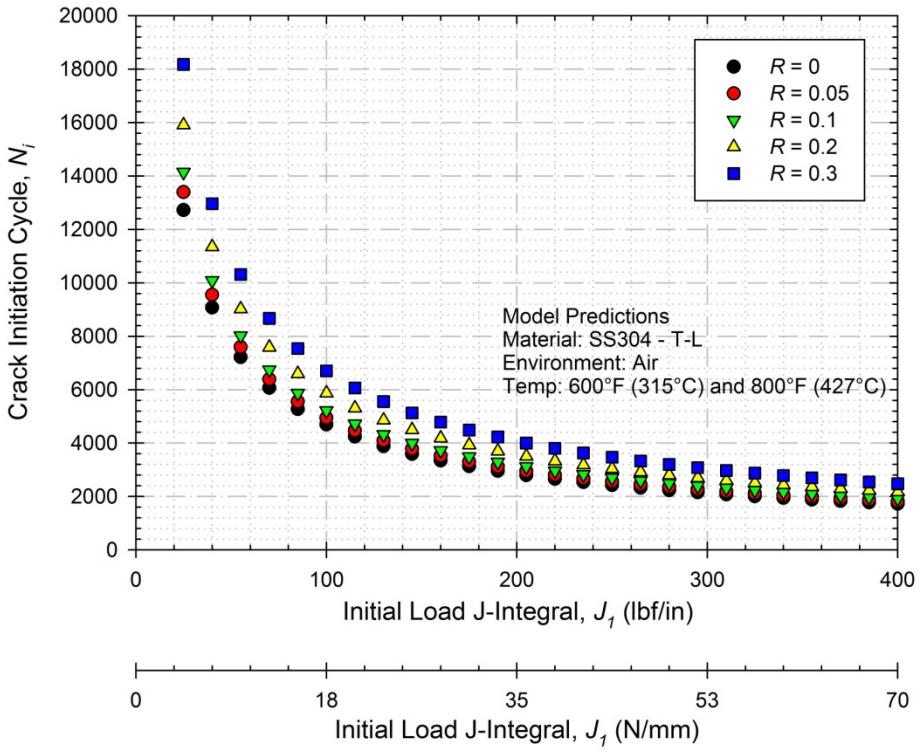

Figure 6.5: Effect of modifying the load ratio exponent, q, to unity on the predicted number of cycles.

Using the prediction method, a prediction to the number of cycles for a test in which no initiation was observed can be made. As noted in Section 4.2.2, a test mimicking the experimental conditions of BN17 was conducted with a load ratio of R = 0.4. The test was stopped after ~5900 cycles, as no signs of initiation had become apparent. Implementing the fit constants for the experimental data, crack initiation would have been expected to occur around 24,000 cycles, a direct result of the deceased alternating stress range at the tip. As this is above the scope of the intended cycling, in which close to R = 0 loading is encountered, such a test would have been unreasonable for the desired model. Ultimately, such experiments can be conducted, as presented in Chapter 8; however, the failure to observe any crack initiation signs in a test that lasted nearly as long as the longest experiment in this investigation provides evidence that extrapolation of the crack initiation model is successful.

Utilizing the baseline scenario of Table 6.1 for the crack propagation rates, the effect of varying parameters on the predicted crack initiation rates are observed. As with the crack initiation model, the major contributing factor to the rate of cracking is in the load ratio at which cycling is conducted, as shown in Fig. 6.6. As the load ratio, R, increases, a significant increase in the crack growth rates is observed, notably towards the higher cyclic-J values. This behavior is expected, as higher mean stresses accelerate the crack growth rates, as in [Forman et al., 1967]. Emphasizing cases involving $R = 0$ cycling, the effect is not as exaggerated; however, caution would be advised when extrapolating out to cases with significantly higher mean stresses at the root of a notch in an extensively plastic region.

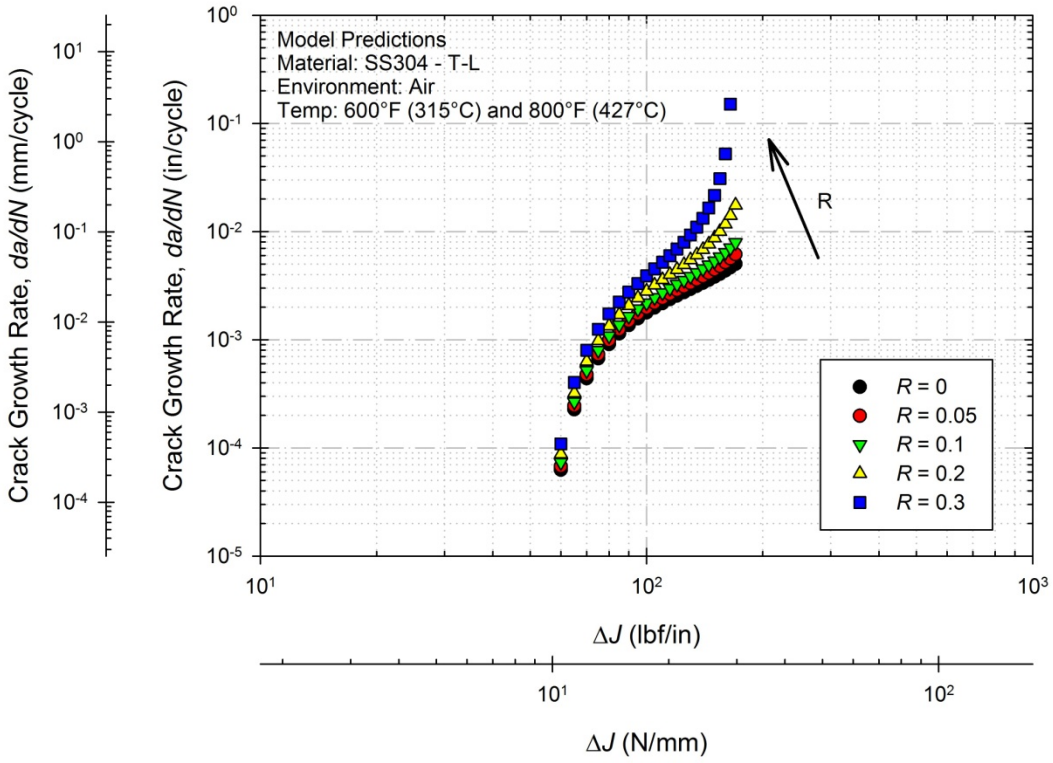

Figure 6.6: Predictions of crack propagation rates over various load ratio values.

Notable differences are observed when varying key parameters of the crack propagation model. The proportional constant C affects the crack growth rate as expected, as any increase or decrease in the value will result in a respective increase or decrease in crack growth rates. Increasing any of the exponents tailored for the Stage I, II or III regime results in a decrease in the crack growth rate, with an example provided in Fig. 6.7. It is readily observed that each exponent for the Stage I, II or III term alters the corresponding crack growth curve when all other constants remain unchanged, as in the case of the baseline in each plot, with emphasis on regions highlighted in blue. The form of the crack propagation model in Eq. (5.2) is such that it allows the crack propagation rate to be highly modified with little changes in the constants chosen for a, b or c. Exaggeration on any one particular regime of crack growth can be made with small variations of the exponent constants.

Utilizing identical constants for C, a, b and c, the most significant changes in predicted behavior in crack growth rates are observed when the values of ΔJ_{stab} and J_c are modified. By changing the rate of constant cycling prior to the initiation of a crack, i.e. the value of ΔJ_{stab}, the prediction accurately captures the cyclic effect, as shown in Fig. 6.8. Decreasing the value of the ΔJ_{stab}, relating to a decrease in the cyclic-J value for crack initiation, provides for a slower acceleration of crack growth rates as ΔJ increases due to crack extension. While the growth rates are higher, as a whole, the rate at which they increase has decreased, as would be expected. In the event that crack growth rates are indeed lower for the lower cyclic-J case, proper adjustments to the fitting constant C can shift the curve to achieve the predictions more closely resembling experimental data.

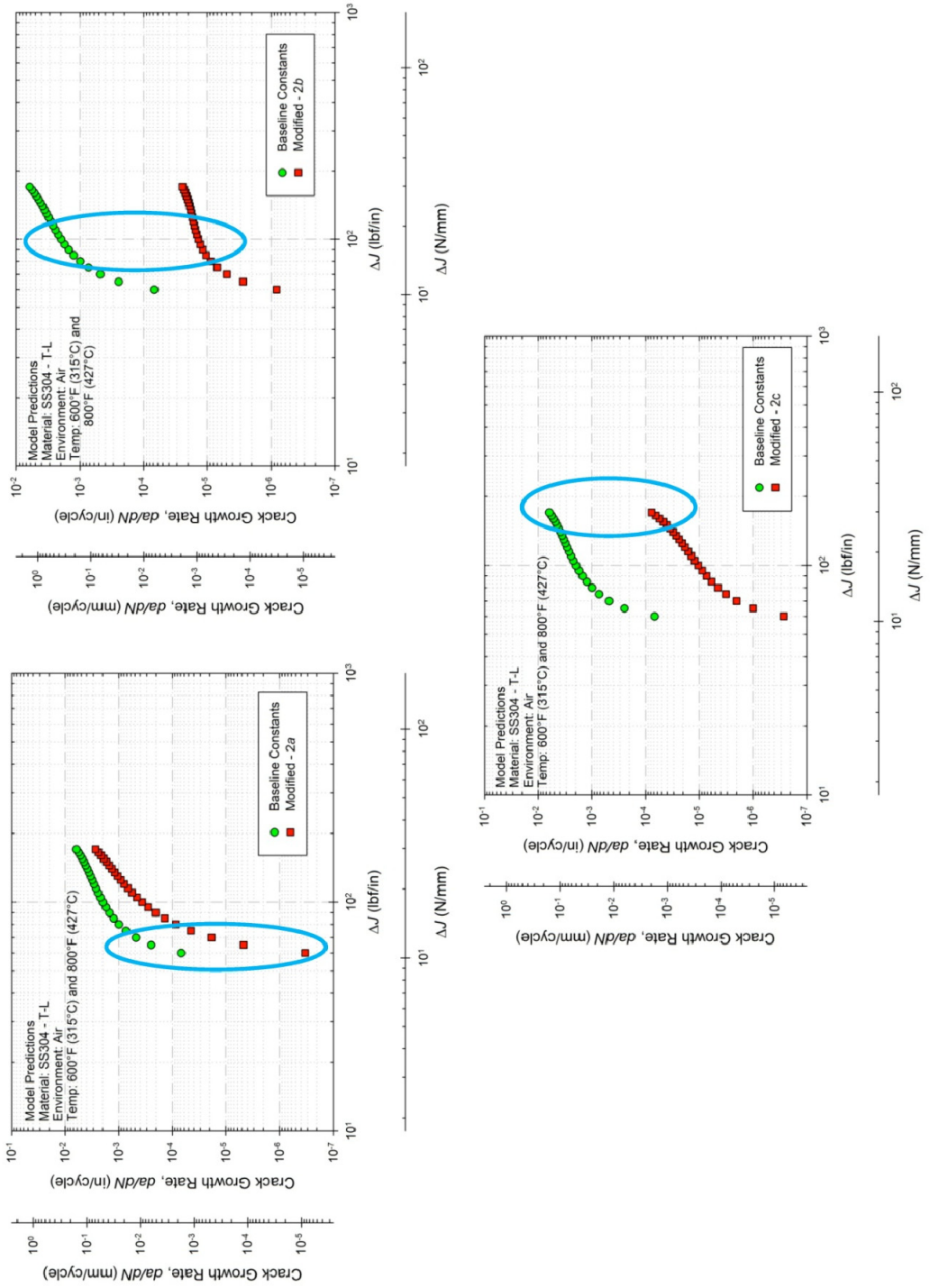

Figure 6.7: The effect of increasing either exponent a, b, or c results in a lower predicted crack propagation rate.

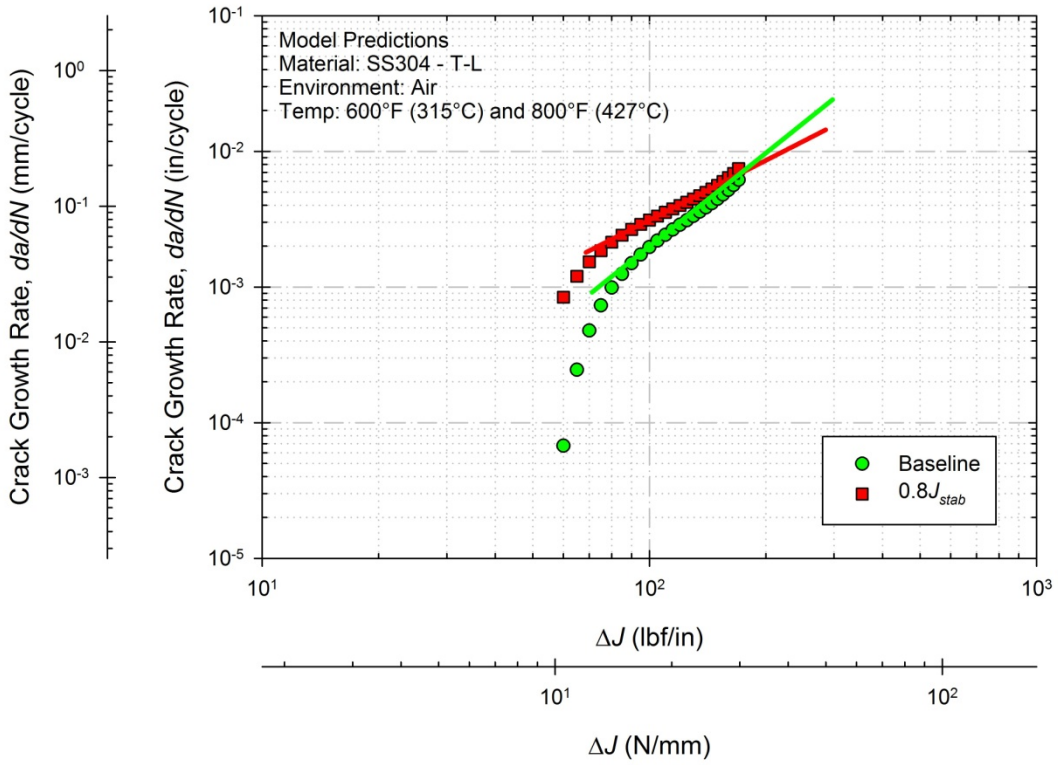

Figure 6.8: Effect of decreasing the J_{stab} parameter for identical test conditions, resulting in a lower acceleration of crack growth rates.

Conversely, the effect of the constant J_c on the crack propagation rate is such that a decrease in the value results in a significant increase in predicted crack propagation rates, as shown in Fig. 6.9. The constant J_c is directly tied to the asymptotic behavior observed in Stage III crack growth, providing the upturn in predicted rates as ΔJ increases due to crack extension. Predicted rates will be highly dependent upon the selection and fit of this value, necessitating that rates nearing the instability of the material be accurately captured. If the value of J_c is too large, predictions will be highly non-conservative, resulting in an over prediction in total life due to lower-than-observed predicted crack growth rates. To counteract uncertainty in the asymptotic value, the value of the proportional constant can be decreased, resulting in a decrease in the predicted crack growth rates, as shown in Fig. 6.10. Furthermore, the exponent constants can be tailored to more closely resemble experimental data; however, would require a more

comprehensive study of all the constants. By simply modifying the proportional constant C, a balance between conservative and non-conservative predictions can be achieved.

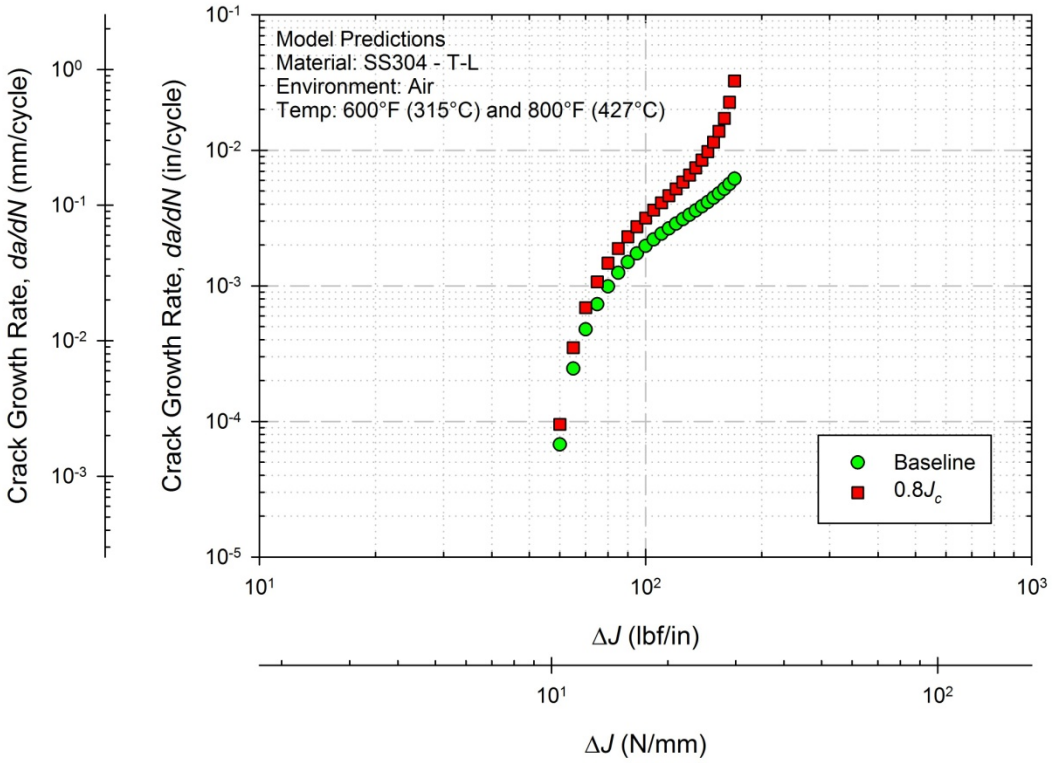

Figure 6.9: A decrease in the J_c constant results in a increase in both the predicted crack growth rate and the acceleration of predicted rates.

Extrapolation of the proposed crack propagation model to additional conditions is exhibited to be straightforward. The components targeted to capture Stage I, II and III crack growth under general plasticity accurately replicate the experimental growth curves. This is of key significance to the model, as tailoring of the constants will allow for predictions based on the crack growth rates observed for additional experimental data sets. In most phenomenological models, this is the key to the success of the model; by varying the constants, the behavior is not changed, just the value of the prediction. It is observed that some constants are more significant that others in terms of behavior, i.e. J_c and ΔJ_{stab}; however, manipulation of the remaining constants readily account for increased or decreased rates, as well the acceleration of rates.

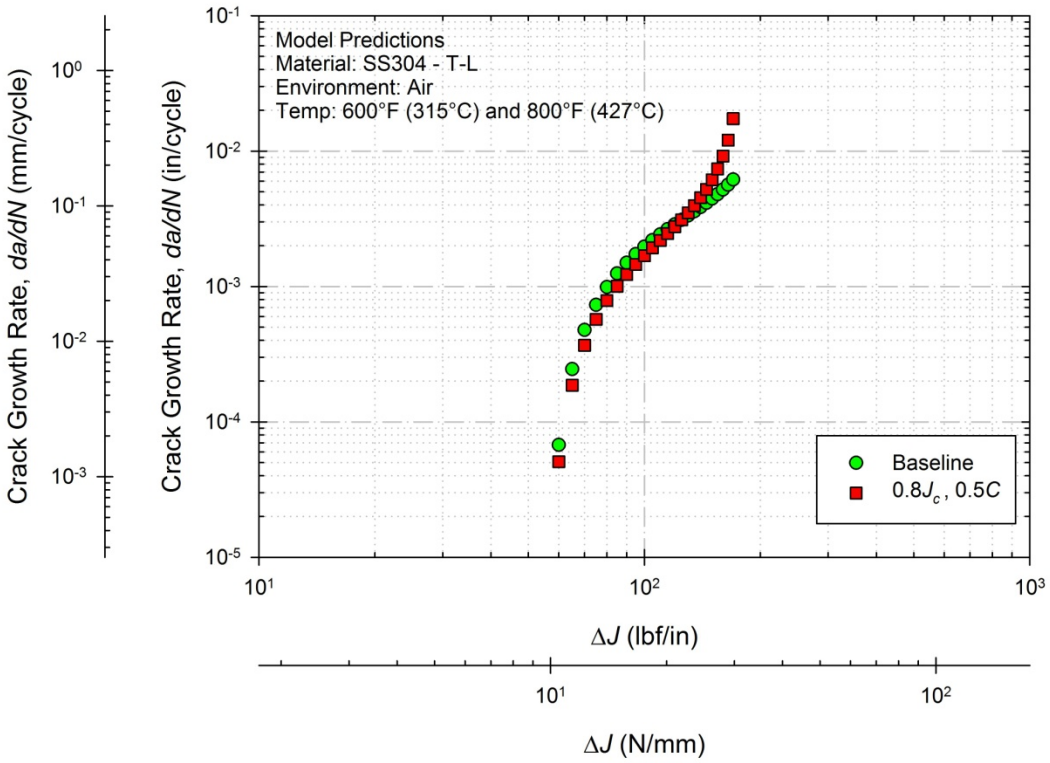

Figure 6.10: Effect of compensating the proportional constant, C, to account for uncertainty in the instability-related constant, J_c.

6.3 Extension of Models to Linear Elastic Scenarios

Extension of the coupled crack initiation and propagation models to linear elastic cases can be made in limited fashions. The use of elastic-plastic parameters, namely the approximation of J_1, limits the extension of the crack initiation model; however, in the event that linear behavior is observed during early stages of crack growth, the propagation model can be carefully implemented. Experimental routines, similar to the one used in this investigation, can be applied to study crack initiation and propagation simultaneously under the case of linear elastic conditions. In the event that small scale yielding is observed throughout the entirety of a test, approximations for linear elastic parameters can be made based on elastic-plastic parameters.

The intended use of the crack initiation model is in the analysis of cracks that initiate at a location in a component that exhibits yielding upon initial loading. In the current investigation, a significant amount of plasticity was observed during the first cycle, directly related to the load applied, specimen geometry and elevated temperatures. The approximation of J for the first cycle included the extensive plasticity; however, it is possible that similar initiation criterion could be implemented, similar to that of Fig. 2.8 [Boukharouba et al., 1995]. Such an approach may require an additional parameter, e.g. a linear elastic equivalent of the proposed ΔJ_{stab} or the notch root radius, to more accurately define the initiation cycle in the absence of plasticity, with several examples presented in Section 2.1.

Extending the crack propagation model to linear elastic scenarios can be done by converting the cyclic parameter ΔJ to the linear elastic equivalent ΔK. Previous research has confirmed the validity of relating elastic-plastic parameters to linear elastic parameters in the presence of small scale yielding, e.g. [Dowling and Begley, 1976; Saxena et al., 1981], using analytical relations, i.e.,

$$\Delta K = \sqrt{E' \Delta J}\,, \tag{6.1}$$

where E' is the elastic modulus. Using specimens with thicknesses not conforming to ASTM plane-strain conditions, the traditional modification to the elastic modulus depending on the state of stress should be made, i.e.,

$$E' = \begin{cases} E \rightarrow \text{Plane Stress} \\ \dfrac{E}{1-\nu^2} \rightarrow \text{Plane Strain} \end{cases}. \tag{6.2}$$

The working form of linear elastic variation of the proposed crack initiation model would include linear elastic counterparts to the elastic plastic parameters in Eq. (5.2), i.e.,

$$\frac{da}{dN} = \frac{C\left(1 - \frac{\Delta K_{stab}}{\Delta K}\right)^{a}}{\left(\Delta K\right)^{b}\left[\left(1-R\right)K_{c} - \Delta K\right]^{c}}. \tag{6.3}$$

Equation (6.3) bears a resemblance to the linear elastic models outlined in the elastic-plastic model developed, outlined in Section 5.2.2, with the main difference being the ΔK_{Stab} parameter. Here, ΔK_{Stab} represents the stabilized value of the cyclic stress intensity at which constant cycling was conducted prior to crack initiation. Coupling Eq. (6.3) with a potential variation of the proposed initiation model, a complete life prediction could then be made, based on the linear-elastic extrapolation of the proposed crack initiation and propagation models

6.4 Summary of Capabilities and Limitations

The current state of the proposed crack initiation and crack propagation models are tailored around the experimental data obtained in Chapter 4. It is envisioned that both are to be implemented into the design and evaluation of structures subjected to creep-fatigue conditions. The strengths and limitations of both the initiation and propagation models are provided.

6.4.1 Creep-Fatigue Crack Initiation Model

The capability of the crack initiation model utilizing the approximated J for the first cycle, J_1, and the load ratio is powerful in the simplicity of the model. In this investigation, the method of calculating J by integrating the load versus load-line deflection curve correlated well with the number of cycles to crack initiation. Semi-automated routines were developed to calculate the area under the curve for selected cycles, simplifying and accelerating the post-processing of experimental data. Using Eureqa to parametrically obtain material constants allowed minimal user-input and provided a set of best-fit constants based on the user selected error metric of R^2. The temperature ranges over which experiments were conducted did not draw

out any temperature dependencies regarding the constants; however, it is intended for future work to establish any such dependency over a broader temperature range, if necessitated. Ultimately, the simplicity of obtaining data, post-processing and fitting required constants enables to model to be employed by structural analysts with relative ease.

Implementing the model, as outlined in the previous section, the designer/analyst would simply need to simulate the response of the structure and obtain the approximate *J*-integral around the area of interest. Nodes are necessary along the region where cracks are expected to grow, thus requiring knowledge of appreciable stress concentrations within the component. Through the use of simplified stress analyses and engineering judgment, nodes will need to be placed at the location of anticipated crack initiation, enabling the calculation of *J*. Integral calculation routines are specific to the software package used, e.g. ANSYS or Abaqus, therefore the analyst will need to be familiar with the proper procedures. With the approximated value of *J* for the initial loading cycle, the life to crack initiation can readily be made.

Currently, the model has been developed and implemented for one specific test geometry. It was noted that using the relation in Eq. (3.3) requires the use of a deeply notched component, such as a C(T) or SENT specimen [Dowling and Begley, 1976]. To accurately capture a meaningful approximation of *J*, such specimen geometries will have to be implemented in the initiation studies, replicating a crack as best as possible in a component. Furthermore, one notch root radius and one specimen width was implemented, leaving the model currently untested for various radii and thicknesses. Specimen thickness will change the crack propagation type, i.e. plane-strain versus plane-stress, but the model is not expected to be affected as the calculation of *J* shall include thickness effects. The radius was chosen for the optimal cost of machining and

similarity to the radius found on components of interest to gas turbine designers; however, the extension to various notch root radii cannot be experimentally verified within this study.

Experimental routines were implemented that utilized temperatures that did not result in significant oxidation or creep contributions during the hold periods, as measured by the DCPD system and CMOD gage. Cracks were not observed to initiate due to oxidation and upon the completion of the first several cycles, the subsequent cycling was noted to be nearly linear, as shown in Fig. 4.23. Extensive plasticity was observed throughout the duration of the test; however, prior to initiation, little accumulated plasticity, either due to fatigue, relaxation, or creep mechanisms, was observed. In the event that non-negligible oxidation and plasticity is accumulated due to elevated temperatures or longer hold periods, respectively, appropriate modifications to the model parameters may be necessary.

To address the current limitations in the creep-fatigue crack initiation model, recommendations for future investigations will be provided in Chapter 8.

6.4.2 Creep-Fatigue Crack Propagation Model

The creep-fatigue crack propagation model allows analysts to calculate the crack growth rates and determine crack lengths after a desired number of cycles. No limitations on specimen size or geometry are imposed, as the EPFM approach readily accounts for plasticity and crack tip blunting. Similar to the initiation model, material constants were observed to be independent of the experimental test temperatures within this investigation. The hold period was not observed to have an effect in the crack growth rates, as the method of calculating J from the area under the load versus load-line displacement curve accounted for any additional deflection during the course of a single cycle. Evaluation of the material constants is straightforward with the use Eureqa to parametrically maximize the correlation with experimental data. The model is suitable

for crack growth analyses following the crack initiation model or as a standalone analysis, depending on the type of structural assessment conducted.

A main limitation of this crack growth model relates to the upper and lower bounds used as asymptotes in Stage I and III crack growth regimes. Traditionally, the lower bound relates to the threshold at which no crack growth is expected below and the upper bound relates to the value corresponding to instability within the material. In LEFM studies, these values for the lower and upper bound are the experimentally obtained values K_{th} and K_{Ic}, respectively. In the proposed model, the threshold value relates back to the approximate value of ΔJ_{stab} that the component cycled at prior to initiation, whereas the upper bound was an approximation based on the maximum ΔJ obtained for all tests. For this investigation, the threshold value was bound between 50lbf/in (9.63N/mm) and 60lbf/in (10.5N/mm), leading to the possibility that rates are dependent upon the initial cycling, as shown in Section 6.2.

Furthermore, the effect of lowering ΔJ below ΔJ_{stab} is observed to result in a breakdown of the crack propagation rates, as shown in Fig. 6.11. If a change in the load during experiments results in a value of ΔJ below ΔJ_{stab}, then the crack propagation model will fail to make predictions, as the exponent a will cause the model to result in negative crack growth rates. To represent the effect of dropping below ΔJ_{stab}, the exponent was changed to 2, enabling positive rates to be predicted. It is observed that crack growth rates are extremely high when this occurs, and should be avoided. The implication is that the model is not intended for fluctuations of ΔJ that result in values being less than ΔJ_{stab}. As such, experimental testing shall be conducted at various maximum load levels, tailoring this value to specific alloys and geometries in actual components. The upper bound value of the instability, J_c, is expected to remain the same for all tests.

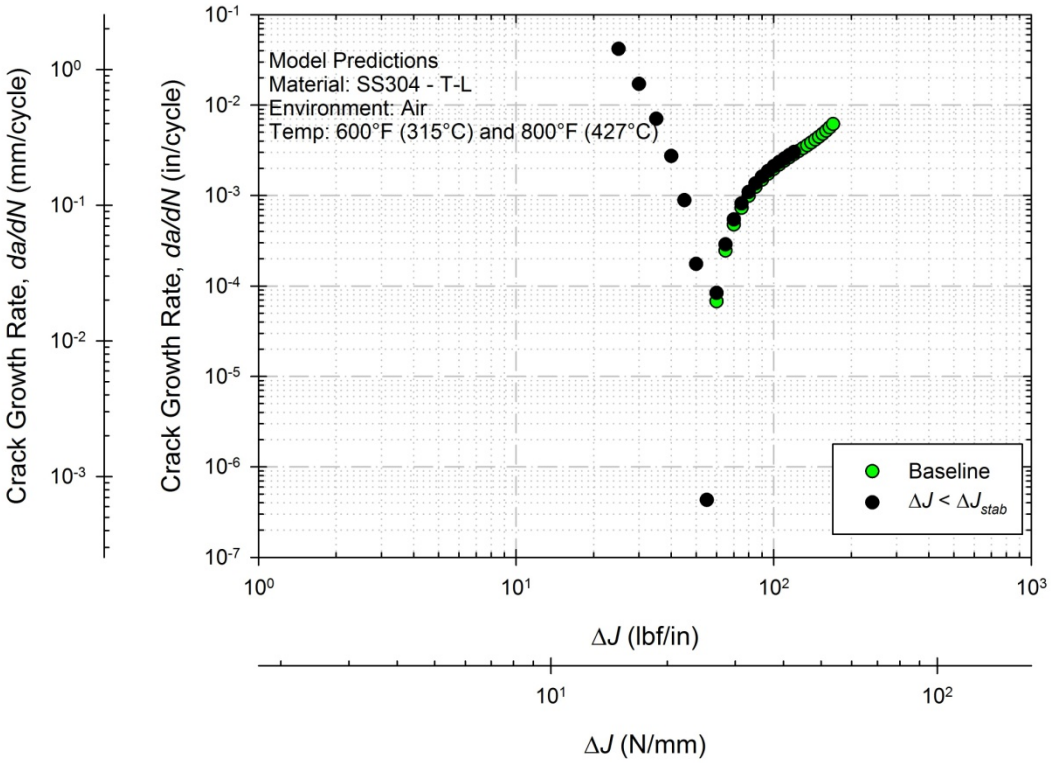

Figure 6.11: The effect of dropping ΔJ below the ΔJ_{stab} value on crack propagation rate predictions.

The other leading limitation to the current form of the crack propagation model is the limited range of temperatures tested within this investigation. Experimental investigations into the crack growth rates of SS304, among other alloys, have shown a dependency on temperature, resulting in an increased rate at increased temperatures for similar stress intensity ranges, e.g. [James and Schwenk, 1971]. Using the elastoplastic analysis in this investigation, crack growth rates were predicted using an approximated form of the *J*-integral, which over the temperature range implemented, was successful in correlating experimental and predicted crack growth rates regardless of the experimental test temperature. Creep deformation mechanisms were not observed, as detailed in Chapter 4, resulting in the inability to definitively conclude that the proposed models inherently incorporate temperature effects and that the constants are useful over a full range of temperatures. This limitation will result in the future testing of experimental

specimens over additional temperature ranges relevant to creep-fatigue and the service temperatures of the particular alloy, outlined in Chapter 8.

Limited amounts of crack growth were able to be sustained within the specimens due to the adherence to ASTM standards on specimen size, in particular the a/W ratio. Traditional crack growth experiments employ a modified specimen, in which the specimen width, W, is elongated in order to capture extensive crack growth data. The scope of this investigation was to focus on lengths that would result in the repair or removal of a component from service in an IGT, but in the event that extensive long crack growth rates are necessary, modifications to the specimen width is necessary. Modification to the test specimen will not result in the modification proposed model, as the crack propagation model is geometry independent. It is capable of replicating data from all stages of crack growth, pending the appropriate constants are fit to the experimental data.

To address the current limitations in the creep-fatigue crack propagation model, recommendations for future investigations will be provided in Chapter 8.

CHAPTER 7
CONCLUSIONS

The dual-use of industrial gas turbines used in the power generation industry has resulted in the need for advanced structural life assessment routines. Traditional approaches have included independent creep and fatigue analyses; however, with the increased use of IGTs as "peakers," coupled creep-fatigue analyses are necessary in life prediction routines. The development of a comprehensive crack initiation and propagation model included the use of a modified fracture specimen used in an experimental setup capable of imparting creep-fatigue conditions similar to those found on the subject SS304 in service conditions. Incorporating both the initiation and propagation stages, two phenomenologically-based models were proposed to be used in tandem to predict the total life of a component subjected to various load waveforms at elevated temperatures. Both the crack initiation and propagation models are observed to be based upon the elastic-plastic fracture mechanics parameter J, as well as the load ratio, R, capturing the effects that both fatigue and creep have on the total life of the component. Material constants were observed to be independent of temperature, requiring minimal parameter determination and optimization. Implementation into routine structural analyses is straightforward, enabling the models to be used in standard life prediction routines with limited amounts of additional work.

An overview of the accomplishments made within this investigation is provided:

- **Implemented a component-like test specimen in experimental approaches capable of capturing both crack initiation and propagation processes.** Using a modified C(T) blunted fracture specimen, crack initiation and propagation was observed within a single specimen. With the exception of the thickness, specimen dimensions outlined in ASTM standards regarding fracture and crack growth studies were adhered to, which enabled the

use of standard test fixtures and monitoring equipment found in mechanical test labs. It was observed that both crack initiation and crack propagation rates could be obtained from one single specimen, eliminating the need for independent experiments or the pre-cracking of fracture specimens.

- **Designed and implemented a universal creep-fatigue test system on a standard electromechanical load frame.** Implementing a standard electromechanical (EM) load frame commonly found in research labs, an experimental setup that included a high temperature furnace, crack mouth opening displacement gage and direct current potential drop crack monitoring system was successfully utilized. Systems requiring active control made use of closed-loop PIDs and all monitoring channels were successfully captured within a single data acquisition system within the load frame software. Main advantages of this system included the reduction of cost of test equipment over a comparable servohydraulic setup and ease-of-use associated with EM load frames.
- **Developed experimental routines used to investigate various factors affecting creep-fatigue crack initiation and propagation.** Experimental routines were developed capable of subjecting test specimens to a variety of load waveforms under isothermal conditions. The main test routine enabled the user to define the test temperature, the maximum and minimum load (thus the load ratio), the waveform characteristics (rise, hold, and fall times) and the rate at which to sample data. Furthermore, custom load waveforms can be readily furnished for future studies, e.g. unsymmetrical load rise/fall times or multi-waveform tests.
- **Developed formulations that estimate the crack initiation and propagation behavior within a single specimen.** Experimental investigations were employed to develop crack

initiation and crack propagation models based on creep-fatigue loading data from single specimens. Employing a test matrix with various parameters relevant to creep-fatigue behavior, two independent models were proposed to be used in tandem to predict the total life of components. Through the use of EPFM parameters in both of the developed models, crack initiation and propagation was observed to be primarily dependent upon the ΔJ approximation and R, accurately accounting for initiation lives and crack growth rates at two temperatures and an assortment of load waveform characteristics. Microscopy of fractured specimens provided microstructural evidence that observed and predicted crack growth rates were physically rooted and based on experimental data.

- **Proposed methods of implementing the creep-fatigue crack initiation and propagation models into routine structural analyses.** To facilitate widespread dissemination and use of the proposed models, methods of implementing the models into life prediction analyses were furnished. The creep-fatigue crack initiation and propagation models are to be used by the structural analyst to make quick and simple, yet accurate approximations of total life, including crack initiation and propagation. By incorporating intended methods of implementation, the ability to make life predictions using the proposed models is more readily achieved.

CHAPTER 8
RECOMMENDATIONS

This investigation, most notably the development of the crack initiation and propagation models for creep-fatigue investigations involving a single specimen, warrants the further exploration into the capabilities of the proposed models. Ideally, the models are intended to be useful for any load waveform and environmental condition outside of the range implemented within this study in which experimental data is available; however, validation is necessary using additional parameters. Furthermore, to address the current limitations presented in Section 6.2, recommendations for future studies are provided for both the crack initiation and propagation models.

- **Conduct experiments on specimens with various notch root radii of five times smaller and larger.** All of the specimens contained within this study utilized a constant notch root radius. Crack initiation cycles were readily predicted with the proposed creep-fatigue initiation model; however, the model did not include a notch root radius term, as any term would have resulted in a constant value for all tests. The multiplicative constant, D, was satisfactory in accounting for this radius used in this study. It is believed that small variations in the approximate value of J_1, as a result of differing notch root radii, will not significantly alter the results; however, this has yet to be experimentally validated. Future investigations shall include at minimum two notch root radii to observe to effect, if any, that the radius has on crack initiation cycle approximations.
- **Conduct extended tests with longer hold periods designed to accentuate the creep and oxidation effects on crack initiation and growth.** To further extend the initiation and propagation models, additional tests with extended hold periods are to be conducted.

Both crack initiation and propagation models incorporate time through the J approximated implemented, as additional elongation over time is measured and used in approximations. The approximation is therefore readily adaptable for long tests, allowing for the investigation into the effect longer hold periods have on the saturation of J_1 and subsequent cycling. By conducting longer hold period tests, conditions resulting in accelerated damage of key components can be predicted and avoided.

- **Conduct experiments with additional and non-isothermal environments on pertinent alloys to the IGT community.** In both the crack initiation and the crack propagation models, the effect temperature had on both was observed to be inherently included as a result of the EPFM parameter approximations implemented. Significant creep or oxidation contributions were not observed in this investigation; however, by using the ΔJ approximation employed here, it is intended that any contribution will be accounted for through increased deflections recorded by the CMOD gage. Additional, increased temperatures are necessary to validate this claim and should be a focus of future testing. Additionally, the use of non-isothermal conditions, i.e. thermomechanical creep-fatigue conditions, should be investigated to more accurately simulate the startup-shutdown process of an IGT used as a "peaker."
- **Development of automated experimental routines, in which values used in ΔJ approximations are readily calculated.** Post-processing of the experimental data, notably the calculation of ΔJ, required a significant amount of time. To prevent excessive and unnecessary time spent in the post-processing of experimental data, one of two solutions should be employed. The first is to have the test control software program calculate the area under the load versus load-line displacement curve and report the value

for each cycle. For the software employed in this study, this was not an option within the program. The second, more general approach, would be to develop a computer program, e.g. Fortran or MATLAB-based, capable of reading in the exported data and calculating the area for each cycle. This would prevent the experimentalist from spending significant amounts of time on post-processing and could be applied to any data set from any experimental frame.

- **Incorporate additional parameters, both specimen and test-control related, to observe the effect on crack propagation rates.** Future tests conducted shall include additional specimen thicknesses and load waveforms, and the proposed models updated as necessary. The thickness of the specimen is not expected to necessitate a change in either the crack initiation or propagation model, as using the EPFM approximation is applicable when yielding or thickness requirements are insufficient for LEFM analyses. Experimental testing on specimens with various thicknesses will provide the verification for this assumption. Furthermore, routines shall include various maximum loads, allowing the values of J_1 and ΔJ to vary over a larger range. Not only will this assist in providing more data for the crack initiation model, the effect on crack propagation rates will be observed and a more physically-based value for J_{stab} will be established.

APPENDIX A
SPECIMEN AND FIXTURE DRAWINGS

Tensile Specimen Drawing 216
Thick Blunt Notch C(T) Specimen Drawing 217
Thin Blunt Notch C(T) Specimen Drawing 218
Specimen Orientation in Raw Material 219
Tension Clevis Adapter Drawing 220
Extension Rod for Clevis Adapter Drawing 221
Resistance Band Heater Drawing 222
Epsilon COD Gage Drawing 223
Custom 80/20 Frame 224

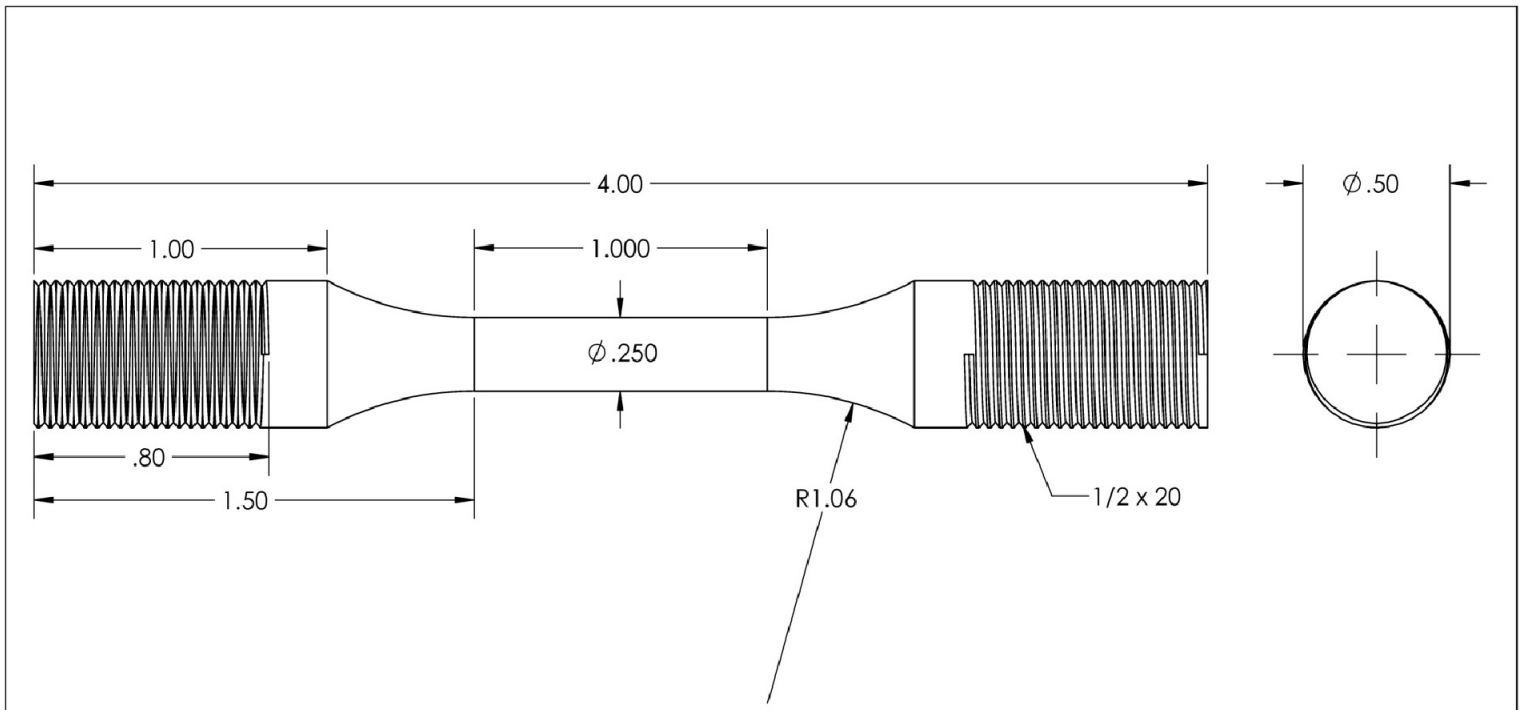

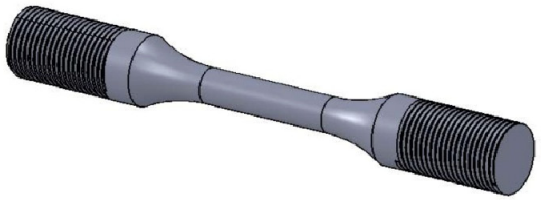

UNLESS OTHERWISE SPECIFIED:	
DIMENSIONS ARE IN INCHES TOLERANCES: .XX - 0.010in .XXX - 0.005in	TITLE: Scott Keller - scott.keller@ucf.edu Ali Gordon - apg@ucf.edu Mechanics of Materials Research Group UCF 4000 Central Florida BLVD Orlando, FL 32816
MATERIAL SS304	
FINISH Smooth	DWG. NO. Tensile_Specimen_UCF
Notes	REV 1
	SCALE: 2:1 SHEET 1 OF 1

4 3 2 1

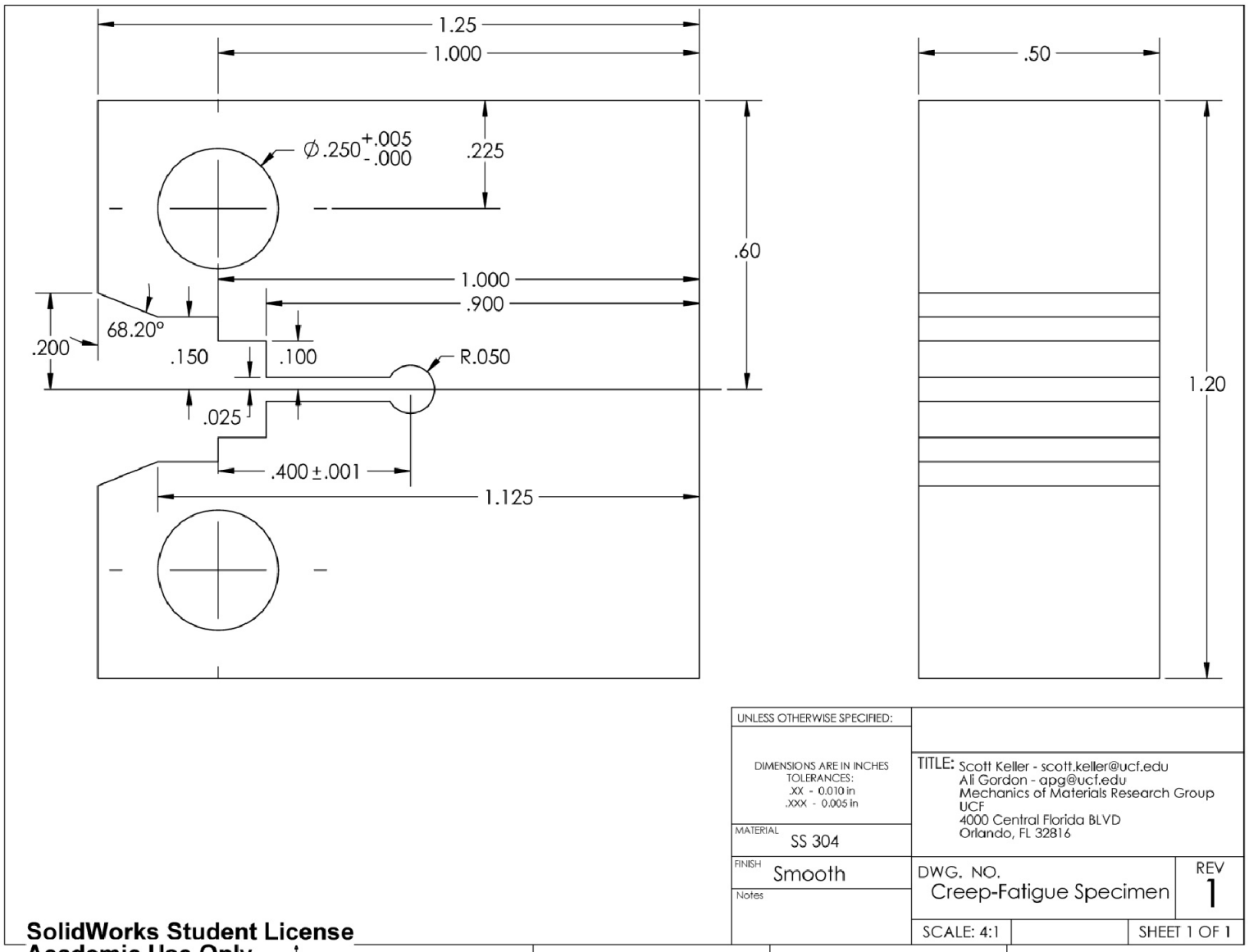
1.25
1.000
.50
Ø.250 +.005 -.000
.225
.60
1.000
.900
68.20°
.200
.150
.100
R.050
1.20
.025
.400 ±.001
1.125
UNLESS OTHERWISE SPECIFIED:
DIMENSIONS ARE IN INCHES
TOLERANCES:
.XX - 0.010 in
.XXX - 0.005 in
MATERIAL
SS 304
FINISH
Smooth
Notes
TITLE:
Scott Keller - scott.keller@ucf.edu
Ali Gordon - apg@ucf.edu
Mechanics of Materials Research Group
UCF
4000 Central Florida BLVD
Orlando, FL 32816
DWG. NO.
Creep-Fatigue Specimen
REV
1
SCALE: 4:1
SHEET 1 OF 1
SolidWorks Student License
Academic Use Only
4
3
2
1

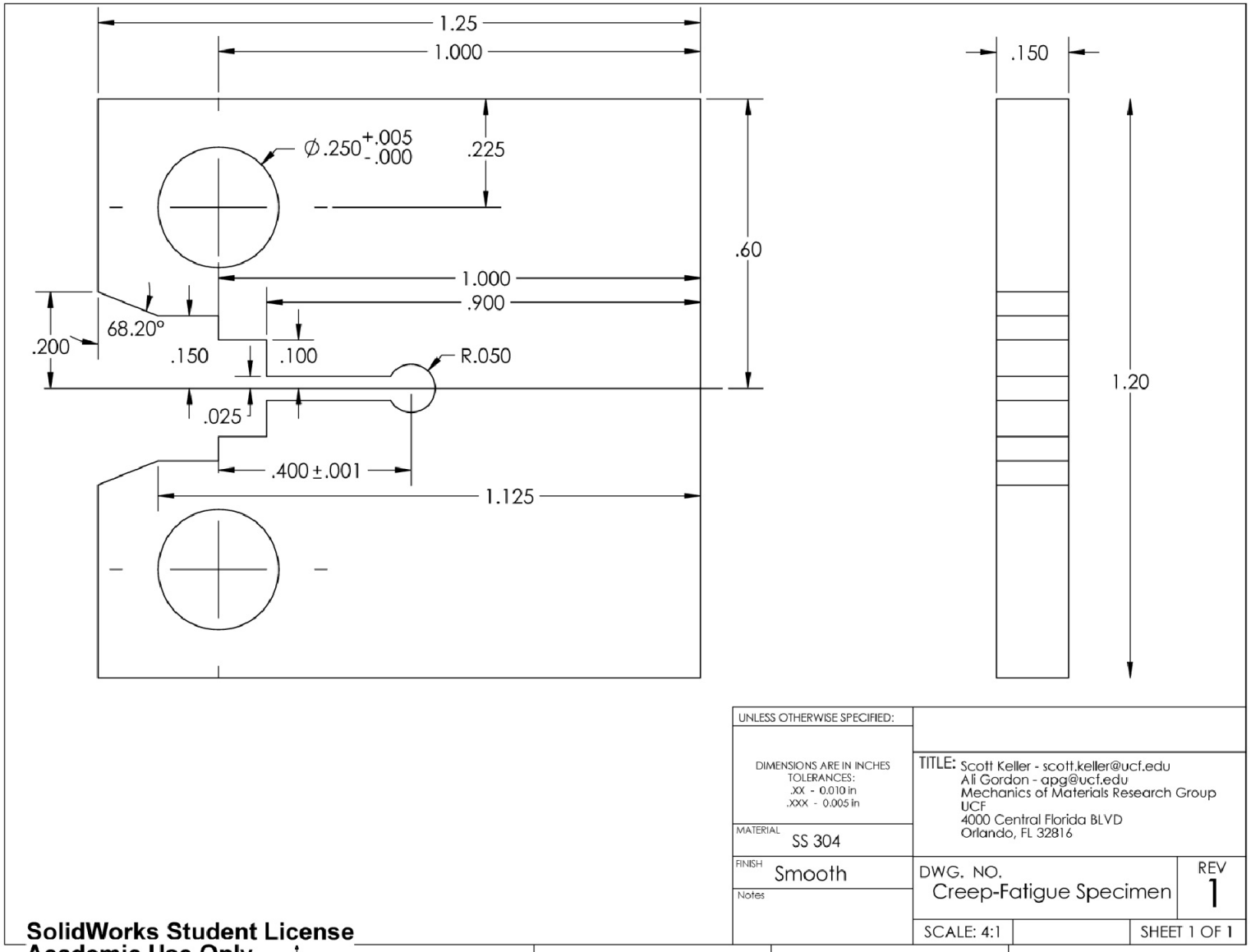
1.25
1.000
.150
Ø.250 +.005 -.000
.225
.60
1.000
.900
68.20°
.200
.150
.100
R.050
1.20
.025
.400 ±.001
1.125
UNLESS OTHERWISE SPECIFIED:
DIMENSIONS ARE IN INCHES
TOLERANCES:
.XX - 0.010 in
.XXX - 0.005 in
MATERIAL
SS 304
FINISH
Smooth
Notes
TITLE:
Scott Keller - scott.keller@ucf.edu
Ali Gordon - apg@ucf.edu
Mechanics of Materials Research Group
UCF
4000 Central Florida BLVD
Orlando, FL 32816
DWG. NO.
Creep-Fatigue Specimen
REV
1
SCALE: 4:1
SHEET 1 OF 1
SolidWorks Student License
Academic Use Only
4
3
2
1

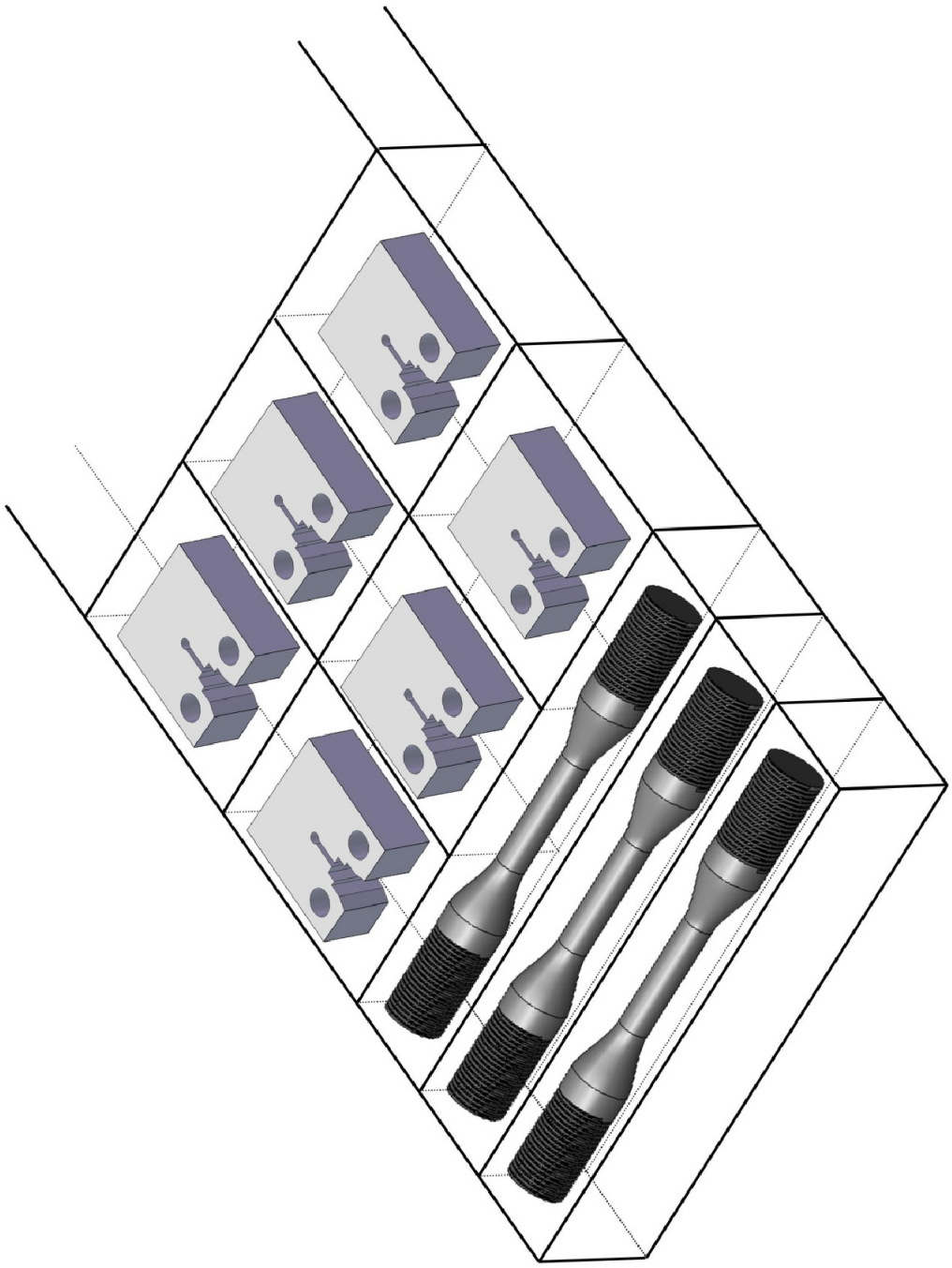

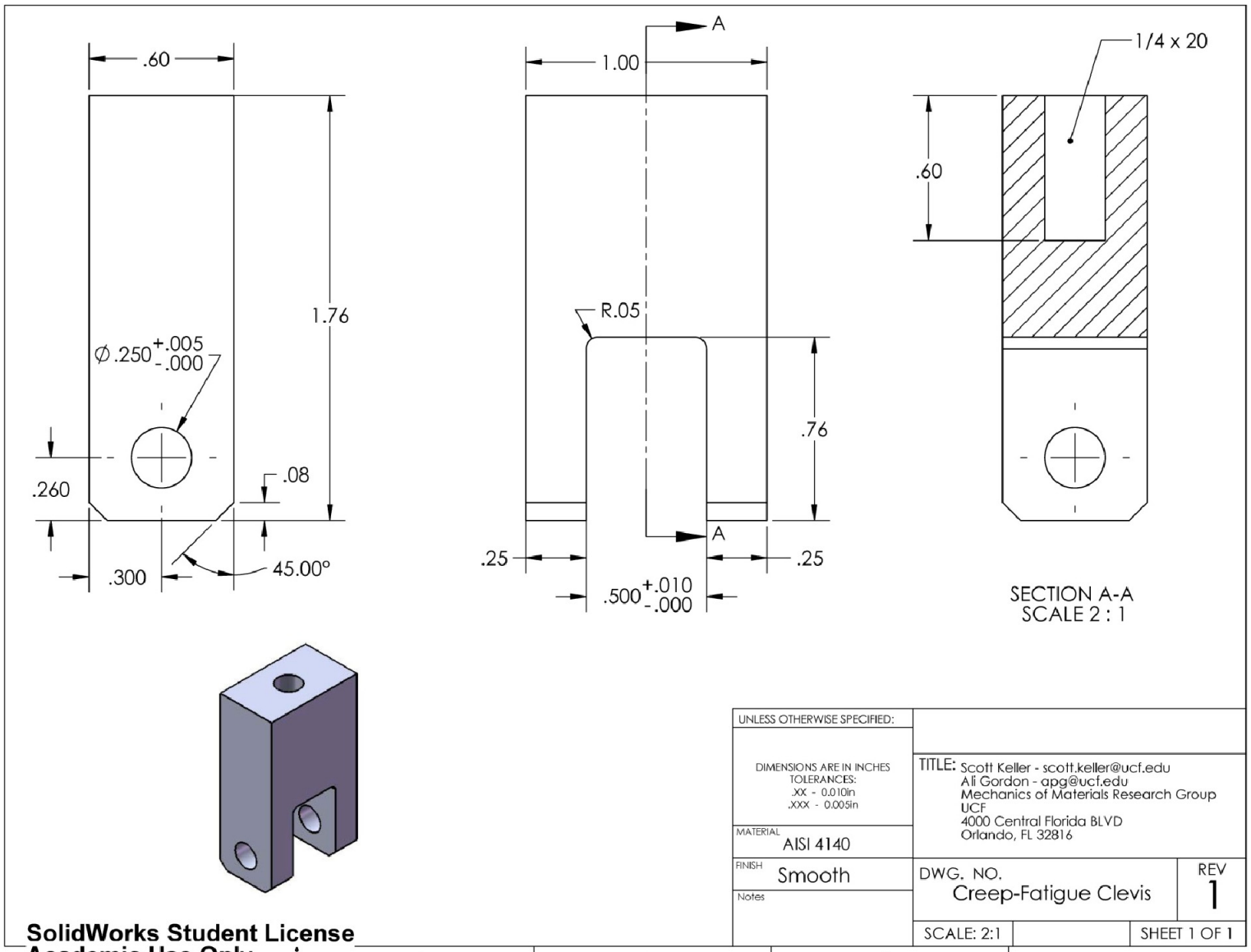
.60
1.76
Ø .250 +.005 -.000
.260
.08
.300
45.00°
A
1.00
R.05
.76
A
.25
.25
.500 +.010 -.000
1/4 x 20
.60
SECTION A-A
SCALE 2 : 1
UNLESS OTHERWISE SPECIFIED:
DIMENSIONS ARE IN INCHES
TOLERANCES:
.XX - 0.010in
.XXX - 0.005in
MATERIAL
AISI 4140
FINISH
Smooth
Notes
TITLE: Scott Keller - scott.keller@ucf.edu
Ali Gordon - apg@ucf.edu
Mechanics of Materials Research Group
UCF
4000 Central Florida BLVD
Orlando, FL 32816
DWG. NO.
Creep-Fatigue Clevis
REV
1
SCALE: 2:1
SHEET 1 OF 1
SolidWorks Student License
Academic Use Only
4
3
2
1

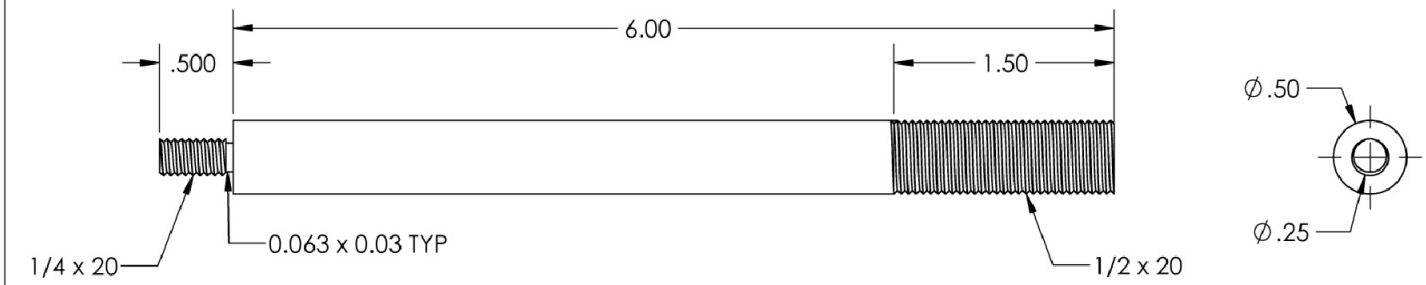

UNLESS OTHERWISE SPECIFIED:	
DIMENSIONS ARE IN INCHES TOLERANCES: .XX - 0.010in .XXX - 0.005in	TITLE: Scott Keller - scott.keller@ucf.edu Ali Gordon - apg@ucf.edu Mechanics of Materials Research Group UCF 4000 Central Florida BLVD Orlando, FL 32816
MATERIAL: AISI 4340	
FINISH: Smooth	DWG. NO. Extension Arms — REV 1
Notes	SCALE: 1:1 — SHEET 1 OF 1

4 3 2 1

2.250	2.500	.500	SCREW CONTACT	500	240
ID	WIDTH	GAP	HOUSING # 2448	WATTS	VOLTS
			OVERLAP FLANGE		

B74772

SHOP #
MAKE
DUE DATE

FINAL OHMS=110

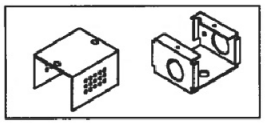

STOCK

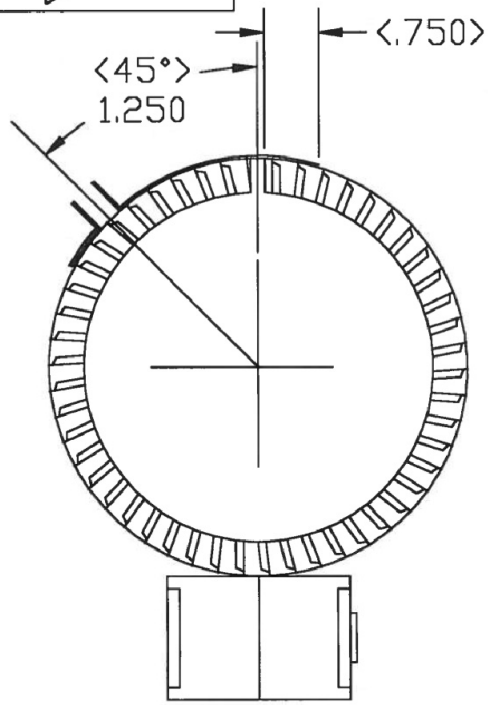

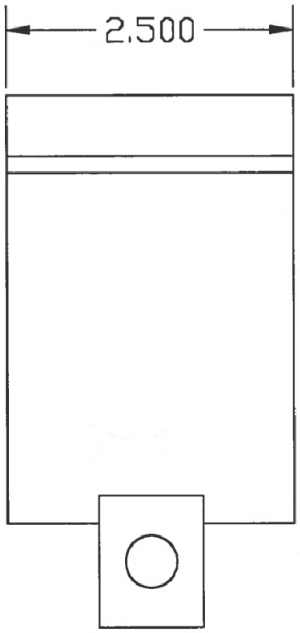

CONTACT HOLES
.375 DIA W C-SINK
.875 APART

CUT FLANGE
20ga ST STL
3.250 X 2.375
2.312 X 2.375

ROLL	N
THICKNEES	.437
NOTCH	.437
MAT SUP	.500
WSI	30
AMPS	2.1

IHCo. DWG	10-18-02	REV-0	BY.HS

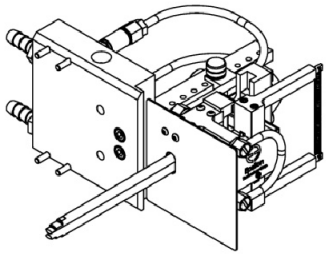

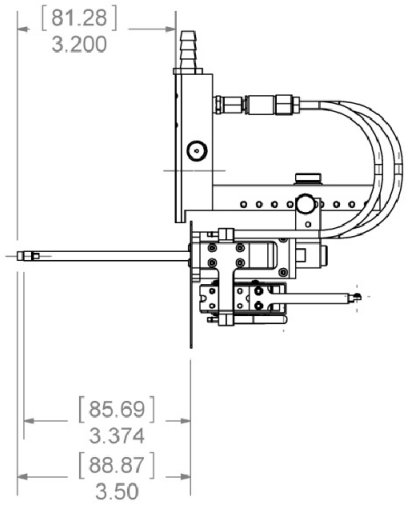

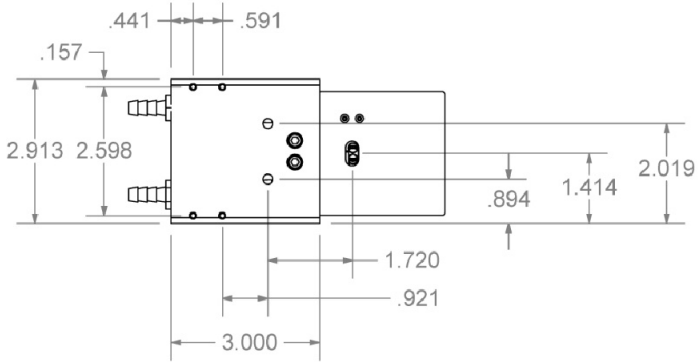

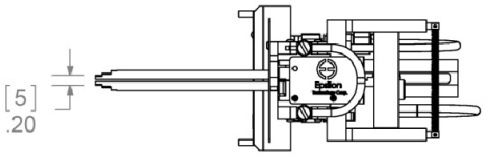

	UNLESS OTHERWISE SPECIFIED : DIMENSIONS ARE IN INCHES. ALL SURFACES 63 OR BETTER. TOLERANCES ARE: 2 PLACE INCHES ±.03; 3 PLACE INCHES ±.005; 4 PLACE INCHES ±.0010; ANGLES ±1°	CAD GENERATED DRAWING, DO NOT MANUALLY UPDATE. DO NOT SCALE DRAWING	Epsilon Technology Corp. Jackson, WY, USA 83001
	MATERIAL	DRAWN SLW 6/23/11	3548COD-005M, Outline
	STOCK SIZE N/A	CHECKED SAA	DWG NO 3548COD-005M-OTNL REV
REVISIONS	FINISH NONE		SIZE A SCALE 1:3 SHEET 1 OF 1

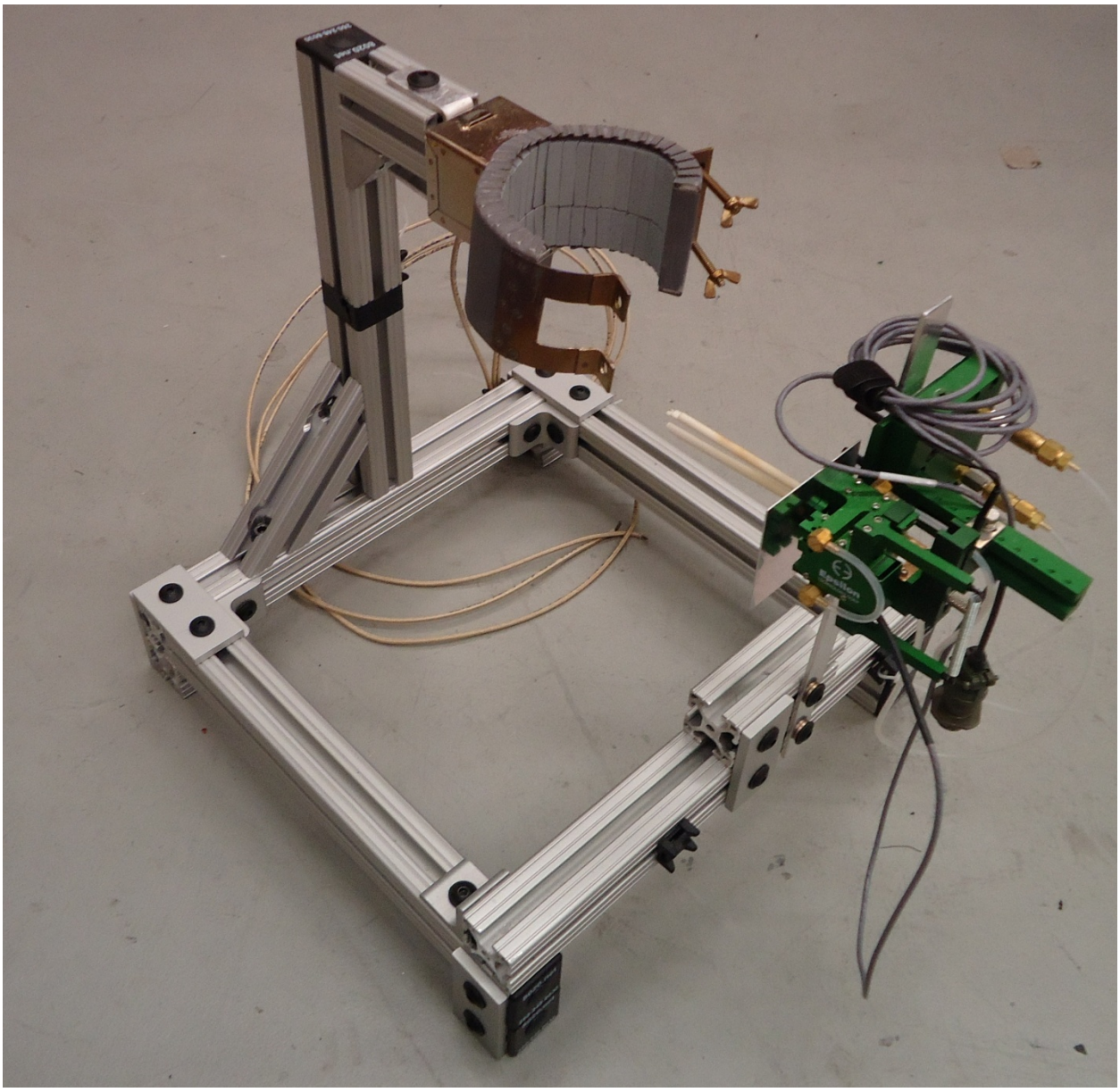

APPENDIX B
CURVE FITTING SOURCE CODE

ASTM Seven Point FCG Reduction Code – Updated Fortran Version.....227

Example Input File for ASTM FCG Reduction Code 232

Example Output File for ASTM FCG Reduction Code.....234

ASTM Seven Point FCG Reduction Code – Updated Fortran Version

```
C*********************************************************************
C*********************************************************************
      PROGRAM Seven_Point_Reduction
C*********************************************************************
C23456789012345678901234567890123456789012345678901234567890123456789012345678901234
C       1       2       3       4       5       6       7
C
C  The purpose of this routine is to reduce da/dN vs. dK data from
C  experimental routines.  Uses the 7-point incremental polynomial method
C  in which regression parameters are determined by least squares method.
C  The value of dK associated with the da/dN value is computed using the
C  fitted crack size, ai, corresponding the the cycle, Ni.
C
C  The code is translated directly from the QB program, without much
C  effort to clean up the code or rename the variables. Future versions
C  should be streamlined to make the code more efficient/updated.
C
C   Source      : ASTM E647 - 08 (QuickBASIC, .bas)
C   Translated  : S. Keller (Fortran, .f)
C   Version             : 1.0
C   Date        : 9/11/2012
C
C*************************  ASTM E647, 2008  ***************************
C  This computer program is for the reduction of experimental FCG data
C  by the Seven Point Increment Polynomial Technique.
C
C  Input parameters as they should appear in the input file:
C   SpecNum: Specimen Number
C   ys: Yield Strength (ksi)
C   B: Thickness (inches)
C   W: Width (inches)
C   Pmax: Maximum load (kips)
C   Pmin: Minimum load (kips)
C   Notch: Notch length (inches)
C   Freq: Frequency of test
C   Specimen: "C(T)" or "CCP"
C   Temper: Temperature (F)
C   Labenviron: Lab Environment
C   n(i), a(i): cycles, crack length (inches) - measured from notch tip
C
C*********************************************************************
C23456789012345678901234567890123456789012345678901234567890123456789012345678901234
C       1       2       3       4       5       6       7
C
```

```
C   Declare Variables
      DOUBLE PRECISION a(9999),bb(3),dadn(200),delk(200),
     &                 aa(10),nn(10),ys,B,W,Pmax,Pmin,Notch,
     &                 Freq,DeltaP,Rratio
      CHARACTER*80 Specimen
      CHARACTER*80 Temper
      CHARACTER*80 Labenviron
      INTEGER i,l,k,kl,SpecNum,npts,Inpt,n(9999),Inum,qq
      DOUBLE PRECISION c1,c2,sx,sx2,sx3,sx4,sy,syx,syx2,x,yy,Term1,Term2,
     &                 Term3,Term4,Term5,Term6,Term7,Term8,Term9,Denom,
     &                 Numer2,Numer3,Numer4,yb,rss,tss,r2,ar,s,snet
     &                 num,den,ft,sec,t,yhat,pi
C
      pi = 3.1416D0
C   Call in the input and output files; read values
      OPEN(unit = 15,file ='input.dat')
      OPEN(unit = 16,file ='output.dat')
      READ(15,*) SpecNum,ys,B,W,Pmax,Pmin,Notch,Freq
      READ(15,*) Specimen,Temper,Labenviron
C
C   Count the number of lines in the file to set npts
      npts = 0
      DO WHILE (.not.EOF(15))
        npts = npts + 1
        Read(15,*) n(npts),a(npts)
C       Not sure why the QB code defines the size of n and a
C       n(npts) and a(npts)
      ENDDO
C
C   Declare constants based on input file
      DeltaP = Pmax - Pmin
      Rratio = Pmin / Pmax
C
C   Add notch length to measure the crack length
      DO Inpt = 1,npts
        a(Inpt) = a(Inpt) + Notch
      ENDDO
C
C   Print Header Information
      WRITE(16,41) SpecNum,npts
41    FORMAT(1X,'Specimen No.: ',I4,T25,'No. of Points: ',I4)
      WRITE(16,42) B,W,Notch
42    FORMAT(1X,'B(in)= ',F5.3,T25,'W(in)= ',F5.3,T50,'A0(in)= ',F5.3)
      WRITE(16,43) Pmin,Pmax,Rratio
43    FORMAT(1X,'Pmin(kips)= ',F5.2,T25,'Pmax(kips)= ',F5.2,T50,'Rratio=
     & ',F5.2)
```

```
      WRITE(16,44) Specimen,Freq
44    FORMAT(1X,'Specimen Type: ',A8,T25,'Test Frequency(Hz)= ',F5.2)
      WRITE(16,45) Labenviron,Temper
45    FORMAT(1X,'Environment: ',A8,T25,'Temperature: ',A8//)
      WRITE(16,17)
17    FORMAT(1X,' No.',T13,'Cycles',T26,'A(Meas.)',T41,'A(Reg.)',T53,
     &       ' M.C.C.',T66,'Delta K',T82,'da/dN'/)
C
C   Print the first three data points
      DO i = 1,3
        WRITE(16,18) i,n(i),a(i)
18      FORMAT(1X,I4,1X,T13,I6,1X,T27,F7.4)
      ENDDO
C
C   Start the routine to reduce the data
      npts = npts - 6
      DO Inpt = 1,npts
        l = 0
        k = k + 1
        kl = k + 6
        DO Iindex = k,kl
          l = l + 1
          aa(l) = a(Iindex)
          nn(l) = n(Iindex)
        ENDDO
C
C   Start calculating the constants
        c1 = 0.50D0*(nn(1)+nn(7))
        c2 = 0.50D0*(nn(7)-nn(1))
        sx = 0.0D0
        sx2 = 0.0D0
        sx3 = 0.0D0
        sx4 = 0.0D0
        sy = 0.0D0
        syx = 0.0D0
        syx2 = 0.0D0
        DO Inum = 1,7
          x = (nn(Inum) - c1)/c2
          yy = aa(Inum)
          sx = sx + x
          sx2 = sx2 + (x**2.0D0)
          sx3 = sx3 + (x**3.0D0)
          sx4 = sx4 + (x**4.0D0)
          sy = sy + yy
          syx = syx + x * yy
          syx2 = syx2 + yy * x ** 2.0D0
```

```
      ENDDO
C
C  Calculate the various terms within the fitting routine
      Term1 = (sx2*sx4 - (sx3**2.0D0))
      Term2 = ((sx * sx4) - (sx2*sx3))
      Term3 = (sx*sx3 - (sx2**2.0D0))
      Denom = (7.0D0*Term1) - (sx*Term2) + (sx2*Term3)
      Numer2 = (sy*Term1) - (syx*Term2) + (syx2*Term3)
      bb(1) = Numer2/Denom
C
      Term4 = (syx*sx4) - (syx2*sx3)
      Term5 = (sy*sx4) - (syx2*sx2)
      Term6 = (sy*sx3) - (syx*sx2)
      Numer3 = (7.0D0*Term4) - (sx*Term5) + (sx2*Term6)
      bb(2) = Numer3/Denom
C
      Term7 = (sx2*syx2) - (sx3*syx)
      Term8 = (sx*syx2) - (sx3*sy)
      Term9 = (sx*syx) - (sx2*sy)
C
      Numer4 = (7.0D0*Term7) - (sx*Term8) + (sx2*Term9)
      bb(3) = Numer4/Denom
      yb = sy / 7.0D0
      rss = 0.0D0
      tss = 0.0D0
      DO Inum = 1,7
         x = (nn(Inum) - c1)/c2
         yhat = bb(1) + (bb(2)*x) + (bb(3)*(x**2.0D0))
         rss = rss + ((aa(Inum)-yhat)**2.0D0)
         tss = tss + ((aa(Inum)-yb)**2.0D0)
      ENDDO
      r2 = 1.0D0 - (rss/tss)
      dadn(Inpt) = (bb(2)/c2)+((2.0D0*bb(3)*(nn(4)-c1))/(C2**2.0D0))
      x = (nn(4)-c1) / c2
      ar = bb(1) + (bb(2)*x) + (bb(3)*(x**2.0D0))
      s = 1.0D+10
      snet = 0.0D0
      qq = Inpt + 3
      IF (Specimen .EQ. 'ct') THEN
         t = ar/W
         num = (0.886D0 + (4.64D0*t) - (13.32D0*(t**2.0D0))
     &          + (14.72*(t**3.0D0)) - (5.6D0*(t**4.0D0)))
         den = ((1.0D0-t)**1.50D0)
         ft = ((2.0D0+t) * num)/den
         s = ys*((pi*W*(1.0D0-t))**0.5D0) / 2.0D0
      ELSE
```

```
          t = (2.0D0*ar)/W
          sec = 1.0D0/(COS(pi*(t/2.0D0)))
          ft = ((pi*t*sec)/2.0D0)**0.5D0
          snet = Pmax/(B*W*(1.0D0-t))
        END IF
C
        delk(Inpt) = (ft*DeltaP)/(B*(W**0.5D0))
        ax = delk(Inpt)/(1.0D0-Rratio)
C
        IF (ax.GT.s .OR. snet.GT.ys) THEN
          WRITE(16,72) qq,n(qq),a(qq),ar,r2,delk(Inpt),dadn(Inpt)
72          FORMAT(1X,I4,T13,I6,T27,F7.4,T41,F7.4,T53,F7.4,T65,
     &            F8.2,T77,F10.8,' *')
        ELSE
          WRITE(16,73) qq,n(qq),a(qq),ar,r2,delk(Inpt),dadn(Inpt)
73          FORMAT(1X,I4,T13,I6,T27,F7.4,T41,F7.4,T53,F7.4,T65,
     &            F8.2,T77,F10.8)
        ENDIF
      ENDDO
C
      j = npts + 4
      k = npts + 6
      DO Iprnt = j,k
        WRITE(16,74) Iprnt,n(Iprnt),a(Iprnt)
74      FORMAT(1X,I4,T13,I6,T27,F7.4)
      ENDDO
      WRITE(16,*) '  * - Data violates specimen size requirements!'
C
      CLOSE(15)
      CLOSE(16)
      END
C*********************************************************************
C*********************************************************************
```

Example Input File for ASTM FCG Reduction Code

Filename: Input.dat

```
1
107
0.25
2
5
4
0.5
5
ct
75F(23C)
Air
0 0.0990
15480 0.1310
22070 0.1560
30240 0.1740
36090 0.1980
41370 0.2180
46850 0.2350
50090 0.2460
54380 0.2530
60320 0.2810
65160 0.3010
70240 0.3210
74690 0.3430
80070 0.3650
83860 0.3860
88080 0.4060
91460 0.4250
95620 0.4450
99000 0.4670
102360 0.4880
105110 0.5080
108440 0.5280
111660 0.5470
113410 0.5670
116810 0.5900
118730 0.6080
121220 0.6280
121880 0.6380
122830 0.6480
124280 0.6660
125820 0.6870
```

127480 0.7070
128700 0.7260
129760 0.7450
130790 0.7770
131480 0.7980
131550 0.8230

Example Output File for ASTM FCG Reduction Code

Filename: Output.dat

Specimen No.: 1 No. of Points: 37
B(in)= 0.250 W(in)= 2.000 A0(in)= 0.500
Pmin(kips)= 4.00 Pmax(kips)= 5.00 Rratio= 0.80
Specimen Type: ct Test Frequency(Hz)= 5.00
Environment: Air Temperature: 75F(23C)

No.	Cycles	A(Meas.)	A(Reg.)	M.C.C.	Delta K	da/dN	
1	0	0.5990					
2	15480	0.6310					
3	22070	0.6560					
4	30240	0.6740	0.6772	0.9969	12.30	0.00000323	
5	36090	0.6980	0.6977	0.9963	12.64	0.00000337	
6	41370	0.7180	0.7156	0.9910	12.96	0.00000319	
7	46850	0.7350	0.7345	0.9925	13.30	0.00000337	
8	50090	0.7460	0.7439	0.9928	13.48	0.00000340	
9	54380	0.7530	0.7579	0.9956	13.75	0.00000347	
10	60320	0.7810	0.7794	0.9965	14.18	0.00000387	
11	65160	0.8010	0.7998	0.9965	14.60	0.00000412	
12	70240	0.8210	0.8225	0.9990	15.10	0.00000444	
13	74690	0.8430	0.8416	0.9995	15.53	0.00000453	
14	80070	0.8650	0.8665	0.9994	16.13	0.00000480	
15	83860	0.8860	0.8853	0.9993	16.60	0.00000493	
16	88080	0.9060	0.9061	0.9992	17.15	0.00000517	
17	91460	0.9250	0.9240	0.9991	17.65	0.00000545	
18	95620	0.9450	0.9465	0.9995	18.30	0.00000583	
19	99000	0.9670	0.9669	0.9992	18.92	0.00000611	
20	102360	0.9880	0.9883	0.9985	19.61	0.00000623	*
21	105110	1.0080	1.0062	0.9971	20.21	0.00000668	*
22	108440	1.0280	1.0283	0.9973	21.00	0.00000693	*
23	111660	1.0470	1.0507	0.9973	21.84	0.00000741	*
24	113410	1.0670	1.0636	0.9976	22.35	0.00000759	*
25	116810	1.0900	1.0910	0.9969	23.50	0.00000843	*
26	118730	1.1080	1.1079	0.9959	24.25	0.00000898	*
27	121220	1.1280	1.1304	0.9986	25.31	0.00001049	*
28	121880	1.1380	1.1372	0.9986	25.64	0.00001109	*
29	122830	1.1480	1.1481	0.9981	26.19	0.00001140	*
30	124280	1.1660	1.1663	0.9993	27.15	0.00001268	*
31	125820	1.1870	1.1854	0.9992	28.21	0.00001342	*
32	127480	1.2070	1.2076	0.9930	29.53	0.00001649	*
33	128700	1.2260	1.2273	0.9946	30.79	0.00002015	*

34	129760	1.2450	1.2494	0.9776	32.29	0.00002794 *
35	130790	1.2770				
36	131480	1.2980				
37	131550	1.3230				

* - Data violates specimen size requirements!

APPENDIX C
EXPERIMENTAL SPECIMEN DATA

Tensile Specimen – Ten1 238
Tensile Specimen – Ten2 239
Tensile Specimen – Ten3 240
Creep-Fatigue Specimen – BN1 241
Creep-Fatigue Specimen – BN2 242
Creep-Fatigue Specimen – BN3 243
Creep-Fatigue Specimen – BN4 244
Creep-Fatigue Specimen – BN5 245
Creep-Fatigue Specimen – BN6 246
Creep-Fatigue Specimen – BN7 247
Creep-Fatigue Specimen – BN8 248
Creep-Fatigue Specimen – BN9 249
Creep-Fatigue Specimen – BN10 250
Creep-Fatigue Specimen – BN11 251
Creep-Fatigue Specimen – BN13 252
Creep-Fatigue Specimen – BN14 253
Creep-Fatigue Specimen – BN15 254
Creep-Fatigue Specimen – BN17 255
Creep-Fatigue Specimen – BN18 256
Creep-Fatigue Specimen – BN19 257
Creep-Fatigue Specimen – BN20 258

Tensile Specimen
Ten1

Specimen	Ten1
Temperature °F (°C)	68 (20)
Elastic Modulus Msi (GPa)	28.2 (194.6)
Yield Strength ksi (MPa)	66.5 (458)
Ultimate Strength ksi (MPa)	101.1 (696.9)
Rupture Strain (%)	58.4

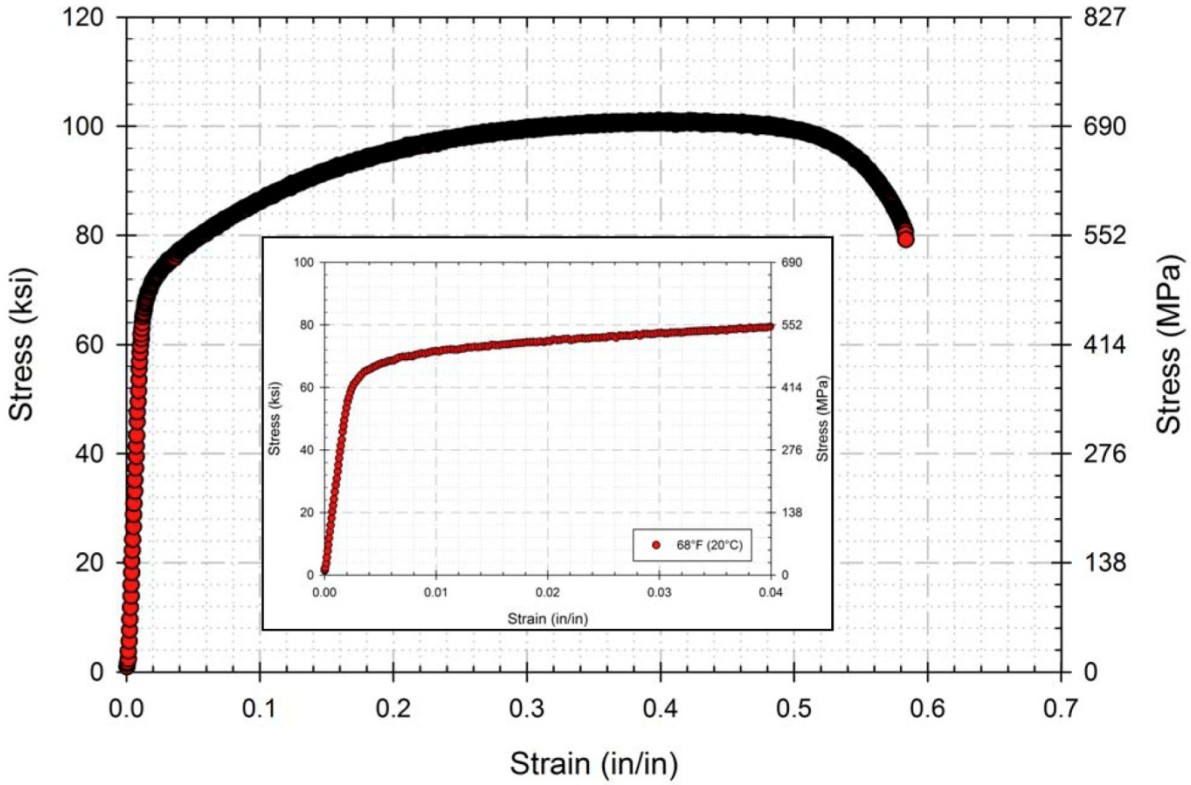

Tensile Specimen
Ten2

Specimen	Ten2
Temperature °F (°C)	600°F (315°C)
Elastic Modulus Msi (GPa)	25.1 (173.1)
Yield Strength ksi (MPa)	43.9 (303)
Ultimate Strength ksi (MPa)	71.56 (493.4)
Rupture Strain (%)	32.8

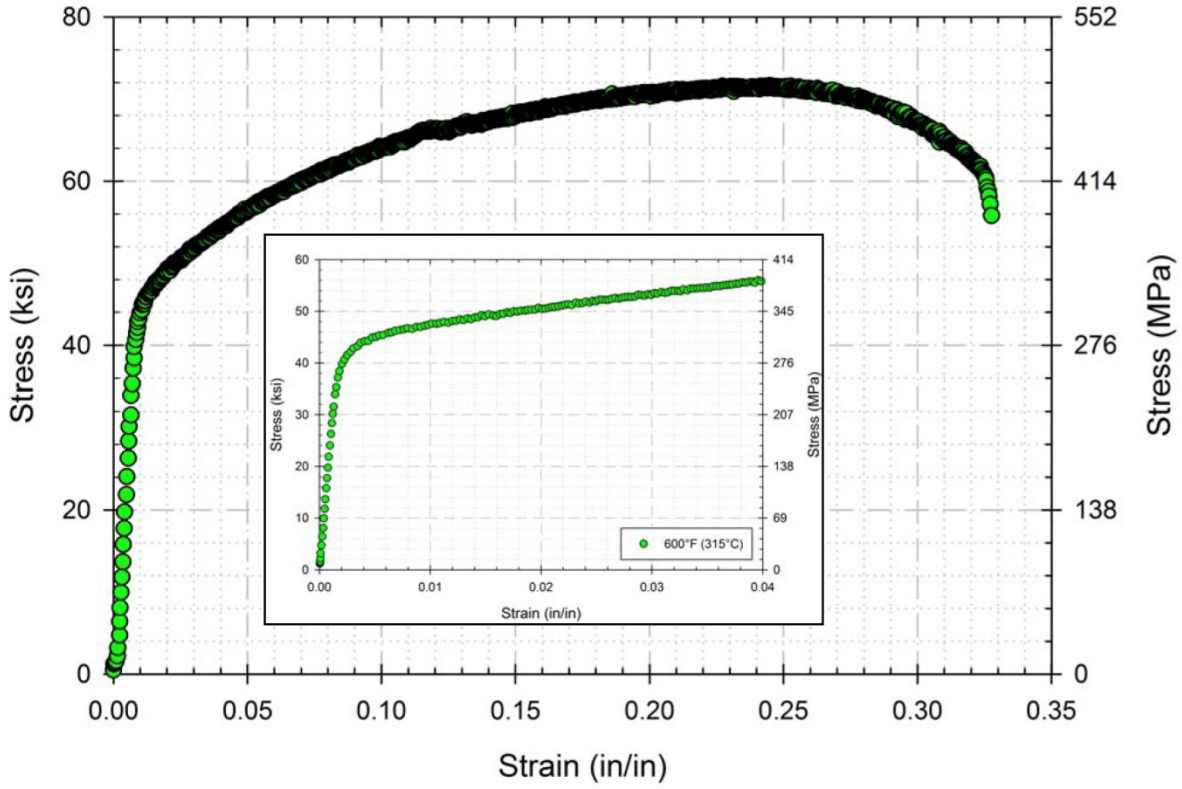

Tensile Specimen
Ten3

Specimen	Ten3
Temperature °F (°C)	800°F (427°C)
Elastic Modulus Msi (GPa)	25.6 (176.3)
Yield Strength ksi (MPa)	40.1 (277)
Ultimate Strength ksi (MPa)	67.02 (462.1)
Rupture Strain (%)	30.9

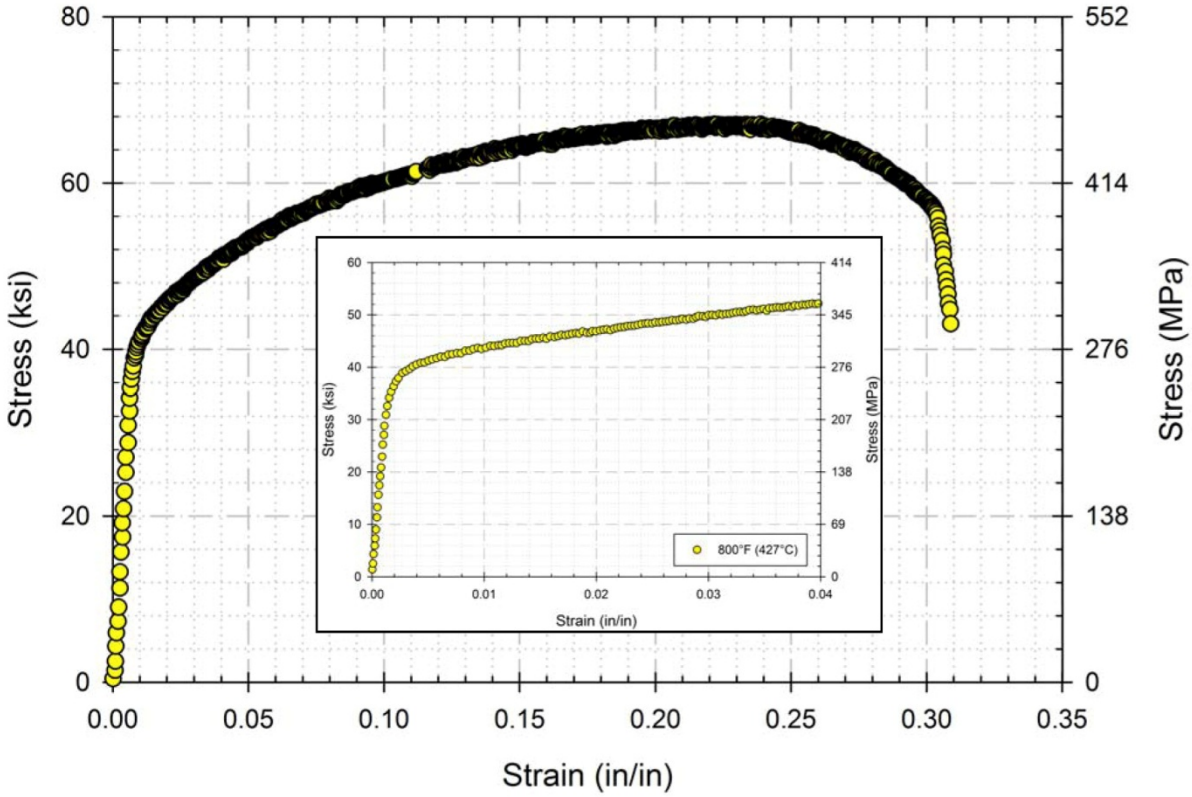

Creep-Fatigue Specimen
BN1

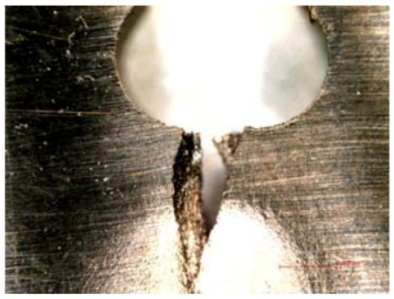

Specimen	BN1		
Temperature °F (°C)	600 (315)	**Load Ratio, *R***	0.1
Hold Time, t_h (s)	2	J_1 lbf/in (N/mm)	140.9 (24.68)
J_{stab} lbf/in (N/mm)	53.96 (9.450)	N_i d(CMOD) Method	5237
Failure Cycle, N_f	6068	a_f in (mm)	0.6621 (16.82)

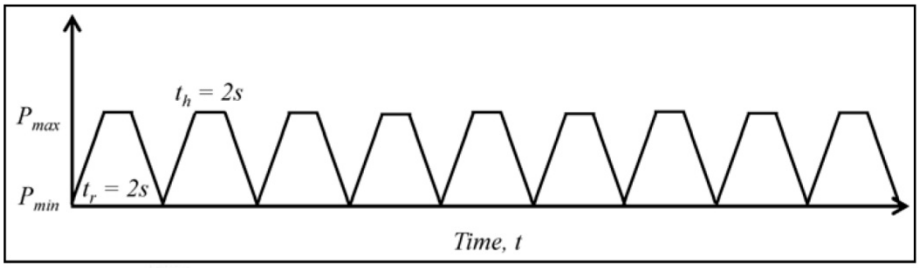

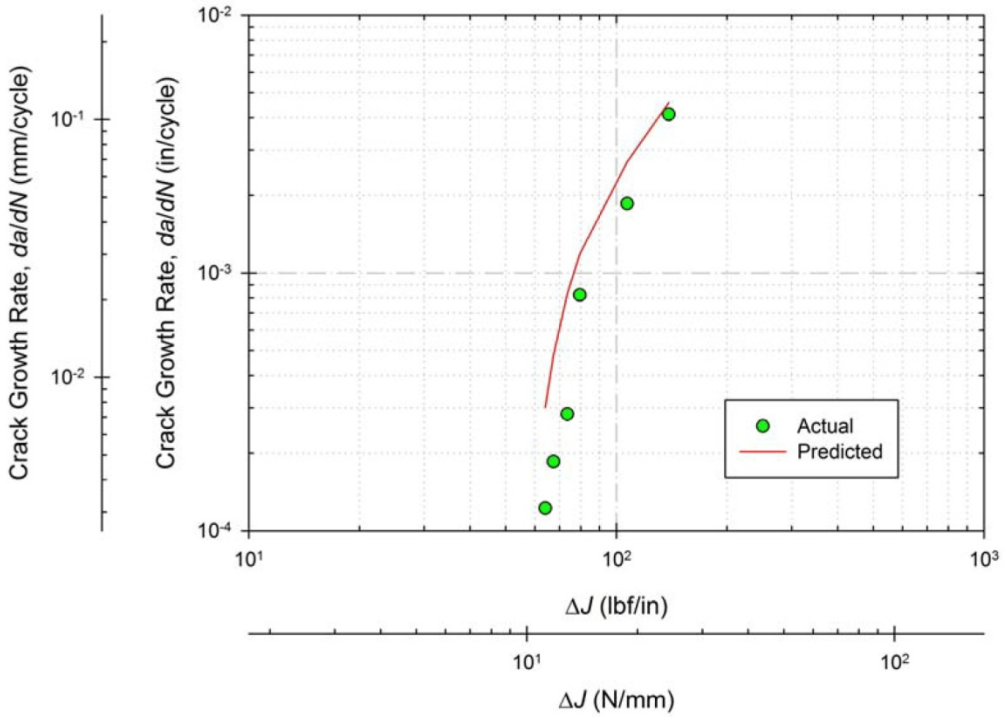

Creep-Fatigue Specimen
BN2

Specimen	BN2		
Temperature °F (°C)	800 (427)	**Load Ratio, *R***	0.1
Hold Time, t_h (s)	2	J_1 lbf/in (N/mm)	214.2 (37.51)
J_{stab} lbf/in (N/mm)	52.83 (9.252)	N_i d(CMOD) Method	3429
Failure Cycle, N_f	3980	a_f in (mm)	0.6424 (16.32)

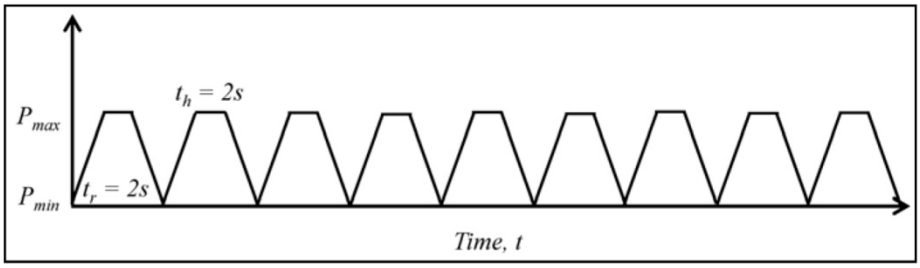

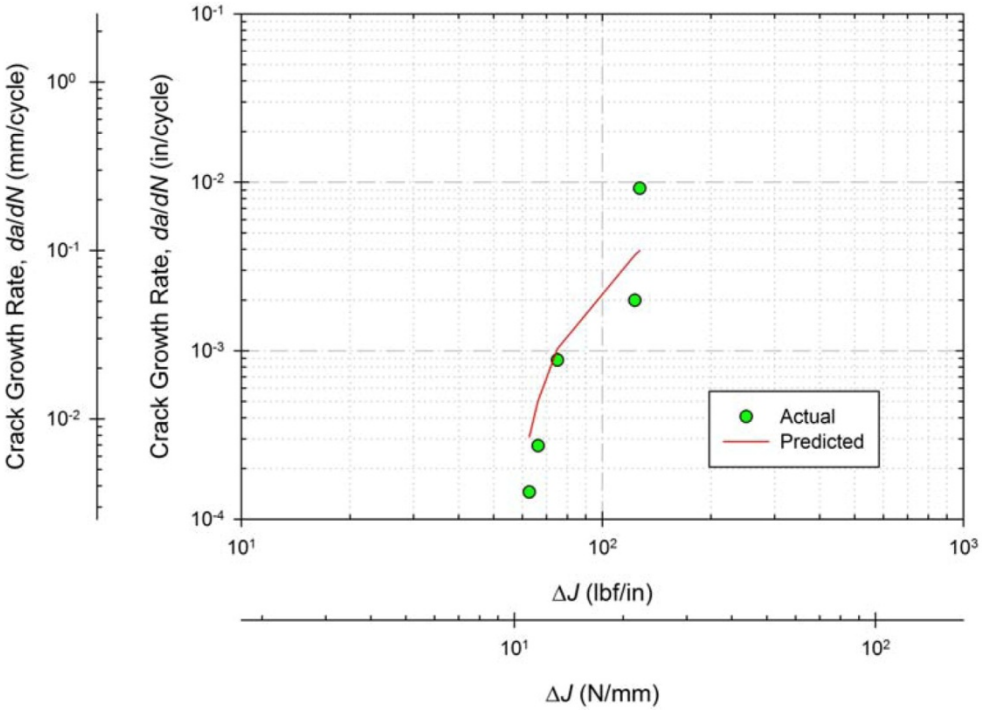

Creep-Fatigue Specimen
BN3

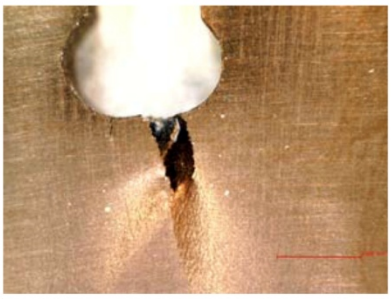

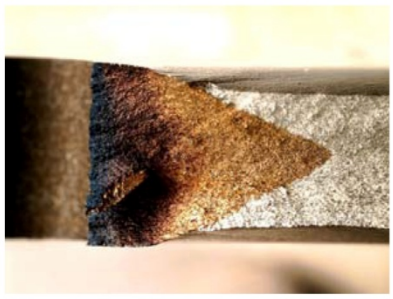

Specimen	BN3		
Temperature °F (°C)	800 (427)	**Load Ratio, *R***	0.1
Hold Time, t_h (s)	20	J_1 lbf/in (N/mm)	227.5 (39.84)
J_{stab} lbf/in (N/mm)	51.12 (8.952)	N_i d(CMOD) Method	4480
Failure Cycle, N_f	5212	a_f in (mm)	0.6426 (16.32)

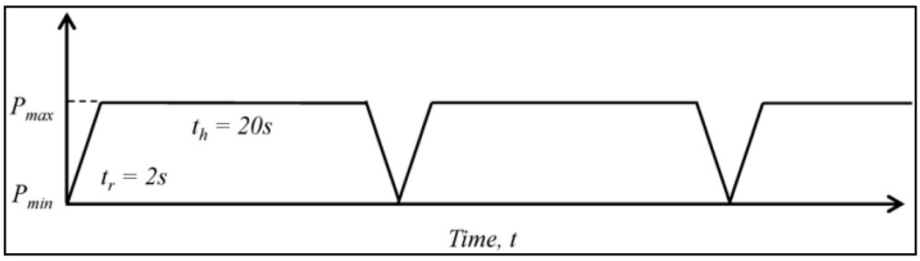

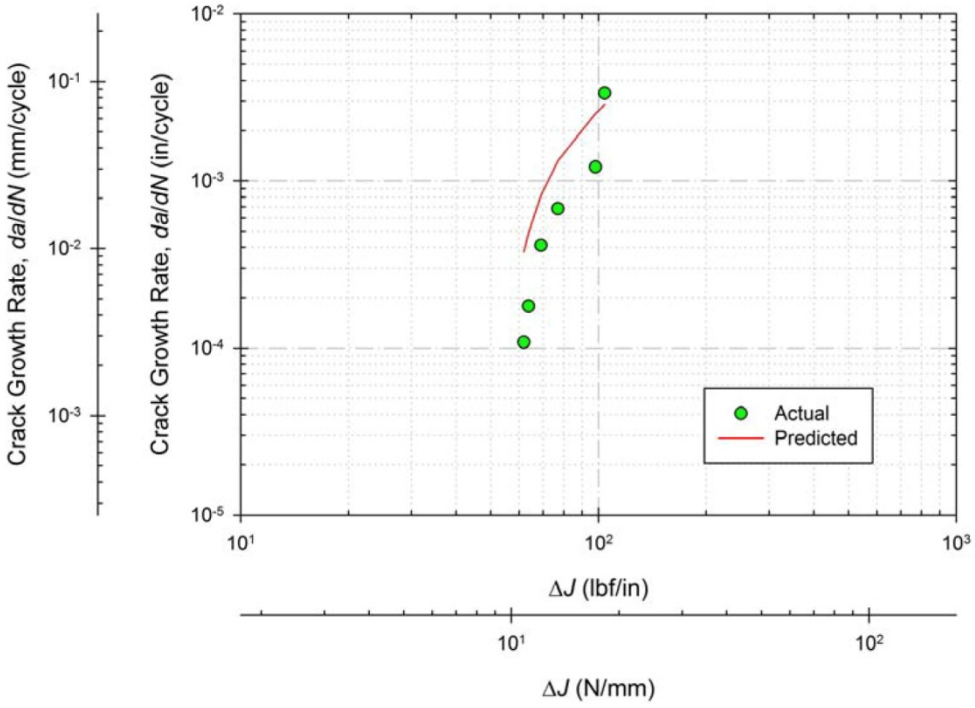

Creep-Fatigue Specimen
BN4

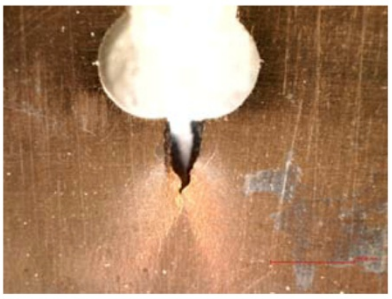

Specimen	BN4		
Temperature °F (°C)	800 (427)	**Load Ratio, *R***	0.1
Hold Time, t_h (s)	100	J_1 lbf/in (N/mm)	228.4 (39.99)
J_{stab} lbf/in (N/mm)	50.15 (8.783)	N_i d(CMOD) Method	4474
Failure Cycle, N_f	5194	a_f in (mm)	0.6395 (16.24)

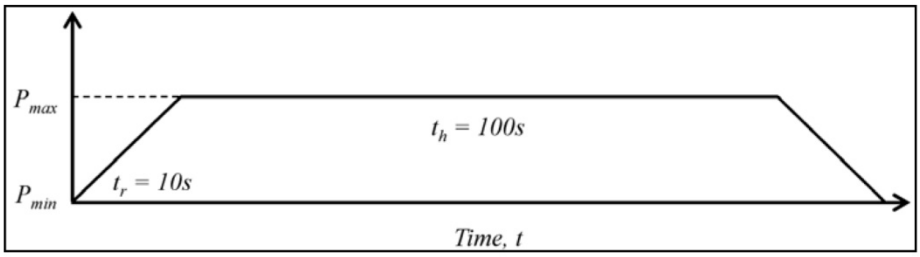

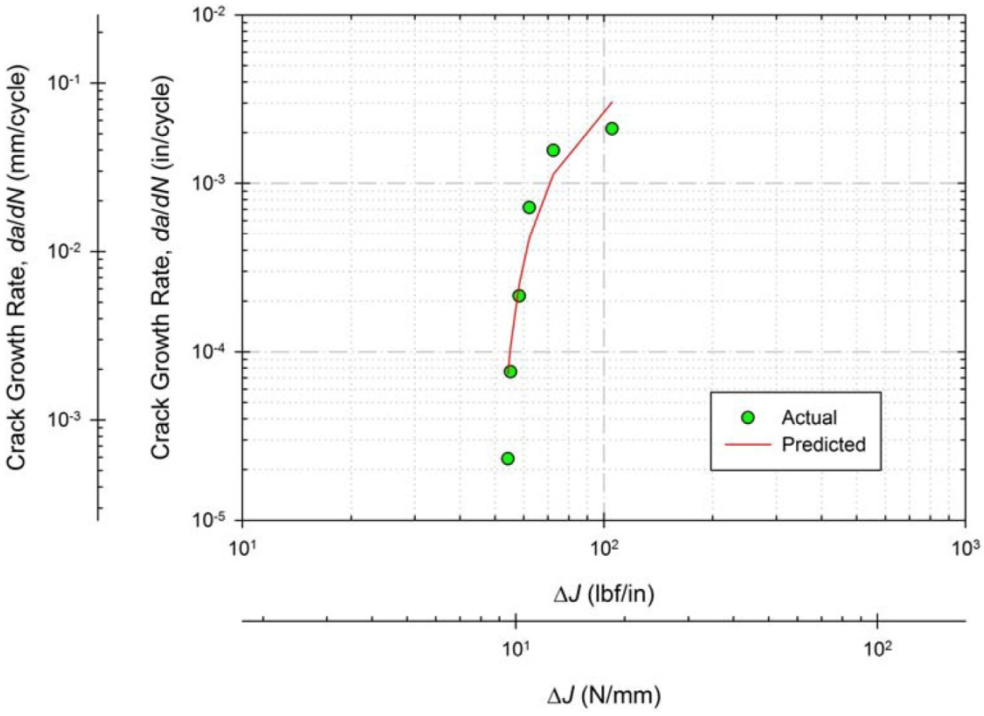

Creep-Fatigue Specimen
BN5

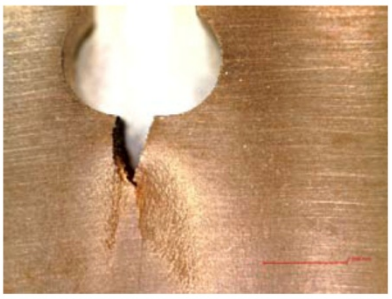

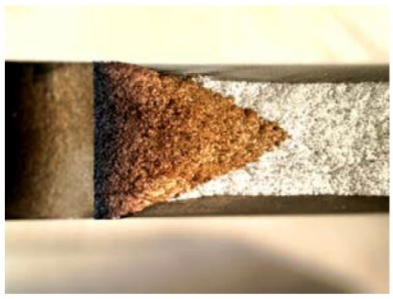

Specimen	BN5		
Temperature °F (°C)	800 (427)	**Load Ratio, *R***	0.1
Hold Time, t_h (s)	10	J_1 lbf/in (N/mm)	234.9 (41.12)
J_{stab} lbf/in (N/mm)	54.62 (95.65)	N_i d(CMOD) Method	2970
Failure Cycle, N_f	3485	a_f in (mm)	0.6337 (16.09)

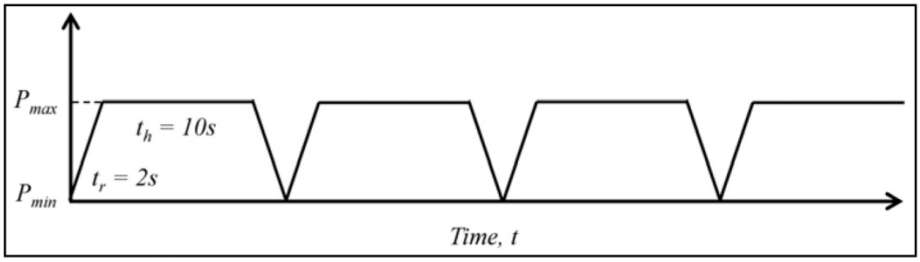

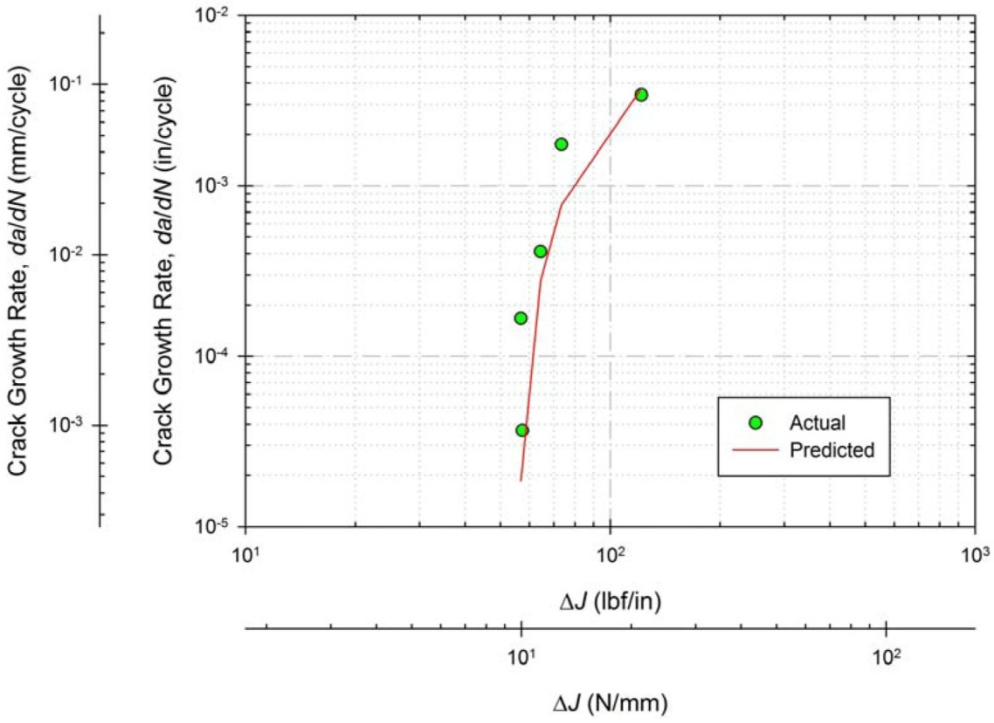

Creep-Fatigue Specimen
BN6

Specimen	BN6		
Temperature °F (°C)	800 (427)	**Load Ratio, *R***	0.1
Hold Time, t_h (s)	50	J_1 lbf/in (N/mm)	193.1 (33.82)
J_{stab} lbf/in (N/mm)	51.87 (9.084)	N_i d(CMOD) Method	3777
Failure Cycle, N_f	4415	a_f in (mm)	0.6584 (16.72)

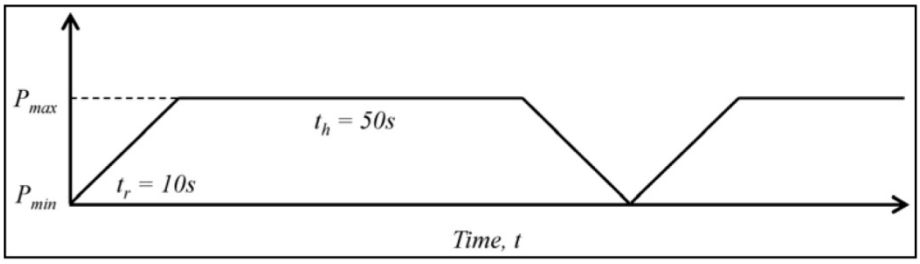

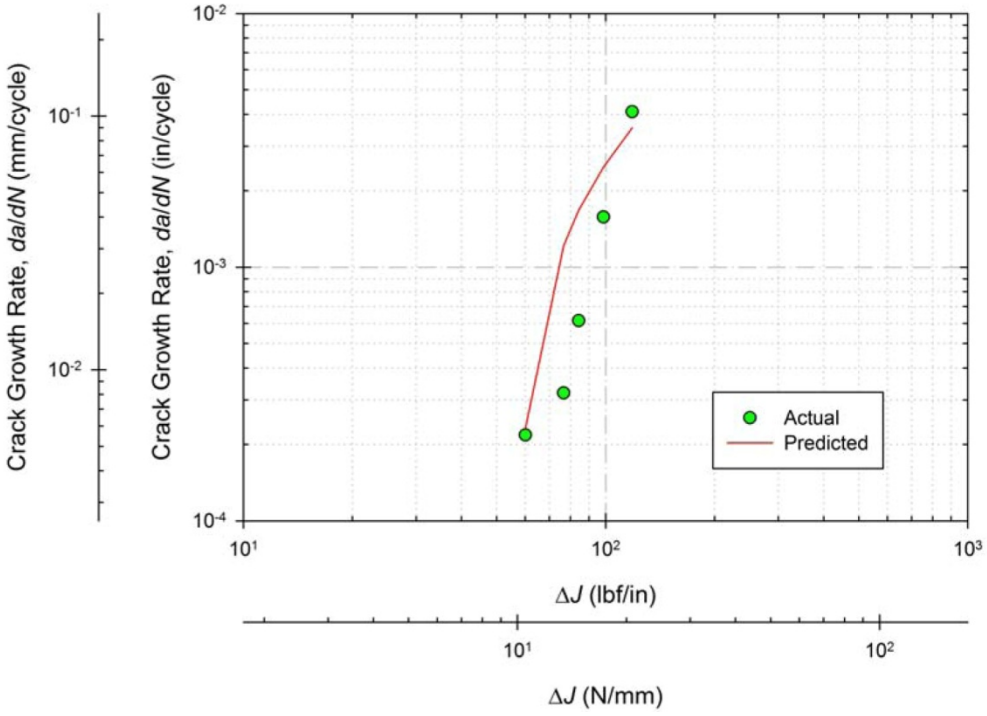

Creep-Fatigue Specimen
BN7

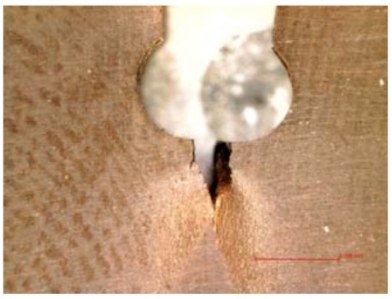

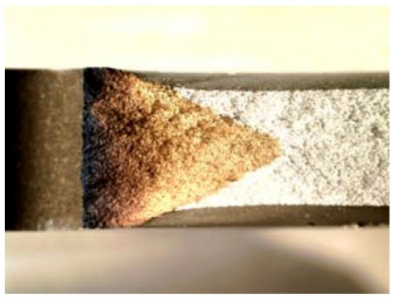

Specimen	BN7		
Temperature °F (°C)	800 (427)	**Load Ratio, *R***	0.05
Hold Time, t_h (s)	20	J_1 lbf/in (N/mm)	212.2 (37.16)
J_{stab} lbf/in (N/mm)	56.88 (9.961)	N_i d(CMOD) Method	3388
Failure Cycle, N_f	3939	a_f in (mm)	0.6372 (16.19)

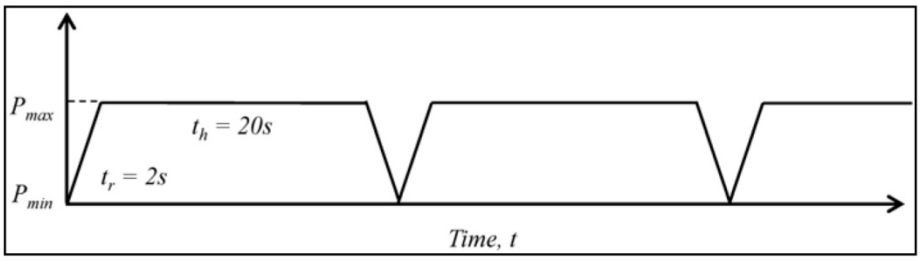

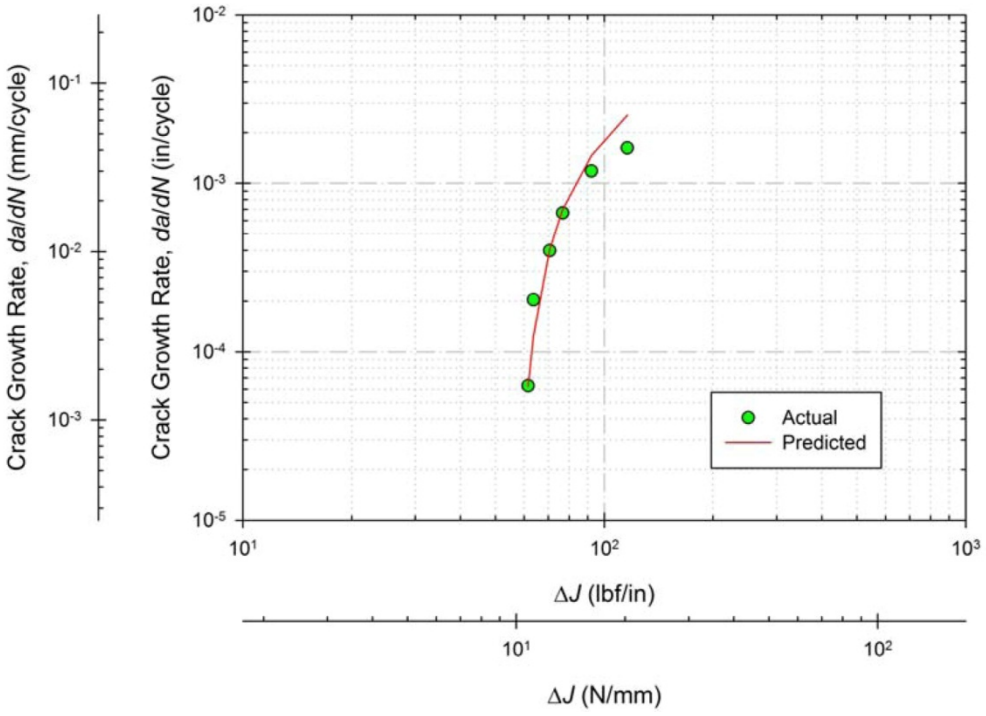

Creep-Fatigue Specimen
BN8

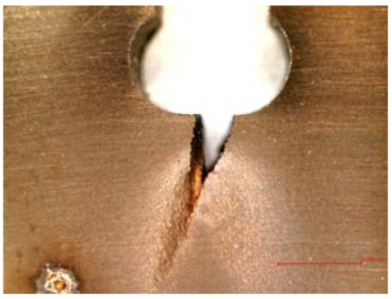

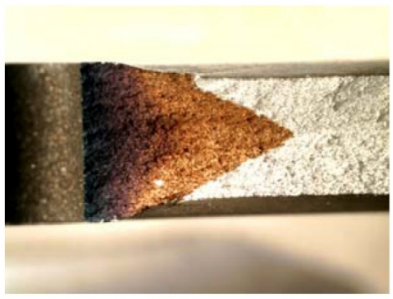

Specimen	BN8		
Temperature °F (°C)	800 (427)	**Load Ratio, *R***	0.05
Hold Time, t_h (s)	100	J_1 lbf/in (N/mm)	227.8 (38.89)
J_{stab} lbf/in (N/mm)	58.34 (10.22)	N_i d(CMOD) Method	2692
Failure Cycle, N_f	3144	a_f in (mm)	0.6447 (16.38)

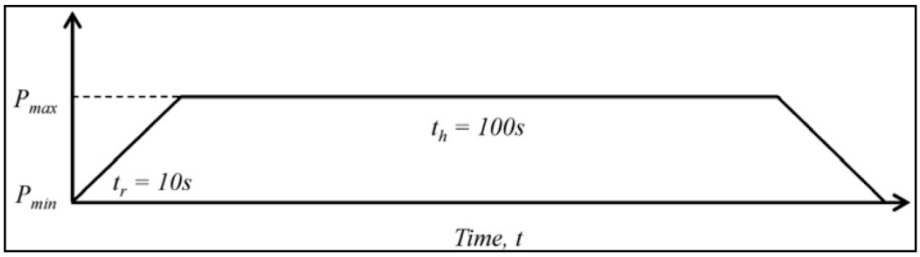

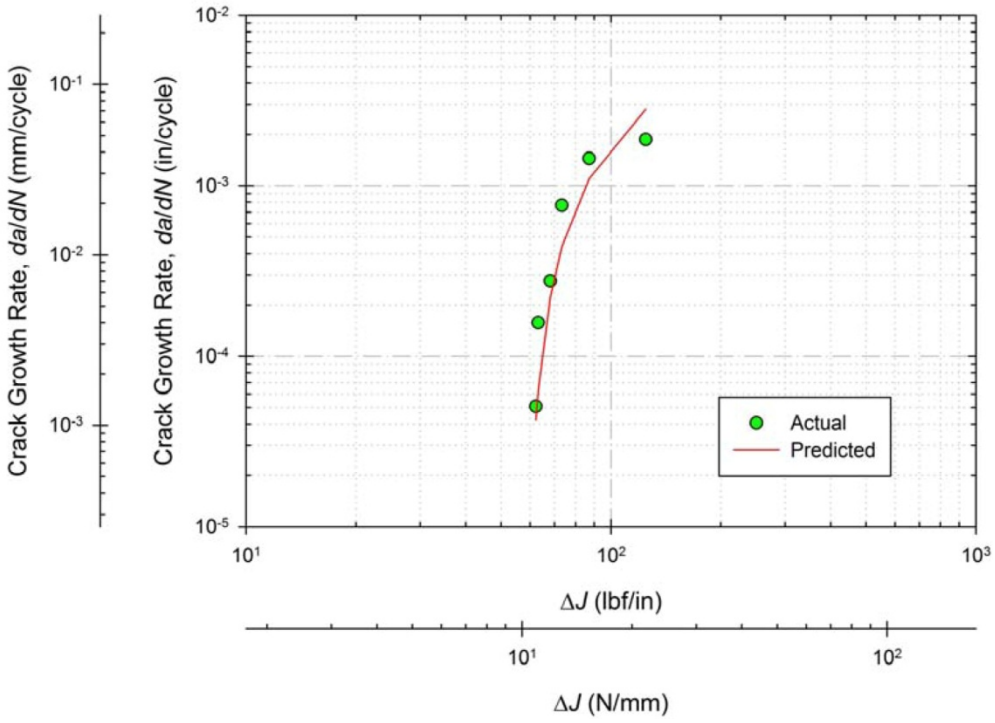

Creep-Fatigue Specimen
BN9

Specimen	BN9		
Temperature °F (°C)	800 (427)	**Load Ratio, *R***	0.05
Hold Time, t_h (s)	10	J_1 lbf/in (N/mm)	202.3 (35.43)
J_{stab} lbf/in (N/mm)	59.21 (10.37)	N_i d(CMOD) Method	3425
Failure Cycle, N_f	3983	a_f in (mm)	0.6587 (16.37)

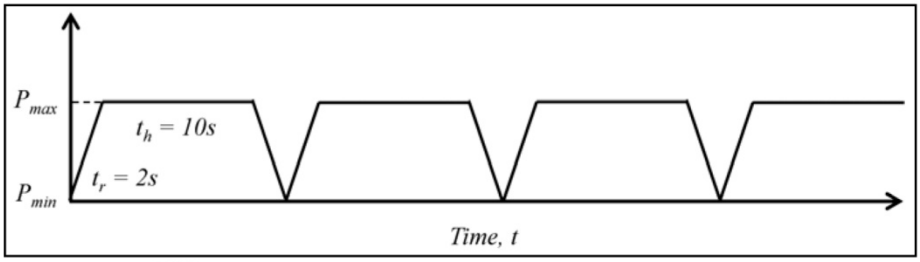

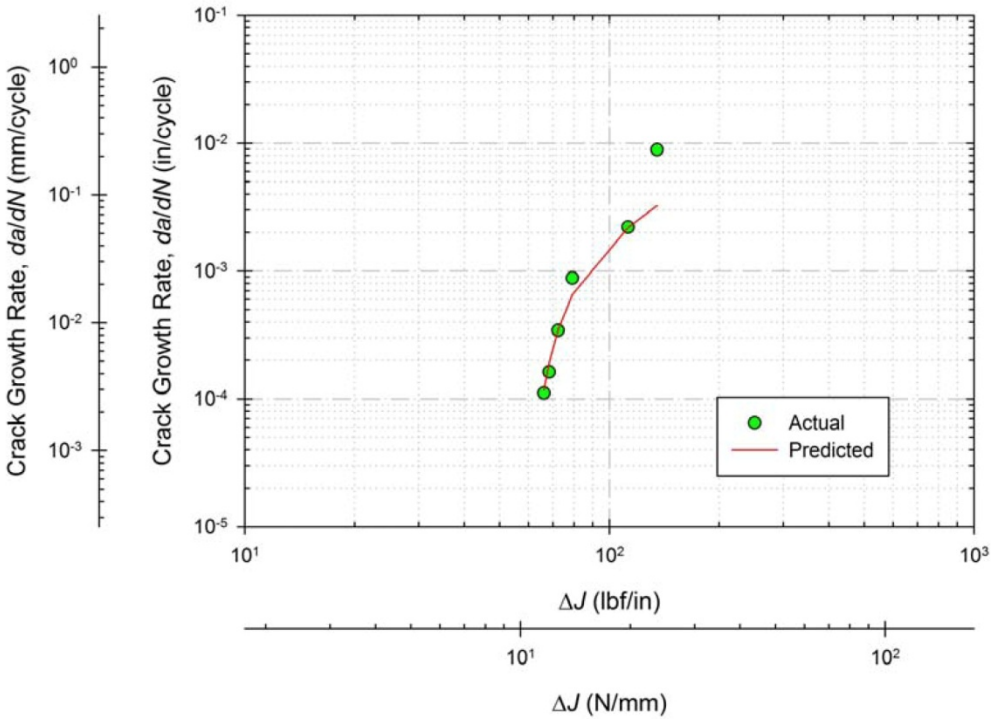

Creep-Fatigue Specimen
BN10

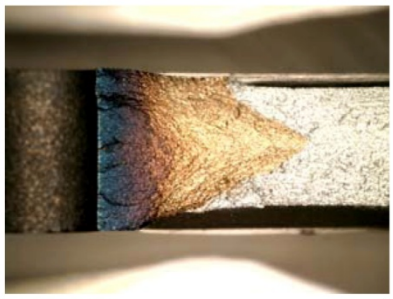

Specimen	BN10		
Temperature °F (°C)	800 (427)	**Load Ratio, *R***	0.05
Hold Time, t_h (s)	50	J_1 lbf/in (N/mm)	227.6 (39.86)
J_{stab} lbf/in (N/mm)	59.47 (10.42)	N_i d(CMOD) Method	3025
Failure Cycle, N_f	3535	a_f in (mm)	0.6416 (16.30)

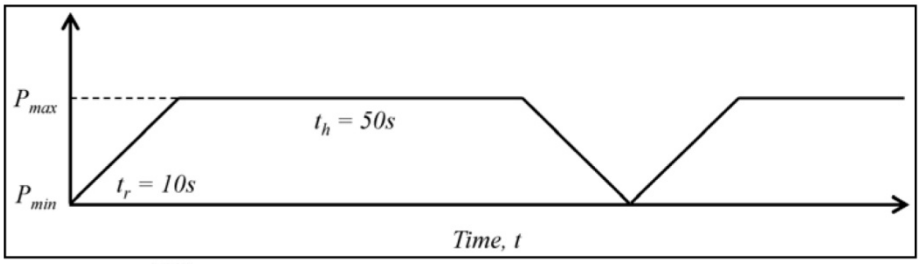

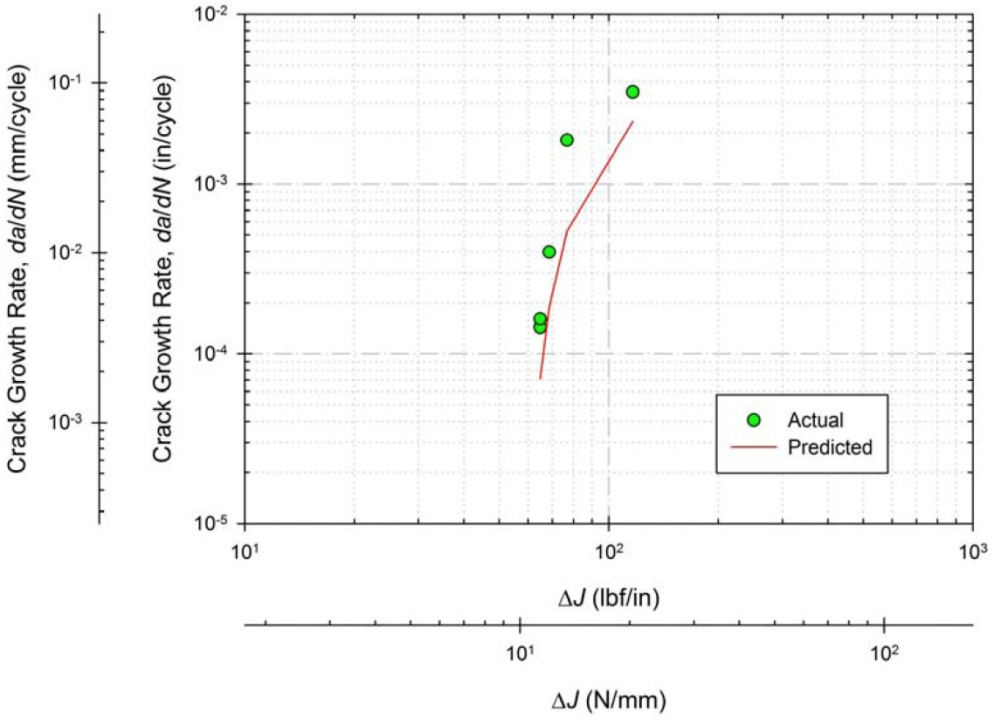

Creep-Fatigue Specimen
BN11

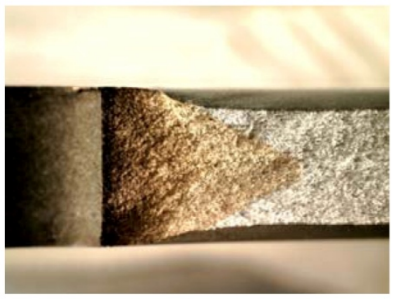

Specimen	BN11		
Temperature °F (°C)	600 (315)	**Load Ratio, *R***	0.1
Hold Time, t_h (s)	20	J_1 lbf/in (N/mm)	163.7 (28.67)
J_{stab} lbf/in (N/mm)	50.88 (8.910)	N_i d(CMOD) Method	5080
Failure Cycle, N_f	5927	a_f in (mm)	0.6375 (16.19)

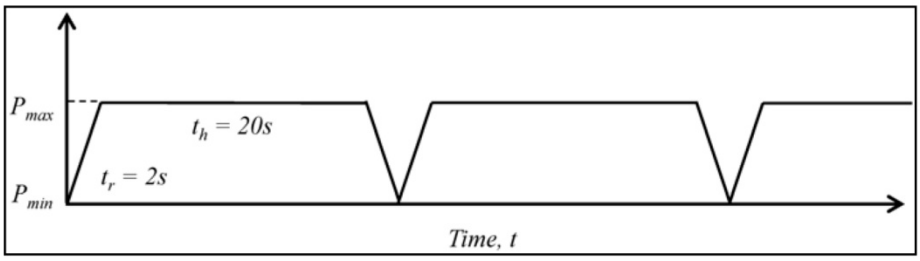

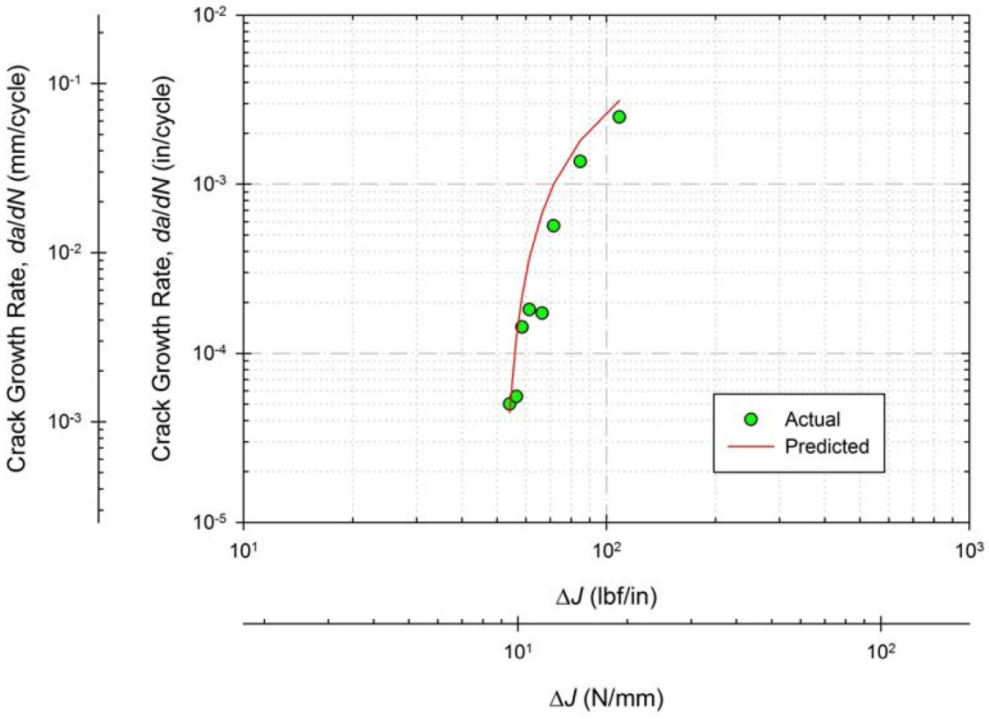

Creep-Fatigue Specimen
BN13

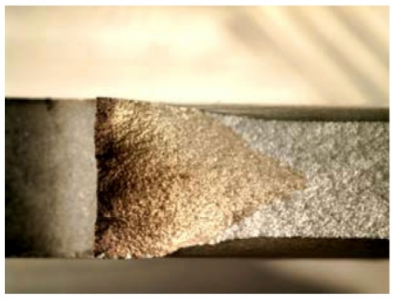

Specimen	BN13		
Temperature °F (°C)	600 (315)	**Load Ratio, *R***	0.1
Hold Time, t_h (s)	10	J_1 lbf/in (N/mm)	140.6 (24.62)
J_{stab} lbf/in (N/mm)	53.69 (9.403)	N_i d(CMOD) Method	5794
Failure Cycle, N_f	6718	a_f in (mm)	0.6449 (16.38)

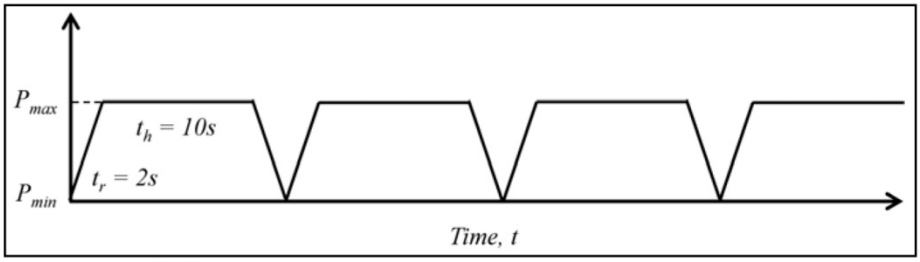

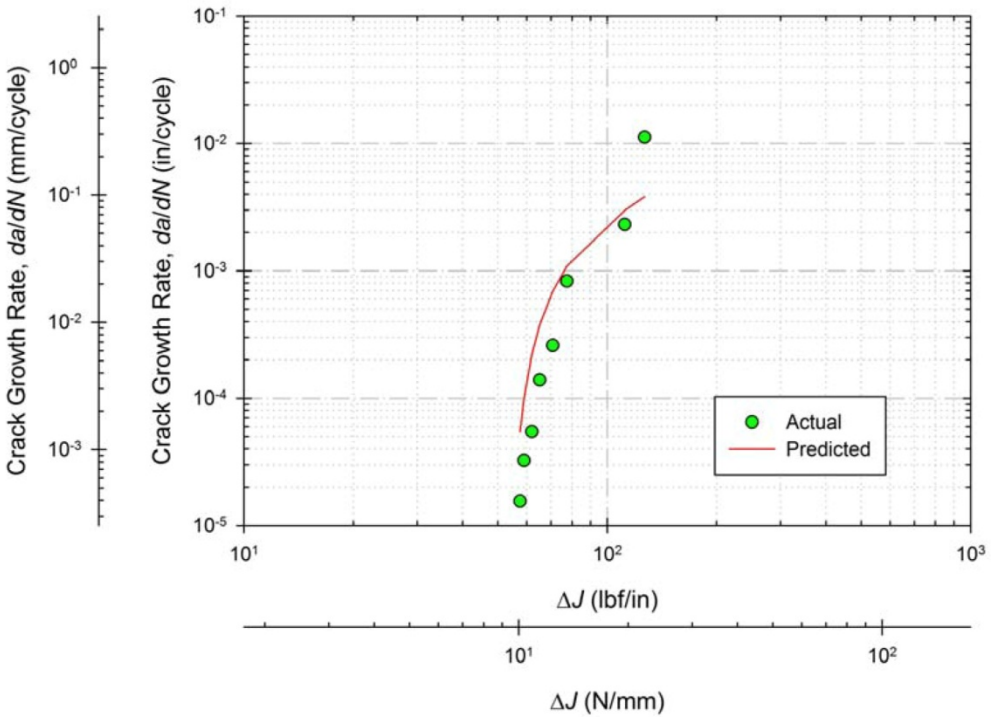

Creep-Fatigue Specimen
BN14

Specimen	BN14		
Temperature °F (°C)	600 (315)	**Load Ratio, *R***	0.1
Hold Time, t_h (s)	50	J_1 lbf/in (N/mm)	181.6 (31.80)
J_{stab} lbf/in (N/mm)	55.58 (9.734)	N_i d(CMOD) Method	5443
Failure Cycle, N_f	6324	a_f in (mm)	0.6487 (16.47)

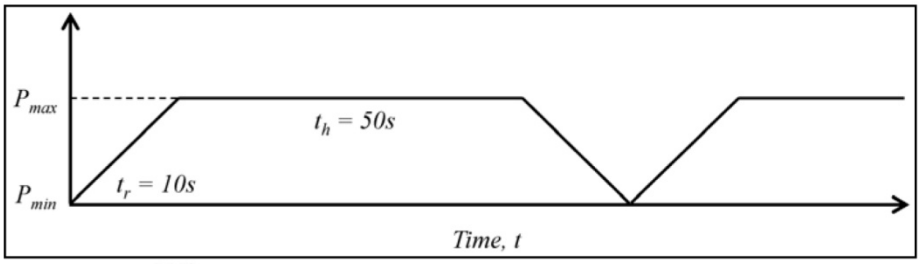

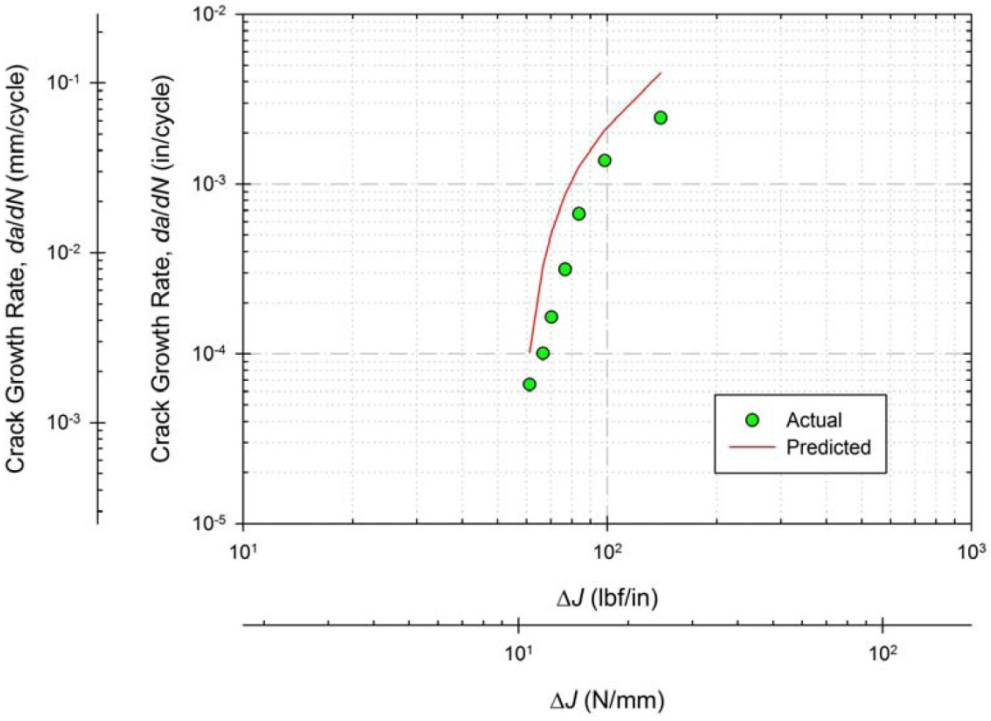

Creep-Fatigue Specimen
BN15

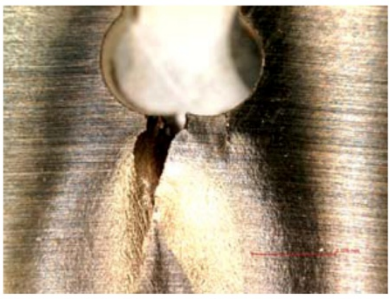

Specimen	BN15		
Temperature °F (°C)	600 (315)	**Load Ratio, *R***	0.05
Hold Time, t_h (s)	20	J_1 lbf/in (N/mm)	121.1 (21.21)
J_{stab} lbf/in (N/mm)	60.40 (10.58)	N_i d(CMOD) Method	4820
Failure Cycle, N_f	5623	a_f in (mm)	0.6636 (16.85)

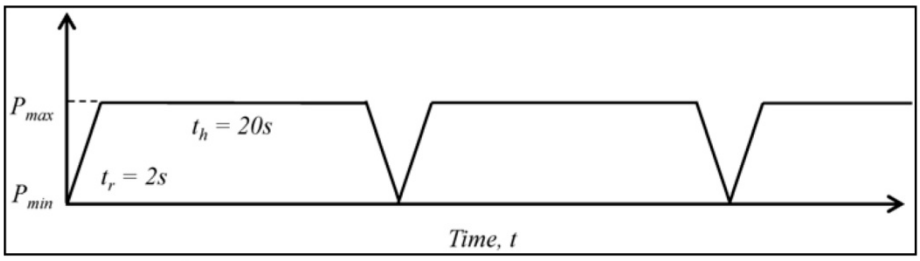

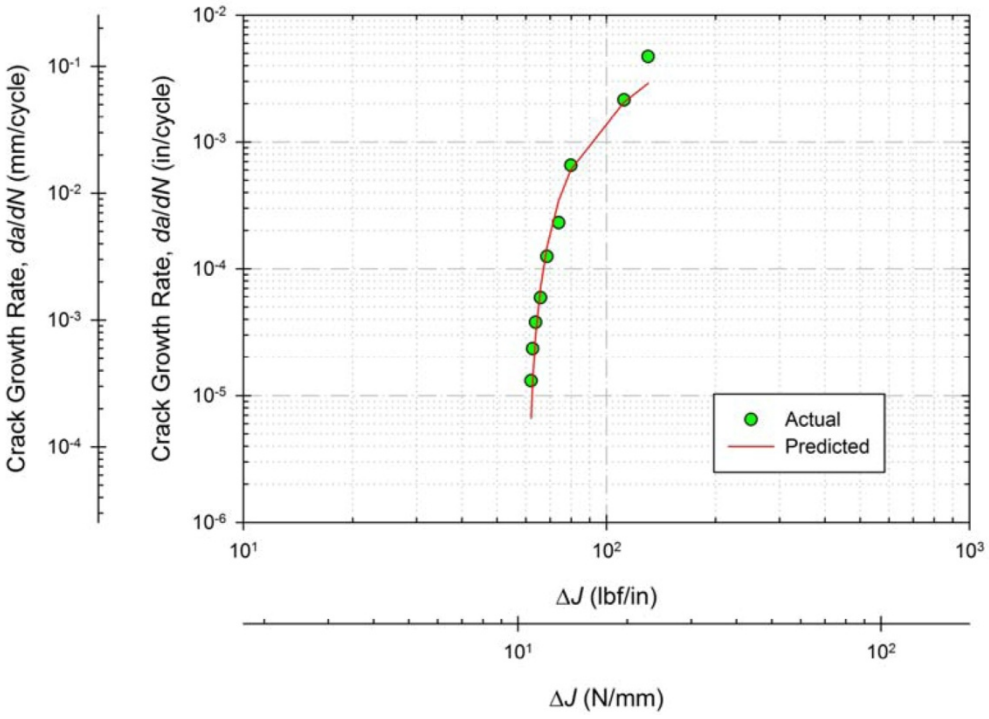

Creep-Fatigue Specimen
BN17

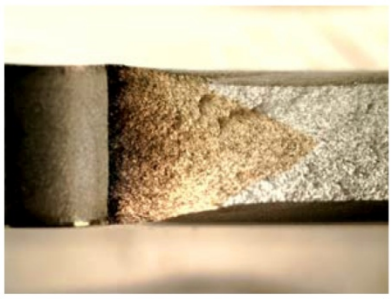

Specimen	BN17		
Temperature °F (°C)	600 (315)	**Load Ratio, *R***	0.05
Hold Time, t_h (s)	10	J_1 lbf/in (N/mm)	178.2 (31.21)
J_{stab} lbf/in (N/mm)	61.37 (10.75)	N_i d(CMOD) Method	2969
Failure Cycle, N_f	3498	a_f in (mm)	0.6443 (16.36)

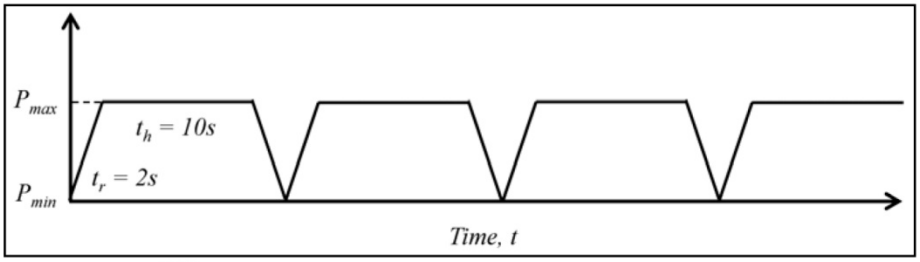

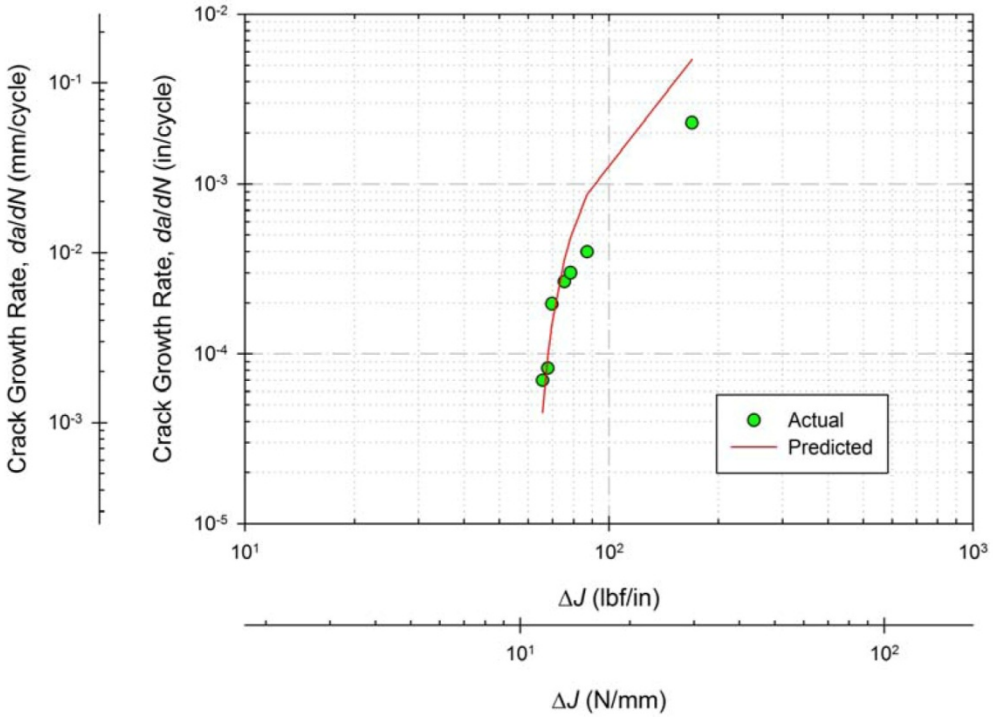

Creep-Fatigue Specimen
BN18

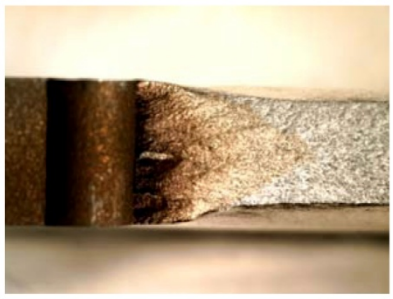

Specimen	BN18		
Temperature °F (°C)	600 (315)	**Load Ratio, *R***	0.05
Hold Time, t_h (s)	50	J_1 lbf/in (N/mm)	184.6 (32.33)
J_{stab} lbf/in (N/mm)	60.87 (10.66)	N_i d(CMOD) Method	4910
Failure Cycle, N_f	5758	a_f in (mm)	0.6392 (16.24)

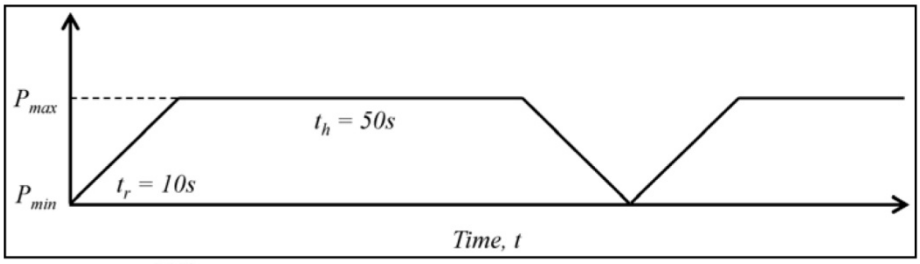

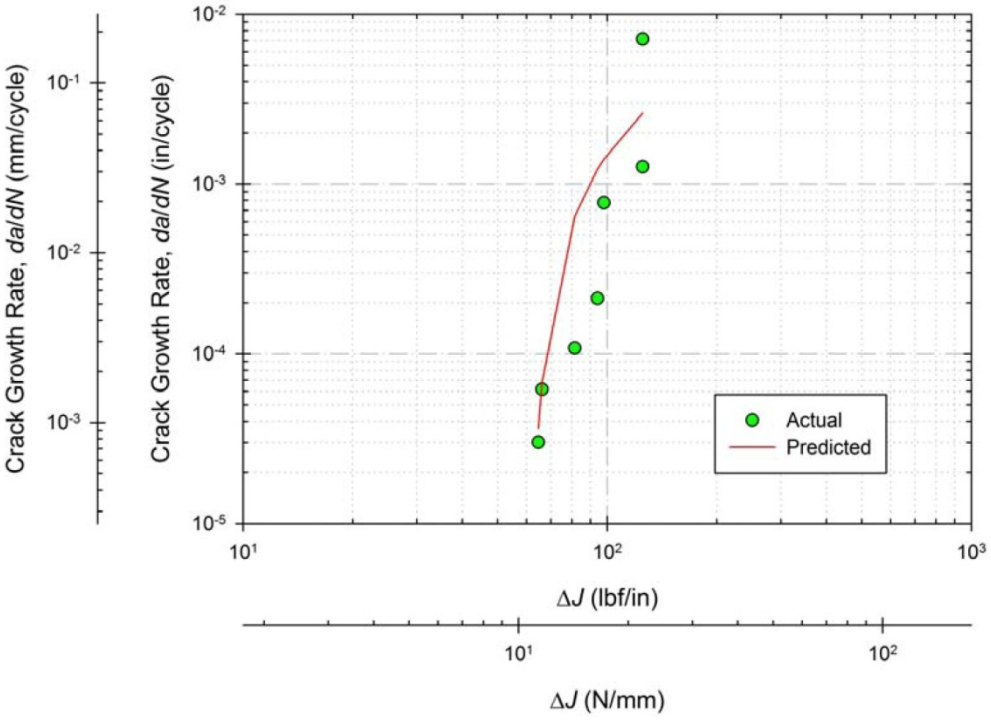

Creep-Fatigue Specimen
BN19

Specimen	BN19		
Temperature °F (°C)	800 (427)	**Load Ratio, *R***	0.05
Hold Time, t_h (s)	2	J_1 lbf/in (N/mm)	325.5 (57.00)
J_{stab} lbf/in (N/mm)	59.15 (10.36)	N_i d(CMOD) Method	2860
Failure Cycle, N_f	3337	a_f in (mm)	0.6166 (15.66)

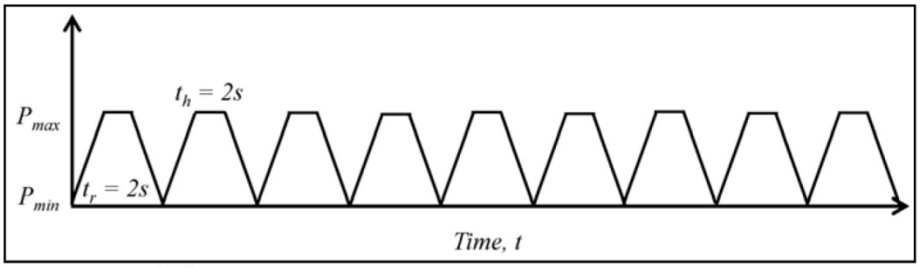

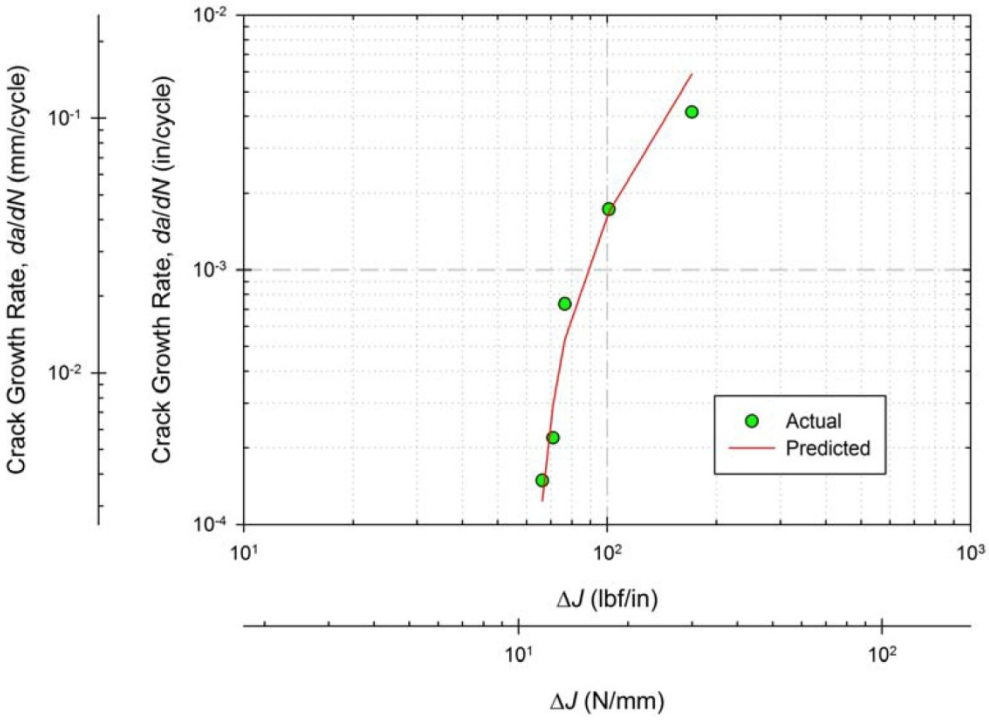

Creep-Fatigue Specimen
BN20

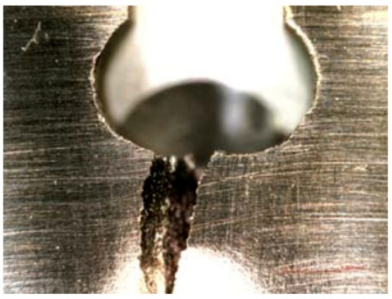

Specimen	BN20		
Temperature °F (°C)	600 (315)	**Load Ratio, *R***	0.05
Hold Time, t_h (s)	2	J_1 lbf/in (N/mm)	127.1 (22.26)
J_{stab} lbf/in (N/mm)	56.27 (9.854)	N_i d(CMOD) Method	5089
Failure Cycle, N_f	5905	a_f in (mm)	0.6561 (16.66)

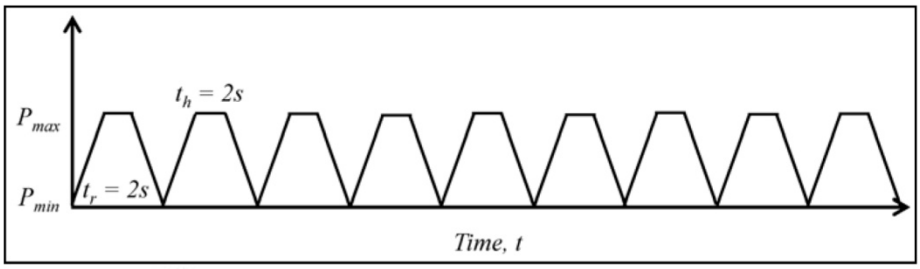

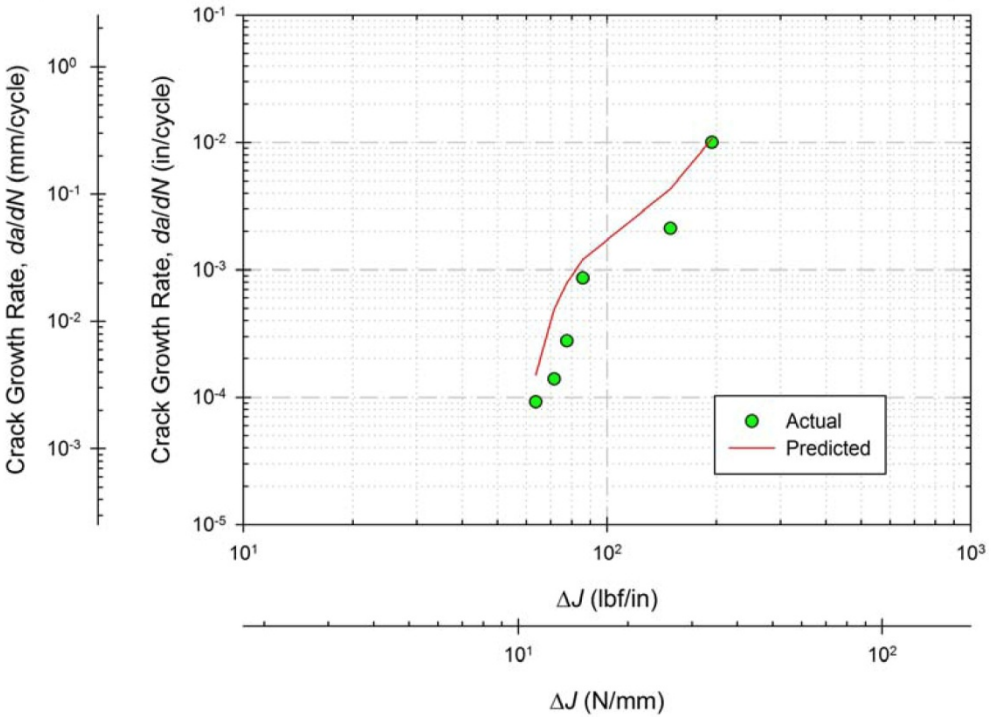

REFERENCES

7FA Heavy Duty Gas Turbine, (2012), Retrieved November 30, 2012, <http://www.ge-energy.com/products_and_services/products/gas_turbines_heavy_duty/7fa_heavy_duty_gas_turbine.jsp>.

Adib-Ramezami, H., Jeong, J., *Advanced Volumetric Method for Fatigue Life Prediction Using Stress Gradient Effects at Notch Roots*, Computational Materials Science, Volume 39(3), pp. 649-663., 2007.

ANSYS Academic, Release v13.0, Help System, *J-Integral*, ANSYS, Inc., 2010.

ASM Handbook Volume 1, *Properties and Selection: Irons, Steels and High-Performance Alloys*, Seventh Printing, ASM International, Materials Park, OH: 2007.

ASTM Standard E8/E8M-09, 2009, *Standard Test Method for Tension Testing of Metallic Materials*, ASTM International, West Conshohocken, PA, DOI: 10.1520/E0008_E0008M-09.

ASTM Standard E21-09, 2009, *Standard Test Methods for Elevated Temperature Tension Tests of Metallic Materials*, ASTM International, West Conshohocken, PA, DOI: 10.1520/E0021-09.

ASTM Standard E399-09$^{\varepsilon 2}$, 2009, *Standard Test Method for Linear-Elastic Plane-Strain Fracture Toughness, K_{Ic}, of Metallic Materials*, ASTM International, West Conshohocken, PA, DOI: 10.1520/E0399-09E02.

ASTM Standard E647-08$^{\varepsilon 2}$, 2008, *Standard Test Method for Measure of Fatigue Crack Growth Rates*, ASTM International, West Conshohocken, PA, DOI: 10.1520/E0647-08E01.

ASTM Standard E1820-09$^{\varepsilon 1}$, 2009, *Standard Test Method for Measurement of Fracture Toughness*, ASTM International, West Conshohocken, PA, DOI: 10.1520/E1820-09.

ASTM Standard E2714-09, 2009, *Standard Test Method for Creep-Fatigue Testing*, ASTM International, West Conshohocken, PA, DOI: 10.1520/E2714-09.

ASTM Standard E2760-10, 2010, *Standard Test Method for Creep-Fatigue Crack Growth Testing*, ASTM International, West Conshohocken, PA, DOI: 10.1520/E2760-10E01.

Baik, Y.M., Kim, K.S., *Crack Growth in Stainless Steel 304 at 538C under Fatigue Loading with and without Hold Time*, Key Engineering Materials, Volumes 183-187(1), pp. 31-36, 2000.

Baik, Y.M., Kim, K.S., *Crack Growth in Stainless Steel 304 Under Creep-Fatigue Loading*, Key Engineering Materials, Volume 353 (1), pp. 485-490, 2007.

Bassani, J.L., McClintock, F.A., "Creep Relaxation of Stress Around a Crack Tip," *International Journal of Solids and Structures*, Volume 17(5), pp. 479-492, 1981.

Bayoumi, M.R., Abd El Latif, A.K., *Low-Cycle Fatigue Behaviour of Notched AISI 304 Stainless Steel Specimens*, Journal of Materials Science, Volume 30(15), pp. 3944-3953, 1995.

Begley, J.A., Landes, J.D., "The J Integral as a Fracture Criterion," *Fracture Toughness, Proceedings of the 1971 National Symposium on Fracture Mechanics, Part II*, ASTM STP 514, American Society of Testing and Materials, pp. 1-23, 1972.

Benachour, N., et al., *Stress Ratio and Notch Effect on Fatigue Crack Initiation and Propagation in 2024 Al-Alloy*, Proceedings of World Academy of Science, Engineering and Technology, Volume 79, pp. 566-569, 2011.

Boukharouba, T., et al., *Use of Notch Stress Intensity Factor as a Fatigue Crack Initiation Parameter*, Engineering Fracture Mechanics, Volume 52(3), pp. 503-512, 1995.

Bouvard, J.L., Chaboche, J.L., Feyel, F., Gallerneau, F., *A Cohesive Zone Model for Fatigue and Creep-Fatigue Crack Growth in Single Crystal Superalloys*, International Journal of Fatigue, Volume 31(5), pp. 868-879, 2009

Boyer, H.E., *Atlas of Fatigue Curves*, Ed. H.E. Boyer, ASM International, Materials Park, Ohio: 1986.

Branco, C.M., Radon, J.C., "Fatigue Crack Growth in Gross Plasticity Cycling," *Proceedings of the Second International Conference on Mechanical Behaviour of Material*, pp. 632-635, 1976.

Chaboche, J.L., *A Review of Some Plasticity and Viscoplasticity Constitutive Theories*, Int. Journal of Plasticity, Volume 24 (10), pp. 1642-93, 2008.

Chopra, O.K., Natesan, K., *Interpretation of High-Temperature Creep of Type 304 Stainless Steel*, Metallurgical Transactions A, Volume 8(4), pp. 633-638, 1977.

Creager, M., Paris, P.C., *Elastic Field Equations for Blunt Cracks with Reference to Stress Corrosion Cracking*, International Journal of Fracture Mechanics, Volume 3(4) pp. 247-252, 1967.

Davies, C.M., *Predicting Creep Crack Initiation in Austenitic and Ferritic Steels using the Creep Toughness Parameter and Time-Dependent Failure Assessment Diagram*, Fatigue and Fracture of Engineering Materials and Structures, Volume 32(10), pp. 820-836, 2009.

Donald, K., Paris, P.C., *An Evaluation of ΔKeff Estimation Procedures on 6061-T6 and 2024-T3 Aluminum Alloys*, International Journal of Fatigue, Volume 21(S1), pp. S47-S57, 1999.

Dowling, N.E., Begley, J.A., "Fatigue Crack Growth During Gross Plasticity and the J-Integral," *Mechanics of Crack Growth*, ASTM STP 590, American Society for Testing and Materials, pp. 82-103, 1976.

Dowling, N.E., Brose, W.R., Wilson, W.K., "Notched Member Fatigue Life Predictions by the Local Strain Approach," *Fatigue Under Complex Loading: Analyses and Experiments*, Ed. R.M. Wetzel, Warrendale, PA: Society of Automotive Engineers, 1977.

Dowling, N.E., "Fatigue at Notches and the Local Strain and Fracture Mechanics Approaches," *Fracture Mechanics: Proceedings of the Eleventh National Symposium on Fracture Mechanics: Part I*, ASTM STP 677, American Society for Testing and Materials, pp. 247-273, 1979.

Dowling, N.E., Iyyer, S., *Fatigue Crack Growth and Closure at High Cyclic Strains*, Materials Science and Engineering, Volume 96, pp. 99-107, 1987.

Dowling, N.E., *Mechanical Behavior of Materials: Engineering Methods for Deformation, Fracture and Fatigue*, Fourth Edition, Upper Saddle River, NJ: Pearson Prentice Hall, 2013.

Dowling, N.E., Wilson, W.K., *Results of Elastic Analysis of Bluntly Notched Compact Specimens*, Engineering Fracture Mechanics, Volume 20(3), pp. 569-572, 1984.

El Haddad, M.H., et al., *J-Integral Applications for Short Fatigue Cracks at Notches*, International Journal of Fracture, Volume 16(1), pp. 15-30, 1980.

Elber, W., "The significance of Fatigue Crack Closure," *Damage Tolerance in Aircraft Structures*, ASTM STP 486, American Society for Testing and Materials, pp. 230-242. 1971.

Fan, F., Kalnaus, S., Jiang, Y., *Modeling of Fatigue Crack Growth of Stainless Steel 304L*, Mechanics of Materials, Volume 40(11), pp. 961-973, 2008.

Fatemi, A., Yang, L., *Cumulative Fatigue Damage and Life Prediction Theories: A Survery of the State of the Art for Homogeneous Materials*, International Journal of Fatigue, Volume 20(1), pp. 9-34, 1998.

Forman, R.G., Kearney, V.E., Engle, R.M., *Numerical Analysis of Crack Propagation in Cyclic-Loaded Structures*, Journal of Basic Engineering, Volume 89(3), pp. 459-464, 1967.

Filippini, M., *Stress Gradient Calculations at Notches*, International Journal of Fatigue, Volume 22(5), pp. 397-409, 2000.

Furuya, Y., Shimada, H., *Fatigue Crack Initiation from Notch Root (Local-Strain Damage Accumulation Process on Crack Initiation*, Engineering Fracture Mechanics, Volume 23(6), pp. 983-989, 1986.

Glinka, G., *Energy Density Approach to Calculation of Inelastic Strain-Stress Near Notches and Cracks*, Engineering Fracture Mechanics, Volume 22(3), pp. 485-508, 1985.

Glinka, G., Newport, A., *Universal Feature of Elastic Notch-Tip Stress Fields*, International Journal of Fatigue, Volume 9(3), pp. 143-150, 1987.

Grover, P.S., Saxena, A., *Modelling the Effect of Creep-Fatigue Interaction on Crack Growth*, Fatigue and Fracture of Engineering Material and Structures, Volume 22(2), pp. 111-122, 1999.

Heckel, K., Wanger, R., *Tensile Fatigue Behavior of C(T)-Specimens with Small Notch Root Radius*, International Journal of Fracture, Volume 11(1), pp. 135-140, 1975.

Hedia, H.S.M, Shabara, M.A.N., *Effect of Notch Tip Sharpness and Pre-Cracking on the Stress Intensity Factor – Part I: Finite Element Analysis of Compact Tension Specimen*, Materialpruefung/Materials Testing, Volume 44(4), pp. 117-121, 2002.

Hertzberg, R.W., *Deformation and Fracture Mechanics of Engineering Materials*, Third Edition, New York, NY: John Wiley and Sons, 1989.

Hyde, T.H., et al., *Fatigue, Creep and Creep/Fatigue Behaviour of a Nickel Base Superalloy at 700°C*, Fatigue and Fracture of Engineering Materials and Structures, Volume 20(9), pp. 1295-1303, 1997.

Issartel, C., et al., *Influence of Nitridation on the Oxidation of a 304 Steel at 800°C*, Corrosion Science, Volume 46(9), pp. 2191-2201, 2004.

Jaber, J.O., Odeh, S.D., Probert, S.D., *Integrated PV and Gas-Turbine System for Satisfying Peak-Demands,* Applied Energy, Volume 76(4), pp. 305-319, 2003.

James, L.A., Schwenk, E.B. Jr., *Fatigue-Crack Propagation Behavior of Type 304 Stainless Steel at Elevated Temperatures*, Metallurgical Transactions, Volume 2(2), pp. 491-496, 1971.

Kacianauskas, R., Stupak, E., Stupak, S., *Application of Adaptive Finite Elements for Solving Elastic-Plastic Problem of SENB Specimen*, Mechanika, Volume 1(51), pp. 18-22, 2005.

Keller, S.G., *Stress Intensity Factor Dependence of Hg-Al Liquid Metal Embrittlement*, Master's Thesis, University of Central Florida, Fall 2009.

Kim, H-K., Mohamed, F.A., Earthman, J.C., *High-Temperature Rupture of Microstructurally Unstable 304 Stainless Steel Under Uniaxial and Triaxial Stress States*, Metallurgical Transactions A, Volume 22(11), pp. 2629-2636, 1991.

Kitagawa, H., Takahashi, S., *Applicability of Fracture Mechanics to Very Small Cracks or the Cracks in the Early Stage*, Proceedings of the Second International Conference on Mechanical Behaviour of Material, pp. 627-631, 1976.

Kitamura, T., et al., *Characterization of Creep-Fatigue Fracture of Type 304 Stainless Steel Based on Initiation and Growth of Small Cracks*, ASME PVP, Volume 303, pp. 377-382, 1995.

Knop, M., et al., *On the Glinka and Neuber Methods for Calculating Notch Tip Strains under Cyclic Loading Spectra*, International Journal of Fatigue, Volume 22(9), pp. 743-755, 2000.

Kuwabara, K., Nitta, A., *Thermal-Mechanical Low-Cycle Fatigue Under Creep-Fatigue Interaction on Type 304 Stainless Steels*, Fatigue and Fracture of Engineering Materials and Structures, Volume 2(3), pp 293-304, 1979.

Labanowski, J., Glowacka, M., *Heat Tint Colours on Stainless Steel and Welded Joints*, Welding International, Volume 25(7), pp. 509-512, 2011.

Landes, J.D., Begley, J.A., "A Fracture Mechanics Approach to Creep Crack Growth," *Mechanics of Crack Growth*, ASTM STP 590, American Society of Testing and Materials, pp. 128-148, 1976.

Lazzarin, P., Tovo, R., Meneghetti, G., *Fatigue Crack Initiation and Propagation Phases Near Notches in Metals with Low Notch Sensitivity*, International Journal of Fatigue, Volume 19(8-9), pp. 647-657, 1997.

Lee, S.R., et al., *Waveform Effect on the Low Cycle Fatigue Behavior of AISI 304 Stainless Steel at High Temperature*, Key Engineering Materials, Volumes 51-52, pp. 1-6, 1991.

Lee, S.B., Kim, J.Y., *Creep-Fatigue Crack Growth Behavior of 304 Stainless Steel at 650°C*, Theoretical and Applied Fracture Mechanics, Volume 24(2), pp. 181-188, 1996.

Leidermark, D., et al., *A Combined Critical Plane and Critical Distance Approach for Predicting Fatigue Crack Initiation in Notched Single-Crystal Superalloy Components*, International Journal of Fatigue, Volume 33(10), pp. 1351-1359, 2011.

Leven, M.M., Frocht, M.M., *Stress-Concentration Factors for Single Notch in Flat Bar in Pure and Central Bending*, Journal of Applied Mechanics, Volume 19(4), pp. 560-561, 1952.

Marahleh, G., Kheder, A.R.I., Hamad, H.F. *Creep Life Prediction of Service Expose Turbine Blades*, Materials Science and Engineering A, Volume 433(1-2), pp. 305-309, 2006.

Merah, N., Bui-Quoc, T., Bernard, M., *Creep-Fatigue Crack Growth in Notched SS-304 Plates at 600°C*, Engineering Fracture Mechanics, Volume 63(1), pp. 39-55, 1999.

Metallography Principles and Procedures, St. Joseph, MI: LECO Corporation, 2012.

Miller (I), A., *An Inelastic Constitutive Model for Monotonic, Cyclic, and Creep Deformation: Part I – Equations Development and Analytical Procedures*, Journal of Engineering Materials and Technology, Volume 98 (2), pp. 97-105, 1976.

Miller (II), A., *An Inelastic Constitutive Model for Monotonic, Cyclic, and Creep Deformation: Part II – Application to Type 304 Stainless Steel*, Journal of Engineering Materials and Technology, Volume 98 (2), pp. 106-13, 1976.

Miller, A.K., et al., *A Unified Model for Fatigue Crack Initiation and Growth, with Emphasis on Short-Crack Behavior, Crack Closure Effects, Variable-Temperature Fatigue and Creep-Fatigue Interaction*, Materials Science and Engineering A, Volume 103(1), pp. 71-93, 1988.

Mills, W.J., *Heat-To-Heat Variations in the Fracture Toughness of Austenitic Stainless Steels*, Engineering Fracture Mechanics, Volume 30(4), pp. 469-492, 1988.

NASGRO User Manual, NASGRO v6.21, Southwest Research Institute, October, 2012.

Neal, S., Zachary, L.W., Burger, C.P., *Three-Dimensional Stress Analysis of the SAE Keyhole Fatigue Specimen*, SAE Technical Paper 780104, 1978.

Neuber, H., *Theory of Stress Concentration for Shear-Strained Prismatical Bodies with Arbitrary Nonlinear Stress-Strain Law*, Journal of Applied Mechanics, Volume 28(4), pp. 444-550, 1961.

Newman, J.C., "Irwin's Stress Intensity Factor – A Historical Perspective," *Fatigue and Fracture Mechanics*, 31st Volume, Eds. Halford, G.R. and Gallagher, J.P., ASTM STP 1389, ASTM International, West Conshohocken, PA, 2000.

Newman, J.A., Riddle, W.T., Piascik, R.S., *A Threshold Fatigue Crack Closure Model: Part II – Experimental Verification*, Fatigue and Fracture of Engineering Materials and Structures, Volume 26(7), pp. 615-625, 2003.

Nix, et al., *The Principal Facet Stress as a Parameter for Predicting Creep Rupture under Multiaxial Loads*, Acta Metallurgica, Volume 37(4), pp. 1067-1077, 1989.

Noda, N.A., Takase, Y., *Stress Concentration Formulae Useful for any Shape of Notch in a Round Test Specimen under Tension and under Bending*, Fatigue and Fracture Engineering Materials and Structures, Volume 22(12), pp. 1071-1082, 1999.

Norton, R.L., *Machine Design: An Integrated Approach*, Third Edition, Upper Saddle River, NJ: Pearson Prentice Hall, 2006.

Palazotto, A.N., Mercer, J.G., *Crack Considerations in a Notched Compact Tension Specimen*, Engineering Fracture Mechanics, Volume 37(3), pp. 473-492, 1990.

Paris, P.C., "Fracture Mechanics and Fatigue: A Historical Perspective," *Fatigue and Fracture of Engineering Materials and Structures*, Volume 21(5), pp. 535-540, 1998.

Paris, P.C., Gomez, M.P., Anderson, W.E., "A Rational Analytic Theory of Fatigue," *The Trend in Engineering*, Volume 13, pp. 9-14, 1961.

Peterson, R.E., *Stress Concentration Factors*, New York, NY: John Wiley and Sons, 1974.

Piascik, R.S., Newman, J.C., *An Extended Compact Tension Specimen for Fatigue Crack Propagation and Fracture*, NASA Technical Memorandum 110243, March 1996.

Pilkey, W.D., *Peterson's Stress Concentration Factors*, Second Edition, New York, NY: John Wiley and Sons, 1997.

Piques, R., Bensussan, P., Pineau, A., *Application of Fracture Mechanics and Local Approach to Creep Crack Initiation and Growth*, ECF6 – Fracture Control of Engineering Structures, Volume 1, pp. 91-100, 1986.

Pulvinage, G., *Fatigue and Fracture Emanating from Notch; The Use of the Notch Stress Intensity Factor*, Nuclear Engineering and Design, Volume 185(2-3), pp. 173-184, 1998.

Rauch, M., Roos, E., *Life Assessment of Multiaxially Cyclic Loaded Turbine Components*, Fatigue and Fracture of Engineering Materials and Structures, Volume 34(6) pp. 441-451, 2008.

Rice, J.R., *A Path Independent Integral and the Approximate Analysis of Strain Concentration by Notches and Cracks*, Journal of Applied Mechanics, Volume 35, pp. 379-386, 1968.

Riedel, H., Rice, J.R., "Tensile Cracks in Creep Solids," *Fracture Mechanics*, ASTM STP 700, American Society for Testing and Materials, pp. 112-130, 1980.

Riley, W.F., Sturges, L.D., Morris, D.H., *Mechanics of Materials*, Sixth Edition, New York, NY: John Wiley and Sons, 2007.

Sakane, M., Ohnami, M., *Notch Effect in Low-Cycle Fatigue at Elevated Temperatures – Life Prediction from Crack Initiation and Propagation Considerations*, Journal of Engineering Materials and Technology, Volume 108(4), pp. 279-284, 1986.

Sanford, R.J., *Principles of Fracture Mechanics*, Upper Saddle River, NJ: Pearson Education Inc., 2003.

Sansoz, F., Brethes, B., Pineau, A., *Propagation of Short Fatigue Cracks from Notches in Ni Base Superalloy: Experiments and Modelling*, Fatigue and Fracture of Engineering Materials and Structures, Volume 25(1), pp.41-53, 2002.

Saxena, A., "Creep Crack Growth under Non-Steady-State Conditions," *Fracture Mechanics: Seventh Volume*, ASTM STP 905, pp. 185-201, 1986.

Saxena, A., "Fracture Mechanics Approaches for Characterizing Creep-Fatigue Crack Growth," *JSME International Journal Series I*, Volume 36(1), pp. 1-20, 1993.

Saxena, A., Williams, R.S., Shih, T.T., "A Model for Representing and Predicting the Influence of Hold Time on Fatigue Crack Growth Behavior at Elevated Temperature," *Proceedings of Fracture Mechanics: Thirteenth Conference*, pp. 86-99, 1981.

Schijve, J., *Fatigue of Structures and Materials*, Second Edition, New York, NY: Spring Science+Business Media LLC, 2009.

Schijve, J., *Stress Gradients Around Notches*, Report LR-297, Delft University of Technology, April, 1980.

Schmidt, M., Lipson, H., *Distilling Free-Form Natural Laws from Experimental Data*, *Science* Magazine, Volume 324(5923), pp. 81-85, 2009.

Shih, C.F., *Relationship between the J-Integral and the Crack Opening Displacement for Stationary and Extending Cracks*, Journal of the Mechanics and Physics of Solids, Volume 29(4), pp. 305-326, 1981.

Shimada, H., Furuya, Y., *Local Crack-Tip Strain Concept for Fatigue Crack Initiation and Propagation*, Journal of Engineering Materials and Technology, Volume 109(2), pp. 101-106, 1987.

Smith (I), E., *The Relationship Between the Peak Stress for a Blunt Flaw and the Stress Intensity Factor for an Equivalent Crack*, Proceedings of the ASME PVP2010, PVP2010-25116, Bellevue, WA, USA, July 18-22, 2010.

Smith (II), E., *A Simple Criterion for Fracture Initiation at the Root of a U-Shaped Flaw*, Proceedings of the ASME PVP2010, PVP2010-25081, Bellevue, WA, USA, July 18-22, 2010.

Stephens, R.I., et al., *Metal Fatigue in Engineering*, Second Edition, New York, NY: John Wiley and Sons, 2001.

Sugiura, R., et al., *Creep Crack Initiation and Growth Characteristics in Weldment for P92 Based on C*, dδ/dt and Q* Parameters*, Strength, Fracture and Complexity, Volume 6(4), pp. 177-189, 2010.

Tanaka, K., Nakai, Y., Kawashima, R., *Fracture Mechanics Approach to Fatigue Crack Initiation from Deep Notches*, Engineering Fracture Mechanics, Volume 18(5), pp. 1011-1023, 1983.

Tracey, D.M., *Finite Element Solutions for Crack Tip Behavior in Small Scale Yielding*, Journal of Engineering Materials and Technology, Volume 98(2), pp. 146-151, 1976.

Tsuji, K., Ando, K., *Effects of Notch Root Radius on Both Crack Initiation Sites and Fracture Toughness of Ceramics and Steel*, Proceedings of 12th Biennial European Conference on Fracture, ECF12, Sheffield, UK, September 14-18, pp. 539-544, 1998.

Vardar, O., Kalenderoglu, V., *Effect of Notch Root Radius on Fatigue Crack Initiation*, Material Science and Engineering: A, Volume 114, pp. L35-L38, 1989.

Wetzel, R.M., *Fatigue Under Complex Loading: Analyses and Experiments*, Ed. R.M. Wetzel, Warrendale, PA: Society of Automotive Engineers, 1977.

Wilson, W.K., *Elastic-Plastic Analysis of Blunt Notched CT Specimens and Applications*, Journal of Pressure Vessel Technology, Volume 96(4), pp. 293-298, 1974.

Wu, Y.S., *The Improved Neuber's Rule and Low Cycle Fatigue Life Estimation*, ASTM STP942, pp. 1007-1021, 1988.

Yamada, Y., Newman, J.C., *Crack Closure under High Load-Ratio Conditions for Inconel-718 Near Threshold Behavior*, Engineering Fracture Mechanics, Volume 76(2), pp. 209-220, 2009.

Yan, X., Nie, J., *Creep-Fatigue Tests on Full Scale Directionally Solidified Turbine Blades*, Journal of Engineering for Gas Turbines and Power, Volume 130(4), pp. 044501(1-5), 2008.

Yang, H., et al., *Creep-Fatigue Crack Growth Behavior of a Nickel-Based Powder Metallurgy Superalloy under High Temperature*, Engineering Failure Analysis, Volume 18(3), pp. 1058-1066, 2011.

Yoon (I), K.B., Saxena, A., Liaw, P.K., *Characterization of Creep-Fatigue Crack Growth Behavior under Trapezoidal Waveshape using C_t-Parameter*, International Journal of Fracture, Volume 59(1), pp.95-114, 1993.

Yoon (II), K.B., Saxena, A., McDowell, D.L., *Effect of Cyclic Overload on the Crack Growth Behavior during Hold Period at Elevated Temperature*, International Journal of Fracture, Volume 59(1), pp. 199-211, 1993.

Zhan, Z.L., Tong, J., "A Study of Creep-Fatigue Interaction in a New Nickel-Based Superalloy," *Damage and Fracture Mechanics VIII*, Eds. Brebbia, C.A. and Varvani-Farahani, A., Ashurst, Southampton, UK: WIT Press, 2004.

Zhang, G., Yuan, H., Li, F., "Analysis of Creep-Fatigue Life Prediction Models for Nickel-based Super Alloys," *Computation Materials Science*, Volume 57, pp. 80-88, 2012.